Technische Universität München

Fakultät für Physik
Lehrstuhl E21/E51

Creation and manipulation of positronium for efficient antihydrogen production at AEGIS

Benjamin Rienäcker

Vollständiger Abdruck der von der Fakultät für Physik der Technischen Universität München zur Erlangung des akademischen Grades eines

Doktors der Naturwissenschaften (Dr. rer. nat.)

genehmigten Dissertation.

Vorsitzender:	Prof. Dr. Martin Zacharias
Prüfer der Dissertation:	
	1. Prof. Dr. Christoph P. Hugenschmidt
	2. Prof. Dr. Roberto S. Brusa

Die Dissertation wurde am 17.03.2021 bei der Technischen Universität München eingereicht und durch die Fakultät für Physik am 11.05.2021 angenommen.

Abstract

Antimatter, although part of our physical reality, can neither be naturally observed in significant amounts on our Earth, nor in the whole known universe. According to our current understanding of physics, however, we should: the Big Bang is supposed to have created both matter and antimatter in equal amounts. Experiments such as AE$\bar{g}$IS (Antimatter Experiment: Gravity, Interferometry, Spectroscopy) at CERN have accepted the challenge to look for the tiny difference between both species that could be the foundation for an explanation of the missing antimatter. The AE$\bar{g}$IS collaboration aims to create a pulsed source of cold and neutral antihydrogen atoms and let them freely fall inside a controlled experimental environment in order to explore the effect of gravity on antimatter with high precision for the first time.

In the course of this thesis, AE$\bar{g}$IS methods will be presented, including the production of cold positronium and its subsequent laser excitation, and the charge exchange reaction between cold antiprotons from the Antiproton Decelerator at CERN and Rydberg-positronium. As an important milestone, the experimental confirmation of 110 ± 25 produced antihydrogen atoms is given. In the next phase, the experiment will be thoroughly upgraded, before gravity will act on a pulse of freely falling antihydrogen. Two research objectives were motivated by AE$\bar{g}$IS requirements, constituting the central part of the presented work. The first objective was a detailed study on the production of Rydberg-positronium, on its velocity distribution and on its self-ionizing behavior within a 1 T magnetic field and 10 K cryogenic environment. The second research topic was the development of positronium targets in transmission geometry, since all commonly used converters so far have worked exclusively in reflection geometry.

Positronium production, its excitation and the charge exchange reaction at AE$\bar{g}$IS happened at three different positions inside the experiment, separated by a few millimeters. This demanded a precise knowledge of the velocity distribution in order to synchronize the two exciting laser pulses with the quickly expanding positronium cloud. Moreover, since the cross-section for the formation of antihydrogen via charge exchange reaction falls rapidly off beyond an upper positronium velocity, the addressed velocity range had to be carefully chosen. The selected Rydberg-levels were close to the ionization threshold, and the strong magnetic field induced a so-called motional Stark electric field that partly caused Ps ionization. Therefore, the correct choice of the effective Rydberg level was also part of the overall optimization achieved in this work.

The cross-section for antihydrogen production not only falls rapidly off beyond an upper velocity limit, but it also gets strongly enhanced below a lower limit that until now had not been accessible. The development of transmission positron/positronium converter targets in the form of nanochanneled silicon membranes finally unlocked this long-desired range. A first sample with about 10 µm thickness yielded about 5 % transmitted positronium with respect to the total number of implanted positrons, but ongoing improvements on the method allow to expect up to 20 % of Ps emission in transmission for membranes with 2 µm thickness.

Zusammenfassung

Obwohl Antimaterie real existiert, kommt sie natürlicherweise weder auf der Erde noch im gesamten bekannten Universum in signifikanten Mengen vor. Nach unserem derzeitigen Verständnis der Physik sollte dies jedoch der Fall sein: Der Urknall sollte sowohl Materie als auch Antimaterie gleichermaßen erschaffen haben. Experimente wie AEgIS (Antimaterie-Experiment: Schwerkraft, Interferometrie, Spektroskopie) am CERN haben sich der Herausforderung gestellt, nach jenem winzigen Unterschied beider Arten zu suchen, der die Grundlage für eine Erklärung der fehlenden Antimaterie bilden könnte. Die AEgIS-Kollaboration erschafft eine gepulste Quelle für kalte, neutrale Antiwasserstoffatome und wird diese Atome in einer kontrollierten experimentellen Umgebung frei fallen lassen. So lässt sich die Wirkung der Schwerkraft auf Antimaterie zum ersten Mal mit hoher Präzision untersuchen.

Im Rahmen dieser Doktorarbeit werden AEgIS Methoden vorgestellt, einschließlich der Herstellung von kaltem Positronium und dessen anschließende Laseranregung, sowie die Ladungsaustauschreaktion zwischen kalten Antiprotonen und Rydberg-Positronium. Als wichtiger Meilenstein wird die experimentelle Bestätigung von 110 ± 25 produzierten Antiwasserstoffatomen präsentiert. In der nächsten Phase wird AEgIS grundlegend verbessert, bevor schließlich die Schwerkraft selbst auf einen Puls frei fallender Antiwasserstoffe wirken wird. Insbesondere zwei zentrale Forschungsziele der vorliegenden Arbeit wurden durch die Anforderungen von AEgIS motiviert. Das erste ist eine detaillierte Studie zur Produktion von Rydberg-Positronium, zu dessen Geschwindigkeitsverteilung und zu dessen Selbstionisierung in einem 1 T starken Magnetfeld und in einer 10 K kalten Umgebung. Das andere Ziel ist die Erforschung von Positroniumsquellen in Transmissionsgeometrie, da bisherige Konverter ausschließlich reflektiv arbeiten.

Die Produktion und Anregung von Positronium sowie schließlich die Ladungsaustauschreaktion fanden an drei verschiedenen Positionen innerhalb der AEgIS-Apparatur statt, die mehrere Millimeter weit voneinander entfernt waren. Dies machte eine genaue Kenntnis der Geschwindigkeitsverteilung erforderlich, um die beiden anregenden Laserpulse mit der sich schnell ausbreitenden Positroniumswolke zu synchronisieren. Da zudem der Wirkungsquerschnitt für die Antiwasserstoffproduktion jenseits eines oberen Geschwindigkeitswertes des Positroniums stark abfällt, musste der Geschwindigkeitsbereich exakt ausgewählt werden können. Ferner lag das adressierte Rydberg-Niveau so nahe an der Ionisationsschwelle, dass ein induziertes elektrisches Feld zu Selbstionisation führte. Daher ging auch die Niveauswahl in die Gesamtoptimierung mit ein.

Der Wirkungsquerschnitt für die Antiwasserstoffproduktion fällt nicht nur jenseits einer Obergrenze schnell ab, sondern steigt auch unterhalb einer Untergrenze, die bisher nicht zugänglich war, stark an. Die Entwicklung von Transmissionskonvertern für Positronium in Form von Nanokanal-Silizium-Membranen erschließt nun diesen lang ersehnten Bereich. Eine erste Probe mit einer Dicke von 10 µm ergab etwa 5 % transmittiertes Positronium bezogen auf die Anzahl implantierter Positronen. Weiterführende Verbesserungen der hier entwickelten Methode lassen erwarten, dass eine Ps Konversion mit einer Effizienz von bis zu 20 % bei 2 µm dicken Membranen erreicht wird.

Scientific revolutions don't change the universe. They change how humans interpret it.

Terry Pratchett, Ian Stewart, Jack Cohen
The Science of Discworld IV: Judgement Day

Contents

Chapter 1

Introduction

It is impressive to see the experimental complexity of an apparatus designed to create just a few atoms of antimatter, whereas a whole universe of matter — but also of antimatter according to our current understanding — was coming to existence from a single Big Bang. Then, the universe's antimatter half was hurriedly locked away from our curious eyes, as if something was just not right about it. In fact, there are many approaches to explain that missing part. One hypothesis states that huge clusters of antimatter galaxies actually might exist, but they are too far away to be detected and possibly even shielded by normal matter, separated by a kind of Leidenfrost-layer[1]; another explanation comprises different net production rates of baryons and anti-baryons plus a violation of the charge symmetry (C-symmetry), of the charge-parity symmetry (CP-symmetry) and of the time symmetry (T-symmetry). These symmetry breakings are required so that imbalanced production processes cannot simply be compensated by anti-symmetric ones (so-called Sakharov conditions, [2]). A new, rather speculative approach states that actually two universes with opposing time directions originate from the Big Bang - one is our matter universe, the other is an antiuniverse developing into the past (from our point of view). Differently put, the pre- and post-Big Bang eras give rise to a universe-antiuniverse pair, working well quantum mechanically, classically and it does not violate universal symmetry [3]. This approach basically shifts the baryon asymmetry problem to how we consider time itself. As a remark, this approach might shade a new light on the reversed time-arrow we assign to antimatter particles since Feynman [4].

The proposed imbalance in baryon-antibaryon production is currently in the focus of experimental physics, because several symmetry violations have already been identified [5, 6, 23]. Despite the efforts, no baryon asymmetry was experimentally established up to this day. In fact, antimatter always behaved as predicted by our current standard model, symmetric to normal matter. But not all features have yet been investigated. For example,

how does gravity affect antiparticles? Can we describe it with a quantum gravity theory[1]? Are really all energy level transitions the same as they are for normal matter? Maybe there are more symmetry violations still hidden from us? And then there is that set of questions which leaves our current standard model of physics completely behind. What actually are dark matter and dark energy that some believe are making up a major part of our universe? Which particles and basic theories haven't we found yet and really, once again, how does gravity work on the quantum level?

Open questions, which initiate not only theoretical work, but also experimental. The CERN institute, an international organization for Nuclear Research (Conseil Européenne pour la Recherche Nucléaire), provides the world's largest hadron collider, namely the well-known LHC, which allows to probe energy densities close to conditions shortly after the Big Bang. A great result has been the discovery of the long-sought Higgs-boson in the year 2012 [7, 8] — the unique boson which proved the existence of the Higgs-field. The 'accelerating infrastructure' at CERN also allows for additional experimental environments such as ISOLDE, AWAKE or AD/ELENA, which are driven by the same initial accelerators. An overview of all CERN's experimental complexes is given in Fig. 1.1. These other, smaller instances of CERN follow individual physics programs with specific goals.

ISOLDE (Isotope Separator On Line DEvice), for example, produces radioactive ion beams by steering a proton beam on a heated target and separating the radioactive nuclei that are emitted. These beams drive plenty experiments in biophysics, medicine or material science. AWAKE (Advanced WAKEfield Experiment) could be considered a prototype for future accelerators, aiming to accelerate charged particles from MeV to GeV over a distance of 10 m only — this is orders of magnitude less than traditional ring or linear accelerators require [10]. The AD (Antiproton Decelerator) is a specialty at CERN, as it actually slows down particles rather then speeding them up. It catches a fast antiproton bunch produced in proton-target collisions and provides, after several cooling stages, a slow antiproton beam with 5.3 MeV kinetic energy for experiments with antimatter. In fact, even colder antiprotons would be preferable for a higher catching efficiency, which is why the ELENA-ring (Extra Low ENergy Antiproton ring) was set up [11]. Antiprotons were already successfully injected in 2017 and ELENA's cooling stage was installed at the end of 2018. Now, it is in commissioning and by 2021 antiprotons with just 100 keV will be supplied to all connected experiments.

So far, the AD has supplied six major experiments with antiprotons: AE$\bar{g}$IS (Antimatter Experiment: Gravity, Interferometry, Spectroscopy), ALPHA (Antihydrogen Laser Physics Apparatus), ASACUSA (Atomic Spectroscopy And Collisions Using Slow Antiprotons),

[1] In fact, a working quantum theory including gravitational effects does not even exist

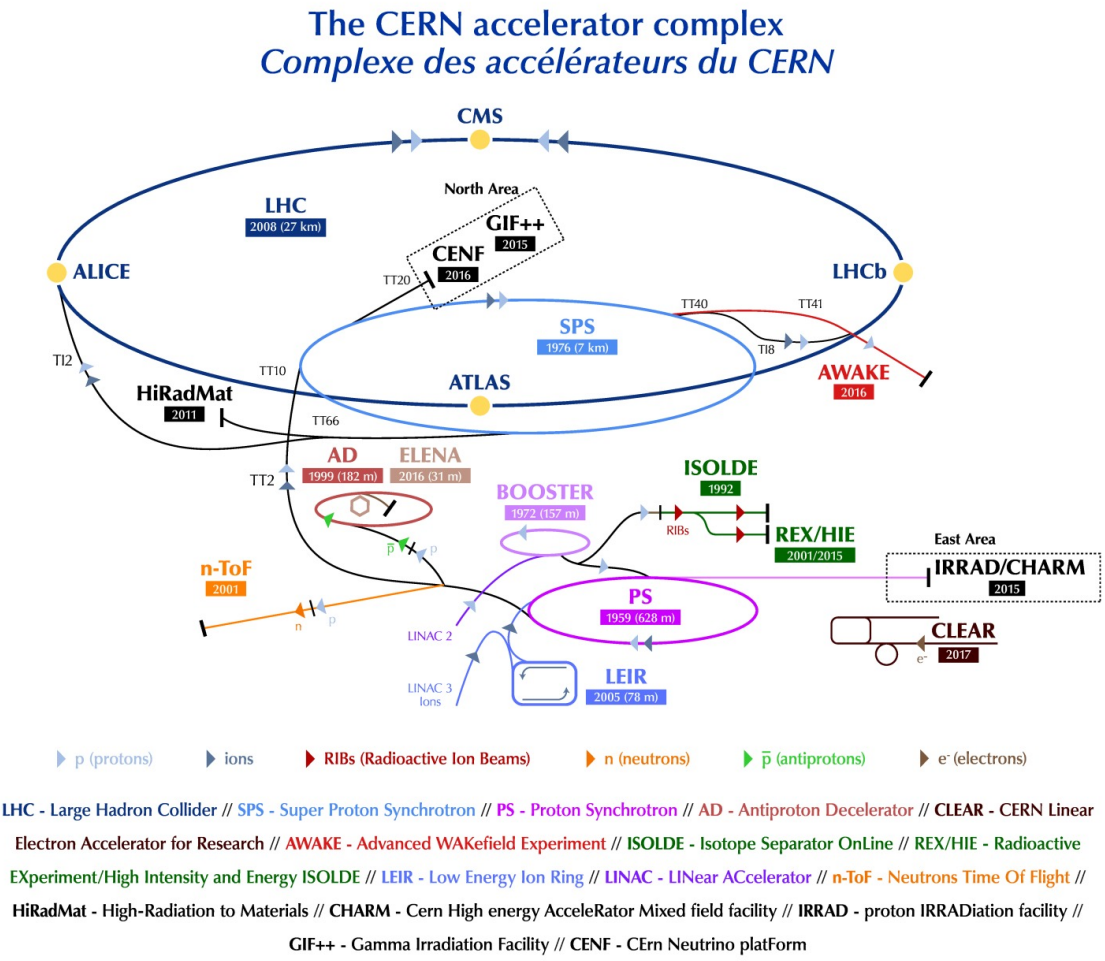

Figure 1.1: Overview of the CERN accelerator complex. (Image from Ref. [9]).

ATHENA, ATRAP and BASE (Baryon Antibaryon Symmetry Experiment). As soon as ELENA takes over, also GBAR (Gravitational Behaviour of Antihydrogen at Rest) and ALPHA-g will be joining in. All these experiments follow two main scientific directions: Testing gravity and testing symmetries on antimatter, aiming to find out a few more truths about our universe.

Charged and neutral antimatter

The first antimatter particle was discovered in 1932, four years after Dirac postulated the existence of a positively charged 'hole in an almost completely filled sea of negative energy electrons' [12]. This was an accurate description of everything around a new particle without actually naming it: the positron (e^+), whose trace Anderson correctly identified among many others caused by cosmic rays on photographs obtained with a cloud chamber [13]. He estimated that its charge has to be similar to the charge of a proton, and its inertial mass had to be less than twenty times the electron mass. In the course of finding the positron, Anderson already predicted the possibility to bind positrons and electrons together in a neutral hydrogen-like state now called positronium (Ps). It took nineteen years more, though, before Deutsch found evidence for the formation of positronium in gases [14].

In 1955, the antiproton $\bar{p}$ was discovered when Chamberlain and others hit a 6.3 GeV proton beam onto a copper target [15]. The energy was just enough to produce very slowly moving proton/antiproton pairs, which could be magnetically separated and identified by scintillators. One year later, also the antineutron $\bar{n}$ was observed. From this moment on, it became possible to craft antimatter atoms by combining different antiparticles, although the efforts and difficulties to do so have always been enormous. Up to now, only few antimatter systems could be produced in such numbers that they became meaningful for experiments with antimatter. These systems are: antihydrogen ($\bar{H}$), which consists of an antiproton and a positron; positronium (Ps), made of one positron and one electron; protonium (Pn), the bound state of an antiproton and a proton; antiprotonic helium, where one electron is substituted with a negatively charged $\bar{p}$. Then, by adding more positrons or electrons to these systems, it is possible to construct positively or negatively charged ions. Even di-positronium molecules (Ps_2) have been produced as reported by Cassidy and Mills [16].

After the first creation of antiprotons, it took about fifty years more before the ATHENA and ATRAP collaborations, both located at CERN, developed reliable procedures to produce several atoms of antihydrogen. This was possible due to the availability of slow antiprotons from the antiproton decelerator, which provided bunches of about 3×10^7

antiprotons every two minutes — the typical cycle length of antiproton production and cooling as presented in Section 2.2. Both collaborations observed antihydrogen formation independently from each other. ATHENA concluded its first successful $\bar{H}$ production from a strong excess of annihilation radiation that occurred at the right time and in the right position [17], whereas ATRAP used the 'background-free' method of field ionization for detection. This way to detect particles works well if the sought-for particle is initially neutral, but internally consists of two charged constituents that can separate under the influence of a strong electric field. Furthermore, since in the case of antihydrogen these constituents also consist of antimatter, they leave a unique energy signature in the moment they touch normal matter and annihilate [18].

ATRAP went on from its first antihydrogen production to a more advanced formation technique: the charge exchange reaction. Cesium atoms were excited to Rydberg-levels with a specially designed laser system and overlapped with a positron cloud. Then, the outer electron from cesium transferred to the positron and formed Rydberg-positronium. This excited positronium in turn reacted with antiprotons creating Rydberg-antihydrogen, fully controlled by the initial laser excitation [19]. A few years ago, they also managed to trap ground state $\bar{H}$ within a 2D-quadruple magnetic field for several minutes [20]. ATHENA was disbanded after cold antihydrogen was produced for the first time and two new collaborations were founded: AE$\bar{g}$IS and ALPHA. Both started with a lot of knowledge in the field of antihydrogen production. By 2011, ALPHA managed to confine hundreds of $\bar{H}$ atoms for more than 1000 s in the field of an octupole magnet [21], while AE$\bar{g}$IS pursued the route of charge exchange in order to produce a pulse of cold antihydrogen (see Section 2.1).

Antimatter and CPT invariance

As was mentioned above, there is a fundamental theorem put up firstly by Schwinger, Lüders and Pauli between 1951-1955 which led to a first formulation of the invariance of simultaneous transformations of charge, parity and time (CPT) [22]. Invariance means that the same physical laws hold before and after such a threefold transformation. The transformation of charge means to switch its sign - thus matter becomes antimatter and vice-versa. This process is also called charge conjugation and the symmetry here denotes that every fundamental charged particle has an antiparticle. Note that for example the neutron actually consists of charged quarks with each having its antiquark, so indeed there is an antineutron. Parity transformation of a particle can be imagined as a point reflection at one point in space. One can assign a handedness to the particle that depends on its spin, and if a parity transformation reproduces the same particle with the same handedness, it

is P-invariant. Time transformation can be quickly noted down as time-reversal, a switch of sign. This may seem a rather risky operation as on the macroscopic scale we seem to experience many asymmetries in the flow of time: It makes quite a difference to us if we get older or suddenly younger again. But for particles on the quantum level both directions work the same way and cannot be distinguished. A visual model would be the elastic collision of two hard spheres on a table. If you record a (not very interesting) video of the two spheres approaching each other, colliding and then moving apart while conserving energy and momentum, you will not be able to say if the video is played forwards or backwards — the process is time-invariant.

Albeit the universal CPT invariance cannot be proved as it is a postulate, so far no violation has been observed. Differently though for 'smaller' combinations like CP-symmetry, where violations have been measured. Interestingly, this seems to imply that there always are corresponding time reversal violations making up for the other asymmetries so that CPT invariance is generally maintained. Time symmetry violation has indeed been experimentally observed for a meson system in 2012 [23]. Summing up, all tests especially over the last two decades showed that CPT invariance holds [24]. Hence, any sign of new violations of CP and T symmetry in the search for all of the missing antimatter in our universe would be very welcome. And since it is doable now, why not testing these symmetries directly with antimatter?

ALPHA, ASACUSA, BASE and ATRAP aim for precision spectroscopy on antimatter systems and already have achieved milestones on that road: ASACUSA first demonstrated in-flight hyperfine spectroscopy on antihydrogen atoms in 2014 [25]. ALPHA achieved the 1S-2S transition of trapped antihydrogen, while the result agrees with CPT invariance at a relative precision of 2×10^{-12} [26]; they also observed the 1S-2P (Lyman-α) transition with a relative precision of 5×10^{-8} in the year 2018 [27]. Recently, BASE reported the so-far best direct estimate for the intrinsic antiproton-lifetime, which is greater than 10 years. This may be still far below the known proton-lifetime of 1×10^{34} years, but protons are clearly a lot easier to handle [28]. They also published the most accurate magnetic moment measurement of antiprotons and constrained CPT violation effects to occur below 1.8×10^{-24} GeV [29]. In conclusion, up to this day no violation of CPT invariance was observed at experimentally accessible precision, which already indicates a high symmetry between matter and antimatter.

Antimatter and gravity

There is yet another postulate that is one of the foundations of general relativity. It has never been disproved up to this day: the Equivalence Principle (EP). Although it

was already implicitly stated in the 17th century by Galileo ('gravitational acceleration of a test mass does not depend on the amount of mass'), it was Einstein in 1907 who described it properly: '[...] and in the discussion that follows, we shall therefore assume the complete physical equivalence of a gravitational field and a corresponding acceleration of the reference system' [30]. This suggested that gravity might be a purely geometrical effect of a deformed space-time, and any free-falling body with no external forces attacking it will just move along its trajectory in a straight line (in accordance to the first Newtonian law). This holds even under the generalization that a 'straight line' in space-time tends to be an unimaginable object, because masses or energies deform the four-dimensional space-time itself. Any non-accelerated moving body must then follow the so-called geodesics, the equivalent of a straight line for curved surfaces. The gravitational lens is an example for this effect. Light from a far-away source seems to bend around great masses on its way to Earth's telescopes. However, this model is less intuitive to deal with. If one imagines a pebble being released from a high tower, it initially seems to be at rest. The apparent acceleration that can be observed immediately after is therefore even today conveniently treated as the effect of a gravitational pull.

However, also in the case of the pebble we can arrive at a different explanation without the concept of a fundamental interaction. Shortly after being released, the pebble may be resting with respect to Earth, but it is still moving relative to a universal rest-frame and most importantly, also through time. It thus has a general velocity vector different from zero, which it will keep in the absence of external forces. If now space-time is locally deformed due to Earth, the 'straight line' again is a curved geodesic. Hence, in order to conserve its total energy, the pebble has to follow this geodesic in space-time, which to our eyes looks just like it is accelerating towards the center of Earth. This also holds for the made-up case in which Earth and the pebble are not moving in space, but only in time. Finally, if the pebble was not moving at all, neither in space nor in time, only then the pebble would truly remain still - we would consider this as being frozen in time. As a side note, also Earth has to accelerate an ever so tiny bit towards the center of the pebble, since its small mass is also able to gently deform space-time.

This geometric modeling has the advantage that it does not need any further assumptions such as a 'gravitational charge', better known as gravitational mass m_g, which is affected by gravity if considered as a real interaction. It also explains why massless photons, the force carriers of electromagnetism, react to gravity. Furthermore, since photons have energy, they are even able to slightly deform space-time themselves, i.e. generate a gravitational effect, but due to its smallness it has never been directly measured until now. Conversely, if gravity was treated in the same manner as the electromagnetic, the strong and the weak interaction, which can be successfully described by the standard model, one

also has to assume force carriers mediating gravity (*gravitons*). However, not only hasn't there been any experimental trace of gravitons until now, but even from the theoretical point of view one cannot apply the usual quantum theories to gravity without producing contradictions. For this reason, one prefers to maintain the traditional model of gravity and to postulate the validity of the Equivalence Principle, which states the identity of inertial mass m_i of an object (i.e. rest mass) and its gravitational mass m_g.

The EP comes in a strong and in a weak form. This is due to the fact that the mass of a body does not only originate from its constituents, but also from the binding energies between them. The Equivalence Principle is called *strong*, when distinguishing the gravitational effects due to (subatomic) rest masses and due to binding energies — including those originating from gravity itself as occurs in huge bodies like stars. Conversely, when subsuming these contributions into just one effective point mass, one obtains the *Weak* Equivalence Principle (WEP). The WEP is very well-suited to describe particles with no or at least weak binding energies such as positronium, where only electromagnetic interaction occurs — neglecting the higher order loop corrections due to virtual particles. Already for protons/antiprotons, however, the majority of the rest mass stems from the strong interaction between the quarks, which is why results regarding the WEP have to be carefully thought through here.

One of the latest and so far most precise direct test of WEP was achieved with the *MICROSCOPE* satellite in 2017. The satellite contains an apparatus designed to measure the force required to keep two test masses in exactly the same orbit. After a first data taking, this resulted in a 'WEP test value' of $(0.1 \pm 1.3) \times 10^{-14}$, compatible with a null result with a relative precision one order of magnitude higher than was ever achieved before [31]. As direct tests of WEP are becoming more and more precise, any possible difference between gravitational and inertial mass is limited to values below the current precision — but only for normal matter. Measurements of this kind for antimatter did not reach a meaningful precision yet. In fact, the only direct measurement on *neutral* antimatter was performed by the aforementioned ALPHA collaboration in a free fall experiment. They released $\bar{\mathrm{H}}$ from a magnetic trap into vacuum. That put limits to the ratio of gravitational to inertial mass of antimatter in the context of WEP, which are $-65 < \bar{\mathrm{m}}_g/\bar{\mathrm{m}}_i < 110$, at a statistical significance level of 5% under the assumption of worst-case systematic effects [32] — a result that does not rule out many suggested models.

The possibility of WEP tests with *charged* antimatter systems was investigated, dating back to 1968. The researchers Witteborn and Fairbank attempted a free fall experiment with electrons and positrons [33]. They arrived at the conclusion that it is not possible to control the experimental environment well enough to perform this measurement. Nonethe-

less, there are indirectly obtained bounds for $\bar{m}_g/\bar{m}_i$ derived from observations like the missing vacuum Cherenkov radiation at the Large Electron-Positron Collider (LEP) that was maintained at CERN until the year 2000. These observations suggest more restrictive bounds for that ratio (1 ± 0.04 as reported by Kalaydzhyan in 2015 [34]), ruling out repulsive anti-gravity. But of course, all indirect bounds are strongly model-dependent, so it remains to develop a direct measurement with acceptable precision.

ALPHA-g, GBAR and AE$\bar{\text{g}}$IS have the declared goal to measure $\bar{\text{g}}$, the gravitational constant of antimatter in Earth's gravitational field and test the validity of the Weak Equivalence Principle for antimatter. All three experiments follow slightly different routes to reach that goal and are still in commissioning. ALPHA-g builds on its well-established $\bar{\text{H}}$ production scheme and plans to use a vertical free fall chamber. The initial precision will be enough to make a statement on the sign of $\bar{\text{g}}$ and possibly give a first estimate of the numerical value. GBAR aims to use the $\bar{\text{H}}^+$ ion, as it can be freely manipulated and easily confined due to its charge. By photodetachment, the ion becomes neutral and $\bar{\text{H}}$ which will be allowed to fall freely. Measuring the time it needs to fall for a known distance reveals $\bar{\text{g}}$ with a precision of 1 %. The construction of AE$\bar{\text{g}}$IS was completed in 2012, since then the experiment has advanced towards a stable and reliable procedure designed to produce cold antihydrogen atoms in pulsed operation by means of charge exchange reaction. The $\bar{\text{H}}$ atoms will be formed into a beam during the next phase and the gravity-caused displacement of the beam will be detected by atomic interferometry. In summary, all three experiments produce and measure with antihydrogen, which requires the reliable provision of cold antiprotons from the AD/ELENA at CERN.

Positronium, the second neutral system that contains antimatter and that can be produced in greater numbers, has also been considered as a test ground for gravity. An experimentally driven study, as reported in [35], led to the statement that within current (2002) technical limits it was hardly possible to use Ps for a gravity measurement. Reasons are the very small mass ($2m_e$) and short lifetime (142 ns in ground state). The latter problem can be avoided by exciting positronium to high Rydberg-states, but then these Rydberg-atoms are highly polarizable and thus are even more subject to smallest environmental influences. Nonetheless, recent developments on Ps manipulation, also some of those presented in this thesis, may eventually overcome the technical difficulties.

Framework of this thesis

The objective of this thesis is to report the advances on positronium production, manipulation and detection, embedded in the experimental environment of the antimatter experiment AE$\bar{\text{g}}$IS at CERN. In Chapter 2, the AE$\bar{\text{g}}$IS apparatus and experimental proce-

dures will be described, giving an insight of how the experiment is designed and performing. This chapter will also present the current state and measurement results obtained between 2015 and 2019, including a newly developed method for determining the absolute fraction of positronium emission from a target surface. Then, two special topics will be treated in Chapters 3 and 4 which comprise the author's main research and contributions to the physics community.

The first research topic will be about velocity studies on Rydberg-positronium emitted from a nanoporous silicon target in reflection geometry, which was required to optimize the antiproton/Rydberg-Ps interaction for $\bar{\mathrm{H}}$ formation in a high 1 T magnetic field and at 10 K cryogenic temperature. Doppler measurements will reveal the transverse velocity distribution aligned with the propagation direction of the exciting laser beams. Delaying these beams with respect to the instant of positron implantation will allow to perform a time-of-flight (TOF) experiment. Results of such TOF measurements will then be used to infer the Ps velocity distribution approximately normal to the target surface. Additionally, due to the movement of excited Ps inside the magnetic field, also ionization due to self-induced electric fields occurs and will be studied in order to find the optimal laser position, the best laser delay and the highest addressable Ps Rydberg-state for a maximum $\bar{\mathrm{H}}$ production cross-section. This research will allow AE$\bar{\mathrm{g}}$IS to significantly enhance their antihydrogen production rate.

The second research topic, presented in Chapter 4, will be about the production and investigation of positron/positronium converter targets in transmission geometry, a technique that experiments involving Ps beam formation would greatly benefit from. Until now, the vast majority of targets used for Ps production have worked in reflection geometry, which means that one had to retrieve Ps from the same surface as positrons got implanted into before. This caused geometrical and procedural restrictions when aiming to generate a Ps beam. In this work, a well-established technique for Ps creation and cooling with porous silicon will be further developed, until thin membranes with the ability to emit Ps in transmission are achieved. First measurements on these membranes will indicate their potential to play an important role in the future of AE$\bar{\mathrm{g}}$IS, and possibly also other Ps beam experiments. A model will be introduced in order to reasonably describe the measured Ps signal, from which the maximum fraction of Ps being emitted in transmission can be estimated.

Chapter 2

AEgIS, an antimatter experiment

The use of antimatter in experiments is challenging, not only because there is almost no natural supply for it, but also because of short lifetimes, small producible amounts and high loss rates following the difficulties of confinement. All these restrictions have to be taken into account when designing a setup aiming to measure the effects of gravity or level splittings on antimatter systems with meaningful precision. This chapter focuses mostly on the AEgIS apparatus and its procedure of antihydrogen production, but many of the techniques introduced here are widely used in all antimatter experiments and, more generally, in the field of nuclear and atomic physics.

2.1 AEgIS experimental overview

AEgIS produces antihydrogen by means of charge exchange reaction between Rydberg-Ps (Ps*) and antiprotons. The production scheme of the experiment is depicted in Fig. 2.1. A bunch of few 10^6 positrons with kinetic energy of 4.6 keV, approximately 5 ns time spread (sigma) and 0.5 mm spot diameter is implanted into a positron/positronium converter target, tilted by 30° against the beam axis. The porous silicon target is designed to efficiently produce and cool Ps by inelastic collisions within the internal structure, so called *nanochannels*, while being able to withstand the cryogenic environment of about 10 K. Positronium with a few hundred meV is then excited after a short delay in two steps by two laser pulses firing at 10 Hz. The first pulse is ultraviolet (UV), around 205 nm, and is used to excite Ps via $1^3\mathrm{S} \rightarrow 3^3\mathrm{P}$. The subsequent pulse is infrared (IR), namely between 1670 nm to 1720 nm, and excites positronium from $3^3\mathrm{P}$ to Rydberg levels ($n \approx 14 \ldots 21$). Excited Ps lives long enough to enter from the open top into a Penning-Malmberg trap storing cold antiprotons. As soon as Rydberg-Ps and antiprotons mix, they can perform

the charge exchange reaction and create excited antihydrogen with a temperature equal to that of the antiprotons, since the mass ratio between positron and antiproton does not allow to exchange more momentum. The supply of a pulse of 3×10^7 antiprotons with a kinetic energy of 5.3 MeV depends on the cycle length of the antiproton decelerator, which is about two minutes. During this time, positrons are accumulated and used to produce Rydberg-Ps on demand.

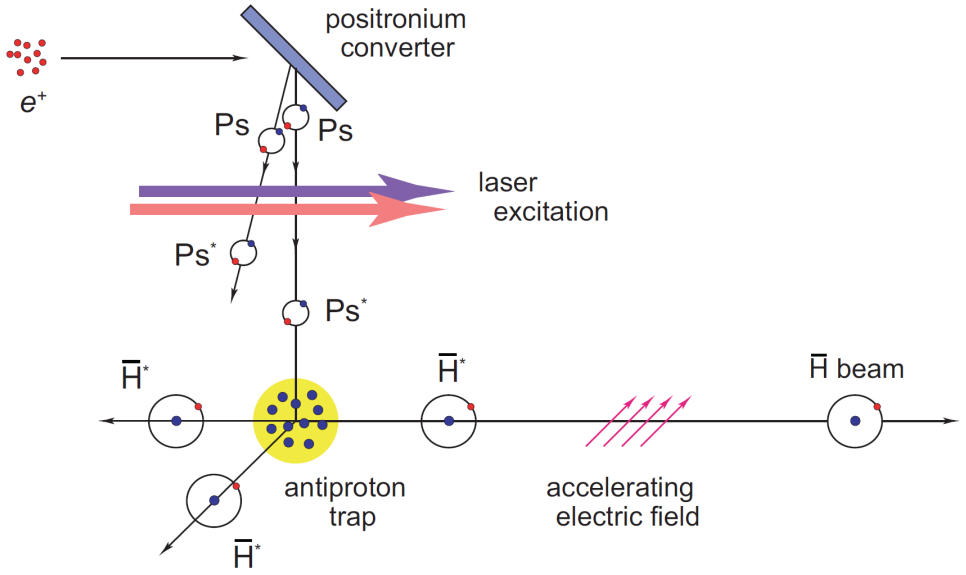

Figure 2.1: Schematic of AEgIS antihydrogen production via charge exchange reaction between cold antiprotons and Rydberg-positronium atoms. (Image from Ref. [36]).

Currently at AEgIS, antihydrogen is expected to come as a neutral particle pulse in a 4π sphere without any confinement or manipulation. If the flux on-axis is high enough, the aspired measurements can be performed directly. Otherwise, an electric field gradient can be applied to the neutral, but polarizable antihydrogen atoms in order to generate a beam in the desired direction [37]. Gravity will affect the $\bar{H}$ atoms in-flight, and it remains to detect the resulting vertical displacement. The envisioned technique to measure the effect of gravity is atomic interferometry by means of a Moiré-deflectometer (see Section 2.7.1). The next sections in this chapter aim to present each of the experimental stages of AEgIS, shading light on the physical background and introducing laws that will be required later on.

2.2 Antiprotons

2.2.1 Pair production

There is no 'natural' supply for antiprotons, i.e. no radioactive substance that would emit this particle. But one can create them by pair production, a process where energy is transformed into a particle-antiparticle pair. The possible products follow from the famous relation $E = mc^2$, hence one has to provide at least the corresponding rest mass energy to bring the pair into existence. In the case of a positron-electron pair, for example, the required energy is $2m_ec^2 = 2 \cdot 511\,\mathrm{keV}$. During pair production, not only the total energy has to be conserved, but also the momentum, the electric charge and the total angular momentum. For this reason, a single particle cannot cause the creation of a particle pair. This is quickly understood when assuming a photon with exactly the energy $E = 1022\,\mathrm{keV}$, creating a lepton pair at rest ($p'_{tot} = 0$). The incident photon, however, must have the nonzero momentum $p_{tot} = \frac{E}{c}$, invalidating the reaction $\gamma \rightarrow e^+ + e^-$. If, on the other hand, there is just one more particle nearby, a so-called collision partner, then all conservation laws can be satisfied and pair production may occur. This is schematized in Fig. 2.2 for the simple case of a single photon interacting with a nucleus Z, which gives birth to a positron and an electron. In fact, even this basic scheme already includes two virtual particles mediating the interaction, before finally the lepton pair is emerging. Since a photon cannot release just a fraction of its energy, it has to be completely absorbed during the process. Thus, any possible energy excess that is not transformed into rest mass here defines the velocity of the produced particles.

Often, the term pair production is associated only with the situation of incident photons, which is probably historically motivated. Photons have no rest mass, they can only transfer their energy as a whole to another particle and, in the classical picture before the QED, photons don't interact with each other. These features enabled several theoretical calculations. It could be shown that the pair production cross-section increases with the photon energy E up to a saturation plateau, and it scales approximately with Z^2 where Z is the atomic number of the target atoms [38]. Of course, if the photon energy exceeds further rest mass limits, also heavier particles like the *muon* ($E_0 = 105.7\,\mathrm{MeV}$) or the *tauon* ($E_0 = 1776.9\,\mathrm{MeV}$) plus their respective antiparticles can emerge. Notably, also quark-antiquark pairs can be created, which was claimed to be experimentally demonstrated in photon-photon collisions already in 1992 [39], leading to the emission of *pions* — in an environment where originally no hadron was present. A charged pion has a rest mass of $139.6\,\mathrm{MeV/c^2}$, which is about three orders of magnitude more than the electron mass, and it comes in two quark-combinations: an up-quark and an anti-down-quark ($u\bar{d}$: π^+) or a

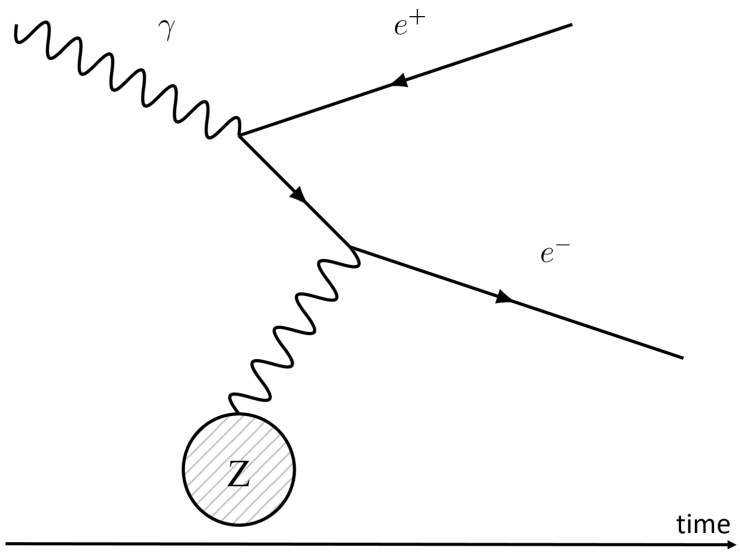

Figure 2.2: Feynman diagram for the production of a positron-electron pair from an initial photon interacting with a heavy collision partner with atomic number Z.

down-quark and an anti-up-quark ($d\bar{u}$: π^-). Predominately, the charged pions decay into muons and muon-neutrinos. But also the creation of neutral pions π^0 with smaller rest mass of $135\,\mathrm{MeV/c^2}$ is possible. It consists of a superimposed state of the quark systems $u\bar{u}$ and $d\bar{d}$ and rapidly annihilates into gamma quanta.

With the creation of pions by photo-photon collisions, which in fact only take place between virtual particles, it became clear that pair production is a very basic principle of the universe. The creation of any particle pair only requires sufficient energy in 'one package' and the possibility to conserve momenta and charges. Therefore, it is possible to observe pair production also for particles taking part in the strong interaction. This can be modeled as follows: if one applies a lot of energy to one of the three quarks which make up for example the proton, this quark is pushed away from the other two. Then, the strong force carriers (gluons) have to convey the strong force over a greater distance. Gluons carry the same kind of so-called color charges as quarks, so they themselves take part in the strong interaction. As a result, when the gluons have to mediate *and* interact over increasing distances, they require much more energy. This favors above a certain threshold the creation of a new quark-antiquark pair. This also means that one can never observe a single free quark, only at least a two-quark system (meson). As a remark, hadrons such as the proton or the neutron, may exchange mesons, which causes an attraction. This is the so-called nuclear force and it is the reason for the formation of atomic nuclei, despite the repulsive electromagnetic forces between the positively charged protons.

The third and last quantum mechanically understood interaction, namely the weak interaction, mediates decays of particles between and within the generations. For example, it is responsible for the decay of the heavier muon to the lighter electron, of the heavier down-quark to the lighter up-quark as it occurs in neutron decays, and many more. But also the reverse process is carried by weak interaction: the fusion reaction best known from our own sun where occasionally a proton is changed to a neutron — a lighter particle becomes a heavier one, which can only occur if one provides some additional energy, e.g. from proton-proton collisions. The force carriers of the weak interaction are the W^+, W^- and Z^0 bosons, where only the Z^0 boson can be fully transformed into a particle-antiparticle due to its neutrality.

However, it is technically not trivial to produce many photons with few thousand MeV, which would be required to transform them into proton-antiproton pairs ($E_0 = 2m_pc^2 = 1877\,\mathrm{MeV}$). For this reason, the required energy is provided by highly accelerated charged particles such as protons hitting onto a static target. Since fast protons can have a considerable relativistic mass, the huge momentum that has to be distributed to all involved particles does not allow the transfer of all kinetic energy into particle production. This can be seen when introducing the so called center-of-mass energy E_{cm}, i.e. the total energy from the point of view of a (moving) reference frame at the center-of-mass where the net momentum p_{tot} sums to zero. When using the general energy-momentum relation:

$$E_{tot}^2 = p_{tot}^2c^2 + m_0^2c^4 \ , \tag{2.1}$$

where m_0 is the total rest mass and c the speed of light, it can first be understood that E_{cm} equals the rest energy of the system when $p_{tot} = 0$, which indeed has to increase by $1877\,\mathrm{MeV}$ when a proton-antiproton pair is created, and second that the minimum total energy for the creation has to satisfy the equation:

$$E_{cm}^2 = E_{tot}^2 - p_{tot}^2c^2 \tag{2.2}$$

For producing a proton-antiproton pair after shooting fast protons onto a proton inside a static target, i.e. $p + p \longrightarrow p + p + p + \bar{\mathrm{p}}$, the center-of-mass energy after the collision is:

$$E_{cm} = 2m_pc^2 + 2m_pc^2 = 4m_pc^2 \ , \tag{2.3}$$

where $m_pc^2 = 938.27\,\mathrm{MeV}$ is the proton rest energy. Combining Eq. 2.2 and Eq. 2.3 for the situation before the collision, i.e. $E_{tot} = E_{proton} + E_{target}$ and $p_{tot} = p_{proton} + p_{target}$, one finds:

$$E_{proton} = 7m_pc^2 \tag{2.4}$$

When subtracting the rest energy of the incident proton from the total energy, finally an expression for the minimum kinetic energy required for the production of a proton-antiproton pair is found:

$$E_{kin} = 6m_p c^2 = 5.6\,\mathrm{GeV} \tag{2.5}$$

This minimum kinetic energy is approximately the same when hitting onto a neutron instead of a proton, but it may decrease by $\approx 1\,\mathrm{GeV}$ when attributing a certain momentum to the nucleon due to the target temperature [15]. Notably, when increasing the momentum of the target nucleon to be equal to the incident one, but with opposite direction, one performs the experiment in the center-of-mass frame and the required minimum energy for production is just the center-of-mass energy. Hence, less initial acceleration is required in order to study high energy physics, which had been the reason for developing circular particle colliders in the first place.

In summary, *pair production* usually refers to the process where a photon transforms into a particle-antiparticle pair in a collision event, which ascertains energy and momentum conservation. The underlying principle of energy-mass conversion, however, is valid in a more general way. In fact, it is also applicable to any type of collision where a lot of energy can be transferred in an instant. The probability of particle production therefore not only scales up with the energy, but also with the cross-section for a collision. In the case of photons, this cross-section scales with Z^2 as was mentioned above. For particles with rest mass, it rather scales with $Z^{2/3}$, which is proportional to the effective area of the targeted nucleus as seen by the incoming particle [40].

2.2.2 Production of antiprotons at CERN

The generation of antiprotons at CERN starts with pure hydrogen from the bottle, which is stripped off its electron by electrostatic forces. The positively charged protons are magnetically focused and accelerated by electric fields. First, in a linear accelerator (LINAC2), then in two ring-shaped proton synchrotrons (PS BOOSTER and PS, see again Fig. 1.1). A bunch of about 10^{13} fast protons with 25 GeV kinetic energy is shot onto an iridium target ($Z = 77$). This energy is inelastically transferred to the target in a very short time, either in the form of *bremsstrahlung* (high energy photons) or as a direct push on the nucleons. This leads to the production of all kinds of particle-antiparticle pairs as explained in the previous paragraph. One of the possible products is of course the proton-antiproton pair. Charge and mass of the antiprotons are well known, namely $-1\,\mathrm{e}$ and $938.27\,\mathrm{MeV/c^2}$, respectively, which allows to separate and focus them by a variant of a magnetic mass filter (a so-called magnetic horn [41]) and inject them with 2.7 GeV kinetic energy into the antiproton decelerator ring of CERN.

Two pulses with up to 5×10^7 antiprotons each are typically collected in the AD-ring, before they are slowed down by retarding electric fields. Even though the axial momentum can be quickly reduced like that, the transverse one unfortunately not. As a consequence, the antiproton beam would quickly diverge and annihilate at the beam tube walls in accordance to Liouville's Theorem, which states that conservative forces can never change the total occupied phase space of a charged particle beam. Consequently, several intermediate steps are necessary in order to cool the momentum spreads efficiently without loosing too many antiprotons. These steps are shown in Fig. 2.3 for a single pulse of antiprotons, but the same principle is also valid if more pulses are stacked in the decelerator — which then require correspondingly longer cooling times [42].

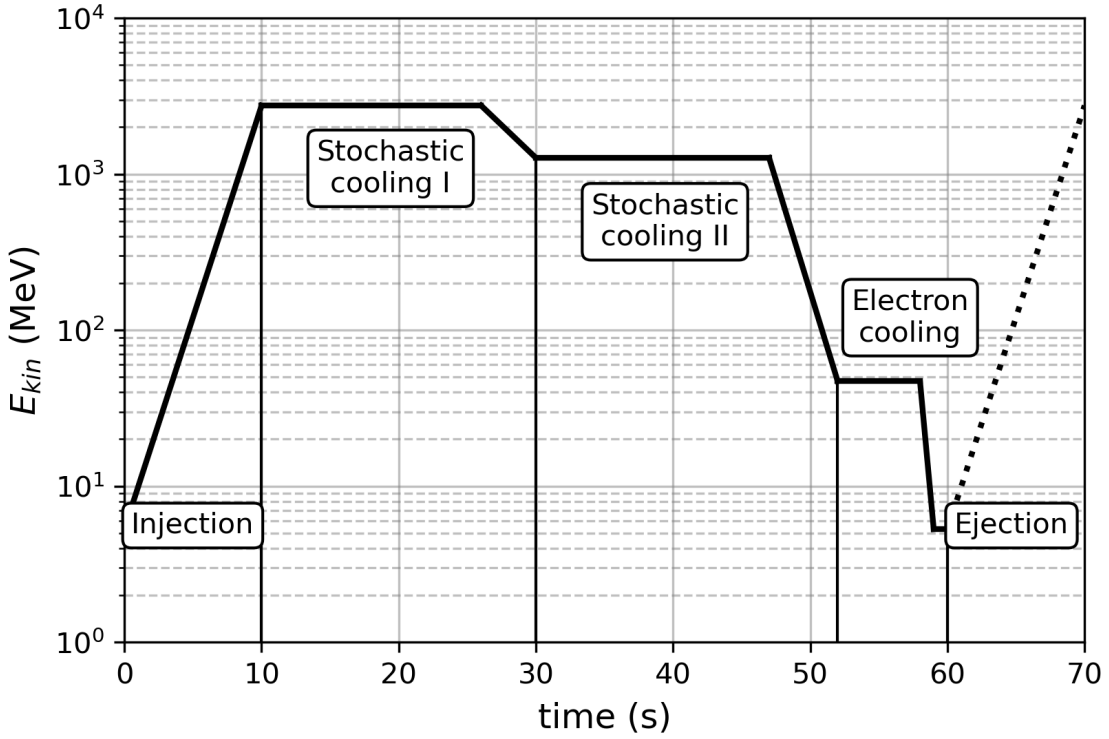

Figure 2.3: Basic AD cooling cycle for up to 5×10^7 antiprotons as detailed in the text.

After injection and an initial bunch shaping, the so-called *stochastic cooling* is applied for about 20 s. This technique is used to reduce the axial and transverse momentum spread by means of synchronized electric pulses that affect mainly individual particles, but also small subgroups, that are straying off too far from the mean value of all the antiproton orbits [43]. When the initial transverse emittance of 200π mm mrad has shrunk to 5π mm mrad and the axial momentum spread $\frac{\Delta p}{p}$ went down from 1.5 % to 0.1 %, the first axial deceleration step down to 1.3 GeV kinetic energy is initiated. Then, a second stochastic cooling step is applied for 15 s, before antiprotons can safely be slowed down to

about 50 MeV kinetic energy. From here, *electron cooling* is used since it is more efficient at these velocities. This technique cools antiprotons sympathetically by merging them with a cool pulse of electrons. These get in thermal equilibrium with the antiprotons by many collisions and are finally steered away from the antiproton beam, making use of the huge mass difference between the two particle species. This effectively reduces the transverse emittance to 1π mm mrad and the axial momentum spread to 0.01 % in few seconds [44].

In practice, up to 3×10^7 antiprotons were typically provided to the experiments after about two minutes of deceleration and cooling, with a kinetic energy of 5.3 MeV and an axial spread of less than 1 keV — corresponding to a maximum pulse length of 500 ns.

2.3 Laser

Enhancing antihydrogen formation via charge exchange using Rydberg-Ps requires specially designed lasers that enable an efficient and controlled Rydberg excitation. The AEgIS laser system consists of two optical setups for two photon resonant excitation, driven by one Nd:YAG (neodymium doped yttrium aluminum garnet) pump as described en détail in the references [45, 46]. The main features are summarized in the following.

The Q-switched Nd:YAG laser generates IR pulses at 1064 nm with a repetition rate of 10 Hz. This commercially available pump from the company EKSPLA comes with two additional outputs, one at 532 nm (second harmonic) and one at 266 nm (fourth harmonic). These three main pulses are used to drive OPG (Optical Parametric Generation) and OPA (Optical Parametric Amplification) stages, which allow to adjust the final wavelengths with high precision. The fine-tuned outputs are then combined in nonlinear optical elements, namely SFG (Sum Frequency Generation) crystals, in order to generate (i) ultraviolet pulses and (ii) mid-infrared pulses. Furthermore, the first harmonic (iii) is also directly used for selective photoionization of positronium from the $n = 3$ level. An overview of all laser beams used at AEgIS and their specifications is given in Fig. 2.4 and Tab. 2.1, respectively.

Laser system (i) enables the $1^3\mathrm{S} \rightarrow 3^3\mathrm{P}$ transition of Ps. The second system (ii) is for the transition to Rydberg states from $n = 3$. In addition, (iii) can be used in order to selectively photoionize all Ps in the $3^3\mathrm{P}$ state. All laser beams have a spatial extent of about 4 mm in diameter (FWHM). Under ideal conditions, i.e. a saturating laser fluence that guarantees excitation of all Ps atoms inside the beam, a broad laser bandwidth and a full geometrical overlap with the whole Ps cloud, the first transition to $n = 3$ occurs with ≈ 100 % efficiency. In a corresponding measurement inside of AEgIS Ps test setup, about 15 % Ps excitation was found [47]. The major differences to the ideal situation were the

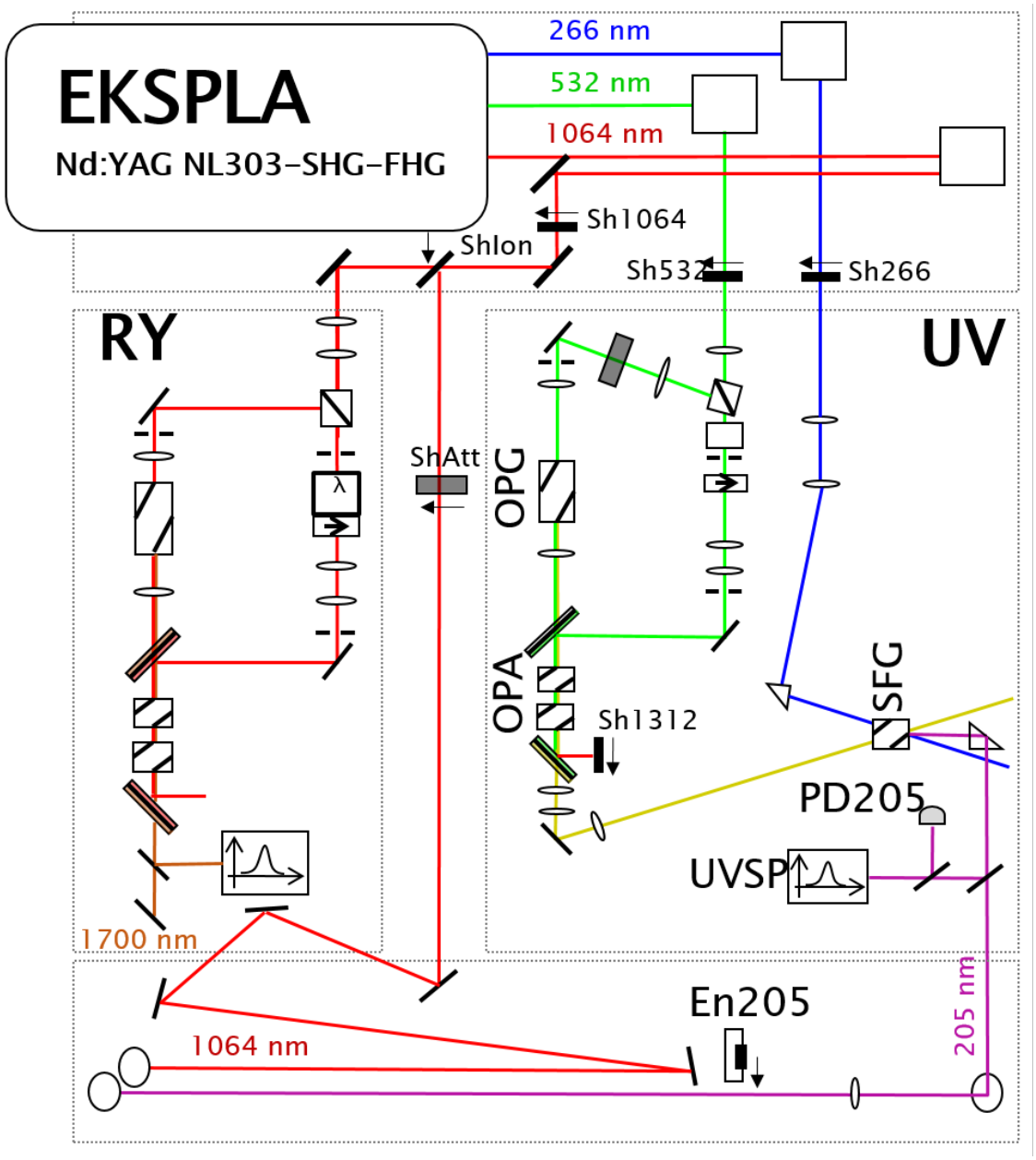

Figure 2.4: Overview of the AEgIS laser system, driven by a commercial Nd:YAG laser (EKSPLA). The system is designed to generate three pulsed beams as detailed in Tab. 2.1. (Image courtesy to Ruggero Caravita).

	λ (nm)	E (mJ)	τ_{Laser} (ns)	BW (GHz)	Ps transition
(i) UV	$204.9 - 205.2$	0.043	1.5	≈ 100	$1^3S \rightarrow 3^3P$
(ii) IR	$1671 - 1715$	1.6	3	430	$3^3P \rightarrow$ Rydberg
(iii) IR	1064	30	3	-	photoionizing 3^3P

Table 2.1: Overview of lasers in use at AEgIS and the specifications of the single pulses. The value of λ denotes the central wavelength of a pulse, τ_{Laser} is its FWHM in time and BW its estimated bandwidth.

limited spatial overlap between laser beam and the moving Ps cloud, and the narrow laser bandwidth, which did not affect the whole broad Ps velocity distribution at once. The bandwidth limitation had been on purpose, though, in order to relax the requirement of extremely powerful light sources and of matching optical elements. A secondary limiting effect is the laser pulse length (a few nanoseconds) which can cause deexcitation of already excited Ps atoms via stimulated emission, in addition to the always occurring spontaneous emission.

2.4 Positrons

Unlike antiprotons, positrons (e^+) are a common product occurring in so-called β^+ decays of numerous nuclides, but also artificial sources exist utilizing the effect of pair production. Both source types are commonly in use for research, whereas in medicine typically the radioactive sources are preferred. An important medicinal application is positron emission tomography (PET), were isotopes like ^{18}F or ^{13}N with 110 min and 10 min lifetime, respectively, are used in order to investigate the metabolism and related diseases. Other than that, positrons are widely used in material sciences as non-destructive nanoprobes for defect analysis, for surfaces or for electronic structures. One particular technique utilizing positrons is the Coincidence Doppler-broadening Spectroscopy (CDBS) [48, 49], where one exploits the extra bit of energy a nonthermal electron introduces to the annihilation process, which then is a signature for the type of defect the positron was trapped in. But positrons are also used in fundamental research. For example, in order to study the positronium fine splitting using single shot positron annihilation lifetime spectroscopy (SSPALS) [50, 47].

2.4.1 Positrons from β^+ decay

For research, a widely used positron source is the sodium isotope ^{22}Na. It has a half-life of 2.6 years and is commercially available with an activity of up to 50 mCi (1.85 GBq). The main decay channel is towards excited ^{22}Ne* under the emission of one positron. Excited neon, however, will rapidly deexcite due to a short fluorescence lifetime of 3.7 ps under the emission of a 1275 keV gamma quantum that is often used as a start signal for positron lifetime measurements. The other, less likely decay channels are electron capture, where no positron is released, and very rare the direct route towards ground state neon, again under the emission of one positron. The decay scheme is depicted in Fig. 2.5.

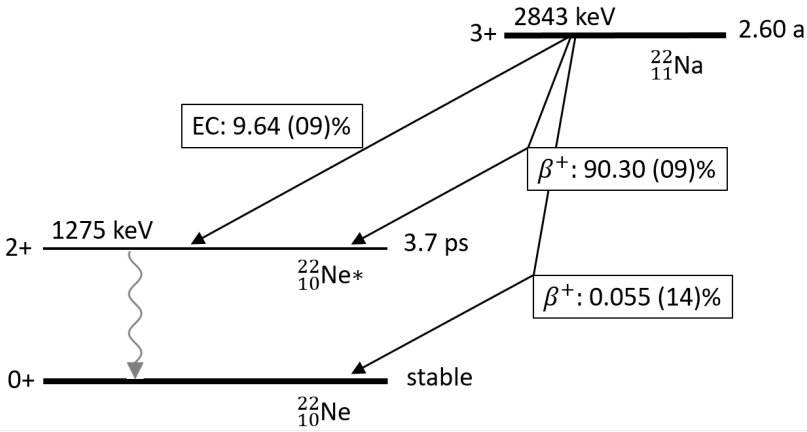

Figure 2.5: Term scheme of the ^{22}Na decay. Only the two decay routes marked with β^+ emit a positron, while the third one marked with EC involves the capture of a nearby electron [51].

The decay channels producing positrons are three body processes which comprise the additional emission of an electron neutrino. Therefore, resulting decay products have a continuous kinetic energy distribution. Leaving aside the unlikely decay channel towards ground state neon, which releases positrons with up to (1821.02 ± 0.21) keV kinetic energy, one usually has to deal with a typical β^+ spectrum ranging from 0 keV to a maximum energy of (546.44 ± 0.21) keV as shown in Fig. 2.6. The average of this continuum lies at (215.62 ± 0.17) keV [51, 52].

2.4.2 Positrons from pair production

The pair production positron sources work similar to the antiproton source. This means, one has to provide energy equivalent to at least the summed rest energies of one electron and one positron, thus 1022 keV, in an instant with a collision partner nearby. For example,

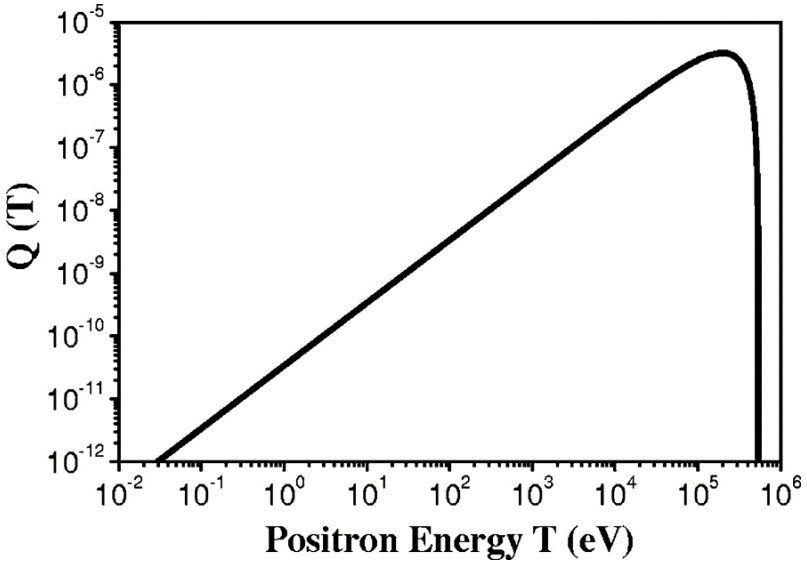

Figure 2.6: Normalized kinetic energy spectrum of positrons from the β^+ decay of ^{22}Na. The maximum energy is (546.44 ± 0.21) keV, the mean value is (215.62 ± 0.17) keV. (Image from Ref. [53]).

the GBAR collaboration at the AD uses a linear electron accelerator (LINAC), shooting an electron pulse with 4.3 MeV onto a tungsten target, which causes bremsstrahlung initiating the positron production with energies up to few MeV [54]. Another example is the NEutron induced POsitron source MUniCh (NEPOMUC). Here, the thermal neutrons originating from the nuclear research reactor Heinz Maier-Leibnitz (FRM II) induce the reaction: ^{113}Cd(n,γ)^{114}Cd, setting free gamma quanta with over 9000 keV. Interacting with the nearby platinum, these gamma quanta transform into electron-positron pairs [55].

2.4.3 Positron moderation

There is one significant characteristic occurring in all mentioned production processes: the broad energy distribution of the resulting antiparticles, ranging from zero up to few MeV. This necessitates efficient cooling before experiments become feasible. In the case of antiprotons, this even requires an entire decelerator facility such as the AD. Luckily, for positrons a relatively easy and straightforward method exists — the use of so-called moderators. These are materials that have a negative work function for positrons. Hence, any implanted positron that thermalizes and diffuses back to the surface will be expelled into vacuum with a well-defined energy perpendicularly to the surface. The resulting kinetic energy is equal to the value of the negative work function plus any residual kinetic energy, broadened by thermal energy. Positron moderators have been thoroughly studied and are widely in use. There are thin foils and meshes designed to moderate positrons

in transmission, solid rare gas moderators that can be remotely grown (and evaporated) directly on the source, and highly efficient single crystals or layers that work in reflection. Table 2.2 summarizes a few of the most commonly used moderators and their properties. The reported efficiencies ϵ are the ratio of moderated positrons to the total amount of emitted positrons, which includes losses due to geometry or absorption in the source itself. The work function ϕ_+ gives, if negative, the energy at which a thermalized positron is expelled from the material. If positive, thermal positrons tend to stay in the bulk, eventually getting trapped in defects or surface states, or they can form positronium. The energy of moderated positrons is characterized with ΔE.

	efficiency ϵ	ϕ_+ (eV)	ΔE (eV)	mode	details
Solid Ne	7×10^{-3}	positive	0.58	reflection	[56]
W mesh	1.2×10^{-3}	$\sim (-3)$	< 0.2	transmission	[57]
W(100) foil	8.8×10^{-4}	$\sim (-2.5)$	< 0.25	transmission	[58, 59]
4H/6H-SiC	1.9×10^{-4}	$\sim (-2.5)$	< 2	reflection	[60, 61]

Table 2.2: Some of the most efficient positron moderators commonly in use. The efficiency is the ratio of moderated positrons to the total amount of produced positrons.

Solid neon moderators provide positrons with a rather broad resulting ΔE. Strictly speaking, solid neon is not even a moderator because the work function is slightly positive. However, the large band gap (about 21 eV) considerably extends the time positrons require to thermalize inside the neon bulk, because below the band gap threshold only phonon excitation with small energy transfer can occur. It is therefore very probable that epithermal positrons arrive back at the surface and are emitted into vacuum with around 20 eV. Applying now a retarding potential, one can obtain a very slow positron beam with outstanding efficiency. In addition, this moderator can be grown in-situ directly on the positron source, only requiring to cool down this region to below 9 K in order to solidify neon gas. But also tungsten moderators, the most commonly used ones, have improved a lot over the years, peaking in annealed multilayered meshes in transmission geometry that have a high efficiency with a narrow ΔE and work well at room temperature. Due to contaminants in vacuum, these moderators need to be regenerated at high temperature every once in a while to restore the original efficiency. Also a treatment with some gases (e.g. oxygen) proved to be beneficial. The rather recently discovered moderator 4H/6H-SiC is working quite well, although its full potential is not yet exhausted. One main advantage seems to be that it does not suffer so much from surface contaminants, making it very

easy to maintain. Especially the silicon carbide moderator is suited for secondary moderation, as impinging positrons are already of a well-defined energy. Under these conditions, moderation efficiencies of up to 65 % have been measured [62].

2.4.4 Positron system of AEgIS

The AEgIS positron system consists of three separate instances, namely the *Source*, the *Trap* and the *Accumulator*. It is sketched in Fig. 2.7 and many more details can be found in the author's Master thesis [63] or in Ref. [64].

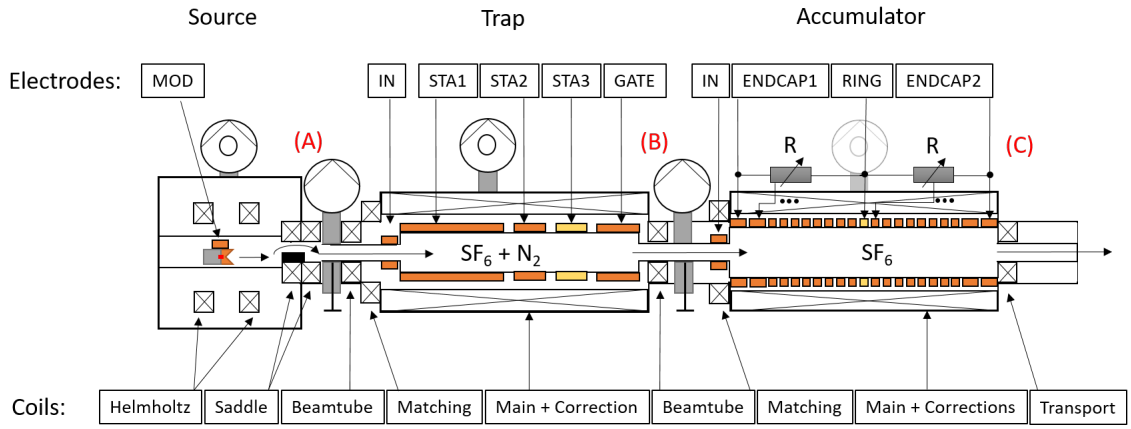

Figure 2.7: AEgIS positron system, consisting of *Source*, *Trap* and *Accumulator*. The Source basically consists of the β^+ decaying isotope ^{22}Na and a solid neon moderator at 7 K, which can be grown directly on the encapsulated sodium. The Trap is a Surko-type buffer gas trap for efficient positron cooling with rotating wall, which produces pulses containing up to 1×10^5 positrons every 152 ms. The Accumulator is designed to catch these pulses and accumulate them. Due to a parabolic potential well with rotating wall, low buffer gas pressure and a homogeneous magnetic field of (100.27 ± 0.02) mT inside the Accumulator, positron lifetimes up to 600 s are possible. A,B and C mark positions at which positron detectors (Na(Tl)I or CsI) are located.

Source

AEgIS positron source is the isotope ^{22}Na, which had an activity of 1.02 GBq (27.6 mCi) on March, 8th 2018. The sodium is deposited on a tantalum plate kept by an aluminum holder, where the tantalum acts as a positron reflector to increase the forward flux. A titanium head with a 5 µm transmission window on the top fully encapsulates the sodium, fit for ultra high vacuum. The capsule is placed inside a copper block with a cone-shaped

opening, which is kept at 7 K during operation by a two stage helium cryocooler. The source region can be flooded with clean neon gas, which solidifies as ice on the cool copper surface and the titanium window. Then, the neon ice has to be annealed at 9.3 K for several minutes. In order to slow down the positrons emitted from the solid neon, a potential of 18.6 V against ground is applied to the whole source region. Emerging positrons are guided by the homogeneous magnetic field of a pair of Helmholtz-coils towards a tungsten obstacle, which filters out too fast positrons. Only the cold fraction can adiabatically follow a curved magnetic field around that obstacle, which is generated by a saddle coil. The continuous beam of slow positrons (≈eV) is then steered towards the Trap. First Point Scientific (Inc), the original manufacturer of this system, gives an overall efficiency for the Source of 2.5×10^{-3}. This includes the moderation efficiency, losses due to geometrical constraints and losses during transport. With the given activity, one expects a maximum rate of $2.5 \times 10^{6}\,\mathrm{e}^{+}/\mathrm{s}$ entering into the Trap.

Trap

The Trap consists of several cylindrical electrodes with 25.4 mm inner diameter inside a vacuum tube. These electrodes enable the axial trapping by applying appropriate potentials to them. In order to confine positrons also radially, a 0.07 mT axial magnetic field is created by solenoids around the vacuum beam tube. A schematic of the whole potential landscape of the positron system during three phases called *Filling*, *Adapting* and *Transport*, is given in Fig. 2.8. The durations of each of the three phases are 150 ms, 2 ms and ≈ 0 ms, respectively. Positrons with several eV can only be efficiently trapped if one sets up a rapid cooling mechanism. Here, a buffer gas is used, with which positrons are cooled by inelastic collisions. The cooling has to occur within the positron flight time towards the last electrode (GATE) and back to the entrance electrode, so that they cannot escape anymore. A relatively high pressure (8×10^{-4} mbar) of a gas mixture consisting of nitrogen and a little bit of SF_6 showed an excellent cooling efficiency in the Trap, which is in agreement with studies on buffer gas cooling of positrons done by Surko et al. [65].

During the *Filling* phase, which lasts much longer than the other two, a continuous flow of positrons enters the trap and cools down gradually. The colder they get, the more they are axially confined. The final stage is the electrode labeled STA3 in Fig. 2.7 where a cloud containing up to 1×10^{5} positrons can be stored. In the next phase, the *Adapting*, potentials are adjusted such that positrons are still trapped in the region of STA3, but have a higher potential than the IN-electrode of the next trapping device, the Accumulator. They are then cooled for two more milliseconds, before the last phase activates, the transport towards the Accumulator. For this, the GATE-electrode of the

Trap is lowered to 0 V and at the same time the IN-electrode of the Accumulator is reduced by 1 V in order to catch the positron pulse. Immediately after, the whole process starts from the beginning.

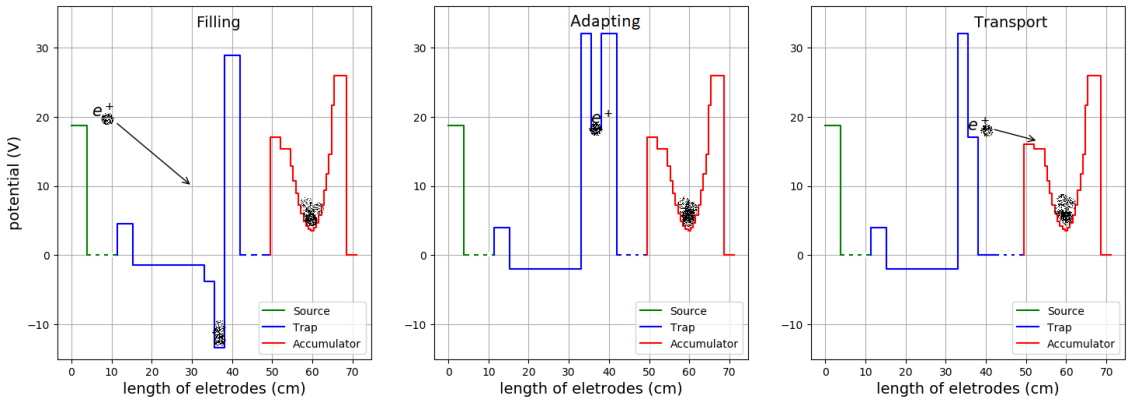

Figure 2.8: Schematic of the trapping potentials of the AEḡIS positron system during three phases, namely 'filling' (150 ms), 'adapting' (2 ms) and 'transport' (<1 ms).

Accumulator

The Accumulator appears quite similar to the Trap, but has many more electrodes in order to create an almost harmonic potential well. Since a positron lifetime of several minutes is required, the base pressure of the gas mixture here is just around 10^{-8} mbar, four orders of magnitude less than in the Trap. Of course, this reduces the cooling efficiency a lot, which is why the potential reduction at the IN-electrode can only be allowed for a short time in order to retain freshly injected positrons upon their return to the entrance of the Accumulator. Already after 300 ns, the inlet potential is set back to its original value. Except for the pulsing of the first electrode, all other electrodes have a constant potential during the whole process of positron accumulation. Only upon user request, i.e. a logical trigger signal for positron ejection, a high voltage pulse is applied to the electrodes via RC-bridges. This produces a linearly falling potential ramp, ranging from 466 V to 0 V as shown in Fig. 2.9. This ramp quickly accelerates all positrons to move out of the Accumulator, a little bit faster from the higher potentials and slower from the lower. Hence, there is one point downstream where the positron pulse has a minimum axial spread. This effect is called *bunching* and is often exploited when positrons need to be focused axially [64, 66]. As the positrons are already mostly contained within the central electrode, which is the bottom of the potential well, the bunching is not a critical component for the Accumulator. Consequently, the average energy of the positron pulse lies at 250 eV. In AEḡIS, the positrons are then magnetically transported into a secondary

acceleration device. Here, the kinetic energy of the positrons is increased to 4.6 keV by rapidly increasing the potential of the beam tube while positrons are flying through. High positron velocities circumvent a major broadening of the axial spread until the positrons reach their final destination.

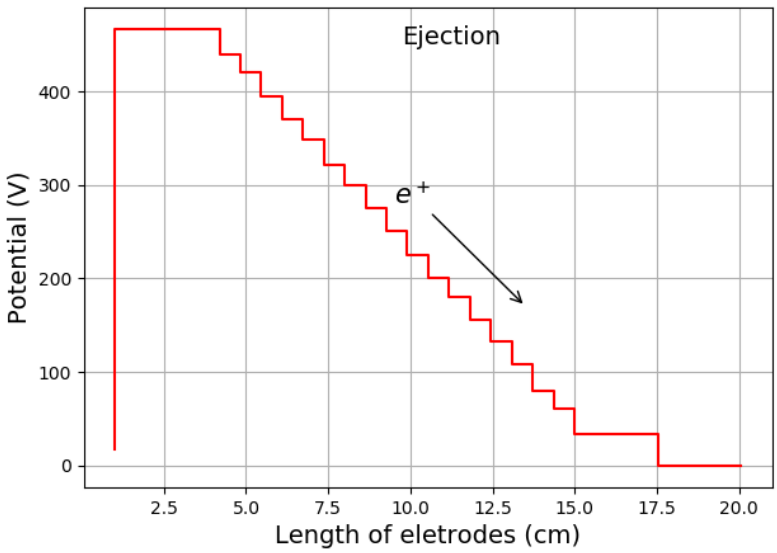

Figure 2.9: Schematic of the accumulator potentials during positron ejection. As most of the positrons are contained in the range of the central electrode at 10 cm, they have an average energy of 250 eV.

One specialty should be mentioned here, which is the use of a rotating electric field (also named *rotating wall*, RW). Its purpose is to compress a charged plasma that is radially trapped by a magnetic field and axially by electrostatic potentials, therefore well applicable in AE$\bar{g}$IS positron and antiproton systems. In case of the positron system inside the Trap as well as inside the Accumulator, there is one electrode that is four-fold segmented, STA3 and RING, respectively. An individual potential can be set to each of these segments. Usually, a high frequency ($\approx$MHz) sinusoidal voltage is applied to each segment, shifted in phase by 90° in order to simulate a rotating field. A single species charged particle plasma tends to expand over time due to the repulsive electrostatic forces between the particles. A properly adjusted rotating wall can not only cancel out this expansion, but it can even invoke a compression as long as the plasma properties allow for a direct coupling of the single particle to the rotating field [67, 68]. This depends on the shielding effect of the surrounding charged particles, and therefore on the plasma density and the average particle velocity. Usually, RW optimization of a positron bunch includes a scan over several RW frequencies and amplitudes until a visual compression of the positron spot can be seen on a microchannel plate (MCP) plus a phosphor screen.

2.5 Positronium

Positronium is the bound state of an electron and a positron similar to the hydrogen atom, but purely leptonic. This makes Ps an ideal test ground for quantum electrodynamics (QED), as no hadrons and corresponding interactions meddle in experiments. It is possible to adapt the established Bohr formula also for positronium energy levels with E denoting the Ps binding energy. Including higher order effects such as relativistic corrections or fine splitting, this formula quickly becomes a precise predictor for measurement outcomes with Ps. Equation 2.6 originally included terms up to $O(\alpha^5)$ as presented in Ref. [69], but since this was beyond current experimental precision, only high order corrections up to $O(\alpha^4)$ were used in the following. As a side effect, the numerical evaluation of Bethe logarithms could be avoided.

$$E = \frac{E_{Ps}}{2n^2} + \frac{E_{Ps}\alpha^2}{4n^3} \cdot \left(\frac{11}{8n} - \frac{4}{2\ell+1} + \frac{14}{3}\delta_{s1}\delta_{\ell 0} + \frac{2\delta_{s1}(1-\delta_{\ell 0})}{\ell(2\ell+1)(\ell+1)} C_{j\ell+\ldots} \right) \tag{2.6}$$

Here, $E_{Ps} = \mu\alpha^2 c^2 = 13.606\,\mathrm{eV}$ (Hartree energy for Ps), $\mu = \frac{m_e}{2}$ (reduced mass of positronium), and α is the fine structure constant. $C_{j\ell}$ is given in Eq. 2.7 and distinguishes between the possible total angular momenta $\vec{J} = \vec{L} + \vec{S}$, consisting of the orbital angular momentum $\vec{L}$ and the total spin $\vec{S}$. Usually, these vectors are simply described by their corresponding quantum numbers j, s, ℓ. The total spin s of Ps consists of both the $\frac{1}{2}$ spins of its constituents, which are fermions. Thus, we can differ between two types of Ps, namely para-positronium (p-Ps, $s = 0$) and ortho-positronium (o-Ps, $s = 1$). The possible integer values for the orbital angular momentum quantum number ℓ range within $0 \ldots (n-1)$. Furthermore, the total angular momentum j can take integer values between $|\ell - s| \leq j \leq \ell + s$.

In the case of o-Ps, one finds three states with $j = |\ell - 1|$, $j = \ell$ and $j = \ell + 1$, which is why it is called a *triplet*. Despite this, all the states with $\ell = 0$ are degenerate, resulting in a single state with $j = 1$. For p-Ps, only one state with $j = \ell$ arises, hence the so-called *singlet*. Note that the whole term that includes $C_{j\ell}$ in Eq. 2.6 vanishes if $\ell = 0$ or if $s = 0$.

$$C_{j\ell} = \begin{cases} \dfrac{-(\ell+1)(3\ell-1)}{2\ell-1} & \text{for } j = \ell - 1 \\ -1 & \text{for } j = \ell \\ \dfrac{\ell(3\ell+4)}{2\ell+3} & \text{for } j = \ell + 1 \end{cases} \tag{2.7}$$

With equations 2.6 and 2.7 it is possible to calculate the energy levels of positronium including (hyper)fine splittings and the Lamb shift in the absence of external fields, which is

schematized in Fig. 2.10. Therein, the energy axis represents the required ionization energy of Ps for a given principal quantum number n without external fields. The fine structure, which at the same time is hyperfine structure since there is no nucleus, is exaggerated on the right side of the graphic (separated by the vertical dashed line), so that the effects can be visually appreciated. As a consequence, the energy axis should not be used to estimate the magnitude of the splittings. Shifts for $n = 1$ are increased by three, for higher levels even by four orders of magnitude. The Ps sub-levels are labeled with $n^{2s+1}\ell_j$ as it is commonly accepted for positronium, with ℓ being expressed in its alternative notation S, P, D, F.

2.5.1 Ps annihilation lifetime

Each state in Fig. 2.10 has an annihilation lifetime written next to it, which is the outcome of steadily improving non-relativistic QED calculations over the last seventy years. The first estimate of Ps annihilation rates Γ_{Ps} (i.e. lifetime $\tau_{Ps} = 1/\Gamma_{Ps}$) was already given in 1949 by Ore and Powell for the $\ell = 0$ states [71], and by Alekseev ten years later for the $\ell = 1$ states. Their results resemble a first order solution of the Bethe-Salpeter equation for a quantum two body system. Higher order corrections were perturbatively solved in the following years, which eventually revealed the so called ortho-positronium lifetime puzzle: Measurements and theory differed by about 0.2 %. Only in 2003, a severe systematic error in most former experiments was discovered: the influence of pick-off annihilation of nonthermal positronium. Correcting for this lead to the experimental verification of the ground state ortho-positronium lifetime: $\tau = (142.04 \pm 0.01)\,\text{ns}$ [72]. The lifetime of para-positronium is more difficult to measure because it is three orders of magnitude smaller. Despite this, a first precise result was already achieved in 1982 by means of an experiment based on singlet-triplet state mixing for positronium in a magnetic field [73]. The measured p-Ps lifetime was $(125.09 \pm 0.17)\,\text{ps}$, confirming the theoretical value.

Precise solutions for Ps annihilation rates are listed in Eq. 2.8 to 2.11. Here again, E_{Ps} denotes the Hartree-energy of positronium with 13.606 eV. Generally, the lifetimes for $\ell = 1$ states are significantly greater than those for $\ell = 0$, which can be modeled via the typical shape of P-orbitals: The probabilities for the electron and the positron to reside in the same part of the 'barbell' is rather small, therefore the chance of interaction is also strongly suppressed. For o-Ps, it is in fact only possible when $j \neq 1$, i.e when the total spin couples with the orbital angular momentum. In these long-lived states, it is more likely that a radiative level transition to lower, short-lived states occurs. It can be expected that for even greater values of ℓ annihilation can be neglected against the dominating optical transitions.

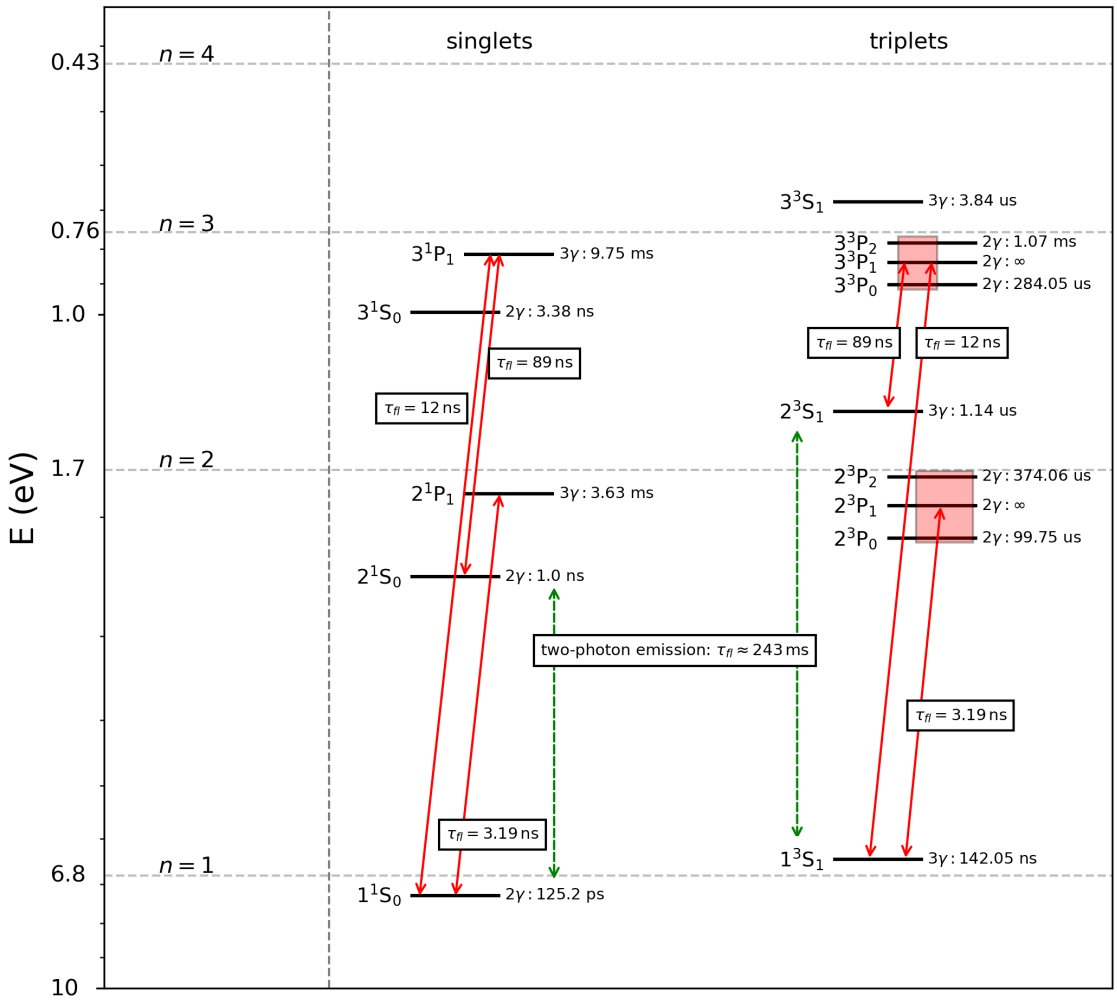

Figure 2.10: Positronium (hyper)fine splitting with correction terms up to order $O(\alpha^4)$ in the absence of external fields for the first three levels with corresponding annihilation and fluorescence lifetimes. The 3D-levels have not been added for clarity. The ground state splitting has been exaggerated by three orders, the higher states by four orders of magnitude. Lifetime values for $n = 1$ and $n = 2$ levels can also be found for example in Ref. [70], with some minor deviations on the last digits due to propagated rounding errors in the reference.

Para-Ps ($\ell = 0$, 2γ) [74]:

$$\frac{1}{\tau} = \frac{E_{Ps}}{\hbar} \cdot \frac{\alpha^3}{n^3} \cdot \left[1 - \frac{\alpha}{\pi}\left(5 - \frac{\pi^2}{4}\right) - 2\alpha^2 ln\alpha + 5.1243\left(\frac{\alpha}{\pi}\right)^2 + ...\right] \tag{2.8}$$

Ortho-Ps ($\ell = 0$, 3γ) [75]:

$$\frac{1}{\tau} = \frac{4(\pi^2 - 9)}{9\pi}\frac{E_{Ps}}{\hbar} \cdot \frac{\alpha^4}{n^3} \cdot \left[1 - \frac{\alpha}{\pi}(10.2866) + \frac{\alpha^2}{3} ln\alpha + 45\left(\frac{\alpha}{\pi}\right)^2 + ...\right] \tag{2.9}$$

Para-Ps ($\ell = 1$, 3γ) [76]:

$$\frac{1}{\tau} = \frac{2(n^2 - 1)}{9\pi} ln\left(\frac{8n^2}{\alpha^2}\right)\frac{E_{Ps}}{\hbar} \cdot \frac{\alpha^6}{n^5} \tag{2.10}$$

Ortho-Ps ($\ell = 1$, 2γ) [77]:

$$\frac{1}{\tau} = \begin{cases} \frac{2(n^2 - 1)}{8}\frac{E_{Ps}}{\hbar} \cdot \frac{\alpha^5}{n^5} & \text{for } j = 0 \\ 0 & \text{for } j = 1 \\ \frac{2(n^2 - 1)}{30}\frac{E_{Ps}}{\hbar} \cdot \frac{\alpha^5}{n^5} & \text{for } j = 2 \end{cases} \tag{2.11}$$

An important aspect about Ps is the number and energy distribution of gamma quanta being produced during annihilation. In general it can be said that the orbital momentum and total spin always have to be conserved, as well as the energy and the momentum of the system. Equations 2.8 to 2.11 only take into account annihilations that produce two or three photons, since these are the primary and faster channels. Single photon emission is excluded by the basic conservation of energy and momentum, but higher numbers are in principle not forbidden.

For ortho-Ps and para-Ps in the $\ell = 0$ state, annihilation can occur into $3, 5, 7 \ldots$ and into $2, 4, 6 \ldots$ gamma quanta, respectively, which follows from the photon spin of 1 and the conservation of j. In the case of $\ell = 1$, one even has to distinguish between different values for the total angular momentum. For $j = 0$ and $j = 2$, ortho-Ps produces $2, 4, 6 \ldots$ gamma quanta, while for $j = 1$ annihilation will only start from producing four photons, which is why in Eq. 2.11 there is written 0 at the corresponding position, since only 2γ-processes were taken into account. This phenomenon can be modeled with $\vec{S}$ and $\vec{L}$ being orthogonal: three photons are required to conserve energy, momentum and the total spin, and one photon more to also maintain the orbital angular momentum. Para-Ps in the $\ell = 0$ state annihilates into $3, 5, 7 \ldots$ gamma quanta, which allows also the conservation of its total angular momentum of $j = 1$.

The energy that needs to be distributed between the photons originates from the Ps rest mass and its motion, while the latter contributes comparably little. For a two photon

annihilation, each photon simply takes half of the total energy and flies in almost opposite direction, with a small deviation from collinearity due to the Ps kinetic energy. For the cases where three photons are created, a three-body problem arises. A good approximation for energies greater than the binding energy of ground state Ps ($> 6.8\,\mathrm{eV}$) is given in Eq. 2.12, which already was derived by Ore and Powell [71]. In this equation, k denotes the photon energy divided by the positron rest mass $E_0 = 511\,\mathrm{keV}$, taking values between 0 and 1.

$$\frac{d\Gamma_{3\gamma}}{dk} = \frac{4m\alpha^2}{9\pi} \cdot \left(\frac{2-k}{k} + \frac{(1-k)k}{(2-k)^2} - \frac{2(1-k)^2\log(1-k)}{(2-k)^3} + \frac{2(1-k)\log(1-k)}{k^2} \right) \quad (2.12)$$

This Ore-Powell spectrum, normalized to the annihilation rate of ground state ortho-Ps, is plotted in Fig. 2.11. The upper limit for the energy of emitted photons is $E_\gamma = 511\,\mathrm{keV}$, which originates from the correlation of all three gamma quanta. If one photon exceeded that upper limit, the summed momenta of the other two would have to be greater than the corresponding momentum of the first one due to triangular inequality, which is in conflict with energy conservation.

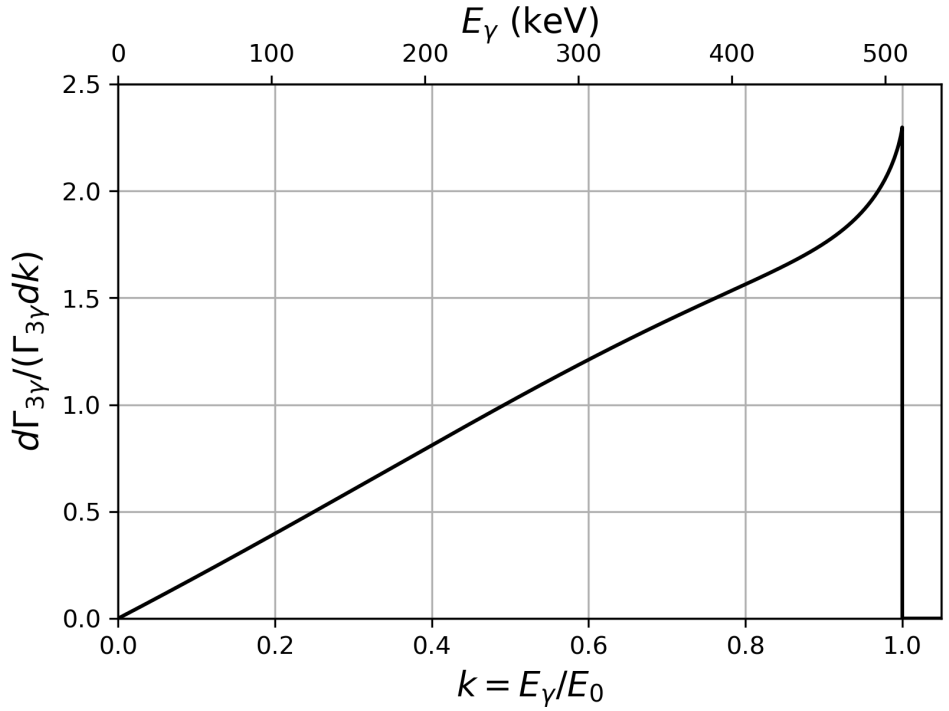

Figure 2.11: Three gamma spectrum of annihilating ground state ortho-Ps, peaking at $k = 1 \mathrel{\widehat{=}} 511\,\mathrm{keV}$.

2.5.2 Ps fluorescence lifetime

For all excited levels in Fig. 2.10 where the annihilation lifetime is comparably long, optical transitions (fluorescence) between the levels become important. These spontaneous deexcitations have specific rates, which is related to the ground state electromagnetic vacuum field — hence similar to stimulated emission with not a single line, but rather an interfering continuum of modes [78]. If one makes the approximation that transitions to lower levels mainly occur under the emission of one photon, which implies Pauli's selection rule that any transition has to suffice $\Delta\ell = \pm 1$, it is possible to express the transition probability, or the so-called Einstein coefficient A, as given in Eq. 2.13

$$A = \frac{16\pi^3 f_0^3}{3\epsilon_0 hc^3} \cdot |\vec{\mathbf{d}}|^2 \ , \tag{2.13}$$

where f_0 is proportional to the energy difference between the initial and the final state. The electric dipole moment $\vec{\mathbf{d}}$ is derived from the transition matrix element between these two states of positronium as defined in Eq. 2.14, where q is the elementary charge, $\vec{\mathbf{r}}$ the position operator and ψ_{nlm} the positronium wavefunction for a certain state.

$$\vec{\mathbf{d}} = q\langle\psi_{nlm}|\vec{\mathbf{r}}|\psi_{n'l'm'}\rangle \tag{2.14}$$

As positronium is so similar to hydrogen, it is possible to apply the same analytical solution of a quantum mechanical one electron system. One has just to take extra care about the reduced mass of Ps, which alters its Bohr radius and the energy levels as mentioned above. Like this, any transition rate can be calculated straight-forward if there are no external fields. For example, the $|210\rangle \rightarrow |100\rangle$ transition with the quantum numbers $|nlm\rangle$ yields:

$$\begin{aligned} \langle\psi_{210}|x|\psi_{100}\rangle &= 0 \\ \langle\psi_{210}|y|\psi_{100}\rangle &= 0 \\ \langle\psi_{210}|z|\psi_{100}\rangle &= \frac{128\sqrt{2}}{243} a_0 \end{aligned} \tag{2.15}$$

Plugging this back into Eq. 2.14 and then into Eq. 2.13, one obtains a decay rate of $A = 313\,319\,445\,\mathrm{s}^{-1}$ or, expressed as lifetime, $\tau_{fl} = 3.19\,\mathrm{ns}$, a value often referenced in literature [50]. A final remark: If there are more than one decay routes for any state, like for example the $3\,\mathrm{P}$ levels who can either decay towards $2^3\,\mathrm{S}$ or $1^3\,\mathrm{S}$, both are happening with their own specific rate at the same time, causing the state to decay faster with both rates summed. Hence instead of separately observing 12 ns and 89 ns, the observed fluorescence lifetime is $\tau_{3P} = \Gamma_{3P}^{-1} = \left(\Gamma_{2^3S} + \Gamma_{1^3S}\right)^{-1} = \left(\frac{1}{12\,\mathrm{ns}} + \frac{1}{89\,\mathrm{ns}}\right)^{-1} = 10.6\,\mathrm{ns}$.

2.5.3 Impact of external fields

The exact analytical solution of the Schrödinger equation (Eq. 2.16) for one electron systems like hydrogen does not take into account external electric or magnetic fields. The so called Hamilton operator $\hat{\mathrm{H}}$ yields the expectation values for the total energy of a measurement, when being applied to the wavefunction $\psi(\mathbf{r},t)$ of a single charged particle.

$$\underbrace{\left(-\frac{\hbar^2}{2m}\Delta + V(\mathbf{r},t)\right)}_{\hat{\mathrm{H}}}\psi(\mathbf{r},t) = i\hbar\frac{\partial}{\partial t}\psi(\mathbf{r},t) \tag{2.16}$$

Magnetic fields affect the total energy which is called the Zeeman effect. Electric fields do their own, which is known as the Stark effect. This includes the so-called *motional Stark effect*, which is induced by the magnetic field and the movement of a charged particle within this field:

$$\vec{E}_{mot} = \vec{v} \times \vec{B} \tag{2.17}$$

Some other effects like diamagnetism (quadratic Zeeman effect) also contribute, but on a different scale that is not easily addressable within experimental precision. The Hamilton operator has to be expanded to include these contributions, which makes exact analytical solutions very tedious. For small perturbations, approaches to solve the Schrödinger equation exist, but for AE$\bar{\mathrm{g}}$IS where positronium is produced and manipulated within a homogeneous 1 T magnetic field, these perturbations cannot be considered small.

Hence, another method had to be used: the numerical diagonalization of the perturbed Hamiltonian, which yields the energy eigenvalues as the principal diagonal [79]. The precision of results only depends on the size and order of the Hamiltonian matrix, and therefore on the type of algorithms and processors available for the calculations. This treatment has been studied specifically for AE$\bar{\mathrm{g}}$IS needs and was published in 2008, [80], as well as in the framework of two dissertations [81, 82]. A few results and remarks in the light of AE$\bar{\mathrm{g}}$IS experimental environment are listed in the following:

- In strong magnetic fields, triplet and singlet states are not strictly separated anymore, therefore optical transitions between such states can occur. The additional fluorescence route reduces the lifetime of corresponding states, which is called 'magnetic quenching'. The same effect also applies to the annihilation lifetime, as due to the mixing of states the generally faster two gamma annihilations dominate over the respective three gamma processes.

- The linear Zeeman effect for Ps is inhibited by the vanishing net orbital magnetic moment of Ps due to the opposite charges of electron and positron. There are con-

tributions, though, arising from the spin magnetic moments and from higher order correction terms [83], albeit both are comparably small.

- The unperturbed solution of the Schrödinger equation is usually acquired in spherical coordinates and suffices the quantum numbers n, m, ℓ as presented above. This approach, however, bears no meaningful result when introducing non-spherical electric fields as occurring in most experimental setups. Using parabolic coordinates instead of spherical ones solves the problem to some extent. More details follow in section 2.7. At AE$\bar{g}$IS, the 1 T magnetic field is inducing a strong motional Stark electric field that certainly needs to be taken into account.

- The required wavelengths for one photon excitation between two levels change: As an example, former 205.048 nm for the unperturbed transition from 1^3S to 3^3P now ranges between 205.044 nm and 205.051 nm under an electric field of $1.5 \times 10^3\,\mathrm{V\,cm^{-1}}$ as can be caused by motional Stark effect in the magnetic field of AE$\bar{g}$IS.

2.5.4 Ps production

The easiest way of producing positronium is to implant positrons into a medium. The many interactions and processes a positron may experience inside the solid are well described in Ref. [84]. In short, fast positrons thermalize within a few picoseconds inside the bulk by inelastic collisions, then they randomly diffuse for a certain time which depends on the core- and electron-density of the bulk, on the type and amount of defects, and on the temperature. The final process can be direct annihilation, delayed annihilation due to trapping in a defect with reduced electron density or reemission into vacuum, either directly or as positronium. The formation of Ps is far more efficient when a medium is involved rather than a procedure where one provides trapped electron and positron plasmas in vacuum, simply because the high electron density comes for free inside a material, while for example in a trap it has to be prepared costly. Also the exchange of momentum is much easier in a medium, which boosts the production a lot. Of course, one has to make sure such formed Ps is able to leave the material, otherwise it would just annihilate. Once in vacuum, Ps can be excited to higher levels by appropriate laser pulses, increasing the Ps lifetime and the probability to react with another partner. Generally, Ps formation can be described with the relation given in Eq. 2.18.

$$e^- + e^+ \rightarrow \mathrm{Ps} \tag{2.18}$$

But also a charge exchange reaction for production of Ps is possible (Eq. 2.19), as first demonstrated by ATRAP [19]. The collaboration used an oven that produced a cloud of

cesium atoms inside a production trap. Next to that trap cool positrons were prepared and waited to be merged with the continuous cesium atom stream. A laser pulse excited cesium to Rydberg states, so that the loosely bound valence electron could jump over to the positron in a region where both particle clouds were finally overlapping. Excited positronium emerged with the same benefits of increased lifetime and reaction probability, while the high temperature (i.e. kinetic energy) stayed with the cesium ion.

$$\mathrm{Cs}^* + e^+ \rightarrow \ \mathrm{Ps}^* + \mathrm{Cs}^+ \tag{2.19}$$

Generally, the formation of Ps becomes dominant when the binding of positron and electron is energetically favored against all other possible processes. The released energy due to Ps formation in vacuum is equal to its ground state level of 6.8 eV. If an interaction partner such as cesium is involved, its outermost electron has first to be released by applying the ionization energy E_i. If no such partner exists, then one can simply assume $E_i = 0$ in Eq. 2.20, where E_{Ps} denotes the Ps formation threshold, i.e. the energy the positron has to provide in order to enable Ps formation [85]. Since the first ionization energy of cesium is about 3.9 eV, even positrons with zero kinetic energy could bind to the outermost electron, as this charge exchange reaction is exothermic. Such Ps would then still have an energy excess of $E_{Ps} = 3.9\,\mathrm{eV} - 6.8\,\mathrm{eV} = -2.9\,\mathrm{eV}$. Other collision partners require the positron to have minimum energy. Atomic hydrogen, for example, has an ionization energy of 13.6 eV, so the positron needs to have at least 6.8 eV before Ps can be formed.

$$E_{Ps} = E_i - 6.8\,\mathrm{eV} \tag{2.20}$$

Since the positron energy could also be used for the excitation of the collision partner to higher states (or induce other excitation processes), one usually also takes the partner's first excitation energy E_1 into account (10.2 eV for atomic hydrogen). As long as the positron energy falls inside the gap defined by the lower threshold for Ps formation E_{Ps} and that first excited level E_1, it can only be elastically scattered or form positronium. This gap is also called Ore-gap as noted down in Eq. 2.21. If the energy is higher than E_1, other inelastic processes start to interfere.

$$E_{Ps} < E_{e^+} < E_1 \tag{2.21}$$

Notably, during positron cooling in buffer gas traps as was presented above, one first exploits such inelastic collisions with molecular nitrogen, but eventually the positron energies fall below 9 eV, which is the average energy required for an electronic excitation in N_2. Then, the dominant process becomes Ps formation and positrons bound to Ps can escape

from the trap, disguised as neutral atoms. Hence, a second buffer gas is required that allows for smaller portions of energy to be taken per collision, until positrons are below E_{Ps} and Ps formation is not possible anymore.

In Chapter 4, the production of positronium will be treated in more detail. The next paragraphs will introduce techniques for estimating the amount of produced Ps and for studying excited Ps, of which some have been developed within the framework of this thesis.

2.5.5 Ps emission as a function of positron implantation energy

The energy-dependent Makhovian implantation profile is most often used to describe the stopping of positrons inside a solid [86]. This profile is given by the derivative of a Gaussian in a general formulation, with material-dependent parameters that are either empirically found or derived from Monte-Carlo simulations [87]. Essentially, it gives the fraction of stopped positrons, i.e. positrons that are almost thermal, at a depth z from the surface after implantation with energy E. The movement of thermalized positrons in the bulk can be described by a diffusion law, which allows to estimate the amount of positrons able to return to the surface $J(E)$. A mathematical expression for this process is given in Eq. 2.22, where J_0 corresponds to the fraction of thermalized positrons that is able to escape from the target through a surface process such as direct Ps production, reemission due to a negative positron work function or trapping in a surface state when arriving back at the surface. However, if some of these positrons are internally backreflected into the bulk, where they most likely would annihilate, a value for $J_0 < 1$ is found. Nieminen et al. derived a temperature dependence of J_0 which showed that for high temperatures J_0 is approaching unity [88]. The parameters n, m, B and $z_0 = BE^n$ are material-dependent parameters. The amount of emitted Ps is then usually expressed via Eq. 2.23, where f_0 is the fraction of positrons forming Ps when returning to the surface [89].

$$J(E) = J_0 \int_0^\infty \frac{m}{{z_0}^m} z^{m-1} e^{-\left(\frac{z}{z_0}\right)^m} e^{-\frac{z}{L_+}} dz \tag{2.22}$$

$$f_{Ps}(E) = f_0 J(E) \tag{2.23}$$

Taking into account the different escape rates ν_i for thermal positrons at the surface, f_0 can be expressed by the ratio given in Eq. 2.24. The different ν_i are:

$\nu_{s,Ps}$: the rate of positrons getting trapped in a surface state and being thermally desorbed as Ps,

$\nu_{0,Ps}$: the rate of positrons that bind to a surface electron to form Ps without trapping,

$\nu_{s,2\gamma}$: the rate of positrons getting trapped in a surface state and annihilating with nearby electrons predominately into 2γ quanta,

ν_{0,e^+} : the reemission of positrons into vacuum; this is only possible for materials with negative or at least very small positron work functions.

$$f_0 = \frac{\nu_{s,Ps} + \nu_{0,Ps}}{\nu_{s,Ps} + \nu_{0,Ps} + \nu_{0,e^+} + \nu_{s,2\gamma}} \tag{2.24}$$

Thermal Ps emerges only from the thermal desorption escape channel. The other, $\nu_{0,Ps}$, occurs only if the material has a negative Ps work function, which usually lies around few eV, or if the electron is nonthermal. Such emitted Ps has a correspondingly high kinetic energy. However, also not fully thermalized (epithermal) positrons can contribute to the nonthermal Ps emission, but these are not correctly described by the diffusion model and have therefore to be treated independently. As a remark, epithermal positrons may also escape directly from the surface if their energy is exceeding the (positive) positron work function.

2.5.6 Ps detection I: Single Shot Positron Annihilation Lifetime Spectroscopy

A well-established method for estimating the fraction of positrons that is converted into positronium is the Single Shot Positron Annihilation Lifetime Spectroscopy (SSPALS). Therein, a short pulse of positrons (about a few ns long) is implanted into the target and occurring gamma radiation is recorded by a scintillation detector with good time resolution for the next few hundred ns [90, 47]. If free Ps is formed, long-living components can be identified in the resulting lifetime spectrum.

Such a SSPALS measurement has been performed with the AE$\bar{g}$IS positronium test setup [63, 64, 91] at room temperature with a $PbWO_4$ scintillation crystal mounted on a photo multiplier tube (PMT). In a first series of four hundred consecutive shots, positrons were implanted into a nanoporous silica target for efficient positron/Ps conversion [92]. In a second series, the positrons were implanted into the aluminum holder of the target. The implantation energy has been set to $\approx$3.3 keV. The resulting spectra have been averaged per series and plotted together in Fig. 2.12. Both spectra, black for the converter target measurement with Ps production and gray for the aluminum reference with no Ps emission, consist of a prompt peak which resembles immediate positron annihilation occurring during implantation, and of a tail that contains long-living components. These can originate from

the detector response to the incident positron burst or from positronium. Sharp bumps in the tail, on the other hand, can only come from after-pulses of the PMT or from reflected positrons. For both averaged series, the peak height is (7.74 ± 0.01) V. The time axis was set to zero at the peak position. Both tails strongly differ, which can only be attributed to the presence of positronium.

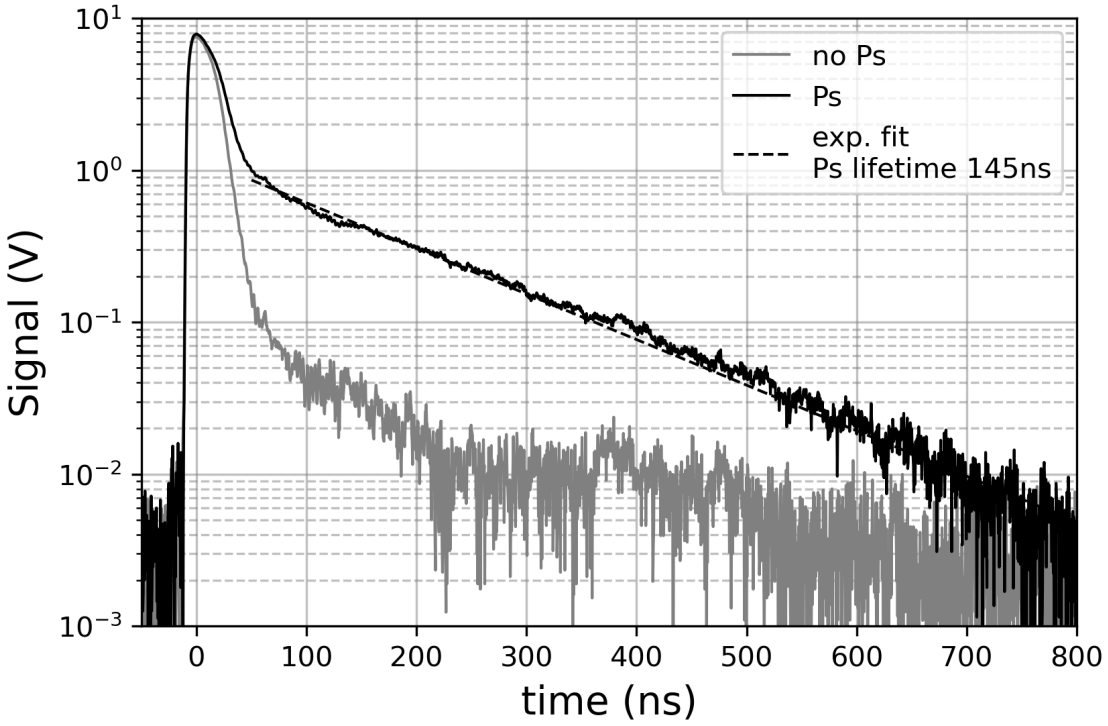

Figure 2.12: SSPALS spectrum of a series with positrons implanted into a nanochanneled Ps converter (black) and into an aluminum target (gray). On average, both show the same behavior in the peak region, which is due to the dominant prompt positron annihilation shortly after implantation, but differ heavily in the tail region due to the Ps formation when using the converter target. An exponential function has been fitted into the Ps data using times ranging from 50 ns to 800 ns. This resulted in a lifetime of (145 ± 4) ns for the delayed tail (dashed black line) The ratio of areas below the tail and below the peak finally amounts to (14.4 ± 0.8) %, which corresponds to the cold Ps fraction with respect to the total of implanted positrons.

One method to estimate the total fraction of Ps in vacuum with respect to the amount of implanted positrons based on SSPALS measurements was developed by Cassidy et al. [93]. Therein, two regions of the spectrum containing Ps have to be integrated independently from each other and put into ratio. The first region is called *tail* and integrates over positron annihilation occurring at delayed times, for the measurement at present this ranges from

60 ns to 370 ns where the spectrum is very 'clean'. In a second region called *total*, all events from 0 ns to 370 ns are integrated. Calculating the ratio *tail*:*total*, one obtains the delayed fraction f_d:

$$f_d = \frac{\int_{60}^{370} \left(V_D + V_{Ps} * V_D\right)\, dt}{\int_{0}^{370} \left(V_D + V_{Ps} * V_D\right)\, dt} \tag{2.25}$$

The term V_D models the peak immediately after the maximum, approximated as the pure detector response function exploiting the delta-function behavior of the incident positron pulse. The natural exponential decay of ground state o-Ps in flight is denoted as V_{Ps}, which has to be convoluted with the detector response. In sum with the peak function V_D, both tail and peak are sufficiently well described. Since the SSPALS measurement presented here had been conducted with a very similar detector as in Ref. [93], the same formalism holds but with slightly different parameters. Specifically, the decay time of the scintillator was 23 ns and the tail included a stronger background than was used in the reference, here about 10 % with respect to the total integral. Evaluating with the referenced method the measured Ps lifetime spectrum as shown in Fig. 2.12, one obtains $f_d = 22.7\,\%$. As a rough estimate, this could be converted into a o-Ps fraction by using $f_{o\text{-}Ps} \approx \frac{3}{2}(f_d - 0.05) = 26\,\%$.

This approach has a few uncertainties. For example, modeling the detector function as a single exponential seems too simple, as there evidently is quite some annihilation activity before time zero. This comes from the finite length of the positron pulse. Then, the 3γ and 2γ detection efficiencies have to be estimated on a purely empirical base (for simplicity it is assumed here that both are equal) and the detector saturation in the peak region leads to an overestimation of the amount of produced Ps. Furthermore, fast atoms of positronium may annihilate too early and mix into the peak region. The best way to deal with most these aspects would be to run a Monte Carlo simulation, e.g. using GEANT4, a toolkit for simulating the passage of particles through matter [94]. Unfortunately, this cannot be generally done once and for all detectors, as the individual geometry and environment plays an important role for each experiment. Two points, however, can be addressed experimentally, which are the background of the delayed signal and the peak saturation.

Tail background subtraction

By performing an additional measurement with the same setup, but on a target which cannot produce Ps such as a metal at high positron implantation energies, one can calculate the difference signal between Ps and no-Ps signals. This difference is basically free of any

background and contains only 3γ radiation due to o-Ps. Therefore, one can drop the approach of using approximate functions describing peak and tail, and directly set into ratio the integrals of both, while using the background free tail. The peak-integral has to be calculated using the no-Ps measurement, since it reliably tells the total amount of implanted positrons. Like this, the realistic modeling of the exponential detector response is not needed.

Integrating the peak of Fig. 2.12 from $-15\,\mathrm{ns}$ to $29\,\mathrm{ns}$ and the difference signal from $0\,\mathrm{ns}$ to $800\,\mathrm{ns}$, one obtains another approximation for the fraction of produced o-Ps. This is done by dividing the difference signal integral I_{diff}, which is proportional to the o-Ps amount, by the peak integral I_{peak}. The given error in Eq. 2.26 is purely statistical, while the result is still affected by the systematic choice where the peak ends and the tail starts, which has been set here to the point where Ps just became evident, by the non-linear behavior of the detector at different signal intensities and by fast Ps components annihilating at nearby obstacles and accidentally contributing to the peak.

$$f_{o\text{-}Ps,\,PbWO_4} = \frac{I_{diff}}{I_{peak}} = (23.8 \pm 2.4)\,\% \tag{2.26}$$

Peak saturation

The non-linear behavior of the $PbWO_4$ detector in the peak region was dealt with by using another scintillating crystal (Strontium iodide SrI_2, from the Lawrence Livermore National Laboratory) with similarly good time resolution, but better linearity in the peak region. This second detector had been acquiring lifetime spectra in parallel to the $PbWO_4$, therefore the same analysis as before could be applied, allowing to directly compare the results (see Eq. 2.27). The final o-Ps fraction of $(14.4 \pm 0.8)\,\%$ differs a lot from the two derived before, but at the same time it is the most model independent one - further improvements should include simulations and investigations of the detection efficiency for different gamma quanta.

$$f_{o\text{-}Ps,\,SrI_2} = \frac{I_{diff}}{I_{peak}} = (14.4 \pm 0.8)\,\% \tag{2.27}$$

PALS versus SSPALS

Generally, there are two similar experimental methods that aim to resolve the time structure of an annihilation spectrum. The first is the aforementioned SSPALS, where in a single shot all available positrons are implanted into the sample. Scintillation detectors

like the SrI_2 or the $PbWO_4$ detector, connected to photomultiplier tubes, convert the total energy that different gamma quanta deposit in the crystal per time unit into an electric signal. The recorded amplitude of this signal ideally is linearly proportional to the deposited energy. When now constructing the tail-to-peak ratio as was done above, one should acknowledge the multiplicities of occurring gamma radiation. The background free o-Ps tail annihilates only into three gamma quanta with energies selected from the continuous Ore-Powell spectrum — which has an average value of $\frac{2}{3}$ of 511 keV. In contrast to this, the annihilation radiation of the positron peak consists mainly of two gamma quanta with an energy of 511 keV for each. Hence, one usually detects 1.5 times more 3γ photons than 2γ photons per time unit, but the averaged energies of the two species have the inversed ratio. As a result, the tail-to-peak ratio is a good direct estimator for the produced o-Ps fraction without the need for a correction factor.

The second method is the so-called PALS, i.e. positron annihilation lifetime spectroscopy, where one aims to count single annihilation events. This requires a slightly different experimental setup that measures the time between positron implantation and annihilation, and converts this time into an amplitude. The different amplitudes are then counted with a multichannel analyzer, building up a histogram of annihilation times. Typically, PALS is either performed with a low positron rate, or one exploits the simultaneous emission of two 511 keV gamma quanta that have to be detected at the same time in two equally far away scintillation detectors. Consequently, the individual energies of the (3γ) photons are not acknowledged in the final histogram and the multiplicities of $2\gamma/3\gamma$ annihilations have to be taken into account.

In conclusion, when setting up a detection system for PALS/SSPALS, one should make sure that the total deposited energy of the gamma quanta is fully accounted for in order to obtain a linearly proportional response. If this is not possible, an energy-dependent correction factor is required to obtain trustworthy results. However, sometimes the estimation of such a correction factor is complicated and very model-dependent. Then, at the very least, one should acknowledge the multiplicities of 3γ and 2γ radiation and approximate any detected gamma as an energy-independent event. For the measurement obtained with the $PbWO_4$ detector, for example, which was indeed saturating in the peak region, the multiplicity-corrected tail-to-peak ratio becomes $\frac{2}{3}(23.8 \pm 2.4)\,\% = (15.9 \pm 1.6)\,\%$. This compares better to the o-Ps fraction of $(14.4 \pm 0.8)\,\%$ as measured with the not saturating SrI_2 detector.

2.5.7 Ps detection II: Spectroscopy with a high purity germanium detector

Another method for estimating the amount of produced Ps comprises spectra with high energy resolution as can be obtained from high purity germanium detectors (HPGe). An example is shown in Fig. 2.13, recorded with the coincidence Doppler-broadening spectrometer (CDBS) in Munich [48]. The lower abscissa denotes the original channels taken from a multichannel analyzer (MCA). These can be converted into energies via calibration with a ^{152}Eu source (upper abscissa). One can find a region in such a spectrum that is very sensitive to ortho-Ps annihilation, the so called valley region as is marked in the figure. The only other contributions to this region originate from the environmental background, from pile-up events (simultaneous detection of two or more gamma quanta with lower energy mimicking one gamma with higher energy), and from small angle Compton-scattered 511 keV photons. The environmental background can simply be measured and subtracted, while the other two contributions are often either roughly estimated or considered negligible. The fraction of produced Ps can then be estimated by scaling the spectrum in question between a 0 % and a $\approx$ 100 % Ps reference spectrum, which recorded with the same experimental setup.

Estimating the amount of produced Ps usually starts by defining a shape parameter, for example the so-called valley-to-peak ratio $R = \frac{V}{P}$. The term V denotes the integral of the background free valley region, while P is the integral of a small window around the photo peak center. Sometimes, R is also defined as $R = \frac{T-P}{T}$, where T is the total integrated spectrum. In both cases, the term f_{Ps}, or the so-called F-parameter, can be calculated with [95, 96]:

$$f_{Ps} = \left(1 + \frac{P_1}{P_0} \cdot \frac{[R_1 - R]}{[R - R_0]}\right)^{-1} \tag{2.28}$$

The subscripts '0' and '1' encode that the corresponding values have to be derived from reference measurements with 0 % and 100 % Ps formation, respectively. Additionally, one must make sure that the values P_1 and P_0 are obtained with the same amount of implanted positrons, since there is no automatic normalization included in their ratio (unlike the R-values). This approach is well established and commonly used, but there are systematic uncertainties that should be addressed:

- In most cases, the experimental setup does not allow the detection of all produced gamma quanta following Ps annihilation. Together with the different detection efficiency for 2γ and 3γ annihilation events, one usually will find a fraction < 1 for the total Ps production.

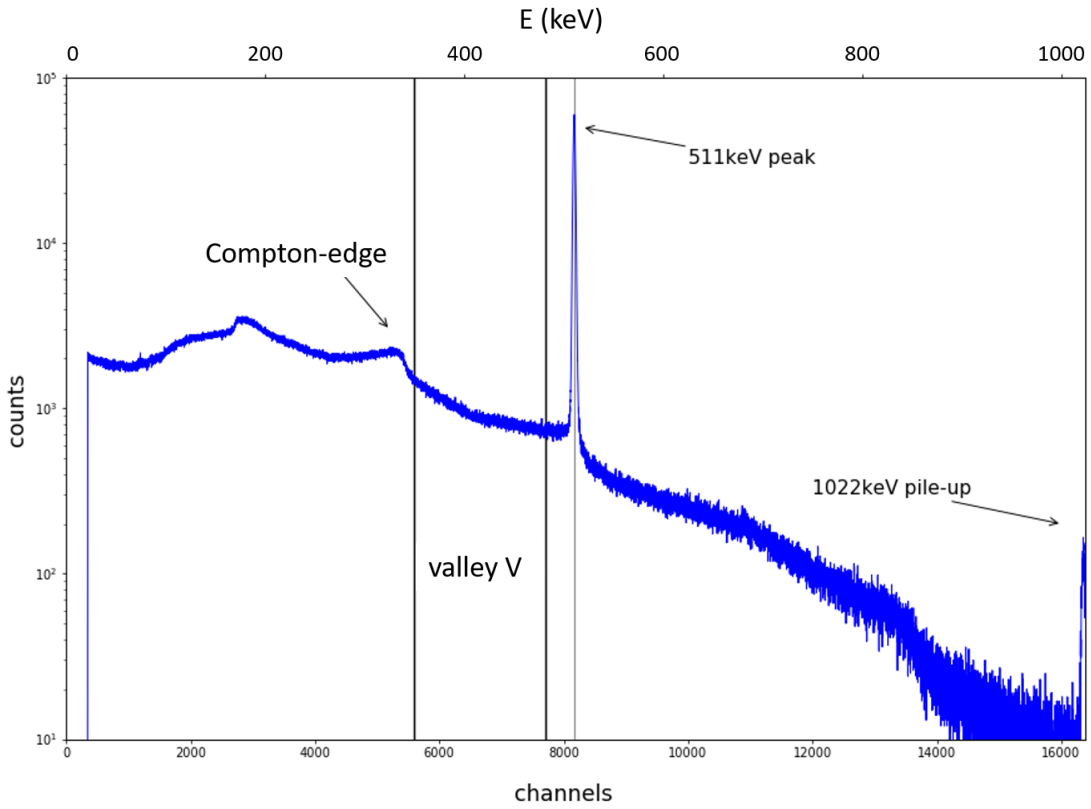

Figure 2.13: Typical gamma spectrum occurring after positron implantation at 15 keV, detected by a high purity germanium detector. Important characteristics of that spectrum are the positron annihilation photo peak at 511 keV, the pile-up peak at 1022 keV, the Compton-edge at 340 keV and the valley region, which is most sensitive to o-Ps annihilation.

- The velocity distribution of ortho-Ps leaving the target leads to a slow fraction annihilating in flight close to the origin and a faster one annihilating rather far from it [97, 98]. Hence, due to the geometric acceptance of the detector, it will weight the occurring radiation differently depending on the position of an annihilation event. Limiting the flight path, e.g. with an obstacle, will lead to pick-off annihilation, which produces 2γ photons and the event is wrongly sorted into the peak region. This is also true for fast ortho-Ps components actually hitting the chamber walls.

- Often, a 100 % Ps reference is obtained by implanting positrons with almost 0 keV into a pure germanium single crystal heated close to its melting point (1210 K). High Ps yield can indeed be achieved like this as was demonstrated in Ref. [99], where the authors found 97 % using positron annihilation radiation induced Auger-electron spectroscopy (PAES). However, one usually just assumes that the obtained Ps amount following from this method is close to 100 %, without further verification. This is challenged by the possible presence of target impurities and other defects, by the difficulty to prepare a positron beam with zero energy, by reemitted or backscattered positrons, and by bulk or surface annihilations.

- Also the reference measurement for 0 % Ps production is not fail-save due to the energy and material dependent backscattering probability of positrons. Such backscattered positrons are subject to the electrostatic forces nearby the converter target, and may end up in an unpredictable state that can include some Ps formation. Of course, large vacancy clusters and pores can also lead to Ps production in the bulk of the target, albeit this contribution has no great impact when choosing a single crystal material.

Example: Ps emission from a Ge(100) target at 1100 K

In order to obtain a reference measurement for 100 % Ps production with the CDB spectrometer mentioned above, a square piece of an undoped Ge(100) wafer was fixed onto a molybdenum plate, which in turn was attached to a controllable heater and to a temperature sensor. The sample was first heated to 870 K for about 2 h in order to clean the surface from contaminants, then the temperature was increased to 1100 K. A continuous beam of 5×10^7 remoderated positrons per second at 20 eV from the positron source NEPOMUC was implanted into the target with energies ranging from 0.4 keV to 28 keV. Typically, the integral over a full spectrum results in about 23 000 detected counts per second.

For analysis, Eq. 2.28 was first used assuming that at 0.4 keV almost 100 % of free Ps, and at 28 keV no Ps was emitted. More specifically, for the valley region the spectra have

been integrated between 340 keV and 500 keV returning a value for V. For the peak, the spectra where integrated around ±2 keV around the center giving back the values for P. The result is shown as the black squares in Fig. 2.14.

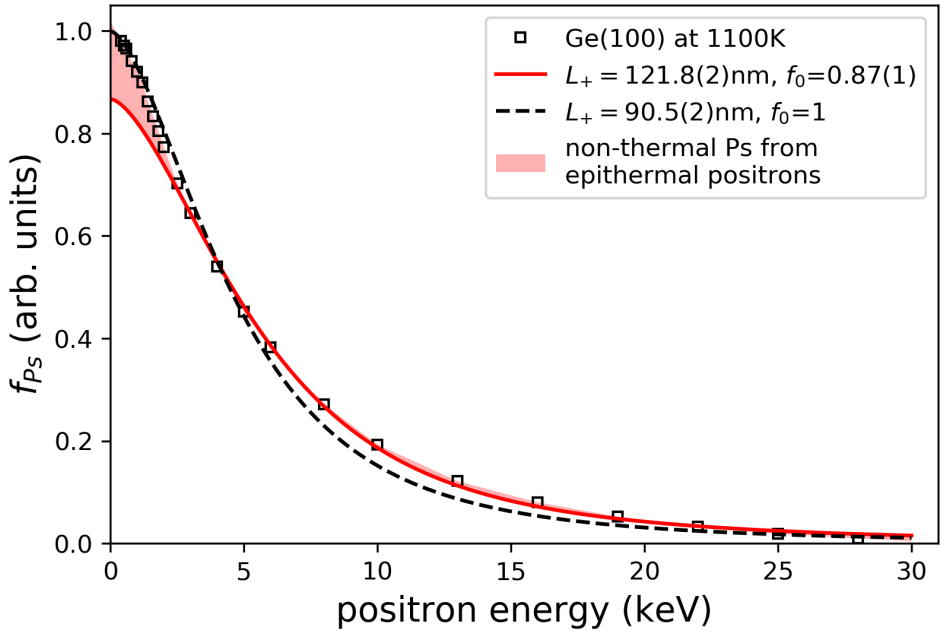

Figure 2.14: Ps yield from pure Ge(100) heated to 1100 K as a function of positron implantation energy. Measured values (symbols) were used for fitting models describing the amount of implanted positrons diffusing back to the surface and forming Ps. The term L_+ is the positron diffusion length and f_0 the respective maximum fraction of Ps formation following from thermal positrons as detailed in the text.

Using the positron diffusion model with subsequent Ps emission as described by Eq. 2.22 and Eq. 2.23 for Ge with parameters $n = 1.6$, $m = 1.68$, $B = 7.48\,\mathrm{nm\,keV^{-n}}$ from Ref. [87], and assuming $f_0, J_0 = 1$ as is required for 100 % Ps-production, one can numerically fit the model to the experimental data (dashed black line). In addition, the term $J(E)$ can be evaluated for the germanium target at 0.4 keV, resulting in 99 % of thermal positrons returning to the surface using the fitted diffusion length of 90 nm. This confirms the initial assumption of $J_0 = 1$, but it does not tell anything about f_0, which denotes the final escape route of the positrons. Indeed, the fit does not well represent the measured data-points for energies ranging between 5 keV and 20 keV. Also the extracted diffusion parameter E_0 connecting the positron diffusion length with the Makhovian material constants by the relation $L_+ = BE_0{}^n$ amounts to (4.8 ± 0.1) keV, which does not correspond to earlier results, obtained for example in Ref. [89] where E_0 for Ge at 1100 K was around 6 keV.

Changing the fit procedure such that f_0 is a fit parameter, too, while keeping $J_0 = 1$ and using only energies $> 2\,\mathrm{keV}$ in order to avoid contributions from not thermalized positrons that are not obeying the simple diffusion law [100], one obtains a better fit with $f_0 = 0.87 \pm 0.01$ and $E_0 = (5.8 \pm 0.1)\,\mathrm{keV}$ (solid red line in Fig. 2.14). This indicates that the contribution of nonthermal positrons reaching again the surface makes up about 13 % of the total Ps formation at zero implantation energy.

This demonstrates that one can fit a plausible model to the measured data points, but in fact the absolute amount of produced Ps remains unknown. It scales up or down with f_0, which originally has just been assumed to approach unity at zero positron implantation energy using the formalism presented in this paragraph. To justify this experimentally, several things have to be avoided such as reemitted positrons, surface contaminants or annihilation of surface-trapped positrons. These difficulties can easily be overcome if the 100 % reference measurements was ultimately not required, which can only be ensured by choosing a method of measuring the absolute Ps fraction directly. Such a direct procedure has been developed within the present thesis, making use of a superposition of 2γ and 3γ spectra obtained from a GEANT4 simulation. This new method, as presented in the next paragraph, has also been published in a condensed form in Ref. [101].

GEANT4-supported determination of absolute Ps formation fraction

The ortho-Ps spectrum consists of $N_{3\gamma}$ photons originating from 3γ annihilations. The 2γ annihilations of para-Ps and quasi-free positrons lead to $N_{2\gamma}$ photons with 511 keV. The ratio of produced ortho-Ps to para-Ps is 3:1 due to the spin multiplicity of the triplet state. As a consequence, in case of 100 % Ps formation and emission into vacuum, a maximum value of 9:2 for the photon ratio $N_{3\gamma}/N_{2\gamma}$ can be reached. The number of detected 3γ photons is proportional to the amount of ortho-Ps atoms, which allows to calculate the fraction of all produced Ps atoms with respect to the total number of implanted positrons via Eq. 2.29.

$$f_{Ps} = \frac{\text{produced Ps atoms}}{\text{total number of } e^+} = \frac{\frac{4}{3}N_{3\gamma}}{N_{3\gamma} + \frac{3}{2}N_{2\gamma}} \tag{2.29}$$

Since detectors usually display a unique, energy- and geometry-dependent response to annihilation radiation, it is not trivial to estimate the absolute amount of produced gammas from a measured spectrum. One approximate solution to find f_{Ps} was presented in Ref. [102], where the integrated 3γ sensitive valley region V was scaled up according to the full theoretical 3γ spectrum derived by Ore and Powell (see again Fig. 2.11). The scaled signal was then divided by the total integral of the measured spectrum, which was assumed to be

proportional to the total amount of implanted positrons. In the present work, the unique HPGe detector response was taken into account by implementing the geometric setup of the CDB spectrometer into a GEANT4 simulation (Fig. 2.15). This allows to include major physical effects such as Compton and Rayleigh scattering, the photoelectric effect and photon absorption within surrounding materials.

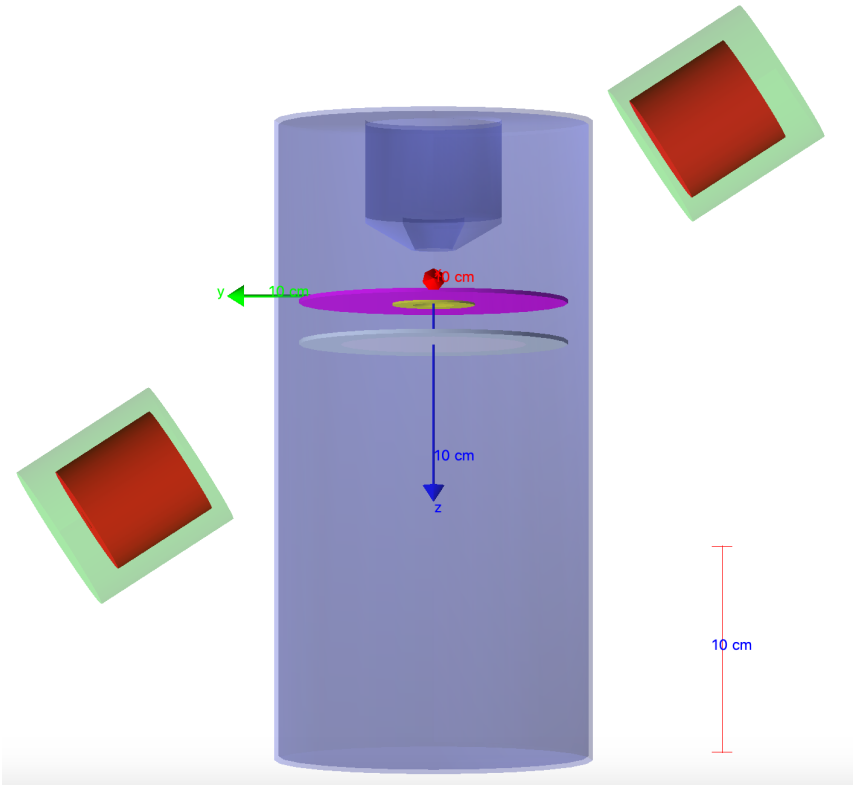

Figure 2.15: Sketch of the (coincidence) Doppler-broadening spectrometer at NEPOMUC as it was set up during the measurements on Ge(100) targets. In the center of the purple disk, a point source of annihilation radiation was assumed. In a first GEANT4 simulation, a pure 2γ source was used, in a second simulation a continuous 3γ source. Spectra as seen by the upper detector were thus obtained.

The central part of the CDB spectrometer consists of a cylindrical steel chamber with 2 mm thick walls and 150 mm as inner diameter; two 2 mm thick aluminum rings with an outer radius of 65 mm working as potential lenses; a molybdenum disk as part of the target heater in the center of the upper aluminum ring; a steel electrode at the top, roughly 60 mm away from the upper aluminum disk as part of the positron beam line. Outside the steel chamber, up to eight HPGe detectors can be installed facing towards the center of the aluminum rings. In the following, only the upper detector was actually simulated. Exact details of the geometrical and functional setup can be found in Ref. [48]. The detector

itself was modeled as a cylinder of solid germanium with radius 28 mm and a length of 54 mm, encapsulated inside an aluminum shell with 1 mm thin walls. The detector front face was 140 mm away from the center between the two disks. The energy resolution of the detector has been measured using the aforementioned ^{152}Eu source, located in front of the detector. A spectrum was acquired for 60 s as shown in Fig. 2.16.

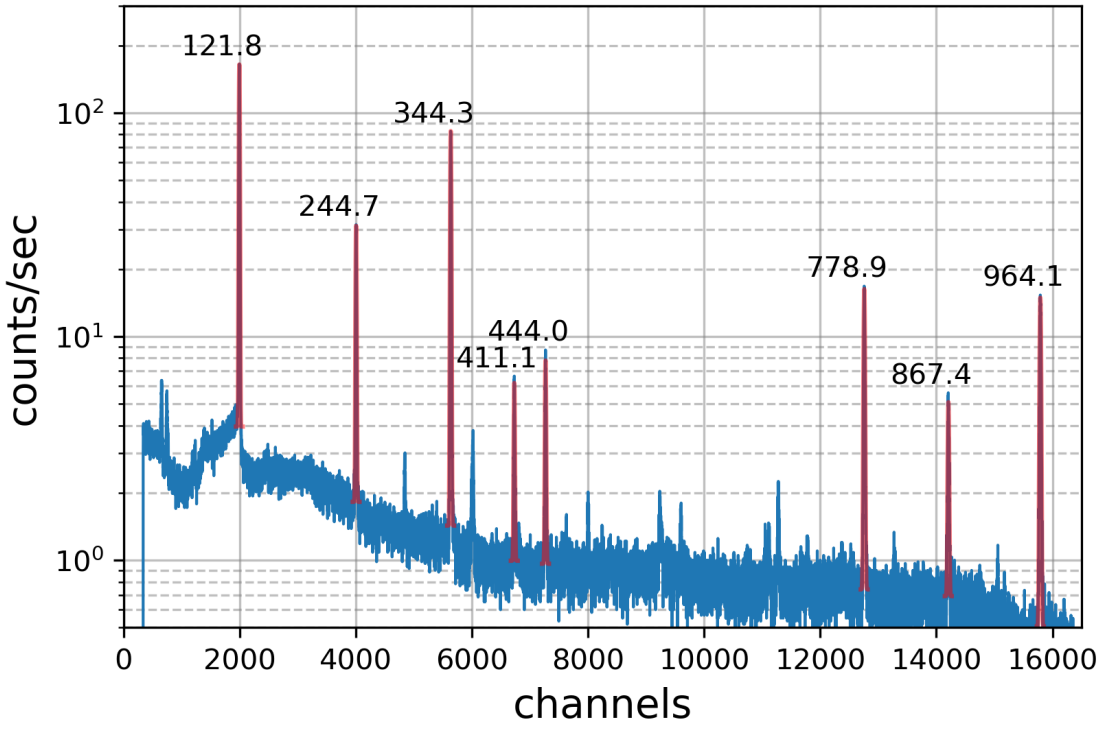

Figure 2.16: Calibration with an ^{152}Eu source in front of the HPGe detector. Corresponding peak energies from Ref. [103]) are printed on top of the peaks in keV.

The eight most intense spectral lines have been cross-linked with the energies from the table of radionuclides for ^{152}Eu [103] and were fitted with Gaussian functions. Like this, the detector channels and the peak broadening could be fitted as a linear function of the photon energy. The fit result is shown in Fig. 2.17, where the left figure displays the channel-to-energy conversion. On the right, the 'sigma' required for the derivation of the energy resolution is shown, which finally was plugged into the GEANT4 simulation. For example, at 511 keV, an energy resolution of $\sigma = 0.65$ keV is found, corresponding to a FWHM of 1.5 keV. The last step before running the simulation was to define point sources located in the center of the upper disk, isotropically emitting gamma radiation. First, a pure 3γ source with energies selected from the Ore-Powell distribution was used, then a pure 2γ source with 511 keV gammas only.

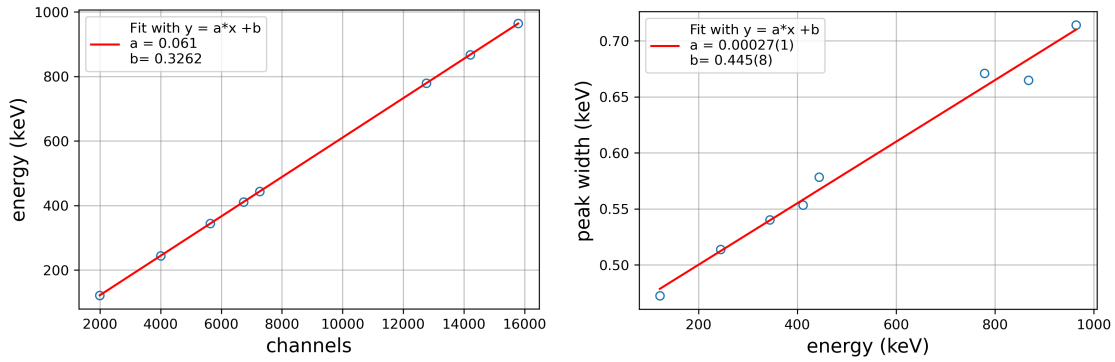

Figure 2.17: Left: Linear relation between channels of the acquiring multichannel analyzer and corresponding gamma energy, obtained from the ^{152}Eu calibration spectrum in Fig. 2.16. Right: Linear correlation between energies and peak widths (sigma).

The two spectra resulting from a simulation with 1×10^9 initial photons are very distinct as can be seen in Fig. 2.18. For the 2γ spectrum denoted as $C_{2\gamma}$, we find the photo peak at 511 keV, the Compton-edge at 340 keV and an edge at 170 keV (so-called backscatter peak) originating also from Compton-scattered photoelectric gammas. These, however, were scattered in the surrounding material rather than in the detector, such that it may have lost up to $\frac{2}{3}$ of its original energy before entering the HPGe crystal. The 3γ spectrum $C_{3\gamma}$ is rather flat, lacking as expected a clear peak structure and is rapidly falling off beyond 511 keV.

The scaling numbers $N_{3\gamma}$ and $N_{2\gamma}$ introduced above can be found by fitting a linear combination of both spectra to any measured data as denoted in Eq. 2.30. Additionally, a positron induced background C_{BG} that might be present in the measurement has been added. Applying this new procedure to the measured Ge(100) data, the values for $N_{3\gamma}$ and $N_{2\gamma}$ can be used in order to derive f_{Ps} via Eq. 2.29. For this, every measured spectrum was first normalized to the same measurement time, which resulted in a constant integrated positron signal, since positrons were implanted at a constant positron rate. Then, an environmental background obtained from a measurement with no positrons was subtracted from all spectra.

$$C_{meas}(E) = N_{3\gamma}C_{3\gamma} + N_{2\gamma}C_{2\gamma} + C_{BG}, \tag{2.30}$$

The positron induced background C_{BG} was found by using a spectrum recorded for Ge(100) at high implantation energy (28 keV) and at room temperature. As before, the expected fraction of back diffusing positrons to the surface at this high energy was estimated via Eq. 2.22 using the positron diffusion length found in the previous paragraph.

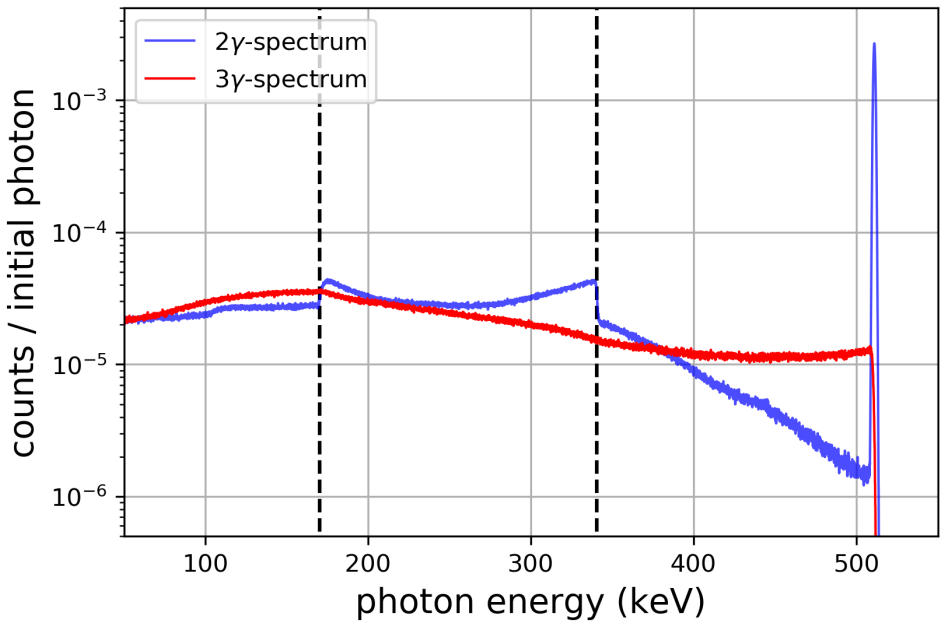

Figure 2.18: Simulated 2γ and 3γ annihilation spectra for the CDB spectrometer at NEPOMUC. Blue: pure 2γ spectrum as from para-Ps or direct positron annihilations. Red: 3γ spectrum produced by ortho-Ps annihilations. The dashed lines mark the energies 170 keV and 340 keV, hence $\frac{1}{3}$ and $\frac{2}{3}$ of the photo peak energy.

This estimated fraction is negligible, allowing us to use the corresponding spectrum as a 0 % Ps reference. Scaling up the simulated $C_{2\gamma}$ so that the integral within an energy interval of $\pm 2\sigma$ around the peak center is equal to the one of the measured spectrum allows us to take the difference between both. This difference corresponded to C_{BG} as shown in Fig.2.19. Artifacts in C_{BG} due to this channel-wise subtraction were smoothed via moving window averaging. The positron-induced background was subsequently subtracted from any other measured spectrum recorded with this geometrical setup, resulting in 'clean' annihilation spectra that consisted only of a superposition of a pure 2γ and a 3γ spectrum.

The weighting factor $N_{2\gamma}$ of a cleaned annihilation spectrum was found by scaling up the simulated spectrum $C_{2\gamma}$ in such a way that its peak integral within $\pm 2\sigma$ around the peak center matches that of the spectrum in question. After subtracting this scaled 2γ spectrum, the simulated 3γ spectrum was also weighted such that its integral between 100 keV and 500 keV photon energy matched the integral of the remainder. From the two determined scaling factors $N_{2\gamma}$ and $N_{3\gamma}$, the amount of detected Ps f_{Ps} was calculated. In Fig. 2.19, Ge(100) spectra are shown with positron energies of 0.4 keV (top) and 28 keV (bottom) for a target temperature of 1100 K. The $N_{3\gamma}/N_{2\gamma}$ ratios following from this

procedure were found to be 1.33 and 0.02, respectively. This corresponds to a Ps fraction of $f_{Ps} = 62.6\,\%$ and $f_{Ps} = 2.1\,\%$.

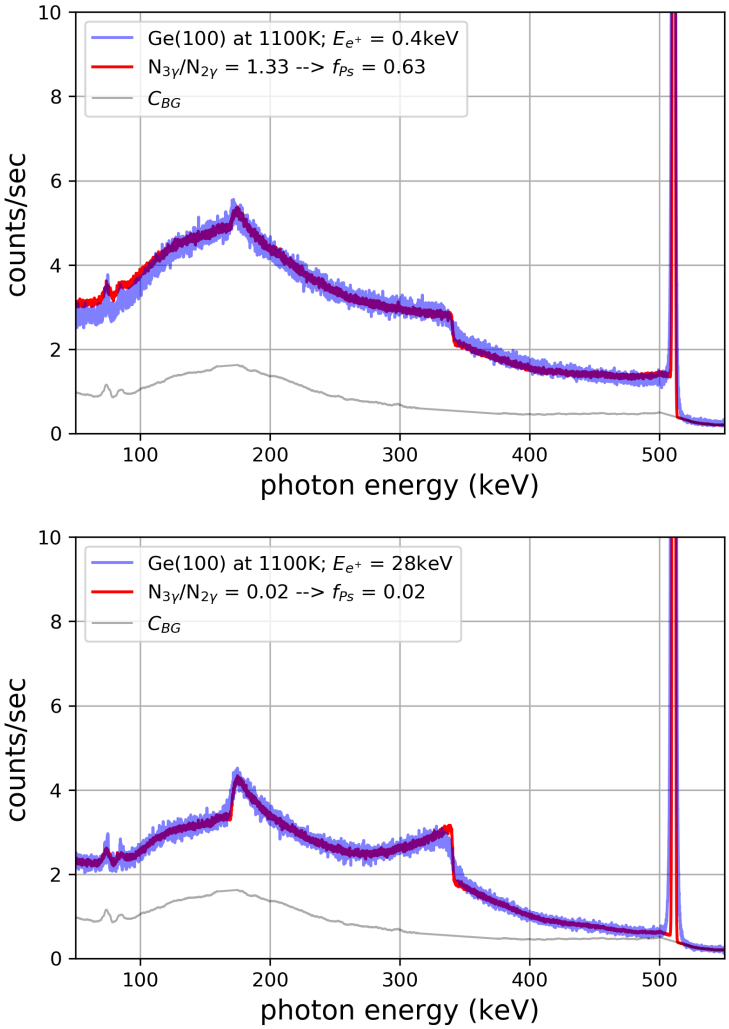

Figure 2.19: Measured spectra (blue) plotted together with correspondingly scaled, superimposed 2γ and 3γ spectra (red) for 0.4 keV (top) and 28 keV (bottom) positron implantation energies. Also the positron-induced background C_{BG} is shown (gray). From the ratio $N_{3\gamma}/N_{2\gamma}$, the amount of emitted Ps f_{Ps} could be calculated, yielding 63 % and 2 %, respectively.

Despite the good fit, C_{BG} seems relatively high compared to the measured spectra, except in the peak region where it is smaller by orders of magnitude. This happens because of differences between measurement and simulation, of which the most important one occurs to be pile-ups. Annihilation gamma quanta arrive at the detector within a limited detection time window of few nanoseconds, while the simulation just 'knows' the precise arrival time of each single gamma. Thus in the measurement, all low energy pho-

tons within this time window are counted as one photon with higher energy. This affects the 3γ annihilation spectrum occurring on the left side of the photo peak. In order to characterize this pile-up spectrum, a uniform distribution of gamma quanta with energies ranging between 0 keV and 340 keV was assumed, approximating the Compton-spectrum. Then, a histogram of all possible two gamma combinations was calculated, which is depicted in Fig. 2.20. For clarity, different types of combinations were distinguished by color in the final histogram, namely the two gamma combinations in blue/green and three gamma combinations in orange/brown. From several measurements on silicon and germanium with the CDB spectrometer, an average value for the ratio of the total counts in the Compton region to the events in the peak region could be calculated, amounting to about 3:1. This ratio was maintained for the simulation, i.e. the low energy gamma quanta from the Compton-spectrum had a three times higher weight than a single gamma from the photo peak. Notably, the edge at 840 keV can also be found in all measured CDB spectra, which confirms that pile-ups are contributing considerably.

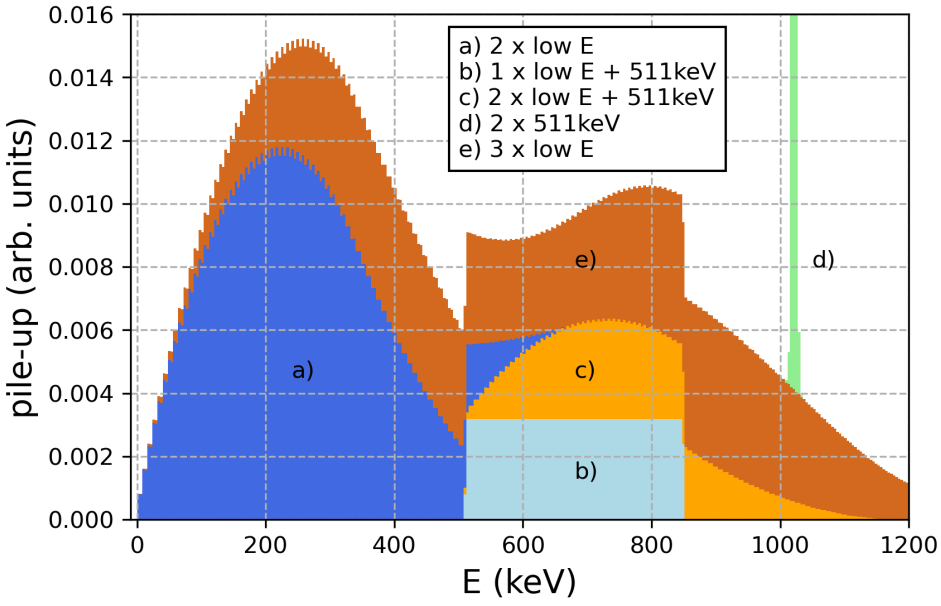

Figure 2.20: Histogram of two and three low energy gamma combinations following from an assumed uniform spectrum between 0 keV and 340 keV (approximating a Compton-background).

The common F-parameter calculation as denoted in Eq. 2.28 includes the term R_0, which essentially comprises all these background events that can not be attributed to Ps production, but evidently occur in the valley region V. See for example Ref. [100], where by using the reported values $R_1 = 11$, $P_1/P_0 = 0.4$ and $R = R_0 = 3.4$, and artificially setting $R_0 = 0$ afterwards, the F-parameter at high positron implantation energies claims

about 50 % Ps production instead of the expected null result. In conclusion, it is reasonable to subtract a positron-induced background in order to find a trustworthy lower limit for the amount of produced Ps.

Another systematic effect originates from the assumption of fixed sources of gamma radiation during the GEANT4 simulation. This is not entirely realistic, because all emitted Ps atoms rapidly move away from their origin. In the case of p-Ps, this is not a big problem because the vast majority will annihilate very close to the target due to the short singlet lifetime. Ortho-Ps, however, will move away several millimeters within a 2π sphere. Most of the atoms will annihilate in flight somewhere above the target. The o-Ps fraction annihilating via pick-off upon collision with an obstacle, on the other hand, will do so quite far away from the origin. In order to quantify this effect, an additional Monte Carlo simulation was required. At first, thermal Ps velocities were modeled with a Maxwell-Boltzmann distribution $P_{\mathrm{MB}}(v,T)$ with $T = 1100\,\mathrm{K}$, equal to the target temperature. Many ortho-Ps atoms were then moved around within the geometric layout of the CDB spectrometer emerging from their common origin in time steps of 1 ns. During every time step in free flight, o-Ps had a chance to annihilate into 3γ's equal to $P_a = (1-e^{-1\,\mathrm{ns}/142\,\mathrm{ns}}) = 0.007$. When approaching an obstacle, the o-Ps atom had a chance of P_{po} to pick off an electron with opposite spin and annihilate as p-Ps. Otherwise, it was reflected and moved on. A simulation result with $N = 10\,000$ o-Ps atoms is depicted in Fig. 2.21. Several aspects can be understood from this simulation for a source that emits 100 % positronium:

- About 95 % of the o-Ps atoms annihilate in flight. This fraction increases even more when the pick-off probability P_{po} is further reduced, because o-Ps can move on for a while after being reflected at an obstacle. As a consequence, the effective flight path increases as well. Varying P_{po} between 0.25 and 1 - the physically possible minimum and maximum values, respectively - a mean flight path extension of up to 4 mm was found. It is therefore sufficient to apply this flight path extension as a positive-only uncertainty in order to legitimate the assumption $P_{po} = 1$.

- The purely geometric acceptance of the HPGe detector for gamma radiation originating from the positron implantation point on the target is 1.00 %. For 3γ radiation of o-Ps in free flight, this becomes on average 1.07 % as follows from the MC-simulation. Consequently, during the measurement the detector saw slightly more three gamma radiation than the GEANT4-simulation assumed and the estimated amount of 3γ quanta is too high. This is treated as a negative-only systematic uncertainty on the three gamma scaling factor, hence $N_{3\gamma} \cdot (1.00_{-0.07})\%$.

- The acceptance of the fraction of o-Ps annihilating via pick-off at an obstacle is on average 1.29 %. Since the pick-off fraction is not more than 5 % even for $P_{po} = 1$,

the average acceptance for 2γ radiation including the initial p-Ps annihilation close to the origin is 1.04 %. This is treated as a negative-only systematic uncertainty on the two gamma scaling factor, i.e. $N_{2\gamma} \cdot (1.00_{-0.04})\%$.

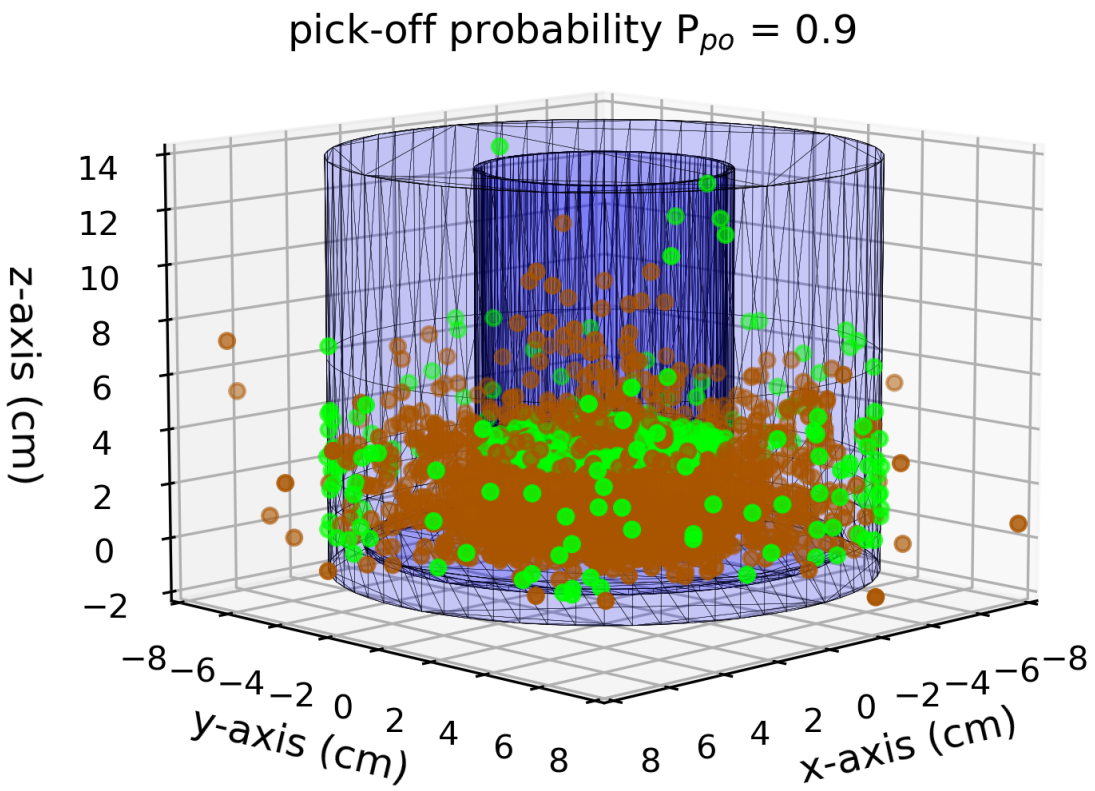

Figure 2.21: Result of a Monte Carlo simulation of o-Ps in free flight after emission from the germanium target inside the CDB spectrometer with Maxwell-Boltzmann velocity distribution at target temperature of 1100 K.

The new $f_{Ps}(E)$-values for the Ge(100) at high temperatures are given in Fig. 2.22 as the black squares. Again, the positron diffusion model introduced in Eq. 2.22 with f_0 and L_+ as free parameters was used. Only data points at implantation energies higher than 2 keV were considered, so that positrons were stopped and thermalized deep enough inside the solid in order to validate the diffusion model. One finds diffusion parameters comparable to the ones of Fig. 2.14, but f_0 is reduced by about 30 %. As expected, the highest

measured Ps formation occurred at 0.4 keV positron implantation energy, amounting to $0.626_{-0.027}$. Again, at least 12 % of the formed Ps leaves the surface as non-thermal Ps.

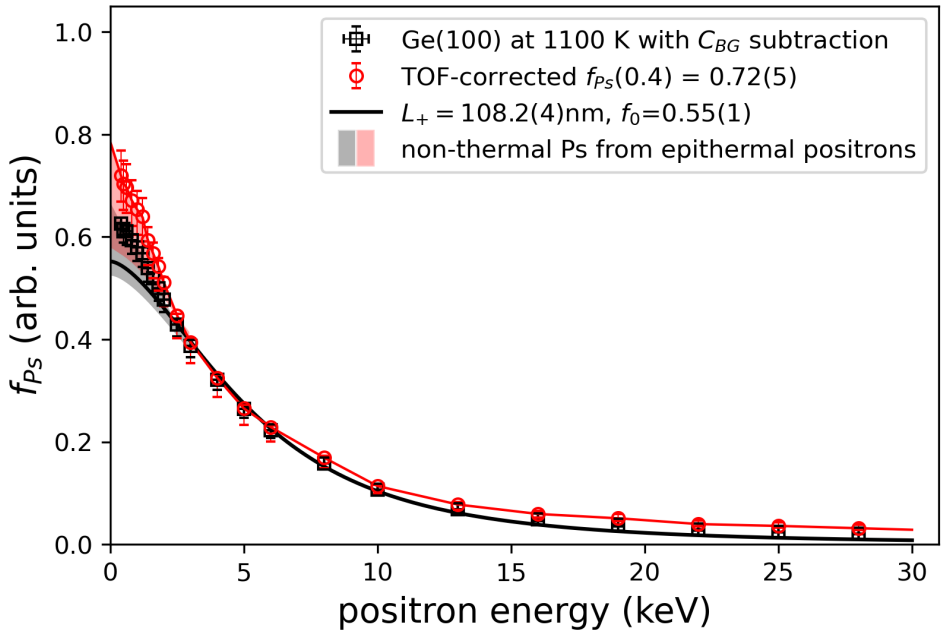

Figure 2.22: Estimated Ps amount following from a superposition of simulated 2γ and 3γ spectra as shown in Fig. 2.19 for all measured positron implantation energies (black squares). Fitting the data with the model of thermal positron diffusion gives back a diffusion lengths L_+ comparable to the one obtained before (solid black line). Applying a correction due to time-of-flight limitations and consecutive pick-off annihilation, the absolute fractions of emitted Ps are estimated (red circles and red solid line as guide for the eye).

Having obtained a lower limit for the Ps production, an estimation for the absolute amount can be derived as well, which means to include all systematic uncertainties. As shown above, the only major uncertainty is caused by movement of o-Ps. In order to acknowledge that different Ps formation channels result in different Ps velocities, one should at least split the total produced Ps fraction into thermal and nonthermal components. The former has already been successfully modeled with the presented Monte Carlo simulation and resulted in a maximum detectable thermal o-Ps fraction of $R_{th} = (95 \pm 1)\,\%$, which — as a reminder — makes up only 75 % of the total production.

For nonthermal o-Ps on the other side, the modeling is similar but can be simplified by assuming constant velocity as it would occur in materials with negative Ps work function ϕ_{Ps}. In case of Ge(100), however, the calculated Ps work function lies around $\gtrapprox 0\,\mathrm{eV}$ [104, 105]. As a consequence, nonthermal Ps following from thermal positron diffusion

can be excluded here, which means $f_{th} = f_0$. But nonthermal Ps can also originate from epithermal positrons, which are not sufficiently well modeled by Makhovian implantation and subsequent diffusion. Despite this, the majority of epithermal positrons will not have much more than a few eV. Assuming therefore Ps with $(3 \pm 3)\,\mathrm{eV}$, which comprises a very conservative uncertainty, only a fraction of this nonthermal Ps $R_{nth} = 0.46 \pm 0.16$ can be detected by the detector before pick-off annihilation occurs (Eq. 2.31). The term x_0 appearing in this equation is the average flight path for o-Ps. It was extracted from the technical drawings of the CDB spectrometer, amounting to $x_0 = (64 \pm 6)\,\mathrm{mm}$.

$$R_{nth} = 1 - e^{-\frac{x_0/v(E)}{\tau_{o-Ps}}} = 0.46 \pm 0.16 \tag{2.31}$$

$$f_{Ps,abs} = f_0\left(\frac{0.75}{R_{th}} + 0.25\right) + (f_{Ps} - f_0)\left(\frac{0.75}{R_{nth}} + 0.25\right) \tag{2.32}$$

Applying both these correction terms via Eq. 2.32 to the thermal and nonthermal Ps components following from the fit on the Ge(100) data, the red curve in Fig. 2.22 is obtained. An absolute amount of $f_{Ps,abs}(0.4) = 0.72 \pm 0.05$ of emitted Ps at 400 eV positron implantation energy is found, with an extrapolated amount of about $(79 \pm 5)\,\%$ at zero energy. It is noteworthy that this result is not compatible with the initial assumption of 100 % Ps formation for the heated Ge(100) target under the presented experimental conditions, even after the TOF and pick-off corrections were applied. Gamma spectra recorded for a set of novel positron/Ps converters, as presented in Chapter 4, will be analyzed with this new method that is based on simulated 2γ and 3γ spectra. It is expected that this yields a more reliable estimation of the absolute amount of emitted Ps.

2.5.8 Ps detection III: MCP imaging of ionized Ps

While the two introduced methods, SSPALS and using a HPGe detector, work well for estimating the amount of produced Ps given the right experimental conditions, not all environments provide the possibility to locate the corresponding detectors nearby the source of Ps due to their size or specific working conditions. The AE$\bar{\mathrm{g}}$IS apparatus is such an example, since the Ps production region is kept at 10 K and within a strong 1 T magnetic field, which are requirements for an ultra high vacuum and for antiproton manipulations, respectively. Also, due to limited internal space, Ps can not survive much longer than a few o-Ps lifetimes, since it will soon annihilate by pick-off upon contact with the first obstacle.

A spatially resolving detection method for observing (excited) positronium via a microchannel plate (MCP from Hamamatsu F2223) and phosphor screen (P46) was developed

by the Ps working group of AEgIS, in order to visualize the Ps cloud emerging from below the target border as shown in Fig. 2.23. The normal on the MCP surface was aligned with the 1 T magnetic field, which defines the experimental z-axis. In the figure, two images acquired by a CMOS camera are presented on top of each other. The one hued in red was obtained with the MCP front face biased to 180 V, which attracted photo electrons released from all surfaces after irradiation with scattered UV light. One specifically sees the positron/Ps converter target (Ps target), the laser screen on the left used for aligning the lasers with the Ps cloud and faintly also the outer rim of the trap electrodes, where antiprotons are kept and manipulated for antihydrogen production. The image hued in green corresponds to a voltage of −180 V, which in turn was attracting 'photo positrons'. These occur, when both the UV laser and the photoionizing IR laser (1064 nm) are superimposed, aligned reasonably well with the Ps cloud and triggered at the same time. Then, the charged photo positrons are, as before the electrons, confined to the magnetic field lines due to a very small cyclotron radius (below 1 µm) and accelerated towards the charged MCP front face. Upon impact, they set free secondary electrons which finally cause a light spot on the phosphor screen.

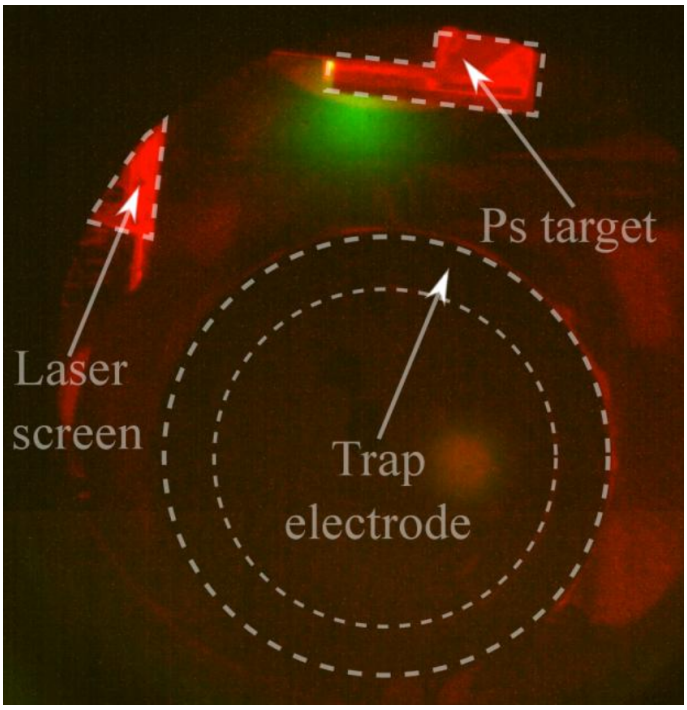

Figure 2.23: Example for positron (green) and electron (red) imaging with an MCP. (Image from Ref. [106]).

This technique lacks a proper way to calibrate the total amount of emitted Ps, especially since a not negligible fraction is just hidden behind the target and its holder, in addition

to a limited laser coverage which only allows to see a selection of available Ps. However, with a single shot one can detect excited Ps, synchronize the timings of the laser pulses and other, more advanced measurements can be performed: Doppler-scans, time-of-flight measurement and Rydberg-Ps self-ionization studies. These topics will be presented in chapter 3.

2.6 Antihydrogen

The most intuitive principle for cold antihydrogen production is called *mixing* of antiprotons and positrons, as demonstrated first by ATHENA [17]. Positron and antiproton plasmas are trapped next to each other in a W-shaped potential-well within a Penning-Malmberg trap, cooled and finally merged. By stochastic three body collisions or spontaneous radiative recombination processes, $\bar{\mathrm{H}}$ is formed (Eq. 2.33). The main advantage of mixing is its 'simplicity', since $\bar{\mathrm{H}}$ already emerges after the first process step on two different routes, but with a small cross-section due to the difficulties of cooling and compressing both plasmas.

$$\begin{aligned} &\text{1a)} \quad e^+ + \bar{\mathrm{p}} + e^+ \quad \rightarrow \quad \bar{\mathrm{H}}^* + e^+ \\ &\text{1b)} \quad e^+ + \bar{\mathrm{p}} \qquad\quad \rightarrow \quad \bar{\mathrm{H}} + h\nu \end{aligned} \tag{2.33}$$

The second approach to create antihydrogen is the *charge exchange reaction* between excited Rydberg-Ps atoms and cool antiprotons (Eq. 2.34). This type of procedure requires pre-processes responsible for the production and excitation of Ps, where the aforementioned techniques for Ps production can be directly utilized. For excitation to high Ps levels, specially tuned lasers are required. Major advantage of using Rydberg-Ps is the scaling of the charge exchange cross-section with n^4. A three step process such as this, however, suffers from the limited efficiency of each stage, which again reduces the final $\bar{\mathrm{H}}$ production rate.

$$\begin{aligned} &\text{1)} \quad e^- + e^+ \quad \rightarrow \quad \mathrm{Ps} \\ &\text{2)} \quad \mathrm{Ps} + h\nu \quad \rightarrow \quad \mathrm{Ps}^* \\ &\text{3)} \quad \mathrm{Ps}^* + \bar{\mathrm{p}} \quad \rightarrow \quad \bar{\mathrm{H}}^* + e^- \end{aligned} \tag{2.34}$$

Antihydrogen ion

The procedure of GBAR, who are aiming to utilize the $\bar{\mathrm{H}}^+$ ion, is a double charge exchange reaction between excited Ps ($n \approx 3$) and antiprotons/antihydrogen denoted as a reaction sequence in Eqs. 2.35. The main advantages of this method are the simple confinement of $\bar{\mathrm{H}}^+$, the good subsequent cooling possibilities and the small background when launching

a free fall measurement after the initial firework of annihilations subsided. The major disadvantage is the heavily reduced total production efficiency due to the need of four consecutive reactions in a very short time. In fact, without the development of ELENA and the higher number of 100 keV antiprotons (10-100 times more), this procedure would seem very challenging.

$$\begin{aligned} &1) \quad e^- + e^+ \quad \rightarrow \quad \mathrm{Ps} \\ &2) \quad \mathrm{Ps} + h\nu \quad \rightarrow \quad \mathrm{Ps}^*_{n=3} \\ &3) \quad \mathrm{Ps}^*_{n=3} + \bar{\mathrm{p}} \quad \rightarrow \quad \bar{\mathrm{H}} + e^- \\ &4) \quad \mathrm{Ps}^*_{n=3} + \bar{\mathrm{H}} \quad \rightarrow \quad \bar{\mathrm{H}}^+ + e^- \end{aligned} \tag{2.35}$$

2.7 Detecting the effect of gravity

The effect of gravity is extremely small. Compared to the strength of the electromagnetic interaction between an electron and a proton, for example, the gravitational pull between both these particles is forty orders of magnitude weaker. When comparing to the strong interaction inside an atomic nucleus in the range of 1×10^{-15} m, the relative strength of gravity shrinks down by two orders of magnitude more. In fact, gravitational effects only become evident in the macroscopic universe, where occurring masses are large. Nobody ever noticed the attraction of his own body to a small grain of sand, but in order to explore gravity, the whole Earth's gravitational influence is just fine.

However, when studying the gravitational behavior of antimatter, not only are there just few and costly produced antimatter supplies for such experiments, but one has also do deal with the systematic influence of electromagnetic forces, which are the main source for uncertainties in gravity measurements. In AE$\bar{\mathrm{g}}$IS experimental scheme, neutral antihydrogen atoms are used, on which homogeneous electric and magnetic fields do not exert first-order forces. This is the starting point and main condition for this experiment. But even neutral atoms can have electric and magnetic dipole moments and, as a consequence, field gradients certainly can generate a vertical force surpassing the effect of gravity. There even is a chance of ionization, because at AE$\bar{\mathrm{g}}$IS antihydrogen is produced at high Rydberg-levels. Therefore, one has firstly to ensure a sufficiently high homogeneity of electric and magnetic fields, and secondly to design a detector able to detect the tiny vertical displacement Δx during the time Δt (few hundred µs) of free fall due to the gravitational acceleration $|\vec{g}| = g = 9.81\,\mathrm{N\,kg^{-1}}$, which in turn is caused by Earth's mass ($m_{Earth} = 5.97 \times 10^{24}$ kg):

$$\Delta x = \frac{1}{2} g \Delta t^2 \approx 1\,\mu\mathrm{m} \tag{2.36}$$

Gravitational influence

In order to understand the impact of fields and field gradients on Rybderg-antihydrogen, the different effects will be quantified and compared to gravity, which can be described by classical Newtonian laws in the given context. The gravitational force law is denoted in Eq. 2.37 using the rest mass of antihydrogen $m_{Hbar} = 1.67 \times 10^{-27}\,\mathrm{kg}$ and the g from the previous paragraph. This defines the expected order of magnitude of the gravitational force and therefore the threshold all other vertical forces should not exceed, so that gravity can be measured on atoms in free flight with a significant result.

$$F_x = m_{Hbar} g = 1.64 \times 10^{-26}\,\mathrm{N} \tag{2.37}$$

Electric dipole force

Even neutral antihydrogen is still affected by electric field gradients. The quantum mechanical approach models ground state (anti)hydrogen as two oppositely charged spherical clouds of probability densities which share the same center. This suggests that on average any permanent electric dipole moment is perfectly averaging out in the absence of fields. This is additionally emphasized when applying an external electric field: the ground state energy level is not affected at first order, only at second (quadratic Stark effect). This can be interpreted as an induced dipole moment caused by the external field which then in turn is interacting with the electric field. The ability of an atom to be polarized as a second order effect is linked to its polarizability α_0, which will explained in more detail in Section 2.7.1. Ground state (anti)hydrogen has a polarizability $\alpha_0 = 4.5 \cdot 4\pi\epsilon_0 a_0^3$ in SI units.

However, already at the first excited level, $n = 2$, (anti)hydrogen reacts to external electric fields also with a linear Stark effect. This supports the existence of a permanent electric dipole moment, but it only emerges for excited states, since these do not have the high symmetry of the ground state. The electric dipole force is scaling proportional to the electric dipole moment as shown in the non-relativistic Eq. 2.38. The highest value for $|k|$ is $|n-1|$, when the projected angular momentum quantum number $|m|$ is zero [107]. The resulting force is parallel to the gradient of the electric field $\nabla\vec{E}$ and rapidly exceeds the regime of gravity for higher n. More specifically, for levels desirable at AEgIS, like $n = 25$ and $k = 24$, already a constant gradient of $0.2\,\mathrm{mV\,cm^{-2}}$ leads to a force of the same strength as gravity. Note that the only problematic component of $\nabla\vec{E}$ is the one aligned with the vertical axis, because it is parallel to $\vec{g}$.

$$\vec{F}_{el.\,dip} = -\frac{3}{2} e a_0 n k \nabla \vec{E} = 7.63 \times 10^{-27} \nabla \vec{E} \tag{2.38}$$

Magnetic dipole force

The second dipole force that should be mentioned is caused by magnetic field gradients. These work on the magnetic dipole moment, which can be approximated for not too strong fields as $\vec{m} = g_j \frac{\mu_B}{\hbar} \vec{J}$. Here, $\vec{J}$ is the total angular momentum of the positron, neglecting the contribution of the antiproton since it is three orders of magnitude smaller. The Landè-factor g_j can be approximated as given in Eq. 2.39, the formula Landè got almost correct in 1923 [108]. It was found that the total angular momentum is quantized, and the component aligned with the magnetic field (gradient) can be expressed as $\hbar m_j$, where m_j can take integer values between $-j \ldots j$ and is thus a secondary quantum number for the projected total angular momentum.

$$g_j = 1 + \frac{j(j+1) + s(s+1) + \ell(\ell+1)}{2j(j+1)} \tag{2.39}$$

The resulting magnetic dipole force is given in Eq. 2.40, which is proportional to m_j. The strongest force is caused by the maximum $\ell = n - 1$ and $s = \frac{1}{2}$, which leads to the highest $m_j = |j| = |\ell + s| = |n - \frac{1}{2}|$. From this, one can see that the magnetic dipole moment is scaling with n for higher levels. Using again $n = 25$ which is in the range of desirable Rydberg states at AEgIS, it becomes evident that a constant gradient of $10\,\mathrm{mG\,cm^{-1}}$ can cause a similar effect as gravity. Conversely, when working with ground state antihydrogen this tough requirement is relaxed, allowing a magnetic field gradient up to $\approx 150\,\mathrm{mG\,cm^{-1}}$.

$$\vec{F}_{mag.\,dip} = \mu_B g_j m_j \nabla \vec{B} = 2.32 \times 10^{-22} \nabla \vec{B} \tag{2.40}$$

There are additional higher order effects, like the quadratic Zeeman effect, but since already the dipole forces impose severe experimental challenges, one should first address those. Fig. 2.24 shows the dipole forces as a function of the respective field gradients for several arbitrarily chosen values of n. This shows that the result of a free fall test for excited antihydrogen is not meaningful as long as the field gradients are not known or controlled so that only negligible displacements occur due to them during the entire time of free fall. However, in reality the only harmful gradients are those aligned with the direction of gravity, so in principal only these need to be kept under control.

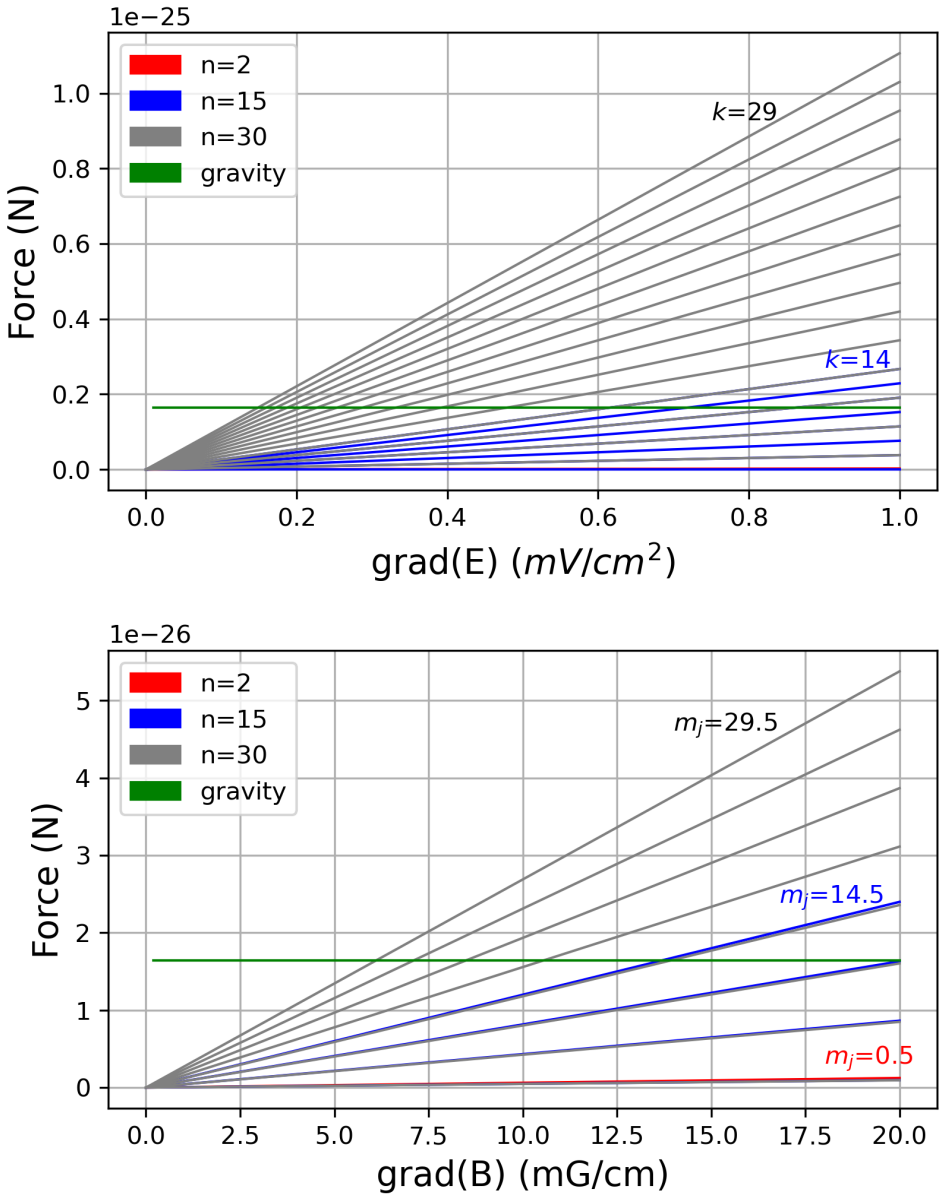

Figure 2.24: Graphical composition of the dipole forces due to field gradients for single states of excited (anti)hydrogen with principal quantum number n.

2.7.1 The Moiré-deflectometer

The temperature of produced antihydrogen at AE$\bar{g}$IS is dependent on the temperature of the former antiproton plasma, which is trapped radially in the 1 T magnetic field and axially by a square potential well. A reasonable value for the achievable axial velocity v_z with the current experimental setup is $\approx 1 \times 10^3\,\mathrm{m\,s^{-1}}$. The homogeneous magnetic field extends over $\approx 30\,\mathrm{cm}$, hence one has to conduct the gravity measurement within this region, expecting vertical shifts ranging between few micrometers for slow components and sub-micrometers for faster components. The concept of measuring such a small shift with high precision is atomic interferometry. A promising candidate is a variant of the Talbot-Lau interferometer, operated in a regime with no interference, which then is also called Moiré-deflectometer [109]. It consists of two parallel gratings at a known distance L which select a narrow range of propagation directions of an initially divergent atomic beam. A position sensitive detector at a distance L from the second grating records the atomic density modulation. Alternatively, a movable third grating plus a counting detector can be used. In any case, one will need to acquire both time and position information in order to evaluate the displacement Δx due to gravity. The periodicity of the gratings d_g, the width of the openings w and the distance L define how precise the Moiré-deflectometer works, because these values limit the transverse velocity spread to the range defined by the inequality: $\frac{id_g}{L} v_z < v_x < \frac{w+id_g}{L} v_z$. The integer value $i = [0, 1, 2...]$ enumerates the number of periods where again an open slit would occur. The general setup of a Moiré-deflectometer is sketched in Fig. 2.25.

While it is important to optimize the geometry of the Moiré-deflectometer for the special case of detecting a shift on antihydrogen atoms due to gravity like it was done in [111], there is an additional limitation for the gratings which originates from the interaction of Rydberg atoms with the walls of the gratings. As Rydberg-atoms have an increased size — the radius is $a_0 n^2$ — they may simply not fit into the opening. This is important on a scale of few tens of nanometers. If the openings are wider, for sure a major fraction is able to enter into the grating. Then, during the time of flight through the individual slits, antihydrogen can be subject to retarded Casimir-Polder potentials at very large distances from the walls [112] and to van-der-Waal potentials at medium distances [113]. Since the aspired geometry of the AE$\bar{g}$IS Moiré-deflectometer will not legitimate the assumption of very large distances, retarded potentials are not further considered here. Van-der-Waal potentials, however, can have an important impact that cannot reasonably be omitted.

Generally, such potentials are described by the law: $V_{vdW}(x) = -C_3 x^{-3}$. Determining the potential strength C_3 is not an easy task, especially if one wishes to include higher excited states for atoms or specific grid geometries. The level mixing due to degeneracy

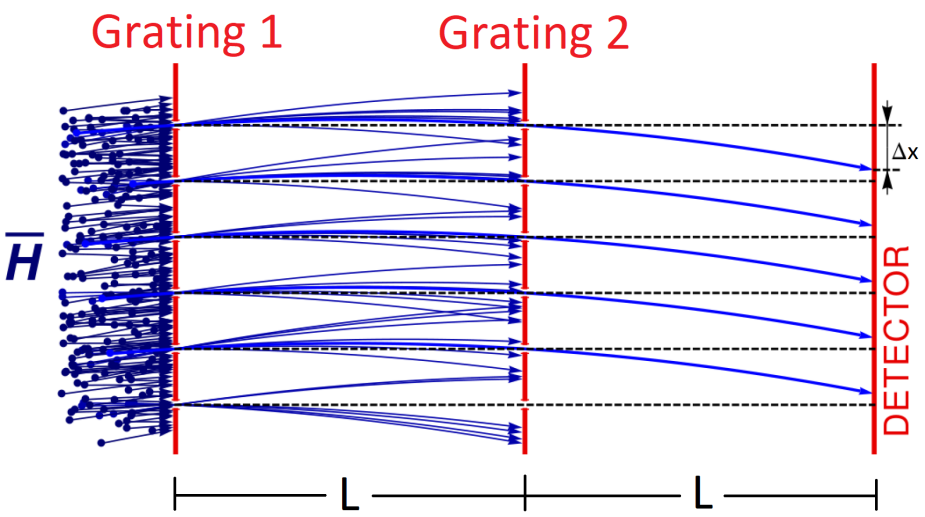

Figure 2.25: Schematics of a Moiré-deflectometer with periodicity d_g and distance between the gratings L. The first two gratings select a small range of propagation directions from an originally divergent, not monochromatic atomic beam. A third, movable grating or a position sensitive detector enable the detection of a displacement due to gravity. (Image courtesy to Francesco Guatieri).

of Rydberg-states strongly affects the induced electric dipole moment and yields a field of study by itself. The strength factor C_3 includes the term α_0, the so called static electric polarizability up to second order [114] as given in Eq. 2.41.

$$\alpha_0(n) = 4\pi\epsilon_0 a_0^3 \cdot \frac{n^4}{8}[17n^2 - 3(n_1 - n_2)^2 - 9m^2 + 19] \tag{2.41}$$

The constant a_0 is the Bohr radius, n the principal quantum number and m the secondary quantum number projecting angular momentum. The so called parabolic quantum numbers n_1 and n_2 are related to the others by $n = n_1 + n_2 + |m| + 1$. Calculations for higher n in spherical coordinates becomes tedious, but by introducing these parabolic coordinates the Schrödinger equation can again separated into two one-dimensional equations, which can be solved analytically [115]. Often, n_1 and n_2 are expressed as $k = n_1 - n_2$, which ranges between $-(n - |m| - 1) \ldots (n - |m| - 1)$ in steps of two.

However, the described method works well only for Rydberg-alkali atoms and for ground state (anti)hydrogen. Higher states are degenerate due to the exceptional symmetry of the hydrogen atom, and the polarizability cannot be determined. In order to model also the Rydberg-states, a different (semi-classical) approach is chosen. Therein, one is exploiting the strongly reduced orbital frequencies of the lepton for Rydberg-states (about three orders of magnitude for $n = 25$), which allows to treat the interaction with the grating adiabatically, i.e. the electrons inside the walls of the gratings adapt so quickly to the atom

passing that at any given time a perfect mirror potential is generated [116]. The electric field following from this image potential is then used as an external electric field, causing together with the magnetic field a shift of the energy levels, which consequently increases the chance for ionization. Additionally, the image electric field can have a field gradient that may induce a vertical displacement. This will be explored in the following.

Image potential

Describing the Rydberg-atom in cylindrical coordinates (ρ, ϕ, x), the total potential witnessed by the lepton when the atom is close to a wall is simply the sum of the individual Coulomb-like contributions between the lepton and the other particles, i.e. the nucleus and the mirrored counterparts (see Fig. 2.26). The effective potential is then approximated via binomial expansion in order to avoid square root denominators and reads as denoted in Eq. 2.42, given in atomic units [117]. Here, D is the distance of the (anti)proton from the surface and the coordinates x and ρ define the position of the lepton relative to the nucleus. As one is only interested in the electric field generated by the surface, i.e. the image potentials, one can omit the first term that is the Coulomb-potential produced by the real, vacuum-sided nucleus. It can be reintroduced when needed as part of the unperturbed solution for the Schrödinger-equation.

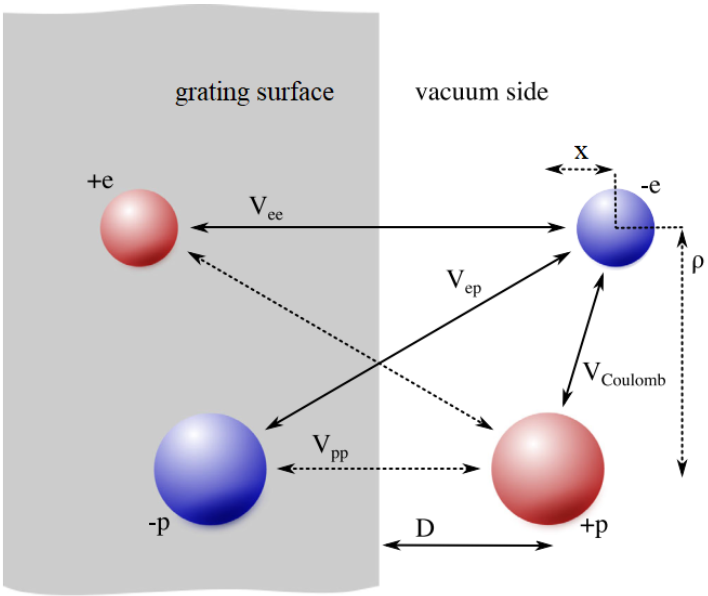

Figure 2.26: Model for the image potential caused by hydrogen or antihydrogen if all signs of charges are switched, described in cylindrical coordinates ρ, ϕ, and x. (Image with adapted coordinate system from Ref. [117]).

$$V_{im} = -\cancel{\frac{1}{\sqrt{x^2+\rho^2}}} - \frac{1}{16D^3}(\rho^2+2x^2) + \frac{3}{32D^4}(x\rho^2+x^3) + ... \tag{2.42}$$

The electric field caused by the image potential in cylindrical coordinates and SI units then is:

$$\vec{E}_{im} = -\nabla V_{im} = \frac{e}{64\pi\epsilon_0 D^4}\begin{pmatrix} 2D\rho - 3x\rho \\ 0 \\ 4Dx - \frac{3}{2}(\rho^2+3x^2) \end{pmatrix} \tag{2.43}$$

This field affects the antihydrogen atoms when passing through the grating just like any ordinary external electric field would. If its gradient has components aligned with the vertical x-axis, it will cause a displacement in x as described by Eq. 2.38.

The field gradient can be found by evaluating $\nabla\vec{E}$ in cylindrical coordinates, which is a tensor with nine components:

$$\nabla\vec{E} = \begin{pmatrix} \frac{\partial E_\rho}{\partial\rho} & \frac{1}{\rho}\frac{\partial E_\rho}{\partial\phi} & \frac{\partial E_\rho}{\partial x} \\ \frac{\partial E_\phi}{\partial\rho} - E_\phi & \frac{1}{\rho}\frac{\partial E_\phi}{\partial\phi} + E_\rho & \frac{\partial E_\phi}{\partial x} \\ \frac{\partial E_x}{\partial\rho} & \frac{1}{\rho}\frac{\partial E_x}{\partial\phi} & \frac{\partial E_x}{\partial x} \end{pmatrix} \tag{2.44}$$

Since $\vec{F}_{el.\,dip} = -\frac{3}{2}ea_0nk\nabla\vec{E}$ and we are only interested in the vertical component F_x, which is caused by the electric field E_{im}, one has to evaluate:

$$F_x \sim \left(\frac{\partial E_{im,x}}{\partial\rho} + \frac{1}{\rho}\frac{\partial E_{im,x}}{\partial\phi} + \frac{\partial E_{im,x}}{\partial x}\right) = \frac{e}{64\pi\epsilon_0 D^4}(-3\rho + 4D - 9x) \tag{2.45}$$

It remains to estimate a typical vertical displacement Δx_g the grating could cause via the electric dipole force. For this, a Rydberg-atom is assumed to pass through the grating at a distance of $D = 1\,\mu\text{m}$ from the nearest surface. This distance is much greater than the dimension of the Rydberg-atom radius, which lies around 50 nm. Thus, the dominant contribution in Eq. 2.45 is the term with $4D$. When further assuming a flight time through the grating of about $\Delta t_g \approx 30\,\text{ns}$, $n = 25$ and $k = 24$, the expected vertical displacement is:

$$\Delta x_g = \frac{F_x}{2m_{Hbar}}\Delta t_g^2 = -\frac{3ea_0nk}{4m_{Hbar}}\frac{e}{16\pi\epsilon_0 D^3}\Delta t_g^2 = -0.7\,\mu\text{m} \tag{2.46}$$

In conclusion, the vertical displacement induced by the gratings via image potentials can be of the same order than a shift by gravity overall the total flight path. It is therefore important to control and choose the parameters entering into Eq. 2.46 sufficiently well. For example, the openings of the grating should be as wide as possible in order to have many anti-atoms passing far away from the surface, i.e. maximizing the average D. The

thickness of the gratings should be minimized in order to reduce the time antihydrogen stays inside. If possible, also the Rydberg-level should be reduced without sacrificing too much of the initial production rate.

Field Ionization

The electric field caused by the surface potential V_{im} inside the gratings also induces Stark shifts. At the same time, one cannot omit the magnetic field that is aligned with the z-axis of the AE$\bar{\text{g}}$IS apparatus, inducing Zeeman shifts (reminder: the z-axis is the beam axis). A study on excited hydrogen atoms in combined electric and magnetic fields was performed in Ref. [107], of which only the first order energy correction to the unperturbed energy is used in the following (in atomic units):

$$E_n = -\frac{1}{2n^2} + |\vec{\omega_1}|n_1 + |\vec{\omega_2}|n_2 \ , \tag{2.47}$$

where n_1, n_2 are again parabolic quantum numbers, each taking values in the range:

$$n_1, n_2 = -\frac{(n-1)}{2}, -\frac{(n-3)}{2}, \ \dots \ , \frac{(n-1)}{2}$$

The scalar values for $|\vec{\omega_1}|$ and $|\vec{\omega_2}|$ were derived from the combination of magnetic and electric field vectors in atomic units:

$$\vec{\omega}_{1,2} = \frac{1}{2}\left(\frac{\vec{B}}{2.35 \times 10^5\,\mathrm{T}} \mp 3n\frac{\vec{E}_{im}}{5.14 \times 10^9\,\mathrm{V\,cm^{-1}}}\right) \tag{2.48}$$

The (anti)hydrogen atom with the energy level E_n will ionize, when its level surpasses the ionization threshold, which is defined by the so called *saddle point* energy E_S. This limit originates from the shape of the surface potential V_{im}, which exhibits a barrier close to the wall. If the lepton overcomes that barrier, the surface of the grating becomes more attractive than the nucleus. From Ref. [107], this threshold can be approximated as:

$$E_S \approx -\frac{1.74a_0}{D}, \tag{2.49}$$

For (anti)hydrogen at the $n = 25$ level with $n_1 = 0$ and $n_2 = \frac{n-1}{2}$ within a 1 T magnetic field, ionization due to the induced Stark shift inside the gratings occurs when the atom has a distance to the wall of 0.1 µm or less. Of course, if ionization happens, the particle cannot contribute to the gravity measurement anymore, which increases the number of required repetitions of the whole experiment. On the other hand, the vertical displacement due to dipole forces at such distances would be anyway harmful as derived in the previous paragraph. As a consequence, ionization could be viewed as a 'cleaning' process of undesirably displaced Rydberg-atoms.

2.7.2 Simulating a Moiré-deflectometer in the AEgIS environment

We are now in the position to simulate a classical Moiré-deflectometer for gratings with a thickness of 30 µm, a distance between two slit centers, i.e. periodicity d_g, of 100 µm and an opening w of 30 µm. Image surface potentials as presented in Eq. 2.42, a 1 T magnetic field along the beam axis and of course gravity have been taken into account within the open volume of the gratings. Outside, only gravity and the magnetic field plus its possible gradients (here assumed with $10\,\mathrm{mG\,cm^{-1}}$) are considered. Since the expected principal quantum number n for produced antihydrogen resides around $n = 25$, a multitude of degenerate sub-levels emerges due to the magnetic field and due to induced image electric fields. This makes it very difficult to simulate the effective forces affecting single atoms, since their real individual level cannot be described. For the simulation, one therefore has to chose a rather low n, whereas the real impact of the effective forces for high n states will better be studied via experiment. The parameters used for a correspondingly performed simulation are listed in Tab. 2.3.

m_{Hbar} (kg)	d_g (µm)	w (µm)	N_{Hbar}/d_g	n	B (T)	$[\nabla \vec{B}]_x$ ($\mathrm{mG\,cm^{-1}}$)
1.67×10^{-27}	100	30	500	2	1.0	10

Table 2.3: Summary of parameters used for a simulation with a pulse of N (anti)hydrogen atoms passing through a Moiré-deflectometer.

A pulse of antihydrogen atoms with Gaussian velocity distributions (associated temperature is $T = 80\,\mathrm{K}$) along the vertical x-axis and the beam axis z is assumed to pass through a first grating. Only those atoms will make it through the second grating at distance L that have a transverse velocity $\frac{id_g}{L} v_z < v_x < \frac{d+id_g}{L} v_z$ as explained above. Having passed the second grating, the vertical velocity v_x is well tamed and the atoms fly towards the detector with an assumed resolution of 10 µm at again the distance L. The simulated outcome is shown in Fig. 2.27, where the two used colors indicate two different velocity regimes of v_z.

Blue stands for all atoms that were faster than an arbitrarily chosen threshold of $400\,\mathrm{m\,s^{-1}}$, red for those that were slower. The split is done, because in order to measure the desired displacement, a reference is required to which the shifted pattern can be compared. This reference can either be obtained by a complementary measurement with a fast pulse of atoms or even with a laser, or instead one uses the timing signature of detected antihydrogen atoms at the position of the detector. If the flight time of a single atom is known with high precision, one knows how long gravity could affect this atom and how fast it was. For this simulation, the individual velocities were sorted into a slow and a

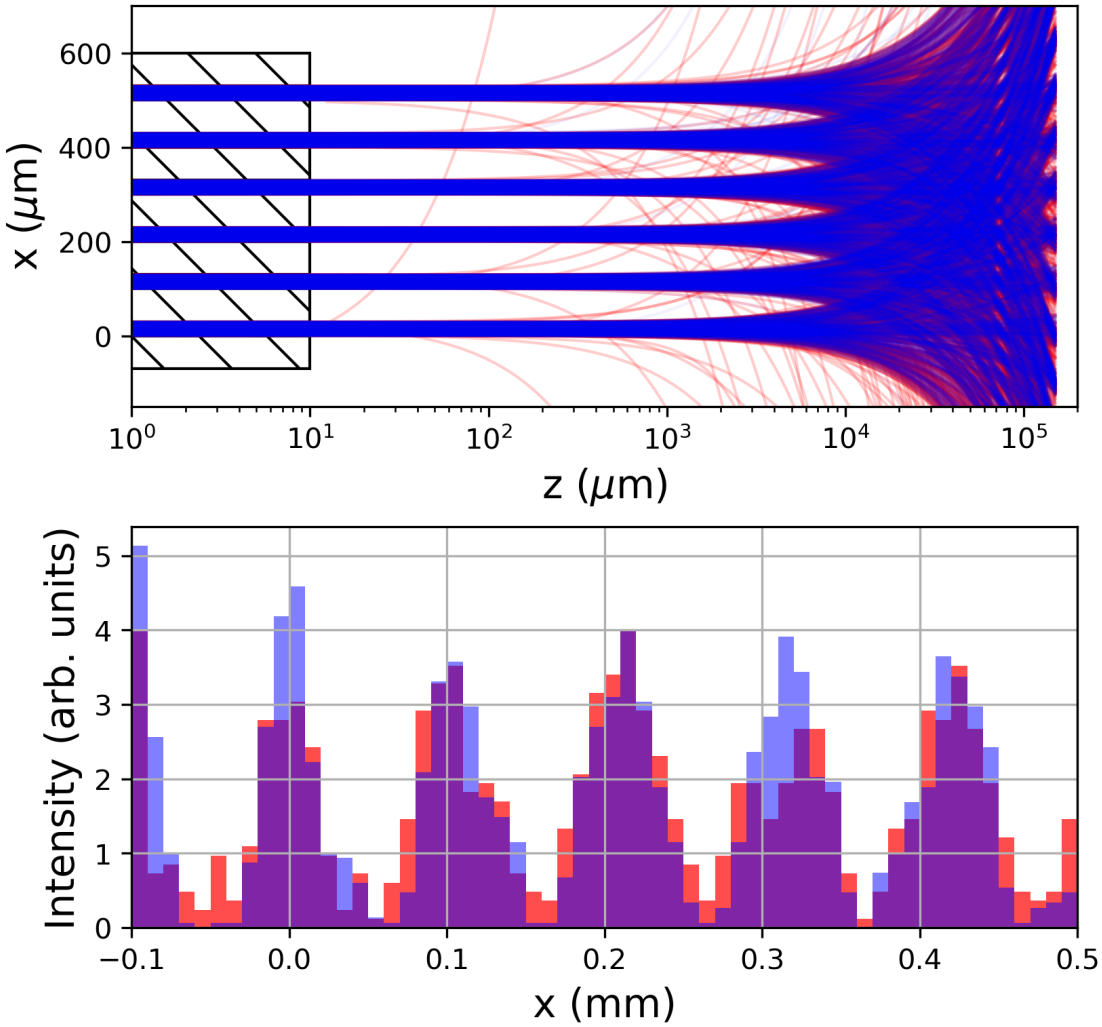

Figure 2.27: Influence of gravity, surface potentials and magnetic field gradients on the trajectories of antihydrogen atoms passing through a matter grating made of silicon with periodicity d_g of 100 µm and openings w of 30 µm. About 99 % of the atoms is able to arrive at the detector, with a difference between the vertical displacements of the slow fraction (red) and the fast fraction (blue), which cannot originate from the symmetrical surface potential. The detector is assumed to have a resolution of 10 µm per bin.

fast regime with average velocities of $v_{slow} = 196\,\mathrm{m\,s^{-1}}$ and $v_{fast} = 923\,\mathrm{m\,s^{-1}}$, respectively. The fast fraction indeed had less time to be affected by gravity with respect to the slow fraction, which is why both patterns differ in their displacement as can be seen in the histogram at the bottom of Fig. 2.27, where one bin corresponds to the detector resolution of 10 µm.

The shift Δ_x between the fringe patterns is too blurry to be evaluated directly by eye, but one can exploit the periodicity of the result by using the *cross-correlation*, a standard technique in signal processing with the ability to verify the similarity between two signals that are merely displaced on one spatial axis against each other. It can be imagined as shifting one discrete function relative to a second in discrete steps and summing at each step over the whole defined range as given in Eq. 2.50.

$$(f * g)[n] = \sum_{m=0}^{N-1} \overline{f[m]}\, g[(m+n)_{mod} N] \tag{2.50}$$

The bar over $\overline{f[m]}$ indicates that this is the complex conjugate of $f[m]$. The maximum of the cross-correlation occurs at x_c, i.e. where both discrete functions are superimposed best. If two similar input signals are perfectly aligned, x_c would reside exactly in the middle of the defined range $[0 \ldots N]$, hence at $\frac{N}{2}$. If the two signals are not well aligned, x_c is shifted with respect to $\frac{N}{2}$. This is exemplified in Fig. 2.28, where the two histograms of Fig. 2.27, each consisting of N bins, were analyzed.

In order to reliably find x_c, all occurring peaks were first fitted with continuous bell-shaped Gauss functions in order to extract their centers. These centers were then averaged, which was possible due to the symmetry of the resulting pattern. For the given example in Fig. 2.28, the mean value for the shifted center was $x_c = 29.6 \pm 0.2$. When subtracting this from $\frac{N}{2}$ and multiplying the outcome with the bin width, i.e. detector resolution, the real shift Δx in SI units is obtained. In the simulation, this shift Δx is the desired displacement between the patterns of slow and fast atoms, respectively, that arrive at the detector. It remains to translate this into a value for the gravitational acceleration using Eq. 2.51 to Eq. 2.53.

$$\Delta x \;=\; \left(x_c - \frac{N}{2}\right)\sigma_{det} \;=\; \Delta x_{slow} - \Delta x_{fast} \tag{2.51}$$

$$\Delta x_{slow,fast} \;=\; \frac{g}{2}\left(\frac{L}{v_{slow,fast}}\right)^2 \tag{2.52}$$

$$g \;=\; \frac{2\Delta x}{L^2}\left(\frac{1}{v_{slow}^2} - \frac{1}{v_{fast}^2}\right)^{-1} \tag{2.53}$$

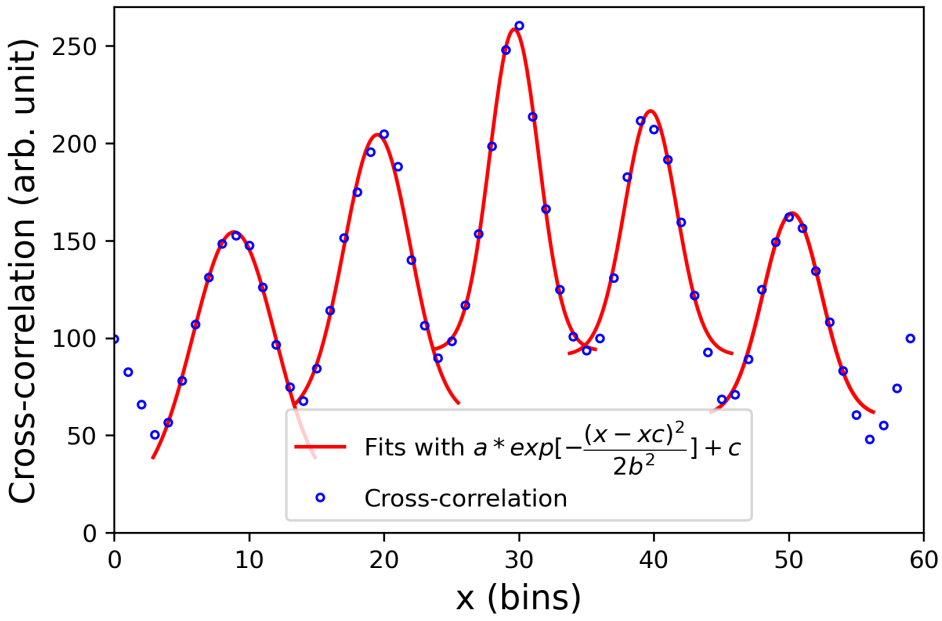

Figure 2.28: Result of a cross-correlation over the whole range of N bins (10 µm per bin) between the slow and the fast fraction of simulated (anti)hydrogen atoms as seen in the lower plot of Fig. 2.27. The coarse binning suggests to fit bell-shaped curves into the peaks. The average peak center x_c deviates from the middle of the range of bins ($\frac{N}{2}$), which is caused by gravity. For details see text.

The presented analysis procedure was applied to the outcome of three repetitions of the Moiré-deflectometer simulation, assuming three different gravitational accelerations, namely $g_{sim} = (-9.81\,,\ 0\,,\ 9.81)\,\mathrm{m\,s^{-2}}$. The 'measured' values for g following the analysis should match these initially assumed values. This is approximately the case as can be seen in Tab. 2.4. The result could be more precise, if a detector with higher resolution, antihydrogen with smaller and less spread velocities, and a better reference in order to quantify the vertical displacement would be used.

$g_{sim}\ (ms^{-2})$	x_c (bins)	$\Delta x\ (\mu m)$	$g\ (ms^{-2})$
9.81	30.3 ± 0.1	$+3 \pm 1$	$+12 \pm 3$
0.00	30.0 ± 0.1	0 ± 1	0 ± 2
-9.81	29.6 ± 0.2	-4 ± 2	-14 ± 6

Table 2.4: Extracted gravitational accelerations g, derived via cross-correlation of the data obtained from a Moiré-deflectometer simulation, which assumed different values for the gravitational acceleration g_{sim}. The gratings of the Moiré-deflectometer were at distance of $L = 15\,\mathrm{cm}$. For the slow antihydrogen fraction, an average velocity of $v_{slow} = 196\,\mathrm{m\,s^{-1}}$ was used, for the fast fraction a velocity of $v_{fast} = 923\,\mathrm{m\,s^{-1}}$.

2.7.3 Conclusion

In summary, a free fall gravity measurement by means of a Moiré-deflectometer for cold antihydrogen close to the ground state, coming from a pulsed source, seems generally feasible. A first design for a Moiré-deflectometer suited for the requirements of AE$\bar{\mathrm{g}}$IS could be introduced into a simulation, which was able to resolve the sign of a gravitational acceleration. The greatest impact on that measurement is dealt by the interleaved high Rydberg-levels of produced antihydrogen in AE$\bar{\mathrm{g}}$IS, which basically demands extremely tight control over the magnetic and electric field gradients and/or urgently suggests to bring antihydrogen to lower states. This requires an additional process step in the experimental scheme of AE$\bar{\mathrm{g}}$IS, still under development: Rydberg-antihydrogen deexcitation. In any case, ground state antihydrogen would also be advantageous from the point of view of minimizing losses. Its diameter is decreasing due to its proportionality to n^2, hence the fraction of atoms annihilating at the wall goes down a bit, as well as the self-ionizing amount which scales proportionally to n^4.

2.8 Results on the $\bar{H}$ production trials in 2018

This last part of the experimental overview of AE$\bar{g}$IS will report on the advances made with respect to antihydrogen production until the end of 2018 (start of Long Shutdown 2 at CERN). At this time, the full procedure for the pulsed production of cold antihydrogen was implemented and tested. A milestone on that road had been the pulsed positronium production, excitation and manipulation, which were a central part of the author's doctoral studies. It will be thoroughly treated in the next chapter. Important results with respect to pulsed antihydrogen production have been published in [118] and will be shortly presented in the following.

Between the months August to December of 2018, up to 3×10^7 antiprotons with 5.3 MeV kinetic energy were regularly available at the AD. These antiproton pulses were injected into the AE$\bar{g}$IS apparatus (see Fig. 2.29), where they first had to pass through a set of thin Si and Al foils. Finally, about 1×10^5 antiprotons per pulse with up to 10 keV were admitted into a first Penning-Malmberg trap within a 4.46 T magnetic field. In this trap, a well cooled electron plasma with about 2×10^8 particles has already been prepared. The antiprotons inelastically collided with the electrons, giving away part of their energy (so-called Coulomb cooling). The electrons immediately dissipated the gained energy by cyclotron radiation due to the high magnetic field and their own small mass. The mixed plasma was then radially compressed by applying the aforementioned rotating wall technique (see also Section 2.4.4 about positrons), where a rotating electric field induced an inward transport of particles inside the plasma.

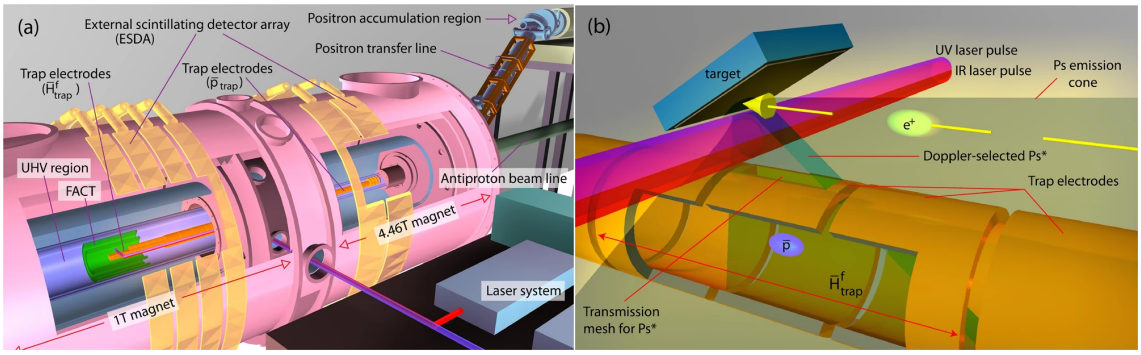

Figure 2.29: Overview of the AE$\bar{g}$IS experimental setup. On the left is shown the whole apparatus, on the right a blow-up of the antihydrogen production area. (Image from Ref. [118]).

Eventually, antiprotons cooled below (440 ± 80) K axial temperature and were transported to the quasi-harmonic potential well formed by five cylindrical electrodes. These had a radius of 5 mm, a length of 4 mm and were separated by 0.5 mm. Additionally, a 1 T

magnetic field was used here for radial confinement. The antiprotons could be stored for about 1000 s, extending over 4 mm in axial direction and about 1.5 mm radially. In this final trap, or the so-called *production trap*, antiprotons were kept until the Rydberg-Ps pulse arrived. As an improvement, during the four months of data taking the experimental procedure evolved until up to eight consecutive antiproton pulses from the AD could be stacked inside the AEgIS apparatus, increasing the final amount in the production trap up to 8×10^5 antiprotons. These were kept there for more than 20 $\bar{\mathrm{H}}$ production cycles, before new antiprotons had to be trapped.

Every minute, few millions of positrons from the AEgIS positron system as described in Section 2.4.4 were implanted into the positronium target. Lasers were positioned such that their centers were aligned with the path between Ps origin and antiprotons. Since the Ps velocity distribution was not known *a priori*, a reasonable range from 8 ns to 20 ns after positron implantation was explored over these four months, with no clear optimum. The Ps Rydberg-level was set to $n = 16$, because here the visible self-ionization losses due to motional Stark effect were moderate, although it was not clear whether the gain in cross-section (scaling with n^4) was anyway compensating for this or not (thoroughly discussed in Chapter 3). With every positron injection into the target, followed by Ps emission and excitation, a so-called $l\bar{p}e^+$ (laser-antiproton-positron) experiment was performed, which could lead to $\bar{\mathrm{H}}$ production. For estimation of all background signals, every third shot was taken without laser, called $\bar{p}e^+$. In addition, also cycles with only the laser on, but no positrons ($l\bar{p}$), and cycles with laser on, but no antiprotons (le^+) were taken. The latter proved to be a negligible background. In total, for each class more than thousand measurements were taken.

The annihilation of antihydrogen, or rather of antiprotons, involves the production of pions. These were detected by 12 plastic scintillating (EJ200) slabs, each 10 mm thick and several centimeters wide. The slabs covered the outer shell (radius ≈ 0.8 m) of the cryostats that contained the two superconducting magnets of AEgIS, and were coupled to two photo multipliers, one at each end, which were connected to the acquisition electronics. The precise timing of the arrival of a pion with respect to the positron implantation into the Ps target allowed to separate the individual events, and by applying a threshold on the signal amplitude, the high energetic pions could well be distinguished from positron annihilation into 511 keV gamma quanta. Like this, time-resolved histograms (5 µs bin width) of raw pion counts could be obtained as shown in Fig. 2.30.

For the measurements without laser, but with antiprotons and positrons, a constant signal over time was observed if the energy threshold of the detection system was set high enough to reject positron annihilation radiation entirely. Furthermore, a count was

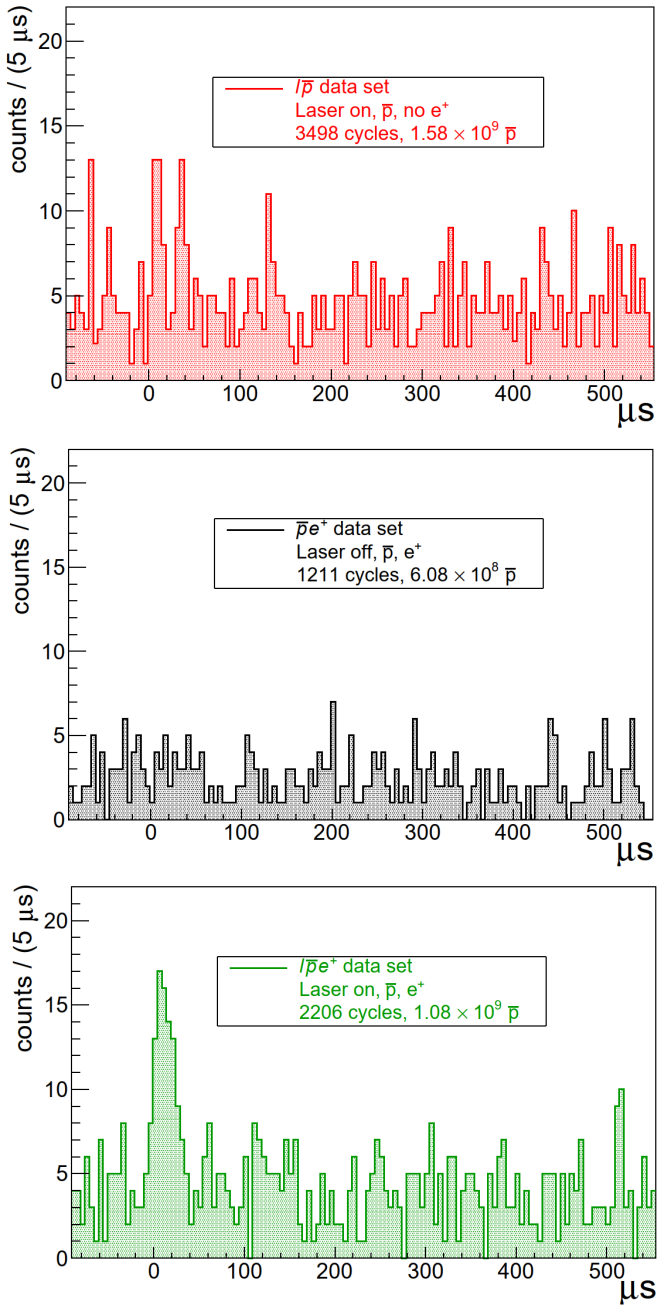

Figure 2.30: Histogram of detected pion counts distributed over time. The top figure shows some count excess, which could be due to laser induced particle desorption from the vacuum chamber and subsequent increased annihilation rate. The middle graph without lasers consists of a homogeneous background signal as for example caused by cosmic high energy particles. The bottom graph shows a peak between 0 µs and 25 µs which is not present in the other histograms. This can only be due to the delayed annihilation of neutral $\bar{H}$ atoms. Note the varying cycle and antiproton numbers, which linearly affect the detected cosmic rays and background annihilations, respectively. A proper normalization is therefore required in order to compare count excesses. (Images from Ref. [118]).

only registered if both PMT's showed a signal greater than 250 mV within a coincidence time window of 50 ns. Monte Carlo simulations of this detector system estimated an $\bar{\mathrm{H}}$ detection efficiency of 41.5 %. The constant background as shown in the middle panel of Fig. 2.30 was attributed to high energy cosmic rays and antiproton boil-off, i.e. some of the antiparticles statistically gain enough kinetic energy to escape the trap and annihilate. On average, this background amounted to 1.7 ± 1.6 excess counts within a signal region between 1 µs and 26 µs with respect to control regions before and after that time window. Note that this result followed after normalization to a reference number of antiprotons of about 1×10^8. In conclusion, within the errorbars there was no excess in the background signal.

When switching off positrons, using only antiprotons and lasers as shown in the top panel of Fig. 2.30, we found 13.7 ± 4.5 excess counts after normalization in the same signal time window as before. Since this could not be due to produced antihydrogen or due to direct interaction of the laser with antiprotons (reminder: laser beams are outside the trap), the best explanation is a local perturbance of the vacuum when the laser was shot onto the surrounding chamber desorbing gas from the material. Occasionally, such gas molecules interacted with the antiprotons and led to an increased annihilation rate coinciding with the laser pulse. This signal has been identified to be the main source of background and could have only been avoided when not switching off the laser, but instead heavily detuning the UV wavelength so that Ps with high v_y was addressed. Since only the vertically moving Ps atoms, i.e. $v_y \ll 4 \times 10^4\,\mathrm{m\,s^{-1}}$, could enter into the trap, which had an opening at its top, the atoms propagating also horizontally would simply miss the trap. This experimental option had just not been available in 2018, beside to the fact that the strong laser-induced background was also not expected.

Finally, with all subsystems active, Rydberg-positronium was produced and traversed towards the trapped antiprotons, resulting in the bottom histogram of Fig. 2.30. Now, the detected excess counts in the signal time window was 59.2 ± 8.9 after normalization to the reference antiproton number as used for the other two measurements. This signal clearly exceeds the result of the other two cases and allows to calculate the rate of detected antihydrogen atoms by simply subtracting the laser induced excess counts, which at the same time also removes the cosmic ray background. What remains is 45.6 ± 10.0 detected antihydrogen atoms, which can be translated to the number of produced antihydrogen atoms by using the simulated detection efficiency. In 2018, AE$\bar{\mathrm{g}}$IS produced 110 ± 25 $\bar{\mathrm{H}}$ atoms in the form of a pulsed 4π source. Antihydrogen was thus formed with a production rate of 0.05 per pulse, requiring on average 5×10^5 antiprotons and 2×10^6 initial positrons. In Tab. 2.5 all the numbers and excess counts are summarized.

class	cycles	excess counts	detected $\bar{H}$ atoms (det. efficiency 41.5 %)	produced $\bar{H}$ atoms
$l\bar{p}$	3498	13.7 ± 4.5	0	0
$\bar{p}e^+$	1211	1.7 ± 1.6	≈ 0	≈ 0
$l\bar{p}e^+$	2206	59.2 ± 8.9	45.6 ± 10.0	110 ± 25

Table 2.5: Overview about the 2018 $\bar{H}$ production with evaluated count rates as also presented in Ref. [118]. The different excess counts occurring for each of the three classes finally show that $\bar{H}$ atoms have been created in the form of a pulsed 4π source.

Summary

AEgIS realized an experimental procedure able to generate a 4π pulse of antihydrogen using the charge exchange reaction between cold antiprotons and Rydberg-positronium. This result is a huge step forward towards a gravity measurement on neutral antimatter atoms which requires well-known timings in order to facilitate a free fall experiment. But also consequent manipulations on formed antihydrogen atoms such as deexcitation and deceleration require a precise timing which just has been unlocked by providing the pulsed source. As a next step, in order to really make use of this new source, the production rate has to be increased as much as possible. This involves a redesign of the trap geometry, relocating the positron/Ps converter target aligned with the beam axis inside the trap, using colder antiprotons and positronium by optimizing the respective systems including the diagnosis, and connecting AEgIS to the new Extremely Low ENergy Antiprotons (ELENA) facility at CERN. Furthermore, with the availability of Ps transmission targets one eventually could switch over to an experimental scheme where antiprotons and Rydberg-Ps atoms propagate into the same direction (see Chapter 4), removing any relative velocity between both particles: the charge exchange cross-section would shoot up as will be shown in Chapter 3. With modest optimism, an $\bar{H}$ production rate of few atoms per pulse seems achievable in the near future.

Chapter 3

Rydberg-Ps velocimetry and self-ionization studies

AE$\bar{g}$IS scheme for antihydrogen production involves the charge exchange reaction between cold antiprotons and Rydberg-Ps. An overview was given in Section 2.1. The challenging task was to maximize the expected yield of antihydrogen without directly observing the produced amount, since no quick diagnostics for $\bar{H}$ annihilation had been available. Optimization included the alignment of the laser beams (UV + IR) with the emerging Ps cloud after positron injection into the converter target. One had to ensure that excited Rydberg-Ps was propagating towards the cold antiproton plasma, which was axially confined at the bottom of a shallow electrostatic potential well (few volts depth) and radially by a 1 T magnetic field. The Rydberg-state should be as high as possible in order to maximize the cross-section of the charge exchange reaction, because it scales with n^4. Opposed to that, the electric field induced by the motional Stark effect inside a magnetic field caused self-ionization of Rydberg-Ps that moved perpendicular to the B-field, hence defining an upper limit for n. Furthermore, the velocities of Rydberg-Ps and antiprotons needed to be matched, since otherwise the cross-section dropped exponentially.

The cross-section for antihydrogen production was studied in Refs. [119, 120, 121]. Therein, classical Monte Carlo simulations up to $n = 50$ were performed and corresponding quantum effects up to $n = 5$ were investigated. Both approaches were found to be consistent due to identical scaling laws. As a result, the cross-section depends on the addressed Rydberg-state and on the Ps velocity, since antiprotons are orders of magnitude slower and can be considered stationary within the small time window of possible charge exchange. In Fig. 3.1, the cross-section is divided by n^4 to emphasize the Ps velocity dependency, hence it becomes a *weighted* cross-section. In addition, the abscissa is expressed

in terms of k_v, which is the Ps velocity in atomic units multiplied by $2n$ as given in Eq. 3.1. In particular, the weighted cross-section displays three distinct regions: at low velocities, where $k_v < 0.3$, it follows $1/k_v^2$. At the fast end, for $k_v > 1.8$, it decreases exponentially. Between those two limits, it stays constant.

$$k_v = \frac{2nv_{Ps}}{2.188 \times 10^6 \,\mathrm{m\,s^{-1}}} \tag{3.1}$$

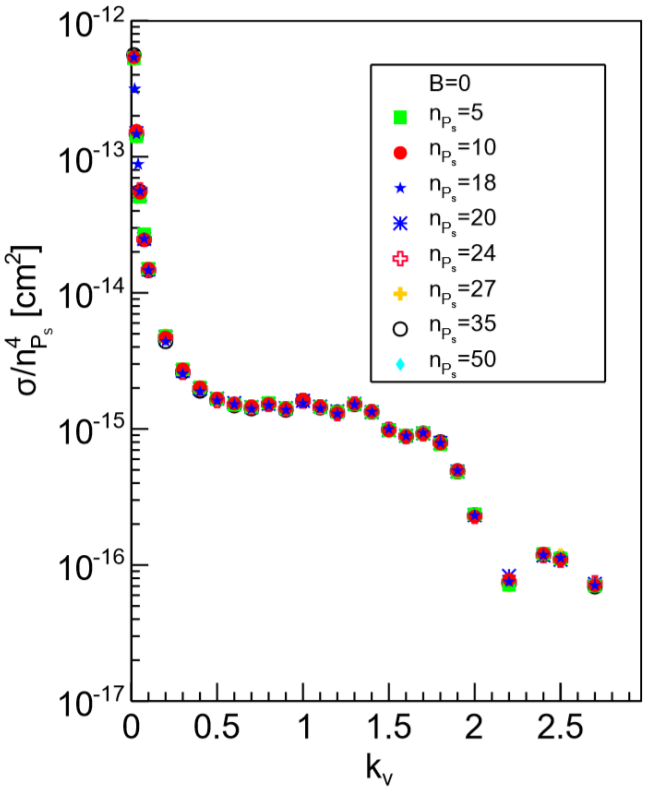

Figure 3.1: The cross-section of the charge exchange reaction for antihydrogen production divided by the principal quantum number n^4. Ps velocities are expressed in atomic units and multiplied by $2n$, denoted as k_v. (Image from Ref. [119]).

The recipe to optimize the resulting $\bar{\mathrm{H}}$ production is to combine the weighted cross-section of Fig. 3.1 with a measured Ps velocity distribution and optimize the opposing effects of Ps self-ionization and the n^4 scaling of the cross-section. In order to do so, a fast method for visualizing excited Ps on a MCP plus phosphor screen was developed (details in Section 2.5.8 and Refs. [106, 122, 123]). A set of velocimetry scans was performed and analyzed with the intention of revealing the velocity distribution of Ps as it is leaving the converter target. Then, also the self-ionization of Rydberg-Ps was studied by scanning all

doable IR wavelengths. The results presented in the following have also been published in a condensed form in Ref. [124].

3.1 Experimental

The Ps velocimetry was performed in the central part of the AEgIS apparatus. An adapted CAD model of this region can be seen in Fig. 3.2. The $\bar{H}$ production trap consisted of the electrodes UC7 to UC9 (internal naming). The antiproton plasma ($< 440\,K$) was usually kept at the position of UC8, i.e. the deepest point of the trap potential well, since like this the Ps flight path was minimized. The laser beams for Ps excitation were always aligned with the y-axis parallel to the Ps target, but could be freely positioned in the x-z plane, guaranteeing best geometrical overlap with those Ps atoms that propagated towards the location of antiprotons. For the measurements in this work, the laser center (x_c,z_c) from the lower edge of the target was set once to $(1.7, -3.2)\,mm$ and once to $(0, -5.9)\,mm$.

Whenever free positrons or electrons were generated in the open 5 mm space below the target, they were confined by the homogeneous 1 T field, only able to move along the z-axis. A small potential ramp spilling out from the trap electrodes gently guided them towards a MCP (Hamamatsu F2223), whose front face could be either biased to $-180\,V$ or to $180\,V$, attracting positrons or electrons, respectively. The MCP output induced an image on a following phosphor screen (P46), which then was acquired by a CMOS camera (Hamamatsu C11440-22CU). A few calibrations were needed before any measurement could be performed. Firstly, the positron impact point on the Ps target, which was hidden from the view, secondly the absolute timing between laser pulses and positron peak, and thirdly the relative timing between UV and IR laser pulses.

3.1.1 Positron implantation position on the target

The vertical steering of the positron bunch was done by adjusting the current of the corresponding vertical deflection coil in the positron beam line. Doing so, one could directly image the positron spot at multiple positions on the MCP and additionally measure its size for all those settings that allowed the bunch to pass below the converter target (see Fig. 3.3). Then, the deflection current was changed so that positrons moved gradually up. The spot shape always stayed the same. A linear correlation between the x-coordinate and current I was found as denoted in Eq. 3.2, with $c_1 = -13.224 \pm 0.155$ and $c_2 = 384 \pm 8$. The conversion factor $\frac{1}{43.5}$ is used to convert pixel into millimeter. The same conversion factor was also used to express the mean width of the positron spot, obtained via Gaussian fits and subsequent averaging of the resulting widths. It was found to be $\sigma_{e^+} = 0.22\,mm$.

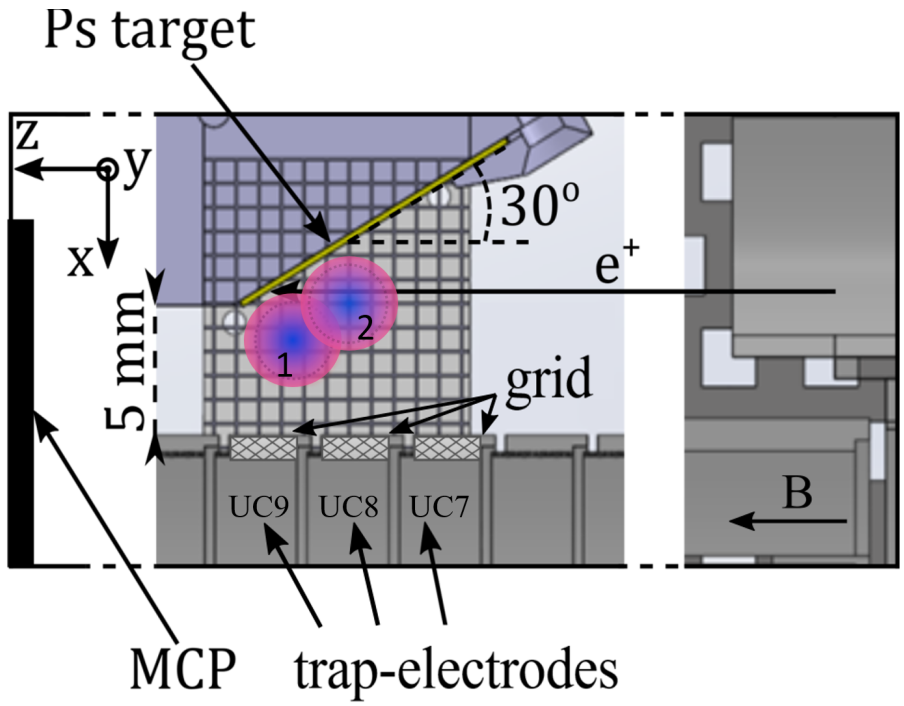

Figure 3.2: Adapted CAD model of the Ps excitation area. As reference, there is a laser light sensitive screen in the back covered with a $1.2 \times 1.2\,\mathrm{mm}$ mesh grid. The positron/Ps converter target and some trap electrodes, labeled UC7-UC9, are also sketched. 5 mm of open space between the lower target edge and the trap enables the Ps velocimetry by means of MCP imaging. The two colored spots mark laser positions of the UV beam (blue), superimposed with an IR laser (red) used for Ps-excitation. The lasers were centered once at $(1.7, -3.2)\,\mathrm{mm}$ from the lower edge of the target and once at $(0, -5.9)\,\mathrm{mm}$.

Using this calibration, the positron bunch could be steered to a position close to the target border on the positron/Ps converter, despite being not directly observable. It is assumed that subsequent positronium emission is centered at that position as well, which is henceforth defined as the origin of the coordinate system. In other words, the term x_0 in Eq. 3.2 now tells the distance between Ps origin and target border along the x-axis.

$$x_0 = \frac{I \cdot c_1 + c_2}{43.5} \tag{3.2}$$

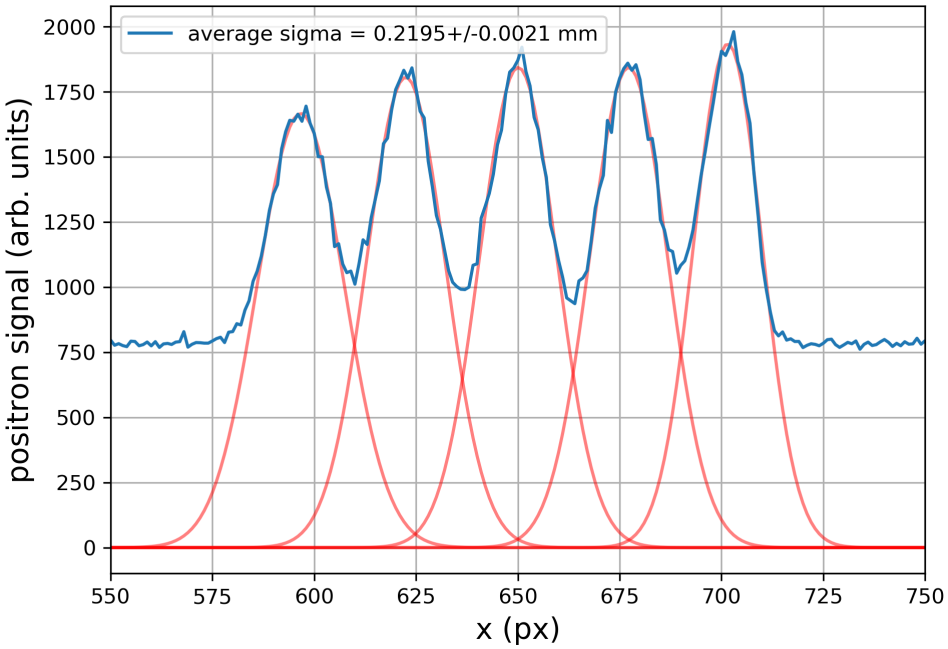

Figure 3.3: Calibration of the vertical steering of positrons: a correlation between the set current and the central x-position of Gaussian fits obtained for the positron spots was found, as well as the mean width of those spots.

3.1.2 Laser timing calibration

The relative laser timing could be calibrated straight forward by using a photodiode positioned in front of a viewport, where usually both superimposed laser pulses enter into the AEgIS apparatus. This photodiode was sensitive to both the UV and the IR laser light. The relative delay between both was then adjusted such that both pulses occurred at the same time. The absolute timing of both lasers had been more tricky to obtain, since it had to be calibrated to the prompt positron implantation peak, later used as $t = 0$. This required a detector able to see both, laser light and positron annihilation radiation. Such a detector had not been foreseen at AEgIS. Annihilation radiation was typically detected

with the aforementioned EJ200 scintillator slabs coupled to photomultiplier tubes (internal name PMT20). These scintillators were not able to detect laser light.

The MCP front face, usually set to ±180 V, was additionally connected to an oscilloscope via capacitor and resistor. This setup resulted in an electric pulse just when the MCP front face was irradiated with scattered UV light from the laser or when photo positrons hit its surface. A measurement series was taken with both lasers alternating between ON and OFF, where the electric readout of the MCP front face did not show a signal when the lasers were OFF. On the outer scintillators, however, when calculating the difference between averaged laser ON and OFF signals, a second peak at later times showed up next to the initial prompt positron peak. This background free second peak had to come from a few thousand photo positrons annihilating on the MCP front face. Aligning the time axes of the scintillator and the MCP front face readout such that the photo positron peaks were overlapping (after correcting for respective flight times), the absolute timing of the laser pulse with respect to the positron prompt peak was found. For some more details, please refer to Ref. [122] where the procedure is also described.

An example of both signals with already aligned time axis is shown in Fig. 3.4. The vertical lines mark the peak positions used for calculating the time difference between positron implantation and laser firing. Note that the laser signal always had the same double-peak structure due to a small electrical impedance mismatch.

3.1.3 Experimental procedures

After calibration, three different measurement types could be performed, listed in the following: Doppler scans, timing scans and self-ionization scans.

(1) Doppler scans are a useful tool to resolve velocity distributions aligned with the propagation axis of the laser. Examples where this technique has been used on positronium are given in Refs. [47, 125]. In this work, the lasers were aligned with the experimental y-axis at position 1, hence one directly obtained the distribution v_y parallel to the target from this type of scan. The MCP front face was set to −180 V, the gain voltage between MCP-IN and MCP-OUT was 1120 V. Here, the laser delays were fixed once to 23 ns and another time to 31 ns, while the UV wavelengths were ramping up multiple times from 204.900 nm to 205.200 nm in steps of 0.005 nm. The subsequent ionization of excited Ps was achieved with an IR laser pulse at 1064 nm.

(2) Timing scans aimed to resolve the Ps velocity distribution along the vertical x-axis by photoionizing Ps atoms via two-step optical transition and by detecting the intensity of photo positrons on the MCP. The first Ps transition, from $1^3S \rightarrow 3^3P$, was done

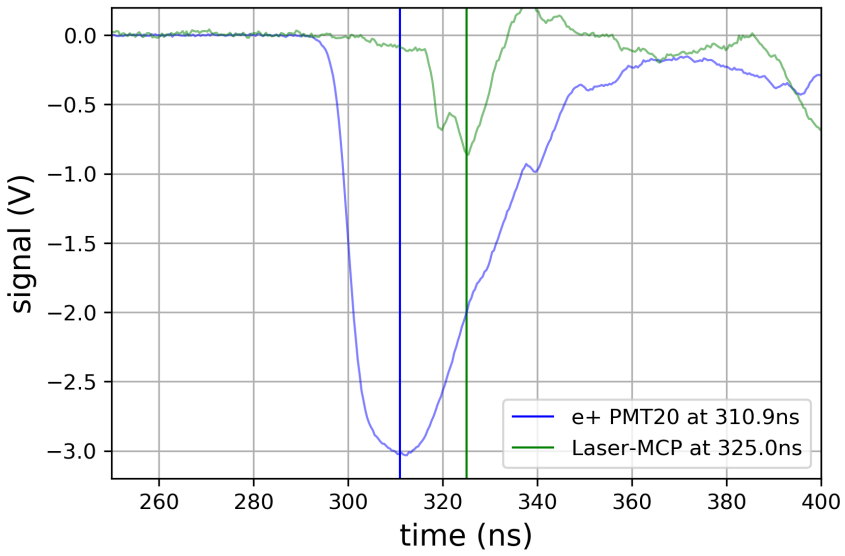

Figure 3.4: Example for the signals produced by prompt positron annihilation on the EJ200 scintillator slabs around the AE$\bar{g}$IS apparatus (blue), and by scattered UV light irradiating the MCP front face (green). The solid vertical lines mark the most prominent peak positions that have been used for the timing calibration. In this example, a delay of 14.1 ns was thus found.

with the UV-laser tuned to maximum efficiency, i.e. to resonance at $\lambda = 205.045\,\text{nm}$. Again, the 1064 nm IR laser was used to produce detectable photo positrons. Set laser delays were ranging from $-5\,\text{ns}$ to 265 ns with respect to the prompt positron peak, while two different positions 1 and 2 were used as labeled correspondingly in Fig. 3.2. The MCP settings were identical to the ones used during the Doppler-scans. With the Ps origin known from the position calibration, resulting distributions could be expressed as velocity distributions with methods from Ps TOF experiments (see Refs. [92, 126]).

(3) Self-ionization, induced by the motional Stark effect in magnetic fields, was investigated by scanning the effective principal quantum number n_{eff} of addressed Rydberg states. This quantum number will be explained later in the text. By tuning the IR wavelength from 1671 nm to 1715 nm, different transitions from $3^3\text{P} \rightarrow$ Rydberg were realized. These wavelengths corresponded to a range of Rydberg-states between $n = 14$ and 22. The UV laser was constantly set to the maximum excitation efficiency as for the timing scans (2). Both laser pulses were synchronously delayed by 25 ns, using laser position 1. Since also this measurement type caused Ps ionization when the laser was fired, positrons could be imaged on the MCP in the same manner as in the other two measurement types. However, since for greater wavelengths one

expects lower intensities of Ps self-ionization, the MCP gain voltage was increased to 1200 V in order to increase the sensitivity.

3.2 Results and discussion

All three types of scans produced several images (1148 × 1148 pixel, 32-bit grayscale). Analysis started with some pre-processing of the raw images, which involved removing empty shots where accidentally no positrons were injected (leading to a significant lower background), a pixel-wise averaging of all images that belonged to exactly the same experimental setting, and finally a rotation of the averaged images by 5.3° counter-clockwise in order to compensate for a slight misalignment of the CMOS camera. An example for the result after these steps is shown in Fig. 3.5. One can easily spot the photoionized positronium cloud emerging from below the target border (red). Several structures like the aluminum target-holder on the top, the MACOR screen (white MAchinable glass ceramic sold by CORning Inc., fit for cryo- and UHV environments) on the left and even the border of the target itself are visible (green). The different coloring indicates the potential set on the MCP front face and therefore which type of lepton is attracted: Red coloring is for positrons, with the potential set to −180 V while green is for electrons with the MCP biased to +180 V. The reason for free electrons to emerge from basically all surfaces is irradiation by scattered UV light enabling the photoelectric effect. In the same manner as for positrons, also the electrons are confined by the strong magnetic field and can only move along the z-axis. Fitting potentials can then guide these electrons to the MCP as well. For analysis, only the pure positron images were further processed.

Several rather narrow windows in the x-y plane were defined, of which three specific ones labeled *roi* 1, *roi* 2 and *roi* 3 are marked in Fig. 3.5. The windows have an extent of 20 x 500 pixel (0.46 x 11.5 mm), which is big enough to have a strong signal in most of the cases while systematic errors due to the window dimension are not yet too disturbing. Using the positional calibration (Eq. 3.2) with a positron deflection current of 23 A, one finds for the distance between Ps-origin and *roi* centers: *roi* 1 with $x_0 = (2.53 \pm 0.38)$ mm, *roi* 2 with $x_0 = (3.91 \pm 0.38)$ mm and *roi* 3 with $x_0 = (5.05 \pm 0.38)$ mm. The systematic errors on x_0 have been estimated by Gaussian error propagation, arising from the positron spot size (±0.22 mm), the calibration measurement (±0.2 mm) and the *roi* width (±0.23 mm).

3.2.1 Ps Doppler Scan

The Doppler scans were repeated five times so that the resulting images could be averaged per wavelength. Subsequently, a constant background obtained from a region on the MCP

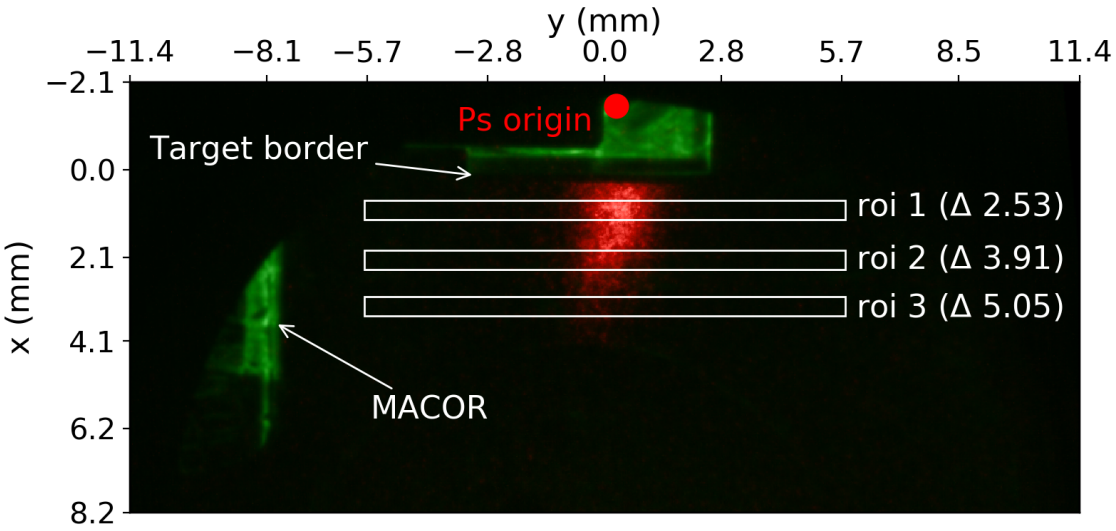

Figure 3.5: Combination of an electron reference image and a Ps photoionization image: Positronium is emerging from the target border and gets instantaneously ionized when the laser pulses are sent. The resulting positrons are then guided towards the MCP and producing a light spot. Regions of interest were defined that have a width of 20 pixel (0.46 mm) and a length of 500 pixel (11.5 mm). They are marked as *roi* 1, *roi* 2 and *roi* 3.

where no positron or Ps atom could reach, was subtracted. UV wavelengths could directly be expressed as Ps velocity components propagating parallel/antiparallel to the laser beam by plugging it into the Doppler equation given in Eq. 3.3, where c is the speed of light in vacuum and $\lambda_r = 205.045\,\mathrm{nm}$, the central wavelength for efficiently exciting the $n = 3$ manifold of positronium in the present magnetic field. Doppler scans strictly distinguish between velocities propagating towards the light source and those directed away from it. This is expressed by positive and negative velocities.

$$v_y = c\left(1 - \frac{\lambda}{\lambda_r}\right) \tag{3.3}$$

At a distance of 5 mm from the Ps origin (position of *roi 3*), 20×500 pixels were integrated and plotted over the corresponding velocity components derived from the set wavelengths. Gaussian fits were calculated and plotted together with the integrated signal as shown in Fig. 3.6. The upper fit (laser delay 23 ns) displays a maximum at $v_y = 0\,\mathrm{m\,s^{-1}}$ and $\sigma_v = (1.03 \pm 0.03) \times 10^5\,\mathrm{m\,s^{-1}}$. The lower fit done for a delay of 31 ns has a sigma of $(0.94 \pm 0.02) \times 10^5\,\mathrm{m\,s^{-1}}$ with the center also at zero and statistical errors only. For the greater delay, the velocity spread of positronium being in the visible region on the MCP seems a bit decreased, which could be due to faster Ps components having moved out of view or due to anisotropic Ps emission from the target.

The obtained σ_v, denoting the one-dimensional spread of velocities aligned with the y-axis, are sometimes used to attribute a temperature to the emitted Ps, assuming an underlying Maxwell-Boltzmann distribution, i.e. ${\sigma_v}^2 = \langle v^2 \rangle$:

$$T = \frac{m_{Ps}}{k} {\sigma_v}^2 \ , \tag{3.4}$$

where k is the Boltzmann constant and $m_{Ps} = 2m_e$ the rest mass of positronium. Since the UV laser has a certain line width, one cannot expect to resolve smaller wavelengths than this — or equivalently smaller velocities. Using again Eq. 3.3, the UV bandwidth $\mathrm{FWHM}_{UV} = 118\,\mathrm{GHz}$ can be expressed as velocity, leading to a lower limit of $\pm 1.2 \times 10^4\,\mathrm{m\,s^{-1}}$. Treating this resolution limit as an systematic error, the fit results for σ_v translate to Ps temperatures of $T_{23\,ns} = (1400 \pm 290)\,\mathrm{K}$ and $T_{31\,ns} = (1166 \pm 260)\,\mathrm{K}$, respectively.

3.2.2 Ps timing scans

The timing scans reveal asymmetrical distributions when plotted over measured delays as shown in Fig. 3.7. Measurements for times greater 120 ns were used to calculate an averaged background signal which was subtracted from all other points. This time was chosen, because from here on no photo positron signal could be identified on the acquired images. This is explained by the absence of Ps components flying slower than $2.5 \times 10^4\,\mathrm{m\,s^{-1}}$, even so few single atoms could still exist. In fact, already from 60 ns onward the observed Ps signal in Fig. 3.7 is almost not distinguishable from background. This is a consequence of several effects, which all have to be taken into account for analysis. The first is natural annihilation of ground state ortho-Ps in vacuum. The longer one waits, the less Ps can be addressed by the lasers, even if Ps was not moving at all. The second is the spatial overlap of the Ps cloud with the laser beams (reminder: laser spot size (FWHM) $\approx 4.4\,\mathrm{mm}$). At all times, only the fraction of Ps is in the laser region and can be ionized. Although Ps atoms are moving with a velocity distribution not known *a priori*, it can be expected that from a certain moment on most of them have moved out of laser view with only very slow components remaining. It is important to note that this effect spreads over two dimensions, x and z, while in y-direction the choice of resonant laser wavelength guarantees a selection of smallest velocities only. For the used UV laser with a bandwidth of 118 GHz, the range of addressed y-velocities was between $\pm 1.2 \times 10^4\,\mathrm{m\,s^{-1}}$. In other words, for all scanned times no Ps atom could move out of the detection view with respect to the y-axis.

The goal now is to derive from these measurement results the desired velocity distributions. The observed signal is in fact not a time distribution, but a sequence of spatial

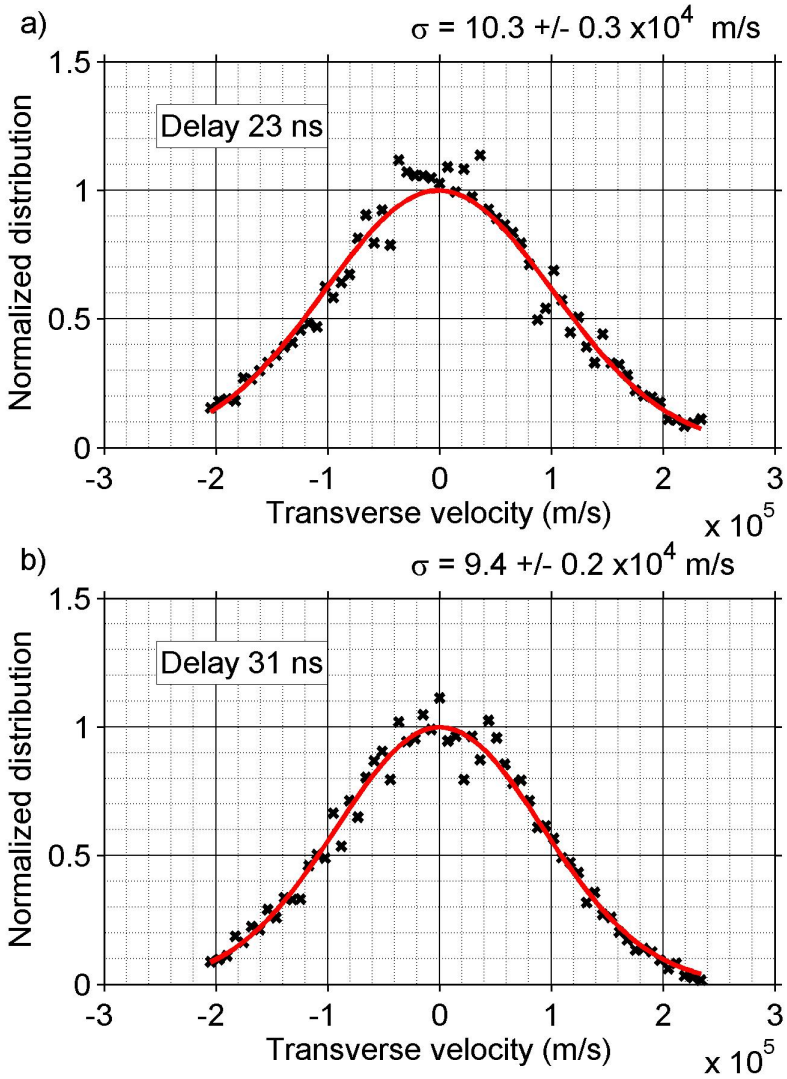

Figure 3.6: Doppler scans with laser delay 23 ns (top) and 31 ns (bottom). Both distributions have a peak at $v_y = 0\,\mathrm{m\,s^{-1}}$, but the later distribution seems a bit narrower, indicating a slightly reduced mean velocity within the detection range of the MCP.

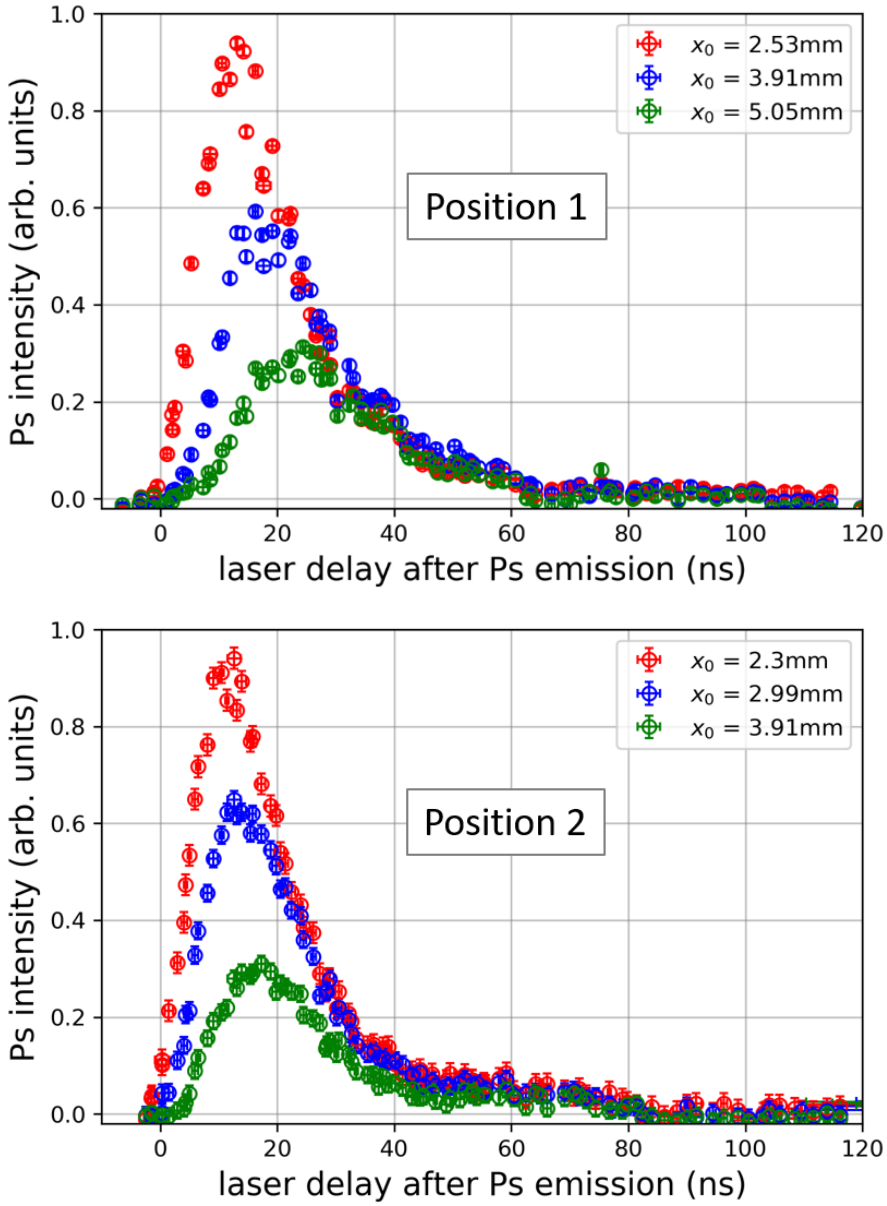

Figure 3.7: Timing scans at distinct laser positions 1 and 2: The observed Ps intensity within three distinct regions of interest (*roi*) as defined in the text. For greater distances x_0 from the Ps origin, the distributions shift towards later times and decrease in amplitude due to the respective spatial overlap with the lasers.

integrals probed at different laser delays t_L. These can be expressed as velocities using the relation $v_x = \frac{x_0}{t}$, where x_0 denotes the distance between Ps origin and the center of different *rois*, and t is the flight time which can slightly deviate from the set laser delay. This deviation stems from the possible contribution of a Ps permanence time t_{perma} [127], since Ps atoms have to move through the converter nanochannels before reaching vacuum after production (see also Chapter 4). Hence it follows: $t = t_L - t_{perma}$. Despite this, one may still use $t_{perma} = 0$ during the following analysis not only for practical reasons, but also because of the time spread (FWHM) of the initial positron bunch ($\approx 14\,\mathrm{ns}$) and the unknown distribution of t_{perma} itself — simulations showed that warmer Ps has interacted less with the converter than cold Ps and therefore has a shorter permanence time [110]. All this renders it very difficult to assume a reasonable value for t_{perma}.

The signal intensities have first to be corrected by the term $e^{t/142\,\mathrm{ns}}$ which is required in order to compensate for naturally occurring ground state annihilation of free Ps. Then, the Jacobian conversion factor t is applied, allowing to express the spatial distribution as a velocity distribution. In literature, this conversion factor is often described as a correction for the different times that faster or slower particles stay in front of a detector with limited detection range [126, 128]. It can be derived using the general relation $x = vt \Rightarrow \frac{dx}{dv} = t$ and the distribution functions f_x and f_v, defined in space realm and in velocity realm, respectively:

$$\begin{aligned} f_x\,dx &= f_v\,dv \\ f_v &= f_x\,\frac{dx}{dv} \\ f_v &= f_x\,t \end{aligned} \tag{3.5}$$

Finally, a sliding window average is used in order to increase the statistics especially for the very slow velocities (late times). The width of this sliding window was chosen to be $\pm 2.5 \times 10^4\,\mathrm{m\,s^{-1}}$, centered at the positions of measured data points. The result of this treatment is shown in Fig. 3.8). Note that the linearly spaced data points plotted over time become hyperbolically spaced when plotted over velocity, which is important to remember when further processing the velocity distribution. The solid lines in the figure are the result of a modeling that will be described further down (Section 3.2.3). The most frequent velocity components lie between $1.4 \times 10^5\,\mathrm{m\,s^{-1}}$ and $1.8 \times 10^5\,\mathrm{m\,s^{-1}}$, where the higher velocities can be found at more distant *rois*.

This shift in velocity between the *rois* becomes not immediately clear. One expects this effect only for the distributions plotted over time, because if a *roi* is further away, also the flight times of all Ps components increase accordingly under the justified assumption of constant speed of each Ps component in vacuum. There are two effects, however, which

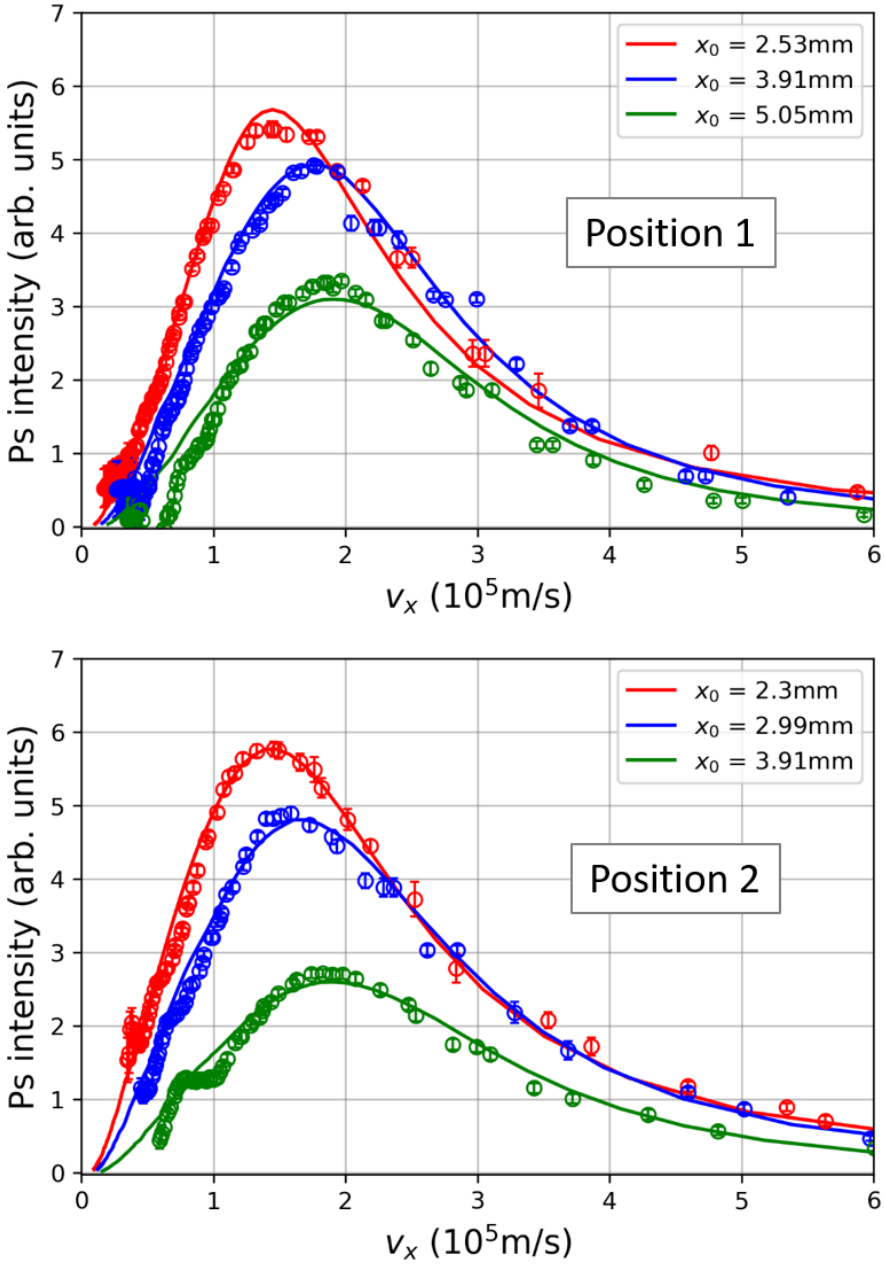

Figure 3.8: The observed Ps intensities of Fig. 3.7 converted into velocity distributions plotted over the corresponding velocities for both laser positions. Both positions result in very similar distributions. The solid lines represent the best fitting model as explained in the text.

also affect the resulting velocity distributions and which allow us to conclude which curve provides the most trustworthy result.

1) The aforementioned permanence time affects the real flight times. If set to zero, one tends to underestimate the real velocities, but more so with smaller flight times where a few nanoseconds can make quite a difference. Without further knowledge of the permanence time, it is safest to maximize the flight times by choosing *rois* as far as possible without leaving the laser beam. This restriction already renders Position 1 the better choice, since the furthest window within the laser here was about 5 mm, while for Position 2 it is merely about 4 mm.

2) The laser beam profile is symmetric under rotation around the y-axis. However when slicing out *rois* along the x-axis, the ratio between contributions of x- and z-components is affected by the circular relation $r = \sqrt{x^2 + z^2}$. The MCP imaging technique has no resolution along the z-axis. Hence, all components hit by the laser along the z-axis are always contributing to the signal, in particular the slowest. As a consequence, velocity distributions for windows with more z-contributions appear faster. In summary, when choosing the furthest possible *roi* of Position 1, and by that maximizing the contribution of x-components, one obtains the best estimate for the velocity distribution aligned with the x-axis.

3.2.3 Modeling the Ps velocity distribution from TOF measurements

In some papers the distribution of kinetic energies (equivalent to velocities squared) for positronium was modeled using a so-called asymmetrical double-sigmoidal function, which was used because it fitted the data well enough, but its parameters could not be attributed to any physical meaning [92, 128]. The solid curves shown in Fig. 3.8, however, were obtained by developing a model that starts from a basic Gaussian velocity distribution f_v for each of the three spatial dimensions x, y, z, applied to the real geometry. These Gaussian functions are centered at $v = 0\,\mathrm{m\,s^{-1}}$ (which also followed from the Doppler scans) and have a velocity spread σ_v that is used as free parameter, but identical for all three dimensions:

$$f_v = f_{vx} \cdot f_{vy} \cdot f_{vz} = \frac{1}{(2\pi\sigma_v^2)^{3/2}} \exp\left[- \frac{x^2 + y^2 + z^2}{t^2\, 2\sigma_v^2} \right] \tag{3.6}$$

Furthermore, the time spread of the incident positron bunch is also modeled with a Gaussian function centered at $t = 0$ and impacting the target at $(0, 0, 0)$, i.e. the Ps origin. The time spread σ_t is used as free parameter, even if it already is heavily constrained by experimental data. It is expected that $\sigma_t \leq 6\,\mathrm{ns}$. Under the assumption that positrons

have the same probability to form positronium at all times when entering the target, then also the Ps time spread is shaped like a Gaussian, albeit shifted to later times by an average permanence time t_{perma} that was introduced above for the analysis of timing scans. This is not entirely correct, because very slow Ps components will most likely have interacted a lot more with the nanochannel walls and therefore require more permanence time than fast components [129], but this effect is convoluted with the dominating positron time spread. Here, the distribution of permanence times is treated as a second order effect, and for the Ps time distribution follows:

$$f_\tau = \frac{1}{\sigma_\tau \sqrt{2\pi}} \exp\left[- \frac{(\tau - t_{perma})^2}{2{\sigma_\tau}^2} \right] \tag{3.7}$$

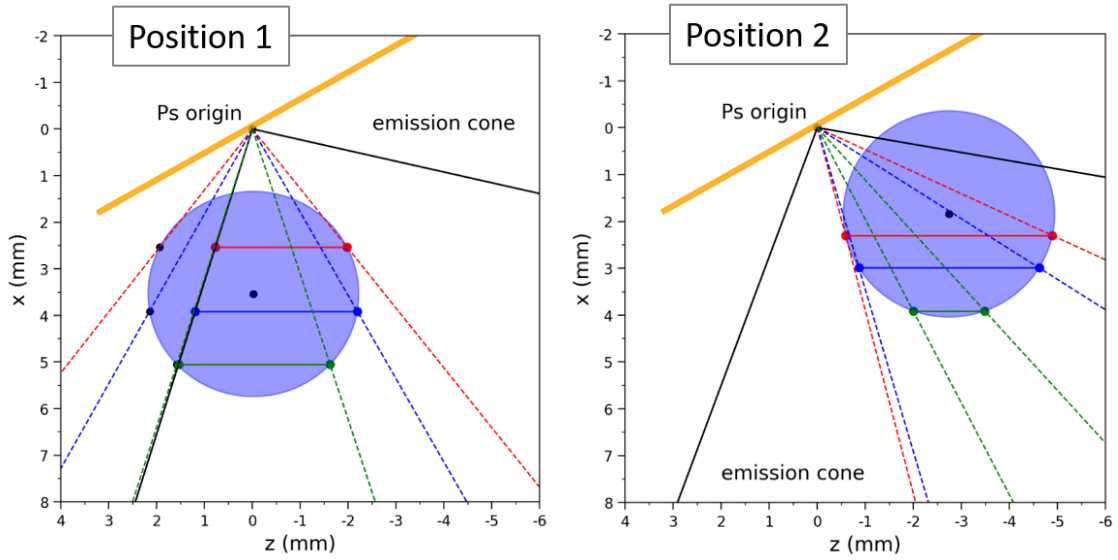

Figure 3.9: Sketch of the geometric setup as used for the timing scans and as it was introduced in the modeling. The positron/Ps converter target (orange) is tilted by 30° against the z-axis, which is aligned with the 1 T magnetic field. The Ps origin - as was found via position calibration (Section 3.1.1) - is marked on the target as black spot, from which Ps is propagating within an emission cone (solid black lines) with half opening angle θ. The two laser positions (left: laser position 1; right: laser position 2) are also given as well as the range where Ps excitation is saturated. The colored lines (red, blue, green) mark positions of the used analysis windows (*rois*), which are geometrically limited by the laser spot.

The relevant geometrical setup is sketched in Fig. 3.9 for both laser positions, here in more detail, in order to introduce the so-called *emission cone* in which Ps is assumed to propagate. Its half opening angle θ against the target's surface normal is used as free parameter, since there is no reliable data for the expected Ps emission. In earlier

experiments with this type of targets, always $\theta = 60°$ was assumed. In any case, not only the emission cone may influence the Ps photoionization signal, but also the laser beam profile. The given beam radius $\Delta r = 2.2\,\mathrm{mm}$ corresponds to the HWHM value of a Gaussian beam profile, until which the Ps excitation is saturated, i.e. the laser fluence is high enough to guarantee an interaction with Ps atoms [80]. This region is not covering the whole x-z plane, and more importantly, not all *rois* in the same way. Hence, for the modeling, one has to integrate only those Ps atoms that are at the same time inside the emission cone, the laser beam and the current *roi*.

The integration of Ps atoms satisfying all three regional boundaries is easiest done in Cartesian coordinates. The limits, also summarized in Tab. 3.1, are for:

x: The chosen width of the *roi*, resulting in $\Delta x = \pm 0.23\,\mathrm{mm}$ around the *roi* center x_0.

y: From the UV bandwidth and its wavelength at resonance follows the range of addressed velocities aligned with the y-axis, and from this at any given time t the maximum spatial spread $t \cdot (\pm 1.18 \times 10^4\,\mathrm{m\,s^{-1}})$ around $y = 0$. For flight times smaller than one microsecond, one will always find the whole addressed y-distribution in view of *roi* which extends for about 12 mm in y, so no additional boundary condition than the given is required.

z: Here, one first has to check if at a distance x_0 from the Ps origin any z-components are within the laser beam, centered at (x_L, z_L). If not, Δz and with this the whole integral becomes 0 (Eq. 3.8). Furthermore, one has to limit Δz further if the emission cone is cutting in, which is demonstrated for position 1 in Fig. 3.9.

$$\Delta z = \sqrt{\Delta r^2 - (x_0 - x_L)^2} \begin{cases} \Delta z \text{ for } |x_0 - x_L| \leq \Delta r \\ 0 \text{ for } |x_0 - x_L| > \Delta r \end{cases} \tag{3.8}$$

Given the initial Gaussian velocity spread per axis, one can now convert this into a space distribution using the same approach as in Eq. 3.5, leading to the conversion rule: $f_x = f_y = f_z = f_v \frac{1}{t}$. Defining two timing ranges, one for flight times t going from $-10\,\mathrm{ns}$ to $250\,\mathrm{ns}$ and one for a convolution with the Ps time spread ranging from $-200\,\mathrm{ns}$ to $200\,\mathrm{ns}$, one can now calculate the spatial integral $I(t)$ for each time t as noted down in Eq. 3.9. The last integral represents the convolution with the Ps time-spread, exploiting the time dependence of $f_v(x, y, z, t)$. Finally, the factor g_r is weighting the excitation efficiency per distance x_0, as was theorized and simulated for the Ps excitation performed at AE$\bar{\mathrm{g}}$IS [80, 81, 124]. Values for g_r are only available for laser position 1, therefore, in the case of position 2, g_r is a free parameter as well.

$$I(t) = \frac{g_r}{t^3} \int_{x_0-\Delta x}^{x_0+\Delta x} dx \int_{-\Delta y}^{\Delta y} dy \int_{z_L-\Delta z}^{z_L+\Delta z} dz \int_{-200\,\mathrm{ns}}^{200\,\mathrm{ns}} f_v\left(t - [\tau - t_{perma}]\right) f_\tau(\tau)\, d\tau \tag{3.9}$$

Having integrated all Ps atoms within the *rois* at a given time t (Fig. 3.10), the same conversion from space to velocity realm as was used for the experimental data could be done by simply multiplying with $t_L = (t + t_{perma})$. The term t_L then corresponds to the observed timings in the experiment. Note that here the exponential correction factor is not needed, since it was not introduced in the first place. The outcome of this modeling was shown in Fig. 3.8 as solid lines for the velocities. In Fig. 3.10, the model is expressed as observed Ps intensity plotted over time, similar to what has been measured directly. The set of parameters that gave the best fit are listed in Tab. 3.1.

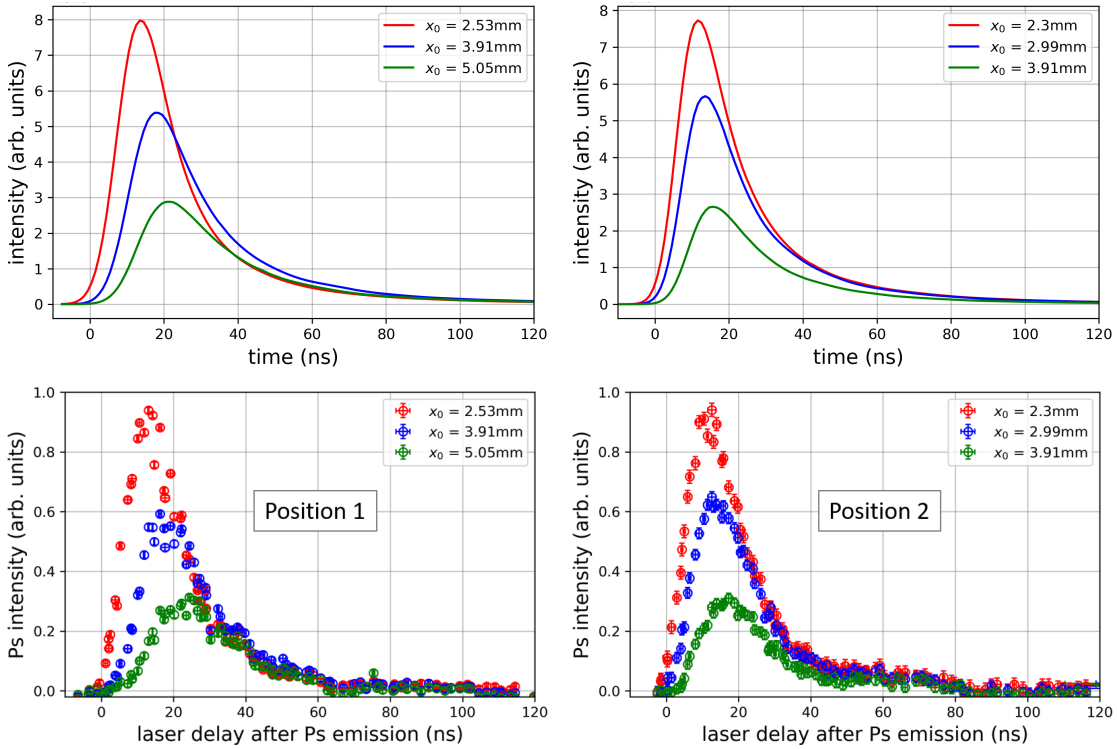

Figure 3.10: Modeled integral of Ps atoms within different *rois* for laser position 1 (left) and position 2 (right) plotted over time using parameters as in Tab. 3.1. For comparison, also the experimental data is shown once more below each model.

Considerations on the Ps permanence time

The velocity distributions display a general shift towards faster velocities for more distant *rois*. As was explained above in Section 3.2.2, this can be due to two effects. One is the

	Laser Position 1	Laser Position 2	Remarks
Δx	$\pm 0.23\,\mathrm{mm}$	$\pm 0.23\,\mathrm{mm}$	from the width of *roi*
Δy	$t \cdot (\pm 1.18 \times 10^4\,\mathrm{m\,s^{-1}})$	$t \cdot (\pm 1.18 \times 10^4\,\mathrm{m\,s^{-1}})$	from UV bandwidth and wavelength
Δz	from Eq. 3.8	from Eq. 3.8	dependent on geometry
x_L	$3.54\,\mathrm{mm}$	$1.84\,\mathrm{mm}$	measured with camera
z_L	$-0.02\,\mathrm{mm}$	$-2.74\,\mathrm{mm}$	measured with camera
Δr	$2.2\,\mathrm{mm}$	$2.2\,\mathrm{mm}$	laser beam profile HWHM
g_r	0.55, 0.62, 0.53	0.50, 0.55, 0.9	Ps ion. efficiency (*roi* 1, 2, 3 [124])
θ	$47°$	$50°$	half opening angle of emission cone
σ_τ	$4.5\,\mathrm{ns}$	$3.5\,\mathrm{ns}$	initial time spread of Ps cloud
σ_v	$2.1 \times 10^5\,\mathrm{m\,s^{-1}}$	$2.4 \times 10^5\,\mathrm{m\,s^{-1}}$	1D velocity spread of Ps cloud
t_{perma}	$2.4\,\mathrm{ns}$	$0.5\,\mathrm{ns}$	assumed mean Ps permanence time

Table 3.1: Set of parameters that best reproduced the experimental velocity distributions.

composition of z- and x-components, which contribute differently for different positions within the laser spot, the other is the Ps permanence time. If one eliminates the dependence on z by narrowing the laser to a narrow line aligned with the x-axis, what remains is only the effect of the permanence time. This step is infeasible for the experimental data, since one always visually integrates the whole fraction of z-components in range of the laser beam, but in the simulation this is easily achievable by just replacing F_z and g_r with a constant for all *rois*.

Doing so for the model obtained using laser position 1, one can plot for example the peak times over corresponding distances as shown in Fig. 3.11. This resembles well a linear function, which then consequently is fitted into the data. Resulting linear fit parameters, slope and offset, can be interpreted as $\frac{1}{v_{real}}$ and t_{perma}, respectively, as shown in Eq. 3.10. The fitted Ps permanence time of the peak component therefore is $t_{perma} = (6.15 \pm 0.45)\,\mathrm{ns}$.

$$t_L = t_{perma} + t = t_{perma} + \frac{x_0}{v_{real}} \tag{3.10}$$

In order to compare this to the overall constant permanence time that was used for the model, this procedure of extracting t_{perma} of a single Ps velocity component is repeated several times for fractions of the peak amplitude ranging from 0.5 % to 100 %. Resulting

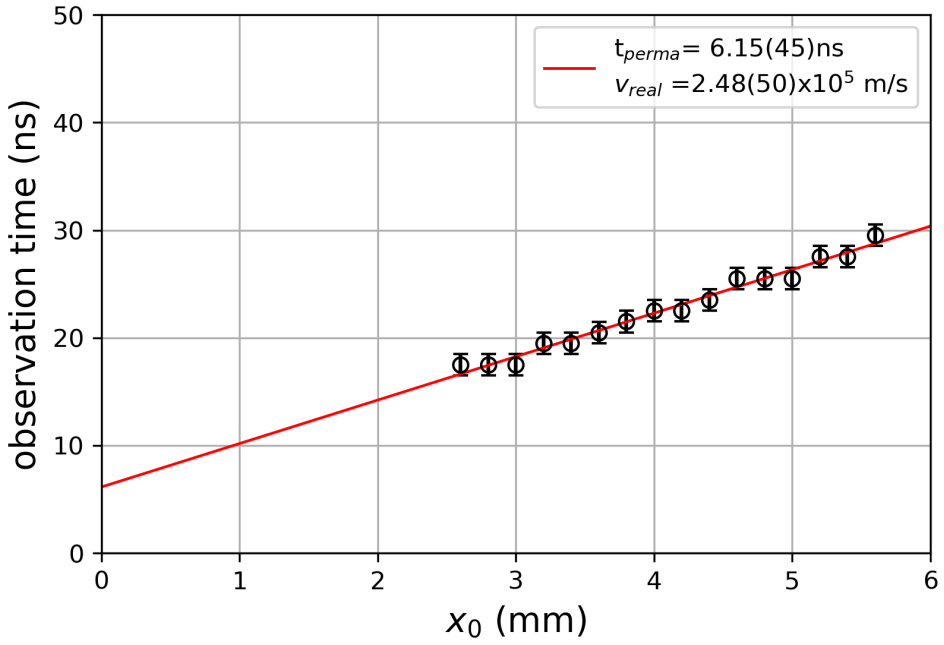

Figure 3.11: Observation times t_L as a function of the distances of *rois* for the peak component. The intersection with the time axis can be interpreted as Ps permanence time.

permanence times are plotted over corresponding real velocities of each component in Fig. 3.12. From this, the weighted average permanence time can be calculated. Note that the weight of a single t_{perma} is the variance following from the linear fitting procedure, i.e. $\frac{1}{\sigma^2_{perma}}$, which inherits the uncertainty of each Ps velocity amplitude. Like this, very low velocities lead to huge uncertainties, and consequently these are considered less important for the calculation of the average permanence time. Similarly for very high velocities, the corresponding timings are all in the range of few nanoseconds and big uncertainties on the velocities themselves emerge.

The obtained weighted average is (2.5 ± 0.1) ns, which compares well to the constantly applied 2.4 ns in the model. Moreover, one can see the general trend that with increasing velocities the permanence time decreases, which is expected since slower and therefore cooler components have interacted more with the porous silicon. Negative values would seem unreasonable, but here it means that the time spread of the positron bunch led to some early Ps creation, i.e. before the peak intensity of positrons, which was used as time reference for $t = 0$, actually was implanted. Excluding the lowest and highest velocities due to the huge uncertainties, one finds a range for permanence times between 12 ns and -3 ns with respect to the timing of the positron peak. This corresponds to Ps velocities between $8 \times 10^4\,\mathrm{m\,s^{-1}}$ and $4.2 \times 10^5\,\mathrm{m\,s^{-1}}$, or to Ps energies between 0.3 eV and 1 eV.

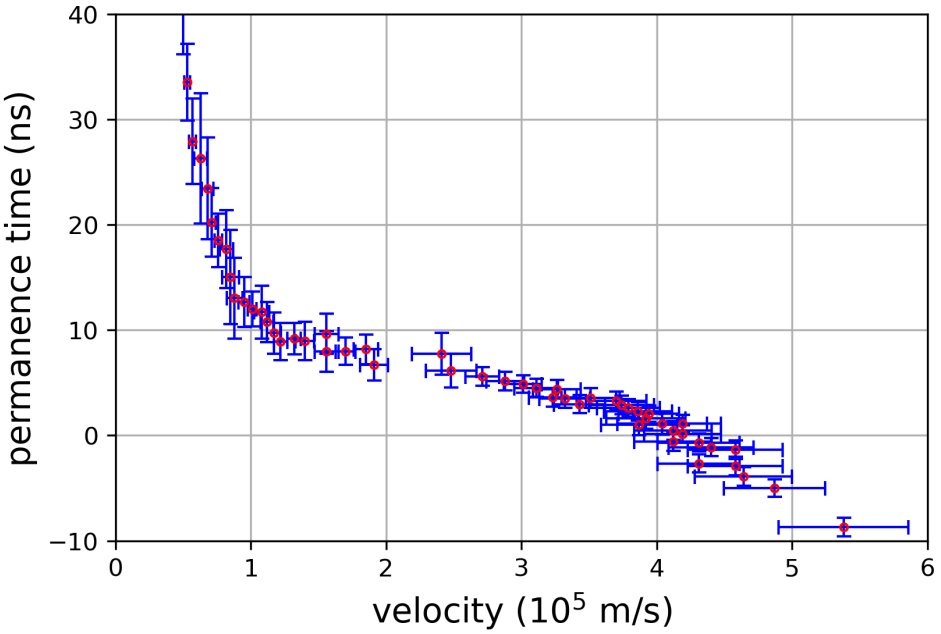

Figure 3.12: Method of Fig. 3.11 repeated for many fractions of the peak (from 0.5 % to 100 %). Resulting permanence times are plotted over fitted real velocities of each Ps component of the model.

Similar positron/Ps converters as first explored in Refs. [92, 129] were found to produce cold Ps in the same range. In this work, the Ps permanence times were resolved for the first time according to velocity components, using a model for Ps velocities that was fitted into real experimental data.

3.2.4 Self-ionization of Rydberg-Ps

Since the production of antihydrogen needs to be performed within a strong magnetic field which confines antiprotons, Rydberg-excited Ps atoms have to move through that homogeneous field. This gives rise to the motional Stark effect, an induced electrical field that can be calculated by $\vec{E}_{mot} = \vec{v} \times \vec{B}$, where $\vec{B}$ is the magnetic field and $\vec{v}$ is the Ps velocity perpendicular to this field. Here, just the v_x is relevant since selected v_y-components are all around zero by correspondingly choosing the UV-wavelength and can be neglected. Furthermore, Rydberg-Ps dipole moments depend on the principal quantum number n. This yields advantages like gaining motional control over otherwise neutral atoms (e.g. via Stark acceleration [130]), but huge dipole moments also bring Rydberg-Ps closer to ionization inside electric fields.

The minimum electric field beyond which Rydberg-Ps ionizes is called the *ionization threshold*, from which a limiting velocity v_{limit} can be calculated. Its derivation is given from Eq. 3.11 to Eq. 3.14, displaying a dependency on the effective principal quantum number n_{eff}^4 [80, 131]. The effective principal quantum number n_{eff}, depending only on the wavelength λ, is introduced instead of the normal integer n, in order to accommodate the almost continuous distribution of high Rydberg-Ps states. The term $Ry_{Ps} = 6.8\,\text{eV}$ is the Rydberg energy for Ps, e the electric charge and a_0 the standard Bohr radius. The presence of a motional Stark field eliminates axial symmetry and determines, via mixing of ℓ and m sub-states, the spread of energy levels for the n-manifold. It also defines the interleaving of nearby n-manifolds, leading to a quasi–continuum of energy levels [132]. As a consequence, the efficiency of $n = 3 \rightarrow$ Rydberg-transitions is essentially governed by the IR laser bandwidth (430 GHz).

$$F_{\text{limit}} = \frac{Ry_{Ps}}{9ea_0} \cdot \frac{1}{{n_{\text{eff}}}^4} \tag{3.11}$$

$$\frac{hc}{\lambda} = Ry_{Ps}\left(\frac{1}{(n=3)^2} - \frac{1}{{n_{\text{eff}}}^2}\right) \tag{3.12}$$

$$F_{\text{limit}} = \frac{Ry_{Ps}}{9ea_0} \cdot \left(\frac{1}{9} - \frac{hc}{Ry_{Ps}\lambda}\right)^2 \tag{3.13}$$

$$v_{\text{limit}} = \frac{F_{\text{limit}}}{B} \tag{3.14}$$

The photo positrons due to Rydberg-Ps self-ionization could also be imaged on the MCP, although the number of detectable particles turned out generally smaller. Therefore, the entire region below the target border until *roi* 3 was integrated for a better signal intensity and subsequently normalized to the measurement result at the lowest possible wavelength ($\lambda = 1671\,\text{nm}$). The outcome is shown in Fig. 3.13 (black circles).

In parallel, the limiting velocity v_{limit} for this lowest wavelength was calculated by using Eq. 3.14, which gave $6 \times 10^4\,\text{m}\,\text{s}^{-1}$. Integrating the most reliable v_x-distribution (green curve in Fig. 3.8, laser position 1) for all velocities greater than this limit and normalizing the result to the total integral led to an estimate for the maximum expected self-ionization fraction, amounting to 97 %. This step could be repeated for all IR wavelengths, so that a model for all expected self-ionization fractions was obtained. The model is plotted together with the measured data points over the wavelengths as blue squares, following roughly the same course as measured self-ionization fractions. This indicates the validity of the found v_x-distribution.

For $\lambda = 1700\,\mathrm{nm}$ (i.e. $n_{\mathrm{eff}} \approx 16$), only about 25 % of Ps ionizes. When going to higher states, i.e. lower wavelengths, the losses increase. Despite this, also the cross-section scales up with n^4 which to some extent could compensate or even exceed the self-ionization losses. This question will be tackled in the next paragraph.

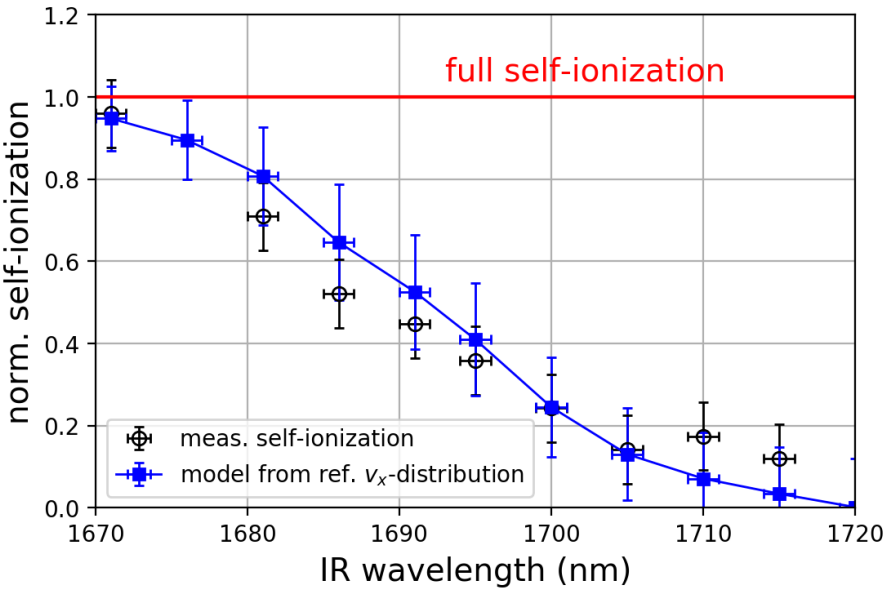

Figure 3.13: Scan over several IR wavelengths corresponding to effective positronium Rydberg states (black circles). The self-ionizing fractions have been normalized to the expected full self-ionization. Around $\lambda = 1680\,\mathrm{nm}$, about 70 % of the Ps ionizes. At $\lambda = 1700\,\mathrm{nm}$, only about 25 % is lost. The self-ionization was modeled as described in the text (blue squares).

3.2.5 Impact on the cross-section of antihydrogen production

In this last paragraph, the simulated results for the cross-section of antihydrogen production (Fig. 3.1) and the measured velocity profile along the x-axis (green curve of Fig. 3.8, Position 1) were combined to a new *weighted cross-section* in order to find the best setting for optimal $\bar{\mathrm{H}}$ production in AE$\bar{\mathrm{g}}$IS. As can be seen in Fig. 3.14, a maximum occurs in the region of $1.2 \times 10^5\,\mathrm{m\,s^{-1}}$, whereas faster components are strongly suppressed due to velocity mismatch. At lowest velocities, the statistical errors do not allow to estimate the weighted cross-section. However, generally are all slow Ps atoms ($v_x \to 0$) very likely to produce antihydrogen due to the increased time for interaction, hence the cross-section grows quadratically in this range.

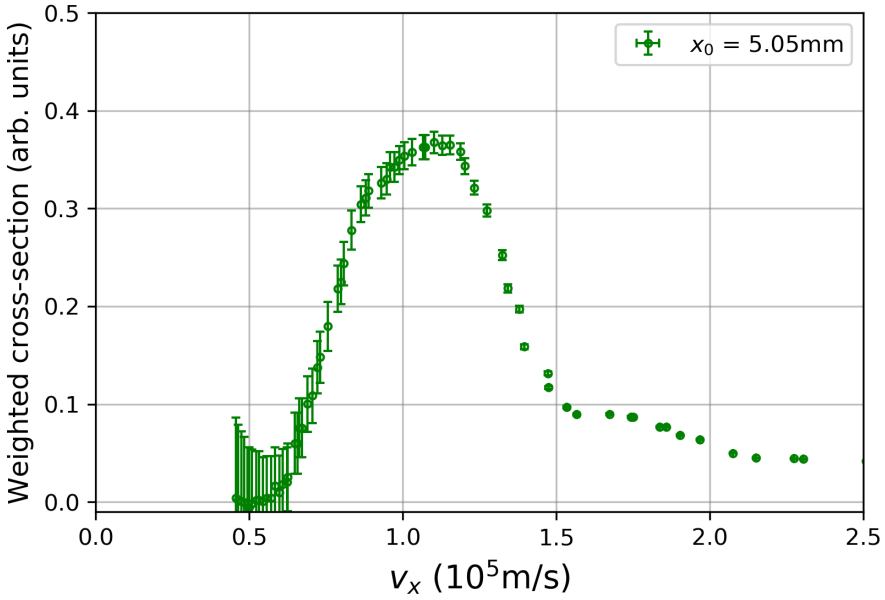

Figure 3.14: Weighted cross-section plotted over vertical velocities v_x. A peak occurred around $1.2 \times 10^5\,\mathrm{m\,s^{-1}}$, which also allowed an estimation of the best laser delay amounting to 35 ns when using laser position 1.

Using laser position 1, one should set the laser delay t_L such that velocity components around $1 \times 10^5\,\mathrm{m\,s^{-1}}$ are within the high efficiency range of the laser which is about 35 ns. Alternatively, one can chose a new laser position that is grazing the target. In this case, after having waited an appropriate time, i.e. the Ps permanence time of about 10 ns), *all* emitted components slower than $3 \times 10^5\,\mathrm{m\,s^{-1}}$ would be excited and contribute to antihydrogen production. Judging from Fig. 3.14, the meaningful range of velocities for a grazing laser position goes from $0.5 \times 10^5\,\mathrm{m\,s^{-1}}$ to $1.5 \times 10^5\,\mathrm{m\,s^{-1}}$. These Ps components would have to travel towards the antiprotons for approximately 7 mm, therefore a resulting antihydrogen pulse would have a time spread of at least 100 ns. Note that indeed the apparent $\bar{\mathrm{H}}$ time spread presented in Section 2.8 was surprisingly large, about 15 µs (FWHM). This would correspond to a few Ps atoms with a velocity of $5 \times 10^2\,\mathrm{m\,s^{-1}}$, which is clearly outside the range with meaningful statistics.

As a last step, one can now combine the results of self-ionization and the weighted cross-section, reintroducing the scaling factor of n^4 which was removed from the simulation in Fig. 3.1. Then, peak velocities and amplitudes have to be identified for each wavelength and compared to the self-ionization limit v_{limit}. If the peak velocities are smaller than the limit, corresponding amplitudes are a good estimate for the real weighted cross-section. However, if they exceed the limit self-ionization occurs and a reduced $\bar{\mathrm{H}}$ production has to be expected. In fact, a neighboring velocity just below the limit then defines the reduced

weighted cross-section valid for this choice of wavelength. The result of this consideration is plotted in Fig. 3.15, showing that the best choice with the maximum weighted cross-section would be an IR wavelength slightly greater 1680 nm, corresponding to a Rydberg-state with $n_{\text{eff}} \approx 20$. This demonstrates that the intuitive choice of 'safe' Rydberg-excitation based solely on barely visible self-ionization signals is not necessarily the best when optimizing the $\bar{\text{H}}$ production.

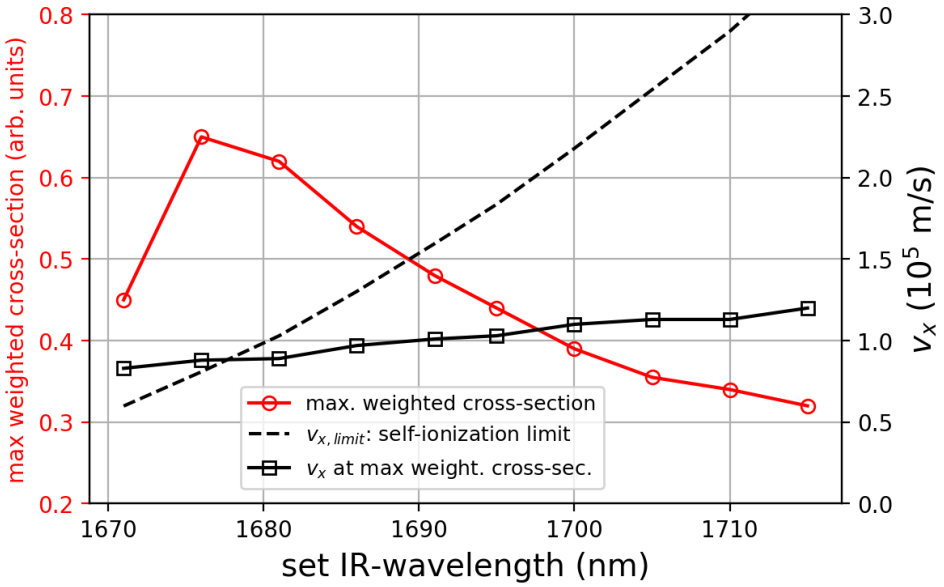

Figure 3.15: Left ordinate in red: maximum of the weighted cross-sections; right ordinate in black: the velocity component v_x; both plotted over the set IR laser wavelength addressing an effective Rydberg-state. The solid lines are guides for the eye, while the dashed line represents the limiting velocity of self-ionization.

An alternative representation of the new weighted cross-section and its dependence on n_{eff}, on the Ps velocity distribution and on the self-ionization inside a 1 T magnetic field is given in the form of a 2D-intensity plot in Fig. 3.16. This time, not only the maximum production cross-section is shown, but all resulting weighted cross-sections at different velocities for a range of effective principal quantum numbers between $n_{\text{eff}} = 0 \ldots 30$. For a fixed velocity distribution, the best choice of the effective Rydberg-state lies around $n_{\text{eff}} \approx 20$, hence shortly before self-ionization starts to destroy a major fraction of the useful Ps.

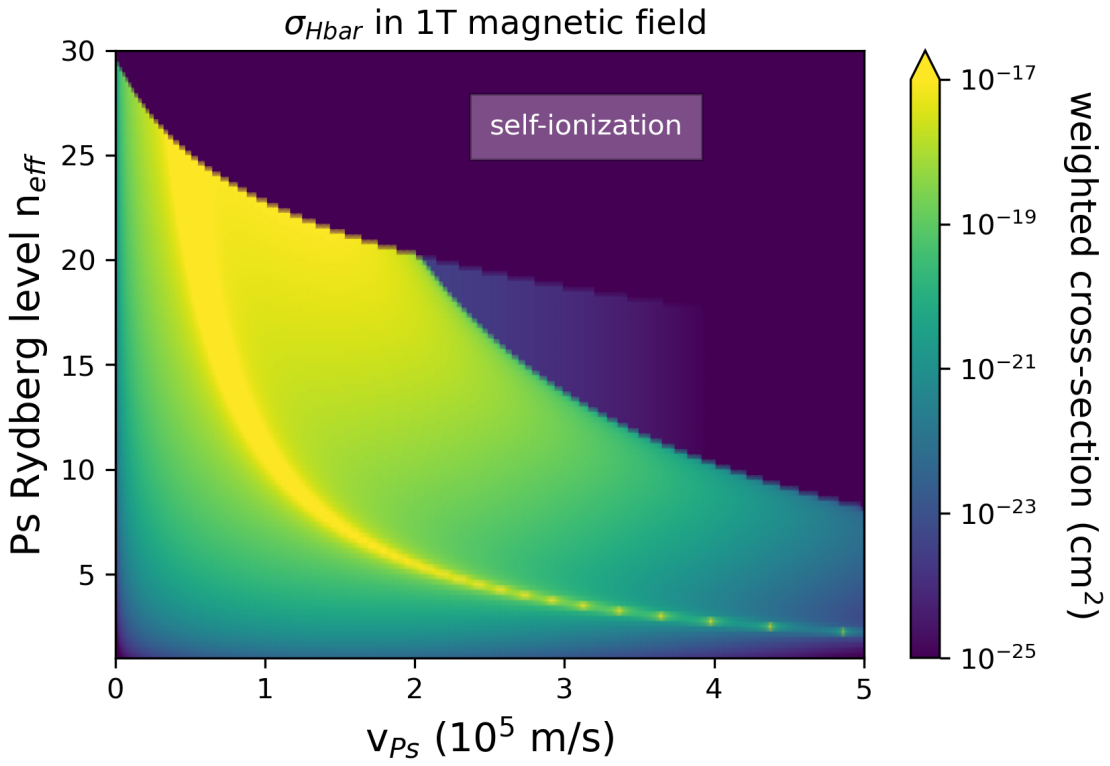

Figure 3.16: Intensity plot for the weighted antihydrogen production cross-section using the basic result from Ref [121], the Ps velocity profile obtained in this work and the self-ionization behavior of Rydberg-Ps, which has an effective principal quantum number n_{eff} and which is moving perpendicular to the 1 T magnetic field.

Chapter 4

Transmission positron/positronium converters

The most common method for the production of positronium is by implanting positrons into a solid medium. After implantation, positrons thermalize within a few ps inside the bulk due to several energy loss mechanisms. Extremely fast positrons in the MeV-regime lose their energy first by inelastic interaction with the effective Coulomb-field of nuclei and electrons, producing *bremsstrahlung*. Then, down to few keV, ionization and in semiconductors/isolators also electron-hole pair creation — so-called excitons — are the dominant loss channels. When finally the energy is getting too low for ionization and exciton creation, phonon excitation takes over. This is especially important for insulators and semiconductors, because the energy gap between the bands inhibits the other energy loss channels much earlier [84].

Thermalized positrons diffuse up to few hundred ps, strongly depending on the material and its internal defect density and distribution. In any case, compared to the depth the positrons can reach after implantation with sufficiently high kinetic energy, the distance they may cover via diffusion is rather small (up to few hundred nm). This is why one usually speaks of *stopped* positrons, albeit strictly speaking they still move. During or immediately after stopping, a fraction of the positrons can be converted into positronium, either by a type of charge exchange reaction with surrounding atoms or molecules (Ore model, which is valid for not fully thermalized positrons), or by binding to a quasi-free electron in the terminal spur of full thermalization (spur model) [133].

In Section 2.5, the Ps formation threshold $E_{\mathrm{Ps}} = E_i - 6.8\,\mathrm{eV}$ was defined for gases, introducing the ionization energy E_i which represented the required energy to entirely remove an electron from the atom. For solids, in order to avoid confusion, one usually

switches to the term *work function* ϕ. The energy required to remove an electron from the solid is denoted with ϕ_- (typically a few eV). But also the positron has its own work function ϕ_+ which, in contrast to that of an electron, can also be negative. In such a case, the positron would be expelled from the solid when reaching the surface. This feature is often exploited for positron moderation as was mentioned in Section 2.4.3, but it can be a competing process when Ps formation is actually preferred over direct positron emission.

The first line of Eq. 4.1, labeled with *Bulk*, gives the resulting Ps work function ϕ_{Ps} for positronium formed in the bulk. The occurrence of a negative work function also here means that the Ps atom is expelled into vacuum when approaching the surface from the bulk. Next to the individual work functions ϕ_- and ϕ_+, and the Ps binding energy in vacuum (6.8 eV), two additional contributions are given. The first is the band gap energy E_G, because the electron may reside in the energetically higher conduction band. In this case, it would be easier to extract the electron from the solid, which is why E_G enters with a minus into the equation. Note that for metals $E_G = 0$, since the valence band and the conduction band overlap. The other extra contribution is due to the Ps binding energy inside the bulk E_B, which typically is smaller than the Ps binding energy in vacuum due to the constant interaction with the surrounding bulk atoms. Since one obtains the Ps work function using the separate work functions for the leptons, the internal Ps binding energy E_B has to be positive.

$$\begin{aligned} \text{Bulk}: \quad \phi_{\text{Ps}} &= \phi_- + \phi_+ - 6.8\,\text{eV} - E_G + E_B \\ \text{Surf}_v: \quad \phi_{\text{Ps}} &= \phi_- + \phi_{+,s} - 6.8\,\text{eV} \\ \text{Surf}_c: \quad \phi_{\text{Ps}} &= \phi_- + \phi_{+,s} - 6.8\,\text{eV} - E_G \end{aligned} \tag{4.1}$$

The second line in Eq. 4.1, labeled *Surf$_v$*, depicts the binding of a thermal positron trapped in a surface state to a valence electron. Here, the Ps binding energy inside the bulk E_B is of course not applicable, since a surface process is described. The electron resides in the valence band, hence also E_G does not enter into the equation. However, the surface state positron work function $\phi_{+,s}$ may differ from the 'bulk extraction' work function ϕ_+ and has to be distinguished. In the third case, *Surf$_c$*, which is only occurring in semiconductors and insulators, solely the band gap energy E_G has to be subtracted, because here a thermal positron binds to an excited electron in the conduction band.

Notably, most materials have positron and electron work functions a lot smaller than 6.8 eV, which opens up a wide range for solids with resulting negative Ps work functions [88, 134]. Efficient Ps converters usually work in *reflection* geometry and are used in many experiments [19, 118, 47, 54, 125, 135, 136]. Generally, it is important to distinguish between hot ($\approx$ eV) and cold ($\ll 100$ meV) positronium. It is rather easy to produce

large amounts of warm positronium, i.e Ps with few hundred meV, by simply implanting positrons with close to zero kinetic energy into a heated semiconducting/metallic target. Due to the high amount of surface states for positrons and efficient thermal desorption, conversion rates close to 100 % can be reached [99]. But warm Ps can still not be efficiently used in experiments that require additional processes such as optical excitation or the charge exchange reaction. In order to obtain colder positronium, a solution could be to implant positrons deeper into the bulk, so that formed Ps cools via inelastic collisions with surrounding atoms before reaching the surface again. This approach, however, is badly impacted by two restrictions. The first limitation is the fact that positronium formation is not even occurring in the bulk of metals and semiconductors due to the shielding effect of surrounding electrons. From the point of view of a single electron, it is more favorable to stay in a quasi-free state inside the bulk rather than binding to a positron. Hence, bulk-formed Ps can only occur in insulators. The second limitation is the short lifetime of para-Ps (125 ps), since on every collision with another atom the Ps has a chance to exchange its electron for one with opposite spin (pick-off) or, less likely, flip the spin of one of its own leptons. The originally long lived ortho-Ps atoms could turn into short lived para-Ps, which is not balanced by the reverse process. In total, almost no Ps is emitted from the bulk.

A smart solution to these restrictions has been the use of nanoporous silicon dioxide, also called silica, with pore sizes of several nm. It is cheap and simple to produce, and quite efficient (up to 84 % conversion rate has been achieved [137]). Positrons implanted into the porous bulk will randomly diffuse towards a pore. On the way, they can pick up an electron and bulk Ps is formed, only few nm away from an open volume. With the possible energy excess after formation either due to a negative Ps work function or due to an epithermal constituent, Ps is expelled into the pore. Additionally, if the positron did not bind to an electron inside the bulk, it still might pick up a surface electron if it brings enough energy to free the electron. This usually works for epithermal positrons, i.e. those that are not fully thermalized when arriving back at the pore surface. As an example with amorphous silica, two energy peaks for emitted Ps are reported in Ref. [134]. A dominant peak lies at 1 eV supposedly originating from bulk formation and a secondary peak emerges at 3 eV, which occurs due to electron capture at the surface.

Ps entering a pore will move unhinderedly through the open volume until it collides with the opposing wall. Although it now again has a chance to turn into short-lived para-Ps, the total rate of this loss process is reduced since most of the time Ps is in free flight. After several ns, all formed para-Ps atoms are annihilated and a great fraction of the ortho-Ps atoms is in thermal equilibrium with the environment. If the pores possess a connection to each other (so-called open porosity) and form a channel all up to the target surface, Ps

atoms can even escape into vacuum. Otherwise, they will eventually annihilate either via pick-off or just in flight.

In the following, a short resume of the positron/Ps converter target used at AEḡIS will be given. Then, relevant processes for the production of nanoporous materials will be introduced and finally, the advances on manufacturing and characterizing positronium converter targets in transmission geometry will be elaborated on.

4.1 AEḡIS nanoporous positron/Ps converter

The positron/Ps target used at AEḡIS is a variant of the porous silica converters. Here, so-called *nanochannels* are electrochemically etched with a solution of hydrofluoric acid (48 %) and ethanol in a ratio of 1:3 into a silicon wafer with high resistivity (0.1-1.5 Ω cm). The channels tend to be aligned with the <100> crystal orientation, thus with an angle of 55° against the surface normal for the used p-type Si(111). The typical channel depth is in the range of 1-2 µm. The channel diameter lies between 8-20 nm. The internal structure depends on all parameters related to the etching process: current, wafer resistivity, type of dopant, acid concentration and etching duration. After the etching, all surfaces remain highly reactive which is exploited by admitting oxygen (air) to the target, which had been cleaned before with pure ethanol. During 1-2 h on a heat plate at 100 °C, the external and internal surfaces get passivated by a ≈10 nm thin layer of SiO_2. Several re-etchings in the acid after passivation and a consecutive heating in air gradually increase the channel diameter up to 20 nm [92, 138]. All process steps had to be optimized in order to obtain a high o-Ps yield in vacuum at cryogenic temperatures (< 10 K).

The reasoning behind this design in view of AEḡIS experimental conditions is the following. Positrons are implanted into the porous silicon with energies adjustable between 1 keV and 5 keV, on average stopping within the first micrometer of depth. These stopped positrons are able to diffuse several nanometers in all directions. Soon, many will reach a channel wall covered with silica and produce positronium either within or at the surface of this thin SiO_2 layer. Ps atoms then escape into the nanochannel, which basically is a very long single pore. After several inelastic collisions with the channel walls (up to 10^4 [129, 139]), Ps eventually reaches the converter surface and escapes into vacuum. The geometry of the channels defines the cooling efficiency of the converter. The smaller the channel diameter a is, the higher is the minimum temperature T positronium can reach in radial direction (quantum confinement in an infinitely deep cylindrical potential well, see Eq. 4.2).

$$T = \frac{\hbar^2 \pi^2}{3 k_b m_e} \frac{1}{a^2} \tag{4.2}$$

For a diameter of ($a = 8\,\mathrm{nm}$), Eq. 4.2 returns a minimum temperature of 46 K in radial direction. The Ps cooling efficiency along the channel axis it not constrained by quantum effects, but if the channel walls are too straight, Ps atoms whose trajectories are almost parallel to the axis will not interact much before leaving the converter and therefore will also not be cooled enough. It is thus desirable to have a zig-zag geometry along the channel axis as is shown in Fig. 4.1 for a Si(100) sample.

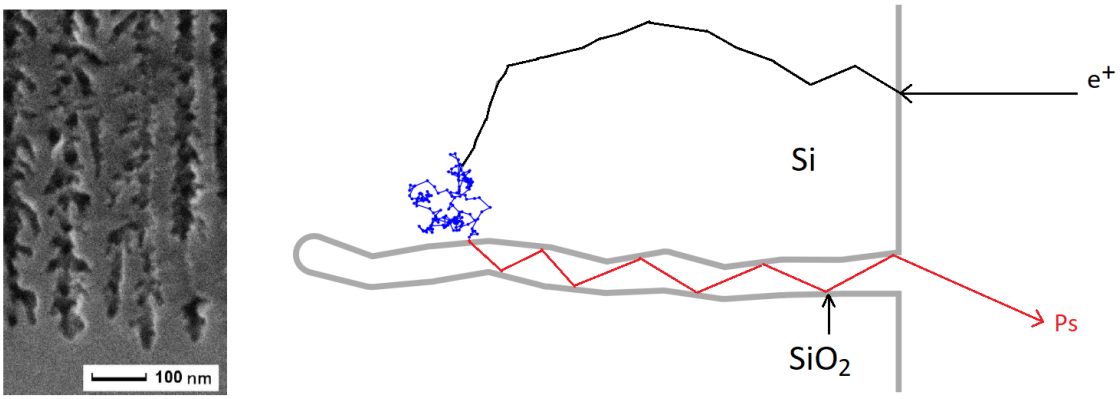

Figure 4.1: Left: Scanning Electron Microscope (SEM) image of a Si(100) nanochanneled target. One can see the vertical orientation of the main channels with many smaller dendrites along the path which allows for high cooling efficiency in all spatial directions. Right: Schematic of a positron/Ps converter. Positrons are implanted with few keV and thermalize dominantly in the remaining silicon structure (black path). Thermalized positrons diffuse through the silicon until they randomly reach a nanochannel that is covered with a thin layer of silica (blue path). The positron can now form Ps and enter the channel, which cools by inelastic collisions with the walls. Eventually, Ps is escaping into vacuum (red path).

The major advantage of this design is that the final Ps temperature is basically set by the environment, which is the reason why it was (and currently is) used at AEḡIS, where the target works at cryogenic temperatures. A time-of-flight measurement for a nanochannel converter made from Si(100) revealed a total positron/Ps conversion of 27 %, of which 9 % cooled well below 20 meV [92]. In Chapter 3, the velocity distribution of the target used within the AEḡIS apparatus was investigated. A mean kinetic energy for the whole Ps velocity distribution of about 150 meV was found here, which is roughly one order of magnitude higher than what had been expected. However, this only became clear after

the velocimetry studies, and it is foreseen to overcome this limitation by testing different morphologies of the porous structure.

4.2 Nanoporous membranes for Ps production in transmission

When designing an experiment with positronium, one big challenge and also constraint is its transport, if one wishes to have a high number of cold Ps atoms at a certain position at a specific time on the nanosecond timescale. This position may then be inside an environment where high field homogeneity is needed such as inside a trap for particle plasma formation, so that one has to put the positron/Ps converter target as close as possible to the designated experimental position without disturbing the other parts. The geometrical extent of the converter, its magnetic properties, the need to implant positrons at high kinetic energies despite other, possibly strict electric requirements, holes to allow interaction with for example laser beams — all these are aspects that put heavy constraints on the experimental setup, sometimes even mutually exclusive.

In its current design, AEgIS has dealt with this problem by installing the converter target 5 mm away from the antihydrogen production trap, tilted by 30° against the positron beam axis. As a consequence, Ps had to travel for these 5 mm plus a few millimeters more inside the trap before actually reaching the antiprotons. During flight, but still outside the trap, Ps had to be excited by lasers to high n Rydberg-states in order to increase its lifetime and the interaction cross-section. Given the limited space an antiproton plasma covers, approximately a cylinder with 2 mm in length and 2 mm radius, one obviously wished to have the Ps source as close as possible to this plasma in order to maximize the solid angle. At the same time, one had to ensure there was enough space and time to laser-excite Ps while not harmfully impacting the antiproton plasma. Additional harmful impacts aside from electric and magnetic stray fields could be laser desorption of gases from close walls or an unwanted introduction of heat.

Advancing from here, one could think of placing the positron/Ps target of AEgIS directly inside the trap. In this case, one electrode would need to have two central holes in order to allow the laser beams to enter and leave the trap again. Doing so with existing and well-explored targets would of course require to use them in reflection geometry. This means, the converter target has to be installed behind the electrodes keeping the antiproton plasma, positrons have to move through this cloud and the view towards an imaging detector like a MCP further downstream would be shadowed by the target, not to mention the restriction of free flight path. Alternatively, a target working in transmission could be

installed upstream before the electrodes keeping the antiprotons, allowing Ps emission into the same direction as the arriving positron bunch. However, transmission targets have only scarcely been explored, and the few examples that showed promising results were extremely fragile and not simple to produce [140, 141, 142]. In these references, the transmission positron/Ps targets were made by means of GLancing Angle Deposition (GLAD), where vaporized SiO_2 was deposited as columns on a suspended thin carbon foil. The 20 nm thin carbon foil acted as basic support for the silica pillars and as stopper/reflector for formed Ps moving in the wrong direction, while the columns themselves created Ps when positrons penetrated at relatively low implantation energies and diffused back to the surfaces of the columns. Subsequent inelastic collisions with the silica structure cooled down emitted Ps similar to the reflection targets described before.

In the next paragraphs, a new type of positron/Ps converter target will be presented, which is based on the production scheme of the nanochanneled reflection targets from Mariazzi et al., but has been further developed to work in transmission geometry. The basic principle of electrochemical HF etching will be explained and the new targets will be introduced. The results of a first investigation using the CDB spectrometer in Munich will be presented with the goal to demonstrate the ability to produce Ps in transmission.

4.2.1 HF etching technique

The production of porous silicon is a well-explored field for more than 40 years now. That said, the exact processes involved in the electrochemical etching with aqueous hydrofluoric acid are still under investigation. Detailed works describing the most important principles and properties are given in Refs. [143, 144, 145]. Therein, also the setup for electrochemical etching as used by Mariazzi et al. and also by the author of this work is explored. A sketch of the used device is given in Fig. 4.2. Since Teflon, platinum and rubber are very resistant against the dissolving powers of hydrofluoric acid, the main vessel, the meshed electrode on top and the o-ring are made of these materials, respectively.

The silicon, typically a 15×15 mm square piece cut from a standard wafer, is used as second electrode and connected from the backside, while the polished topside is in direct contact with the acid. Like this, a rather homogeneous electric field is generated between the silicon and the platinum electrode, while the interface between the aqueous acid (i.e an electrolyte) and the semiconductor is often modeled as a Schottky contact. Although this leads to some inconsistencies, for example there is no difference in the apparent chemical reactions when using n- or p-type silicon, it reproduces the typical current-density/voltage characteristic of such a contact. In Fig. 4.3 on the left (a), the Schottky-characteristic for p-type silicon doped with an electron acceptor is shown, where the charge carriers are

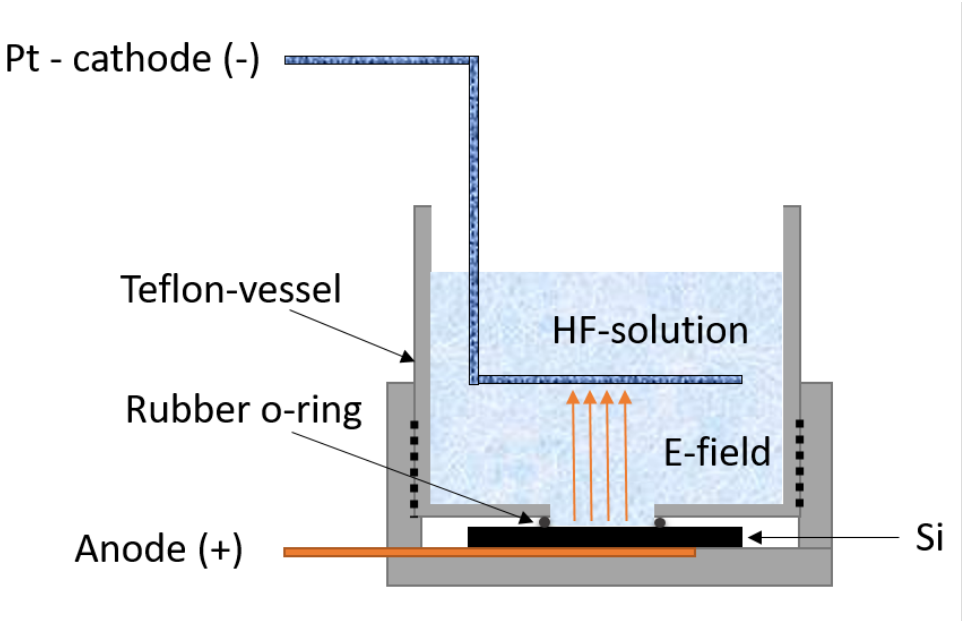

Figure 4.2: Sketch of a typical device suited for the production of porous silicon by means of electrochemical HF etching. The vessel is made of Teflon, the o-ring of rubber and the electrode of platinum, materials which withstand dissolution through hydrofluoric acid.

positively charged holes. Here, typical dopants are boron or gallium (B,Ga). On the right (b), n-type silicon doped with an electron donator such as phosphorus or arsenic (P,As) is described, where electrons are the charge carriers. Both types of silicon can be set on negative (cathodic) or positive (anodic) potential, in the presence of light or in the absence of it (dashed and solid lines, respectively, in the figure). This leads to eight different cases, of which half do not show etching at all — namely the cathodic ones where only water is reduced to gaseous hydrogen, which quickly disappears from the reaction interface. This leaves only the anodic configuration, where one finds three distinct regions colored blue, orange and red in Fig. 4.3 for p-type silicon with or without light, and for n-type silicon only in the presence of light. These three regions mark different porous morphologies due to different dominating effects during the dissolution of silicon.

Only in the first (blue) region, the desired pore formation occurs. If current densities are increased, one enters into a transition region (orange) in which electropolishing starts to occur as a competitive process to pore formation. This can be imagined as pores getting so macroscopic that less and less silicon remains between the single pores, until one finally enters into the red region, where electropolishing dominates. No porous structures survive here. If n-type silicon is kept in utter darkness, however, one has to increase the voltage a lot in order to reach the breakdown point of the Schottky-junction. From this point, the current is abruptly increasing and with this the dissolution of silicon, again first via pore

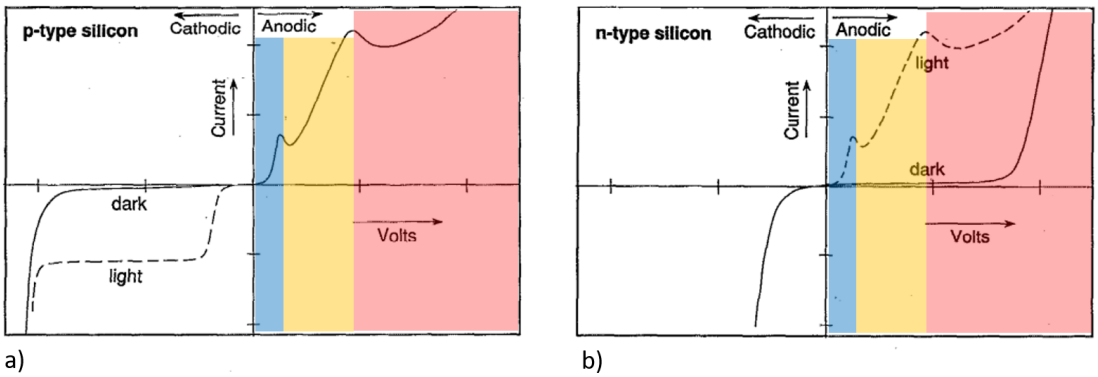

Figure 4.3: Electric characteristic for a) p-type silicon and b) n-type silicon, in the presence of light (dashed line) and in darkness (solid line). Due to the direct contact with hydrofluoric acid, the characteristic is typical for a Schottky-junction. (Images from Ref. [143]).

formation, then quickly also via electropolishing. Here, it is rather difficult to balance both effects due to the steep slope after breakdown. There are three models that aim to describe and explain why pore formation occurs in the first place, and not only planar dissolution as it happens during electropolishing. These are the diffusion-limited model, the Beale model, and the quantum-limited model. All three suggest ways by which the remaining silicon structures become passivated so that they do not work as Schottky-junction anymore, despite being in direct contact with the acid.

Diffusion-limited model

By applying standard diffusion laws, a depletion of charge carriers occurs in the porous layer over time, because the charge carriers have to diffuse through the bulk of silicon with the limited agility defined by the diffusion parameters. If the charge carrier 'consumption' at the Schottky-interface is faster than the provision from the bulk, the most likely attack point for the dissolution is just the pore tips. As a consequence, with the concentration of hydrofluoric acid and the set current one directly influences this charge carrier diffusion and therefore the resulting porous morphologies [146].

Beale model

The Beale model relies on several assumptions that are not required by the diffusion-limited model. It uses electrostatic and dielectric laws to describe the movement of charge carriers, assuming that the Fermi-level at the junction is pinned at the midband gap and

builds up an energy barrier for charge carriers (space-charge zone) [147]. This barrier can be overcome if a supporting potential is applied, but this potential comes with electric field lines overall the electrodes surface, which tend to concentrate at defects such as the pore tips. Hence, charge carriers rather approach those, while the remaining porous silicon structure is being depleted of charge carriers. This depletion can be further enhanced if the space charge zones of two opposing interfaces, e.g. at heavily thinned-out walls, overlap. If completely depleted, no chemical reactions and dissolution can occur at corresponding local interfaces.

Quantum model

Adding to both of the other two models, the quantum model introduces quantum confinement effects for extremely thin silicon walls between two pores, of the order of few nanometers. In this case, thermalized charge carriers from the bulk do not possess the required energy to enter these thin silicon structures. This effect can occur in parallel to the diffusion limit or the Beale model.

Global anodic chemical reaction

The dissolution of Si can occur, since charge carriers are available at the interface towards the acid which enable the transition from electric current to chemical transport of charged ions. For simplicity, only the most basic chemical reactions are given here, but in fact there are several intermediate steps and alternative reactions that have been reason for vivid discussions. During pore formation, the global reaction can be written as in Eq. 4.3. In the regime of electropolishing, it is Eq. 4.4. In both reactions, the only gaseous reaction product is molecular hydrogen, either direct formation or from dissociated H_2SiF_6, whose hydrogen radicals will quickly bind to each other. During the etching, one clearly can observe hydrogen bubbles emerging from the silicon surface when the current is switched on.

$$\text{Pore-formation:} \quad \mathrm{Si} + 6\mathrm{HF} \rightarrow \mathrm{H_2SiF_6} + \mathrm{H_2} + 2\mathrm{H^+} + 2\mathrm{e^-} \tag{4.3}$$

$$\text{Electro-polishing:} \quad \mathrm{Si} + 6\mathrm{HF} \rightarrow \mathrm{H_2SiF_6} + 4\mathrm{H^+} + 4\mathrm{e^-} \tag{4.4}$$

Having introduced the principles of electrochemical etching with aqueous HF, this paragraph will conclude with a short table of several etching parameters and their impact on the pore formation, partially taken from the mentioned references, but also concluded from own observations (Tab. 4.1). The so-called *porosity* defines the amount of open space

(pores) inside a reference volume of the bulk. A high porosity therefore corresponds to a lot of open space or to a low average density.

	Porosity	Pore-size	Etching rate	Thickness of porous layer
Fewer p-type dopants	⇑	⇓	↓	↓
Fewer n-type dopants	⇓	⇑	↓	↓
Longer etching time	→	→	→	⇑
Higher current-density	⇑	⇑	↑	↑
Lower HF-concentration	↑	↑	↓	↓

Table 4.1: Contribution of different etching parameters to pore formation in silicon, if all the other parameters are kept constant. Horizontal arrows mean that no effect was observed, a double arrow means that a parameter has great influence.

As final remark, one should note that despite there are three main crystal orientations of silicon wafers, namely ⟨100⟩, ⟨110⟩ and ⟨111⟩, the electrochemical etching predominately occurs along the ⟨100⟩ = (100) + (010) + (001) orientations, since these have the most favored steric geometry for breaking apart the divalent bonds that protrude far into the acid. If the wafer is of a different orientation than Si(100), the main pore formation is not propagating perpendicular to the surface, but under an angle: in the case of Si(111), this angle is 54.7°, for Si(110) it is 45° [143, 148].

4.2.2 Structured membranes

It is possible to commercially obtain silicon wafers with thicknesses down to 2 µm, a single one with 10 mm diameter costing about 350 €. These thin and highly fragile membranes can, in principle, be inserted into a similar etching device as introduced in the previous paragraph and nanoporous structures might be producible. However, depletion of charge carriers could occur earlier since the membrane is so thin that no major supply from the bulk below exists, and together with the extreme difficulty of handling such fragile wafers it seems not worth trying. In fact, following this approach one would rather decide on the method of glancing angle deposition of silica on a thin graphene layer which is more robust at such dimensions.

Changing paradigm, a new method for creating nanostructured membranes was adopted. First, a porous layer was produced using a standard silicon wafer with few hundred µm thickness as was introduced before (Section 4.1). After the desired etching time, the

current was increased by at least one order of magnitude for several seconds, before the current was completely switched off. This jump in current dramatically increased the pore size and porosity - but *only* in the region of pore tips, since the depleted structure above was not anymore affected by the electrochemical dissolution. At the pore tips, however, the regime of electropolishing was entered. A macro pore of the same size as the whole Schottky-junction (diameter about 10 mm) was forming below the nanostructured layer. An audible click occurred and a reflective, dome shaped membrane was *detaching* from the bulk, bending outwards. This might be due to a slightly higher porosity at the surface, since the initial pore formation is a purely stochastic process: several pores do not propagate any further after few nm because charge carriers got snatched away by neighboring pores. Tension is building up within the layer, which is finally released by the membrane bulging outwards after complete detachment from the center. The process steps of the production and detachment are shown in Fig. 4.4.

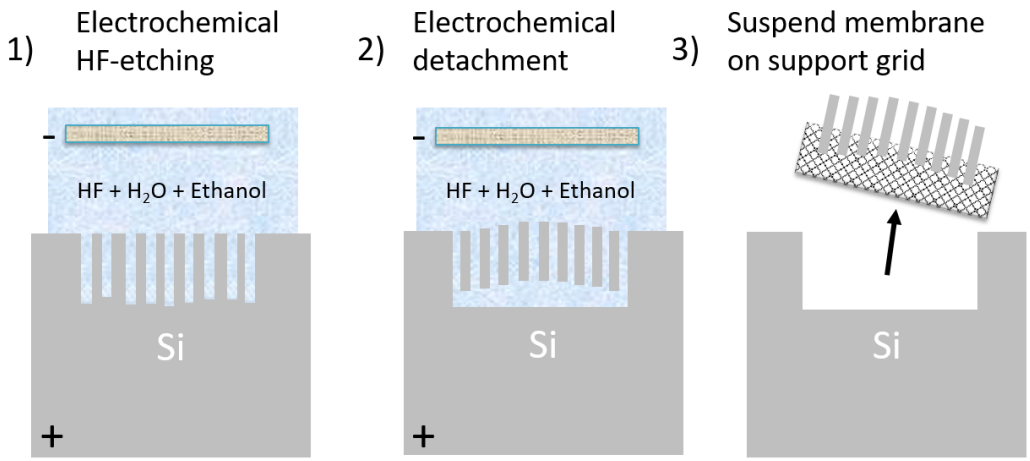

Figure 4.4: Anodic etching with aqueous HF solution: Step 1: few tens of mA for several hundreds of seconds. Step 2: several hundreds of mA for few seconds. Step 3: Lift out the membrane with a grid.

Immediately after detaching, the platinum electrode was removed and the HF solution disposed into a designated container. The wafer with the dome-shaped, at the borders still attached membrane was flushed with ethanol. The membrane then was fully coming off and started to float. It was lifted out with an aluminum grid and slowly dried at room temperature, before being put onto a heat plate set to 110 °C for few hours. A forth step can be added, in which a thin layer of photoresist (PMMA, layer $\approx$ 200 nm) is being spin-coated on the surface, building up a blockage for produced Ps moving into the wrong direction, i.e. not in transmission.

Specimen suited for Ps measurements in the CDB spectrometer

All produced membranes that could be measured with the CDB spectrometer are summarized in Tab. 4.2. Parameters and properties that are common for all specimen are listed in the following:

- Active circular area of the silicon acid interface: 78 mm^2 (10 mm diameter)
- Wafer material: p-type Si(100), highly doped with boron, low resistivity $0.01-0.02\,\Omega\,\mathrm{cm}$
- Concentration of hydrofluoric acid diluted with deionized water: 16 %
- Detachment: 390 mA for about 7 s
- Membrane suspended on a meshed grid ('1') or on an aluminum ring with 3 mm hole in the center ('0')
- Surface spin-coated with a $\approx$ 200 nm layer of photoresist (PMMA) ('1') or not treated ('0')
- Baking at 110 °C for two hours ('1') or no treatment ('0')

Images of not yet detached samples taken by means of scanning electron microscopy (SEM) allowed to estimate the etching rates and the expected thicknesses of resulting nanoporous layers after detachment. Fig. 4.5 shows the result for three different etching currents: 39 mA, 50 mA and 90 mA. The etching rate increased with higher current, which led to thicker porous layers with constant etching times. One can also visually appreciate the increase of pore size and porosity with increasing current in the other two figure series Fig. 4.6 and Fig. 4.7.

An etching current of 39 mA produced channels with 10 nm in diameter, which is very similar to the result described in Ref. [138]. However when using this current, the thinnest membrane that could be achieved was about 19 µm. Below this limit, the membrane was always rupturing during detachment. With increasing current the channel diameter increased, but also several dendrites branched off from the main channel. This indicates that passivization of the channel walls was not fully occurring. A reason could be the usage of low resistivity silicon, providing more charge carriers than for example the wafer used in the reference. Therein, silicon with fewer dopants and ten times higher resistivity of $0.15-0.20\,\Omega\,\mathrm{cm}$ was used. From the ratio of holes, i.e the black spots on the SEM surface image, to the total surface area, an upper limit for the density of the porous layer can be estimated. A density of $1.9\,\mathrm{g\,cm^{-3}}$, corresponding to roughly 20 % of open area, was found by Mariazzi et al. in Ref. [138]. From the SEM images obtained for the porous targets of

	Current (mA)	Etching time (s)	Baked?	PMMA?	Grid?	Est. thickness (um)
A0	90	570	1	1	1	27
A2	50	600	0	1	0	24
A3	39	600	1	1	1	19
A4	39	600	0	1	0	19
A5	39	600	0	0	1	19
A7	90	300	1	1	1	14
A8	90	300	0	1	0	14
A9	90	300	0	0	1	14
A12	39	600	0	1	0	19
A13	39	600	0	0	1	19
B1	50	340	1	1	1	14
B5	39	600	1	1	1	19
B7	39	510	1	1	1	16
B13	90	240	1	1	1	11
C3	10	1800	1	0	1	10

Table 4.2: Overview about all produced nanoporous membranes. The last one, C3, was attempted with a different wafer material, Si(111), as will be detailed in the text.

the present work, densities of $1.9\,\mathrm{g\,cm^{-3}}$, $1.8\,\mathrm{g\,cm^{-3}}$ and $1.5\,\mathrm{g\,cm^{-3}}$ were found for 39 mA, 50 mA and 90 mA, respectively. Due to the increasing amount of dendrites with higher current, indeed a higher porosity with reduced mean density has to be expected. Since all these targets are based on Si(100), the channel propagation direction is perpendicular to the surface as mentioned above, and it is reasonable to assume a single channel extending beyond every hole at the surface.

When choosing the same material as was used for the AEgIS targets, i.e. p-Si(111), high resistivity between $0.1 - 1.5\,\Omega\,\mathrm{cm}$ and an etching current of 10 mA, the thinnest membrane that had been successfully detached was 10 µm (specimen C3). The open area at the surface makes up again about 20 %. This time, however, each hole should be rather associated with three channels along the directions (100), (010) and (001), respectively, because for Si(111) channels are drilled under an angle of about 55° against the surface normal. As a consequence, for this wafer orientation an upper limit for the density of $1\,\mathrm{g\,cm^{-3}}$ is expected, corresponding to an open volume of about 60 %.

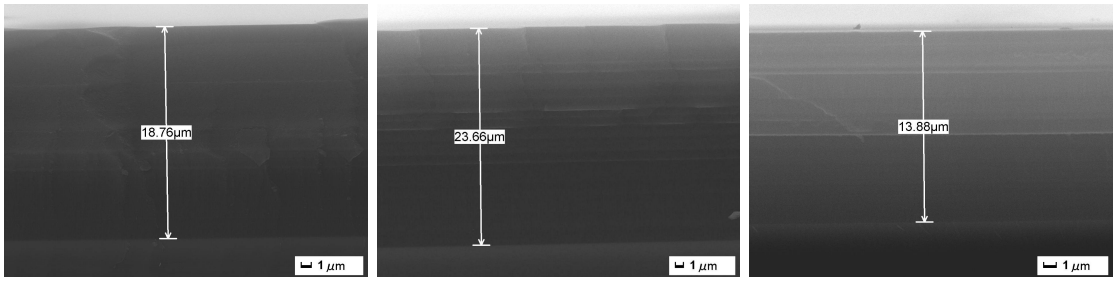

Figure 4.5: Thickness of nanoporous layer for different etching currents and times. Left: 39 mA for 10 min, middle: 50 mA for 10 min, right: 90 mA for 5 min.

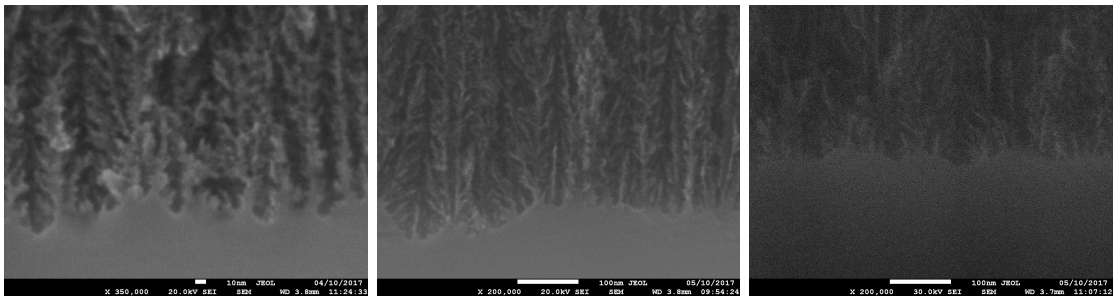

Figure 4.6: Nanochannels due to different etching currents. Left: 39 mA, middle: 50 mA, right: 90 mA.

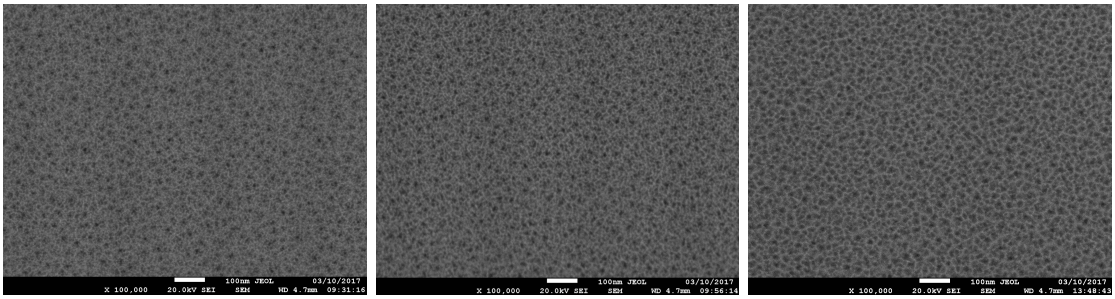

Figure 4.7: Surface morphology with different etching currents. Left: 39 mA, middle: 50 mA, right: 90 mA.

4.3 Measurements on porous silicon membranes with positrons

The specimen of Tab. 4.2 were inserted one after another into the CDB spectrometer of NEPOMUC. Positrons were implanted at energies ranging between 0.1 keV and 30 keV, while each spectrum was acquired for 300 s. At first, targets were measured upside down in *reflection* geometry, which allowed to estimate the depth from which Ps can be emitted into vacuum. Then, the samples were installed in *transmission* geometry, so that positrons were implanted from the side covered with photoresist. For several targets in transmission geometry, a third scan with an aluminum blockage approximately 1 mm below the target was performed, so that a major fraction of emitted Ps could not annihilate into 3γ photons during free flight, but rather hit the aluminum obstacle and produce 2γ due to pick-off annihilation.

For analysis, the technique developed in Section 2.5.7 was applied in order to count the number of 3γ and 2γ annihilation events occurring after positron implantation. From this, the fraction of positronium f_{Ps} was estimated. It is also important to account for big variations in the number of implanted positrons, because such jumps can affect the fraction of detected Ps. Generally, the newly developed method acknowledges this by building the ratio of 3γ's to the weighted sum of two and three gamma quanta, hence spectra are 'self-normalizing' to the total amount of implanted positrons. However, a higher positron rate causes a more prominent pile-up background, which adds to the counts of the pure 3γ spectrum and can lead during analysis to a systematic overestimation of the real Ps signal. This will be evident in some f_{Ps} signals as nonphysical steps and bumps.

Results for Si(100) targets with 39 mA etching current

Two targets produced with 39 mA etching current were first measured in reflection geometry in order to get an idea of the possible Ps yield. The result is shown in Fig. 4.8. It

immediately strikes the eye that the signal is generally very small, aside from the typical increased Ps emission from the surface for lowest implantation energies. This surface fraction is probably even higher, since no time-of-flight correction was applied here. What we see is therefore a lower limit, but in any case the mean velocity of the surface positronium is too high to be useful, because almost no cooling in the nanochannels occurred.

For higher positron implantation energies, the small amount of detected Ps not necessarily means low production efficiency, but rather that most of the Ps atoms generated inside the porous structure annihilated via pick-off. Either the movement of Ps in the channels themselves was heavily restricted, or the region close to the surface was reflective for Ps. Target A4 was never baked and shows a low Ps signal over a large range of energies. The baked target B7 just dips down at 2 keV, while for greater energies the Ps signal saturates at a maximum value of 6 %. Statistical errorbars on the data points are smaller than the symbols. It appears that before baking the channels were clogged with remnants of the acid/water/ethanol solution, which then were partly removed at elevated temperatures. However, the dip close to the surface is still very evident and indicates a strong restriction to Ps emission even after baking. This can either be a purely geometrical consequence (effect of a bottleneck) or due to persisting contaminants. It follows that the observed Ps fraction was mainly originating from 3γ annihilation inside the target.

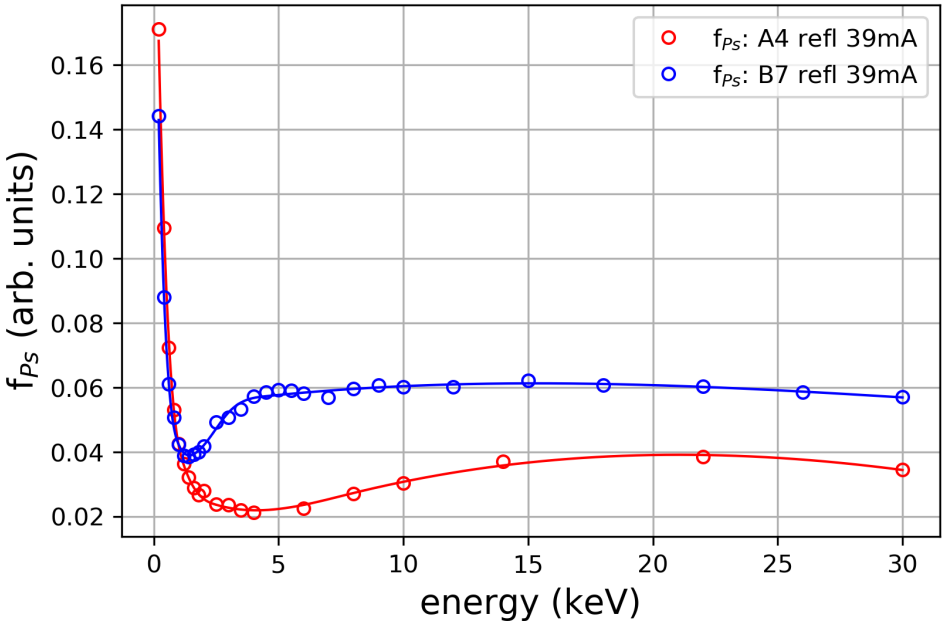

Figure 4.8: Ps fraction f_{Ps} in reflection geometry for targets with etching current 39 mA. Target A4 has never been baked and shows a reduced Ps production compared to target B7, which was treated thermally. Solid lines are guides to the eye.

In order to quantify the amount of Ps that actually was annihilating inside the target, the baked samples A3, B5 and B7 have been installed in transmission geometry with and without the aluminum blockage. If f_{Ps} was only due to internal annihilations, no difference between the two modes is expected. Fig. 4.9 shows the outcome. Energy scans without aluminum stopper below the target are colored in red or green in both the left and the right panel, while results with the stopper are presented in blue. In all cases, there is a sharp dip down to zero at about 2.5 keV, corresponding to positron implantation into the middle of the photoresist layer. For greater energies, the Ps signal increases again due to positrons entering the porous silicon. But more important is that indeed no significant difference between the blocked and the free targets emerges with the exception of a few data points that show an increase for the free target. However, these excesses can be attributed to artifacts originating from some fluctuations in the positron number of up to 30 % relative to the basic level of 28 000 counts per second during the measurement.

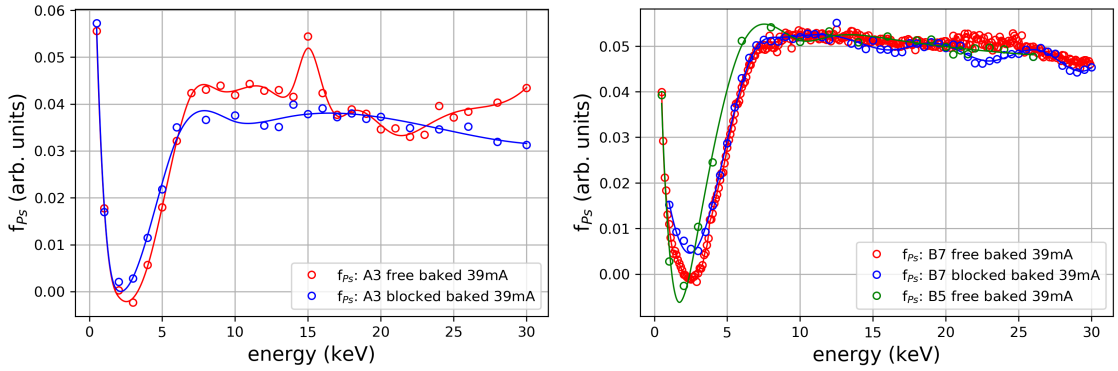

Figure 4.9: Ps fraction f_{Ps} in transmission geometry for targets with etching current 39 mA and with an estimated thickness of $16 - 19\,\mu$m. Blue curves represent blocked targets, for the red/green curves Ps could freely move behind the target. Except for some artifacts in the left panel, there is no evidence for Ps transmission.

In principle, there could have also been positrons shooting through the membrane, which might then have been slowed down due to the negative potential of the target holder, have been repelled and accelerated backwards until they were reimplanted into the target. This could have caused some Ps formation. But also in the blocked case, some crossing positrons might have been backreflected from the aluminum surface and have been reimplanted into the membrane. Whether these 'parasitic' Ps formation channels due to crossing and reimplanted positrons is a possible scenario was modeled with a Makhovian positron implantation profile for compound systems. At first, the fraction of positrons stopping in the 200 nm layer of photoresist with parameters for PMMA from Ref. [87] was calculated. Then, the fraction of remaining positrons that is stopping in the following layer,

i.e. the porous silicon with a density of $1.9\,\mathrm{g\,cm^{-3}}$ and a thickness of 19 µm taken from the SEM images, was estimated. The result is shown in Fig. 4.10. It becomes immediately clear that no positron can cross the entire membrane, if the density is assumed to be homogeneous. This is also experimentally confirmed, since no clear Ps signal reduction occurred at high positron implantation energies during the reflection measurements.

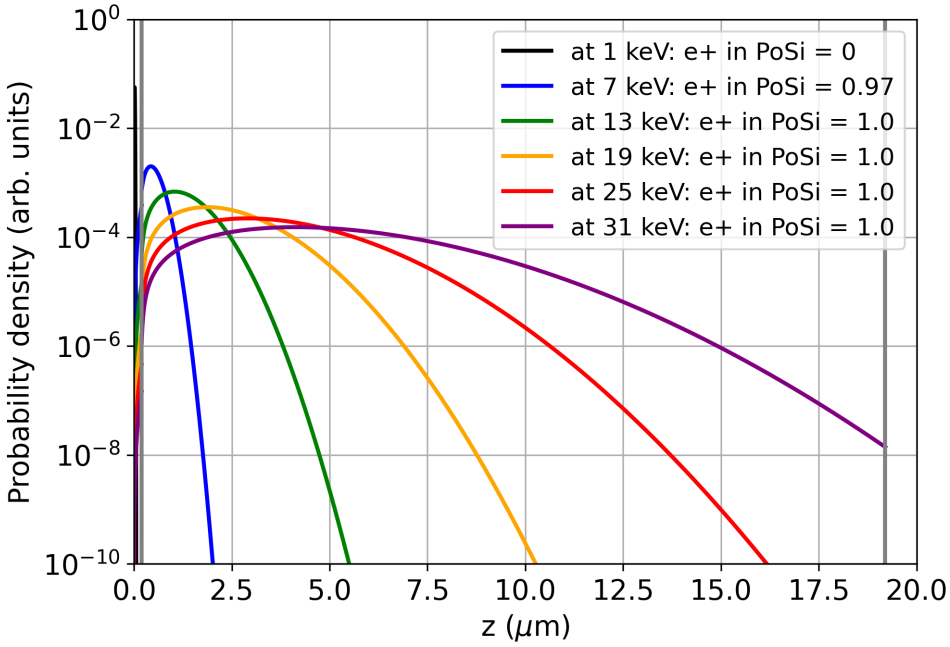

Figure 4.10: Makhovian positron implantation profiles for a compound system consisting of 200 nm photoresist on top and of a 19 µm thin layer of porous silicon with a homogeneous density of $1.9\,\mathrm{g\,cm^{-3}}$. Until 31 keV implantation energy, positrons cannot pass through the compound system.

In summary, the membranes etched with 39 mA are not able to emit Ps in transmission. This is due to the rather high density and thickness of the membrane, causing all produced Ps atoms to annihilate internally. Consequently, a constant Ps signal of about 5 % is observed. It is clear that the membrane has to become a lot thinner than 19 µm, before Ps emission in transmission can occur in the range of positron implantation energies that is feasible with the CDB spectrometer.

Results for targets with 50 mA etching current

In the same manner as before, also the targets etched with 50 mA, which resulted in a lower mean density of $1.8\,\mathrm{g\,cm^{-3}}$, were measured both in reflection and transmission geometry over the full range of possible positron implantation energies. The result for reflection

geometry is shown in Fig. 4.11. Target A2 was never baked, just like target A4, and indeed shows the same reduced Ps signal. The baking procedure increased this signal to about 6 % with the usual exception of high Ps yield at the surface. One should note that also here the Ps signal at high implantation energies is very constant, already indicating a negligible fraction of crossing positrons.

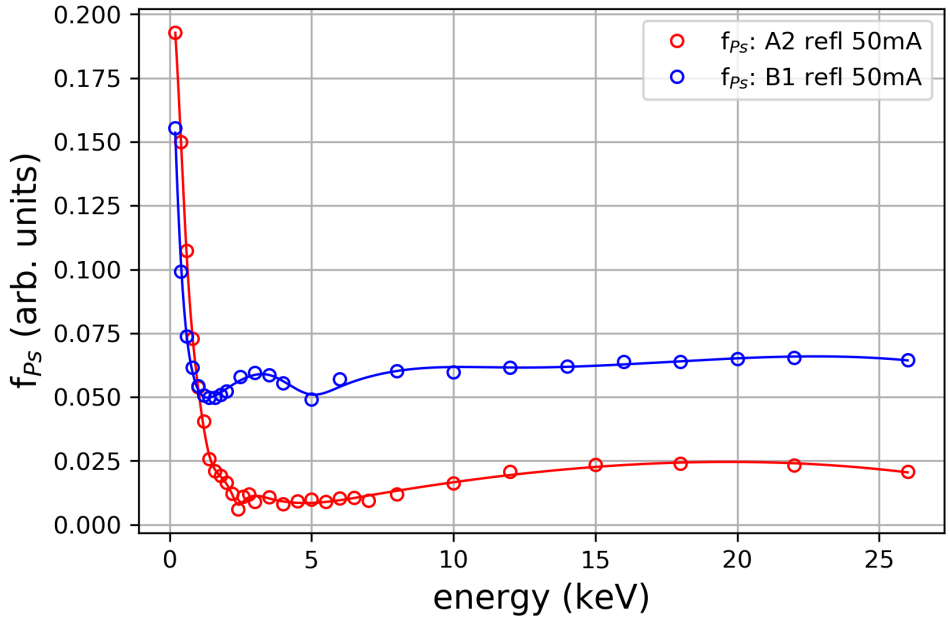

Figure 4.11: Ps fraction f_{Ps} for targets with etching current of 50 mA and with an estimated thickness of 14 µm. Reflection geometry for unbaked target A2 (red) and baked target B1 (blue).

The spectra recorded in transmission geometry display a new feature that can be seen in Fig. 4.12. Here, at energies greater than 10 keV the fraction of detected Ps is gradually decreasing. Also different from the 39 mA targets, the maximum Ps amount seems a bit higher, which could simply come from the increased porosity and the bigger pores. As a consequence, Ps would survive slightly longer and the internal annihilation signal would go up. However, again there is no clear difference between the blocked and the free membrane, allowing to conclude that over the full scanned energy range no Ps emission in transmission occurs, with maybe the exception of highest implantation energies. Here, a systematic difference starts to build up that should be further investigated.

Calculating the Makhovian positron stopping profile for targets etched with 50 mA, again only a negligible fraction (< 0.2 %) of positrons is able to cross without stopping even at highest energies, which is confirmed by the measurement in reflection geometry. Despite this, the Ps signal decreases both for the free and the blocked target. One reason might be

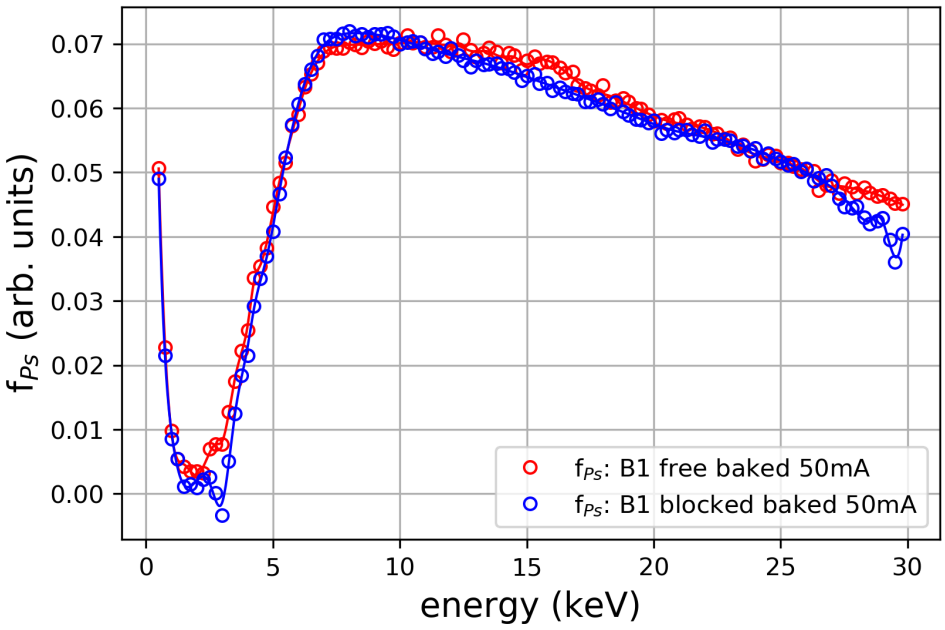

Figure 4.12: Ps fraction f_{Ps} for targets with 50 mA etching current and estimated thickness of 14 µm. Transmission geometry for baked target B1, once with aluminum blockage (blue) and once without (red).

Ps escaping into vacuum. Then, however, one should find a clear difference between the free and the blocked sample, where the latter should display an almost constant Ps signal as was the case with the 39 mA targets. Another possible candidate for the progressing signal reduction could be macro vacancies, which were accidentally formed during spin coating a layer of photoresist on top of the porous membrane. When positrons are implanted into the porous silicon and Ps ia produced, a fraction should be able to return to the interface between the photoresist and the porous structure, where the macro vacancies are located. Ps inside the open volume of a vacancy has then an increased lifetime and a greater chance to annihilate into 3γ quanta. With higher implantation energies, less Ps atoms can reach the interface and therefore the f_{Ps} signal should approach the minimum level that has been measured in reflection geometry.

From 27 keV onward, the detected Ps fractions for the free and the blocked target start to diverge. Since no direct positron transmission is expected, the signal difference can best be explained with Ps escaping from the transmission side of the free target and annihilating at a greater distance from the detector into 3γ quanta, while for the blocked target escaping Ps is hitting directly onto the aluminum and has a high probability to annihilate via pick-off into 2γ quanta. For the 14 µm membrane, one therefore finds the first indication that Ps was emitted in transmission.

Nonetheless, Makhovian positron implantation in silicon with reduced homogeneous density does not seem a reliable assumption for nanochannel converters, especially since the crystal orientation Si(100) was aligned with the trajectories of incident positrons, possibly providing open passages. As a consequence, one cannot completely exclude that some positrons entering into a channel with high energy could propagate straight through it and leave on the other side with still some kinetic energy. In this case, one would expect either positron implantation into the aluminum blocker, where no Ps is formed in the bulk, or reimplantation into the membrane or into nearby materials due to the negative potential of the whole target holder. Unfortunately, it is not trivial to exclude this 'parasitic' Ps formation, unless the channel orientation with respect to the positron trajectories would be modified.

Results for targets with 90 mA etching current

Also the series produced with 90 mA etching current, which led to a mean density of $1.5\,\mathrm{g\,cm^{-3}}$, was investigated. This time, only baked targets were tested with the CDB spectrometer. In Fig. 4.13, three scans in reflection geometry are shown. There is the typical big fraction of surface Ps, the dip down in the transition area between surface layer and the porous bulk at 2 keV, and a plateau at about 10 % Ps formation which decreases for higher energies. This enhanced Ps signal can be attributed to the increased porosity and pore size. The fading plateau of detected Ps could either come from positrons shooting through the target, which then could not properly [1] contribute to the 3γ spectrum anymore, or from Ps atoms produced so deep inside the converter that they annihilated via pick-off before reaching the (partially) open end of the nanochannels.

The spectra recorded in transmission geometry (Fig. 4.14) display a broad plateau for intermediate energies. The single bump on the free target B13 at 10 keV was a tremendous jump in the positron rate of the system and can safely be ignored. For greater energies, though, the Ps signal decreases gradually. Again, this can be attributed to macro vacancies at the interface between the layer of photoresist and the porous silicon, which provided a higher probability for Ps to annihilate into 3γ quanta for a range of moderate positron implantation depths. In case of the free target, the reduction occurs at a lower pace, which means there is an additional channel for 3γ annihilations just as considered for the former 50 mA series.

Evaluating the Makhovian implantation profile with the reduced homogeneous density and layer thickness for this porous silicon, an increasing fraction of positrons is able to shoot

[1] *Properly* in the sense that crossing positrons end up in an undefined state that might include Ps formation, but that also can lead to 2γ annihilation radiation which reduces the Ps signal

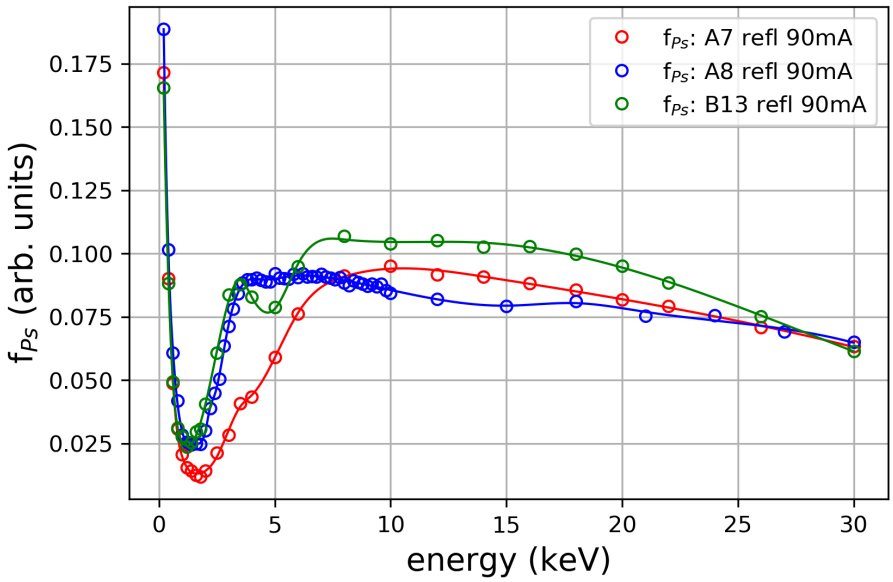

Figure 4.13: Ps fraction f_{Ps} in reflection geometry for targets with 90 mA etching current.

through the membrane starting from 22 keV, with up to 6 % of all implanted positrons at 30 keV. It is very unlikely, though, that the entirety of these crossing positrons was returning to the membrane and got reimplanted only at the surface, which is the only mechanism that could possibly account for the 1 % difference in the Ps signals at high energies. Moreover, a fraction of positrons hitting onto the aluminum could also be backreflected and cause some secondary Ps formation, which would partially counteract the other 'parasitic' Ps production channel on the free target. It can therefore be concluded that these thin membranes etched with 90 mA were able to emit up to 1 % Ps into vacuum from the transmission side. Vice versa, the decrease of f_{Ps} of about 2–4 %, which one could observe for the measurement in reflection geometry between 10 and 30 keV, can therefore be partly explained with the ability of the targets to emit Ps from the open end of the nanochannels.

Results for targets with Si(111) and 10 mA etching current

Many targets presented so far suffered from an ambiguity whether the occurring Ps signal in a certain range of energies happened due to real emission in transmission or simply because crossing positrons were reimplanted from the backside. Using another wafer material, Si(111) with high resistivity ($0.1 - 1.5\,\Omega\,\mathrm{cm}$), adapting the etching parameters so that channels with about 10 nm in diameter were created and using a grounded target plus target holder, this ambiguity could be overcome. Now, it could be excluded that too many positrons accidentally pass through the open space built by the nanochannels without interaction, because the channel drilling occurred under an angle of 55° with respect to

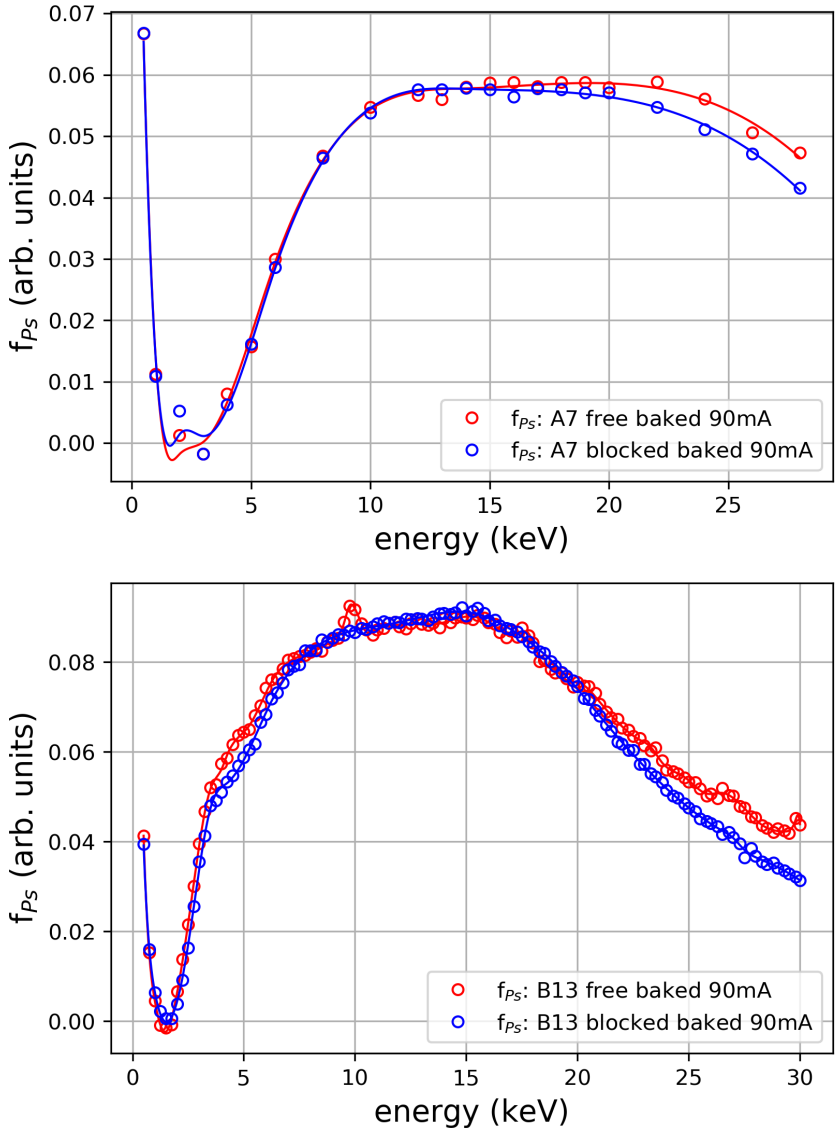

Figure 4.14: Ps fraction f_{Ps} in transmission geometry for targets with 90 mA etching current. Estimated thickness: 14 µm (A7, top), 11 µm (B13, bottom).

the surface normal. Additionally by grounding the target holder, any fraction of crossing positrons was not guided back to the target, hence undesirable Ps contributions could entirely be avoided. Moreover, for the presented target C3 no PMMA was spin-coated on the surface, so that Ps also could escape from the reflection side. Scanned energies ranged from 1.5 keV to 27 keV and again f_{Ps} was estimated using the $3\gamma/2\gamma$ ratio. The result is shown in Fig. 4.15 as blue squares, while the solid line is the outcome of a Ps emission model that will be detailed in the following paragraph.

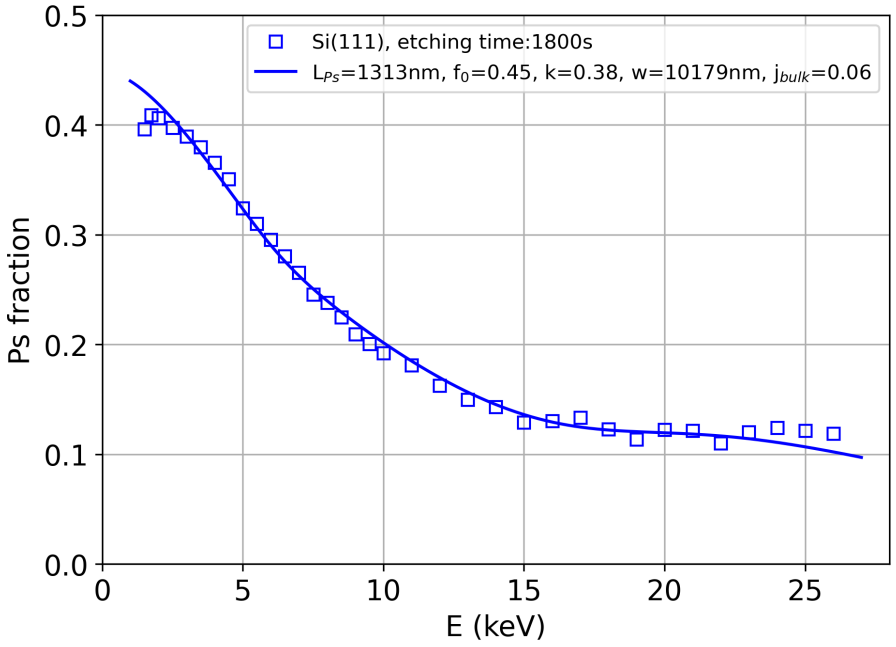

Figure 4.15: Ps fraction f_{Ps} for target C3, wafer material Si(111), etching current 10 mA and etching time 1800 s. Estimated thickness from SEM image: 10−11 µm.

The first striking difference to the other targets is the missing dip at low implantation energy. This comes from the omitted photoresist layer, so Ps can always leave the nanochannels in reflection geometry even if positrons are implanted a little deeper. Close to the surface, the model expects even more Ps than was measured, but this can be easily explained by an increasing fraction of fast Ps moving away from the detector without proper cooling and possibly also by an altered morphology for the surface layers, which is typical for electrochemical HF etching. Then, the overall production efficiency went up, reaching 40 % at zero implantation energy, which is consistent with other measurements performed on similar targets with the same wafer material and etching parameters as in Ref. [138]. The total thickness of the porous layer was estimated via SEM, being ≈ 10 µm after 1800 s of etching. It is expected that the detached membrane has the same or a slightly smaller thickness, but this could not directly be verified via SEM imaging. Furthermore, the Ps

fraction is still above 10 % for highest energies, which can be due to 3γ annihilations inside the membrane or due to Ps being emitted in transmission geometry, but not anymore due a considerable amount of Ps escaping from the reflection side.

In the next paragraph, a Ps emission model is presented whose free parameters were fitted to this measurement result. The three completely free fit parameters were the Ps diffusion length $L_{Ps} = (1313 \pm 150)\,\mathrm{nm}$, the maximum Ps yield $f_0 = 0.45 \pm 0.03$ and the internal annihilation parameter $j_{bulk} = 0.06 \pm 0.01$. The target thickness w was already restricted by the SEM pictures, hence only some margin around this measured thickness was allowed during fitting, namely $w = (10.5 \pm 0.5)\,\mu\mathrm{m}$. Also for the porosity a lower limit could be extracted from the measurements, giving $(1 - k) = (62 \pm 5)\,\%$. Altogether, with this set of parameters, one finds a fraction of 5 % Ps emission in transmission geometry at high implantation energies, which clearly surpasses all other samples so far. However, this result strongly depends on the applied model, which must be carefully investigated. Even so, it seems rather unlikely that the evident Ps signal at highest implantation energies solely originates from internal annihilations into three gamma quanta.

4.4 Modeling of bidirectional Ps emission

The modeling starts by combining the Makhovian implantation profile for positrons and subsequent diffusion as was introduced in Section 2.5.7. This resulted in the amount of positrons $J(E)$ that was able to diffuse back to the surface. This formalism is now adapted for the new case, in which positrons thermalize in porous silicon that has a reduced density denoted with $(1 - \text{porosity})\,\rho_{Si} = k\,\rho_{Si}$. Furthermore, now the target thickness w is not assumed to be infinite, but only several micrometers, which generally allows particle emission from the two surfaces at the same time. The most impacting change, however, is the substitution of the positron diffusion length L_+ with the Ps diffusion length L_{Ps}. This change is justified by the fact that stopped positrons will only diffuse for few nanometers before they actually are transformed into Ps (or annihilate). For porous targets, diffusion therefore predominately occurs for Ps and allows this substitution even for a model originally derived for positrons inside the bulk of a solid. In works of others, this method has already successfully been applied, see for example Refs. [92, 149, 150].

Since crossing positrons cannot return to the sample anymore due to its grounding, it is possible to integrate the distribution $p(z)$ of stopped positrons within definite integration boundaries. This yields the total percentage P of positrons stopped inside the membrane as is denoted in Eq. 4.5, with $z_0 = \frac{A_0}{k\rho_{Si}} E^n$. The corresponding Makhovian material

constants $A_0 = 28.01$, $m = 1.99$ and $n = 1.729$ were taken from Ref. [87], the density of silicon was set to $\rho_{Si} = 2.336\,\mathrm{g\,cm^{-3}}$.

$$P = \int_0^w p(z)\,dz = \int_0^w \frac{m}{{z_0}^m}\, z^{m-1} \exp\left[-\left(\frac{z}{z_0}\right)^m \right] dz, \tag{4.5}$$

Positrons stopped at depth z will either annihilate into 2γ quanta, or they will form Ps which is being emitted into the open space of the nanochannels. Let J_{Ps} be the positron/Ps conversion rate. Then, one can apply an exponential diffusion law which describes how much Ps can be found at $z + \Delta z$. With this, Eq. 4.5 can be utilized to describe how much Ps finally arrives at each of the two surfaces of the membrane. For the reflection side one gets:

$$j_r(z) = J_{Ps}\, p(z) \exp\left[-\frac{z}{L_{Ps}} \right] dz \tag{4.6}$$

and correspondingly for the transmission side:

$$j_t(z) = J_{Ps}\, p(z) \exp\left[-\frac{w - z}{L_{Ps}} \right] dz \tag{4.7}$$

Finally, a fraction J_0 of produced Ps may annihilate into 3γ quanta even inside the porous structure, which is modeled using a simple rectangular window function $R(z)$. Positrons that are converted into Ps as far away from one of the two surfaces as the Ps diffusion length L_{Ps} are assumed to annihilate with a constant probability j_{bulk} into 3γ quanta. Otherwise, Ps would either leave the target contributing to $j_r(z)$ or $j_t(z)$, or annihilate via pick-off into 2γ quanta which is subsumed in J_{Ps}.

$$R(z) = \begin{cases} j_{bulk} & \text{for } L_{Ps} < z \leq (w - L_{Ps}) \\ 0 & \text{else} \end{cases} \tag{4.8}$$

$$j_0(z) = J_{Ps}\, p(z)\, R(z)\, dz \tag{4.9}$$

The resulting model function describes the measured Ps fraction f_{Ps}. It is denoted in Eq. 4.10, where J_{Ps}, L_{Ps}, j_{bulk} enter as completely free parameters, while the possible values for k and w can be restricted. The range for w was limited by the result of the SEM thickness measurements. Consequently, only a small window around the measured values can be used during the fitting, for example $w = (10.5 \pm 0.5)\,\mu\mathrm{m}$. The density weight factor k could be constrained by the observation of positrons crossing the membrane at higher energies, i.e. from where the total sum of detected counts started to decrease. This was the case at 18 keV, which led to $k = 0.40 \pm 0.05$ when evaluating the Makhovian

implantation profile for porous silicon as was denoted in Eq. 4.5. This result also confirms the expectation of up to 60 % porosity in the case of etched Si(111), since here the channel drilling occurred along the three directions (100), (010) and (001) at the same time.

$$f_{Ps} = \int_0^w [\, j_r(z) + j_t(z) + j_0(z) \,]\, dz \;=\; J_r + J_t + J_0 \tag{4.10}$$

The fitted model describing best the measurement performed on target C3 is plotted as the solid line in Fig. 4.15. Using the obtained values for the fit parameters, one can extract individually the transmitted fraction J_t, the reflected fraction J_r and the internal 3γ annihilations J_0 as a function of the positron implantation energy E as shown in Fig. 4.16. The highest amount of Ps emitted in transmission is expected to be about 5 % at high implantation energies, while about 4 % of produced Ps atoms annihilate inside the porous structure into 3γ quanta. From the pure Makhovian positron implantation profile derived with these parameters follows that at 27 keV a fraction of roughly 30 % of all positrons simply pass through the membrane. With decreasing implantation energies, fewer positrons can directly pass through the target, which leads to an increase of the internal annihilations. But also the transmitted amount of Ps is going down while the fraction emitted in reflection is shooting up, dominating the Ps emission at energies of 15 keV and below.

4.5 Discussion and conclusion

A promising technique was developed for the production of inexpensive porous silicon membranes with thicknesses in the micrometer range with the ability to convert implanted positrons into positronium and emit Ps atoms in transmission. Electrochemical etching with aqueous hydrofluoric acid allowed the production of nanochannels with adjustable depth by altering the etching time. In particular, the porous layer could be detached from the remaining silicon wafer in a subsequent process step by increasing the etching current. Since nanoporous silicon targets in reflection geometry are well established to work as efficient positron/Ps converters with high yield of cold Ps in vacuum, a comparable performance in transmission can be expected by the newly developed membranes.

Before these new membranes can be used in an experiment such as AEgIS, the Ps yield in transmission should be maximized. This can be achieved with thinner membranes, ideally in the range of $1-2\,\mu$m, while a biased grid immediately after the target could stop crossing positrons, which then are reimplanted and partially also converted into Ps. A very thin coating (e.g. graphene) on top of the implantation side of the membrane could act

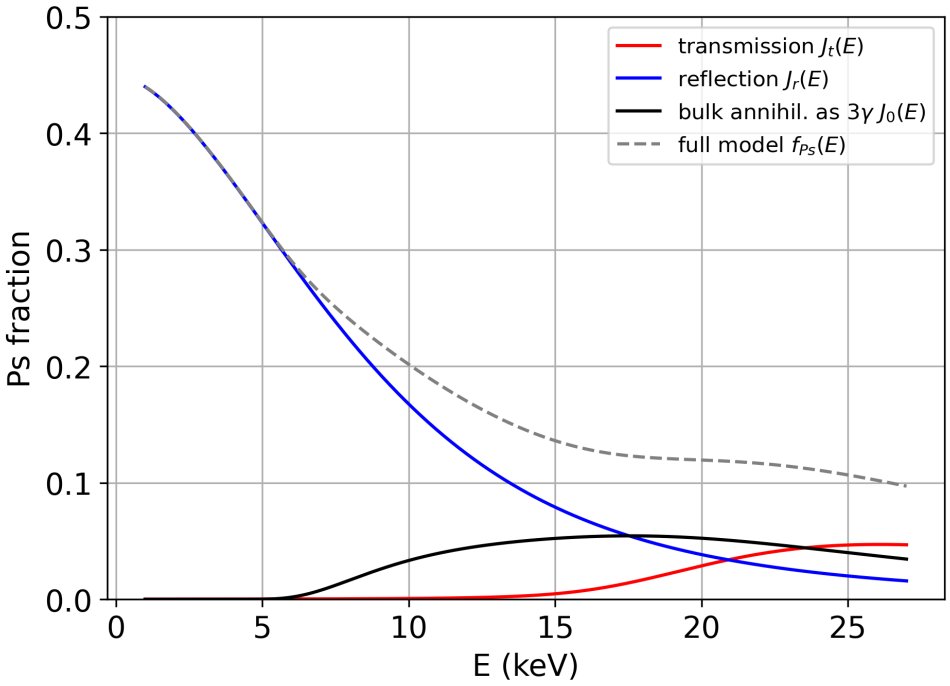

Figure 4.16: The Ps emission model as given in Eq. 4.10 was fitted to the measurement data of target C3. From this, the transmitted Ps fraction J_t (red), the reflected fraction J_r (blue) and the internal annihilations into 3γ quanta J_0 (black) could be extracted. Also the sum of all three is given (dashed grey), corresponding to the measured Ps fraction f_{Ps}.

as a reflector for Ps arriving back at the entrance. Hence, some of the reflected Ps atoms could also reach the transmission side due to the estimated diffusion length of $\approx 1\,\mu m$, which further increases the Ps yield.

A positronium emission model for transmission targets was developed to reasonably describe experimental data. Fitted parameters obtained for the target produced with Si(111) (specimen C3) made it possible to estimate the maximum achievable amount of Ps in transmission. Applying the obtained fit parameters to hypothetically thinner membranes, which yet have to be produced, allows to extrapolate the maximum Ps yield in transmission that can be achieved with this new technique. The result of the estimation is shown in Fig. 4.17. As one can see, the highest Ps transmission is expected to occur for a target with 1.5 µm thickness. Thinner membrane would probably surpass this, but even if those were producible, they would be extremely difficult to handle as was experienced with similarly thin samples (reported in Ref. [142]). With a 1.5 µm thin membrane, a Ps yield of 25 % in transmission is expected when using a positron implantation energy of 7 keV.

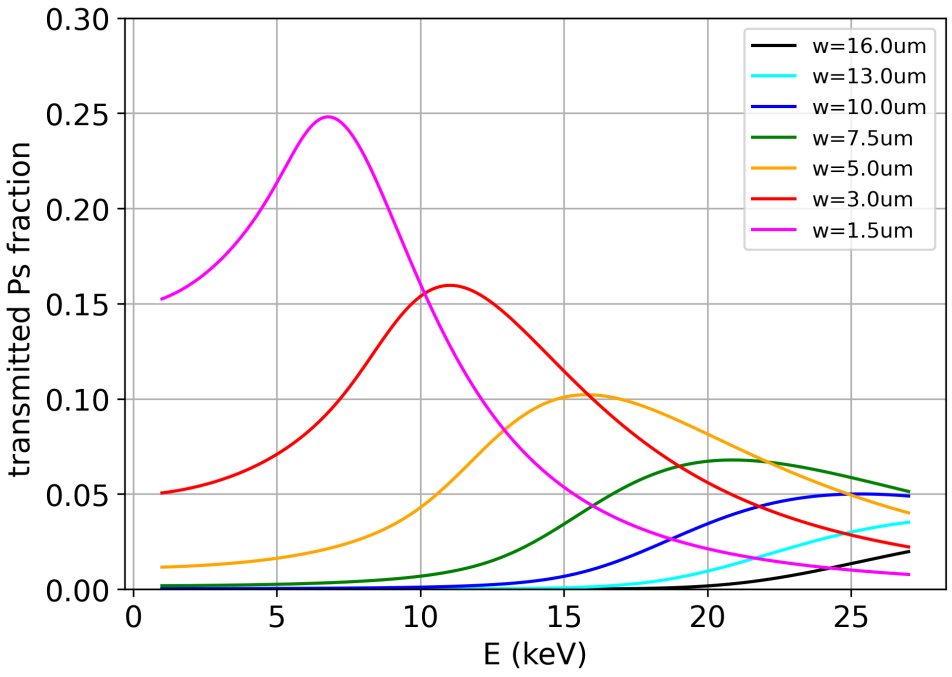

Figure 4.17: Transmitted Ps fraction J_t calculated for different membrane thicknesses. All parameters besides w were kept constant, using the values found for the model describing best the experimental data obtained for sample C3.

It remains to investigate the velocity profiles of transmitted Ps, transversal and normal to the converter, in order to fully characterize these new membranes and their usability in Ps beam experiments.

Chapter 5

Summary and outlook

Experimental research, but also theoretical studies, on antimatter is an intriguing topic in physics. This doctoral thesis has mainly dealt with positronium, the atom-like bound state of a positron and an electron. Being in itself a reason for several technical developments and fundamental measurements, the studies here have been driven by the requirements of the AEgIS experiment at CERN. AEgIS aims to use antihydrogen, the first *stable* neutral antimatter atom that can be thoroughly investigated, in order to answer fundamental questions: how does Earth's gravitational field affect antimatter? Are the inertial mass and the gravitational mass of antimatter identical as postulated by the Weak Equivalence Principle?

The route AEgIS follows for the production of antihydrogen comprises the charge exchange reaction between cold antiprotons from the antiproton decelerator of CERN, and positronium excited to Rydberg-levels in the range of $n \approx 20$. This technique requires excellent control over positronium production and manipulation, which has been achieved during the last few years of doctoral studies. Besides to a profound understanding of the purely leptonic Ps atom and its quantum mechanical properties, two topics were especially emphasized within the present thesis. Firstly, the Rydberg positronium velocimetry along two axis in high magnetic field and cryogenic environment, and secondly the development of positron/positronium converter targets working in transmission geometry with high efficiency. Evolving from and through these two research topics, a tremendous effort has been made in order to contribute to the first successful pulsed production of 110 ± 25 antihydrogen atoms at AEgIS. Next to organizing and running shifts, maintaining the positron system throughout the years and contributing to the scientific output of the collaboration, the author also was deeply involved in the analysis and discussion of central topics of AEgIS such as antiproton and antihydrogen detection, positronium spectroscopy and beam formation.

The Ps velocimetry was performed using two established techniques. The first was a time-of-flight analysis of atoms in free flight, the second was a scan of the transverse velocity profile by means of a narrow-banded laser system with adjustable wavelengths. The novelty here has been that these two scans were achieved with Rydberg-Ps inside a 1 T magnetic field and cryogenic environment at 10 K using a microchannel plate and phosphor screen for imaging the ionized Ps cloud. This quick and efficient detection scheme had to be developed as well, because the first publication by another group regarding the MCP method for detecting Rydberg-Ps [151] only appeared during these velocity studies. Advancing from the experimentally derived Ps velocity profiles peaking between $1.4 \times 10^5\,\mathrm{m\,s^{-1}}$ and $1.8 \times 10^5\,\mathrm{m\,s^{-1}}$, a third scan of different excited Rydberg-levels, ranging from an effective principal quantum number $n_{\mathrm{eff}} = 14$ to 22, characterized the Ps self-ionization due to the motional Stark effect. The asymmetric velocity profile, the n^4 scaling law of the charge exchange cross-section and the limiting velocity for self-ionization, which is proportional to n^{-4}, have been finally combined in order to extract the ideal setting for efficient antihydrogen production at AEgIS. These results have been published in [124], showing that a higher Rydberg-state could have safely been addressed in order to enhance the antihydrogen formation.

From the velocimetry and self-ionization studies, a couple of conclusions for future developments could be drawn. First and most basic, the obtained average velocity was unexpectedly high. Similar targets had shown a better yield of cold positronium reaching room temperature, but the AEgIS sample might have just been an unlucky exception. Furthermore, the nanochannel positron/Ps converter targets improve their efficiency dramatically when occasionally being baked at 100 °C for few hours, which had not been possible for the target installed within the AEgIS apparatus. For the next experimental phase, a well characterized target with high Ps yield at room temperature and a proper heater should be installed. The reduced average velocity combined with an increased Rydberg-level ($n_{\mathrm{eff}} \approx 25 - 30$) is expected to enhance the antihydrogen production tremendously.

The development of transmission positron/Ps converter targets has been a scarcely explored topic. Until now, the most promising technique had been to grow silica columns onto few tens of nm thin graphene films via glancing angle deposition, which is a very interesting technique assuming that one has the materials and machines at hand. In the present work, an alternative method has been developed based on the well-established principles of porous silicon production. In fact, the starting point here was the nanochannel converter target already in use at AEgIS, which comprised electrochemical etching with hydrofluoric acid in order to drill a multitude of nanochannels with diameter of several nanometers. By adding a process step with increased etching current (electropolishing) for several seconds after the main channel production, an entire layer of silicon below the

porous structure was being removed. The resulting thin membrane in the micrometer range could be easily detached and fixed onto a holder, either with some vacuum glue or a grid. Since the nanoporous structure could be produced in the same manner as already explored reflection targets, a similar performance of Ps production and cooling was expected.

A first series of measurements with a high purity germanium detector was performed. The commonly accepted method of evaluating obtained annihilation spectra for the determination of the absolute fraction of emitted positronium was too prone to systematic uncertainties. Therefore, a new technique making use of simulated 2γ and 3γ radiation sources inside the exact geometry of the CDB spectrometer of NEPOMUC had to be developed as published in [101]. The new membranes showed up to 5 % of Ps emission in transmission, with the possibility to increase the yield by producing thinner membranes. Thinning out the porous structures would only be a question of reducing the etching time and at the same time maintaining a certain stability for handling, which puts a limit to approximately 2 µm thin membranes judging from experience with these materials. It would be of great advantage for AE$\bar{\text{g}}$IS, but also other experiments requiring to transport and manipulate positronium, if an efficient converter with high yield of cold Ps in transmission geometry was at hand. The convenient and straight-forward technique presented here can achieve this. Of course, the knowledge of the Ps velocity profile after emission is important, too, which — regardless of the production principle of the transmission converter — will always be the first step when setting up an experiment using membrane converter targets.

Bibliography

[1] B. Lehnert. Problems of matter-antimatter boundary layers. *Astrophys. Space Sci.*, 46:61–71, 1977.

[2] A. D. Sakharov. Violation of CP invariance, C asymmetry, and baryon asymmetry of the universe. *Sov. Phys. Usp.*, 34:392–393, 1991.

[3] L. Boyle, K. Finn, and N. Turok. CPT-Symmetric Universe. *Phys. Rev. Lett.*, 121:251301, 2018.

[4] R. P. Feynman. The Theory of Positrons. *Phys. Rev.*, 76:749, 1949.

[5] A. Alavi-Harati et al. (KTeV Collaboration). Observation of Direct CP Violation in $K_{S,L} \to \pi\pi$ Decays. *Phys. Rev. Lett.*, 83:22, 1999.

[6] B. Aubert et al. (BABAR Collaboration). Direct CP Violating Asymmetry in $B^0 \to K^+\pi^-$ Decays. *Phys. Rev. Lett.*, 93:131801, 2004.

[7] ATLAS Collaboration. Observation of a new particle in the search for the Standard Model Higgs boson with the ATLAS detector at the LHC. *Phys. Lett. B*, 716:1–29, 2012.

[8] S. Chatrchyan, V. Khachatryan, A. M. Sirunyan, A. Tumasyan et al. (CMS Collaboration. Observation of a new boson at a mass of 125 GeV with the CMS experiment at the LHC. *Phys. Lett. B*, 716:30–61, 2012.

[9] CERN. *The CERN accelerator complex - August 2018.* CERN, 2018. https://cds.cern.ch/record/2636343?lde.

[10] M. Turner et al. (AWAKE Collaboration). Experimental Observation of Plasma Wakefield Growth Driven by the Seeded Self-Modulation of a Proton Bunch. *Phys. Rev. Lett.*, 122:054801, 2019.

[11] W. Oelert et al. (ELENA Collaboration). The ELENA Project at CERN. *Acta Phys. Polon. B*, 46:181–189, 2015.

[12] P. A. M. Dirac. A theory of electrons and protons. *Proc. R. Soc. Lond. A*, 126:360–365, 1930.

[13] C. D. Anderson. The positive electron. *Phys. Rev.*, 43:491–498, 1933.

[14] M. Deutsch. Evidence for the Formation of Positronium in Gases. *Phys. Rev.*, 82:455, 1951.

[15] O. Chamberlain, E. Segrè, C. Wiegand, and T. Ypsilantis. Observation of Antiprotons. *Phys. Rev.*, 100:947–950, 1955.

[16] D. B. Cassidy and A. P. Mills Jr. The production of molecular positronium. *Nature*, 449:195–197, 2007.

[17] M. Amoretti et al. (ATHENA collaboration). Production and detection of cold antihydrogen atoms. *Nature*, 419:456–459, 2002.

[18] Gabrielse, G. et al. (ATRAP Collaboration). Background-free observation of cold antihydrogen with field-ionization analysis of its states. *Phys. Rev. Lett.*, 89:213401, 2002.

[19] G. Gabrielse et al. (ATRAP collaboration). First laser-controlled antihydrogen production. *Phys. Rev. Lett.*, 93:263401, 2004.

[20] G. Gabrielse et al. (ATRAP collaboration). Trapped Antihydrogen in Its Ground State. *Phys. Rev. Lett.*, 108:113002, 2012.

[21] G. Andresen, M. Ashkezari, M. Baquero-Ruiz et al. (ALPHA collaboration). Confinement of antihydrogen for 1,000 seconds. *Nature Phys.*, 7:558–564, 2011.

[22] W. Pauli. *Exclusion Principle, Lorentz Group and Reflection of Space-Time and Charge*. Vieweg+Teubner Verlag, 1955. Niels Bohr and the Development of Physics Z.5069.

[23] J. P. Lees et al. (BABAR Collaboration). Observation of Time-Reversal Violation in the B^0 Meson System. *Phys. Rev. Lett.*, 109:211801, 2012.

[24] V. A. Kostelecký and N. Russell. Data tables for Lorentz and CPT violation. *Rev. Mod. Phys.*, 83:11, 2011.

[25] N. Kuroda, S. Ulmer, D. Murtagh et al. (ASACUSA collaboration). A source of antihydrogen for in-flight hyperfine spectroscopy. *Nat. Commun.*, 5:3089, 2014.

[26] M. Ahmadi, B. X. R. Alves, C. J. Baker et al. (ALPHA collaboration). Characterization of the 1S–2S transition in antihydrogen. *Nature*, 557:71–75, 2018.

[27] M. Ahmadi, B. X. R. Alves, C. J. Baker et al. (ALPHA collaboration). Observation of the 1S–2P Lyman-α transition in antihydrogen. *Nature*, 561:211–215, 2018.

[28] S. Sellner et al. (BASE collaboration). Improved limit on the directly measured antiproton lifetime. *New J. Phys.*, 19:083023, 2017.

[29] C. Smorra, S. Sellner, M. Borchert et al. (BASE collaboration). A parts-per-billion measurement of the antiproton magnetic moment. *Nature*, 550:371–374, 2017.

[30] A. Einstein. On the relativity principle and the conclusions drawn from it. *Jahrbuch der Radioaktivität und Elektronik*, 4:411–462, 1907.

[31] P. Touboul et al. *MICROSCOPE* Mission: First Results of a Space Test of the Equivalence Principle. *Phys. Rev. Lett.*, 119:231101, 2017.

[32] C. Amole, M. Ashkezari, M. Baquero-Ruiz et al. (ALPHA collaboration). Description and first application of a new technique to measure the gravitational mass of antihydrogen. *Nat. Commun.*, 4:1785, 2013.

[33] F. Witteborn and W. Fairbank. Experiments to determine the Force of Gravity on Single Electrons and Positrons. *Nature*, 220:436–440, 1968.

[34] T. Kalaydzhyan. Gravitational mass of relativistic matter and antimatter. *Phys. Lett. B*, 751:29–33, 2015.

[35] A. P. Mills Jr. and M. Leventhal. Can we measure the gravitational free fall of cold Rydberg state positronium? *Nucl. Instr. Meth Phys. Res. B*, 192:102–106, 2002.

[36] A. Kellerbauer et al. (AEgIS collaboration). Proposed antimatter gravity measurement with an antihydrogen beam. *Nucl. Instr. Meth. B*, 266:351–356, 2008.

[37] T. Breeden and H. Metcalf. Stark Acceleration of Rydberg Atoms in Inhomogeneous Electric Fields. *Phys. Rev. Lett.*, 47:1726, 1981.

[38] J. H. Hubbell and S. M. Seltzer. Cross section data for electron–positron pair production by photons: a status report. *Nucl. Instr. Meth. B*, 213:1–9, 2004.

[39] A. E. Blinov, V. E. Blinov, A. E. Bondar, et al. Pion pair production in photon-photon collisions. *Z. Phys. C - Particles and Fields*, 53:33–39, 1992.

[40] J. V Allaby et al. Total cross-sections of π^-, k^-, and antiprotons on protons and deuterons in the momentum range 20–65 gev/c. *Phys. Lett. B*, 30(7):500–505, 1969.

[41] D. Boimond, M. Frauchiger, T. Kurtyka, M. Lubrano di Scampamorte, R. Maccaferri, S. Maury, Nikitina L., and J. C. Schnuriger. Consolidation of the 400 kA magnetic horn for AAC antiproton production. *Internal Report CERN/PS 94-02 (AR)*, 1994.

[42] S. Maury. The antiproton decelerator: Ad. *Hyperfine Interactions*, 109:43–52, 1997.

[43] J. Marriner. Stochastic Cooling Overview. *Nucl. Instrum. Meth. A*, 532:11–18, 2004.

[44] G. I. Budker and A. N. Skrinskii. Electron cooling and new possibilities in elementary particle physics. *Usp. Fiz. Nauk.*, 124:561–595, 1978.

[45] S. Cialdi, I. Boscolo, F. Castelli, F. Villa, G. Ferrari, and M. G. Giammarchi. Efficient two-step positronium laser excitation to Rydberg levels. *Nucl. Instr. Meth. B*, 269:1527–1533, 2011.

[46] R. Caravita. Laser apparatus for exciting positronium in AEḡIS positronium spectroscopy experiment. Master Thesis, 2011.

[47] S. Aghion et al. (AEgIS collaboration). Laser excitation of the n = 3 level of positronium for antihydrogen production. *Phys. Rev. A*, 94:012507, 2016.

[48] T. Gigl, L. Beddrich, M. Dickmann, B. Rienäcker, M. Thalmayr, S. Vohburger, and C. Hugenschmidt. Defect imaging and detection of precipitates using a new scanning positron microbeam. *New J. Phys.*, 19:123007, 2017.

[49] S. Seidlmayer, I. Buchberger, M. Reiner, T. Gigl, R. Gilles, H.A. Gasteiger, and C. Hugenschmidt. First-cycle defect evolution of $Li_{1-x}Ni_{1/3}Mn_{1/3}Co_{1/3}O_2$ lithium ion battery electrodes investigated by positron annihilation spectroscopy. *J. Power Sources*, 336:224–230, 2016.

[50] A. M. Alonso, B. S. Cooper, A. Deller, S. D. Hogan, and D. B. Cassidy. Positronium decay from $n = 2$ states in electric and magnetic fields. *Phys. Rev. A*, 93:012506, 2016.

[51] M. Galan. *Table de Radionucléides Na22*. BNM-LNHB/CEA, 2009.

[52] M. Shamsuzzoha Basunia. Nuclear Data Sheets for A = 22. *Nuclear Data Sheets*, 127:69–190, 2015.

[53] P. J. Förster, P. Mascher, A. P. Knights, and P. G. Coleman. Implantation profile of ^{22}Na continuous energy spectrum positrons in silicon. *J. Appl. Phys.*, 101:043702, 2007.

[54] L. Liszkay et al. (GBAR collaboration). Linac-based positron source and generation of a high density positronium cloud for the GBAR experiment. *J. Phys.: Conf. Ser.*, 443:012006, 2013.

[55] C. Hugenschmidt, H. Ceeh, T. Gigl, F. Lippert, C. Piochacz, M. Reiner, K. Schreckenbach, S. Vohburger, J. Weber, and S. Zimnik. Positron Beam Characteristics at NEPOMUC Upgrade. *J. Phys.: Conf. Ser.*, 505:012029, 2014.

[56] A. P. Mills Jr. and E. M. Gullikson. Solid neon moderator for producing slow positrons. *Appl. Phys. Lett.*, 49:1121–1123, 1986.

[57] H. M. Weng, C. C. Ling, C. D. Beling, S. Fung, C. K. Cheung, P. Y. Kwan, and I. P. Hui. Tungsten mesh as positron transmission moderator in a mono-energetic positron beam. *Nucl. Instr. Meth. B*, 225:397–401, 2004.

[58] K. G. Lynn, B. Nielsen, and J. H. Quateman. Development and use of a thin-film transmission positron moderator. *Appl. Phys. Lett.*, 47:239, 1985.

[59] G. Amarendra, K. F. Canter, and D. C. Schoepf. Study of positron yield of W(100) single crystalline foil with in situ surface characterization. *J. Appl. Phys.*, 80:4660, 1996.

[60] J. Störmer, A. Goodyear, W. Anwand, G. Brauer, P. G. Coleman, and W. Triftshäuser. Silicon carbide: a new positron moderator. *J. Phys.: Condens. Matter*, 8:89–94, 1996.

[61] C. C. Ling, H. M. Weng, C. D. Beling, and S. Fung. Experimental investigation of slow-positron emission from 4H-SiC and 6H-SiC surfaces. *J. Phys.: Condens. Matter*, 14:6373–6381, 2002.

[62] A. M. M. Leite, P. Debu, P. Pérez, J-M. Reymond, Y. Sacquin, B. Vallage, and L. Liskay. Efficient positron moderation with a commercial 4H-SiC epitaxial layer. *J. Phys.: Conf. Series*, 791:012005, 2017.

[63] B. Rienäcker. Investigation of positron/positronium converter targets at AEgIS (CERN). Master Thesis, 2015. Open Access http://gateway-bayern.de/BV043045610.

[64] S. Aghion et al. (AEgIS collaboration). Positron bunching and electrostatic transport system for the production and emission of dense positronium clouds into vacuum. *Nucl. Instr. Meth. B*, 362:86–92, 2015.

[65] C. M. Surko, M. Leventhal, and A. Passner. Positron Plasma in the Laboratory. *Phys. Rev. Lett.*, 62:901–904, 1989.

[66] J. Mitteneder, M. Dickmann, G. Kögel, W. Egger, P. Sperr, and G. Dollinger. Micrometer positron beam characterization at the Scanning Positron Microscope Interface. *J. Phys.: Conf. Series*, 791:012006, 2017.

[67] R. G. Greaves and C. M. Surko. Radial compression and inward transport of positron plasmas using a rotating electric field. *Physics of Plasmas*, 8:1879–1885, 2001.

[68] R. G. Greaves and C. M. Surko. Inward Transport and Compression of a Positron Plasma by a Rotating Electric Field. *Phys. Rev. Lett.*, 85:1883–1886, 2000.

[69] A Pineda and J. Soto. Potential NRQED: The positronium case. *Phys. Rev. D*, 59:016005, 1998.

[70] D. B. Cassidy. Experimental proress in positronium laser physics. *Eur. Phys. J. D*, 72:53, 2018.

[71] A. Ore and J. L. Powell. Three-Photon Annihilation of an Electron-Positron Pair. *Phys. Rev.*, 75:1696, 1949.

[72] Y. Kataoka, S. Asai, and T. Kobayashi. First test of O(alpha2) correction of the orthopositronium decay rate. *Phys. Lett. B*, 32:219–223, 2008.

[73] D. W. Gidley, A. Rich, E. Sweetman, and D. West. New precision measurements of the decay rates of singlet and triplet positronium. *Phys. Rev. Lett.*, 49:525–528, Aug 1982.

[74] G. S. Adkins, N. M. McGovern, R. N. Fell, and J. Sapirstein. Two-loop corrections to the decay rate of parapositronium. *Phys. Rev. A*, 68:032512, 2003.

[75] G. S. Adkins, R. N. Fell, and J. Sapirstein. Two-loop corrections to the decay rate of orthopositronium. *Annals of Physics*, 295:136–193, 2002.

[76] A. I. Alekseev. Three-photon annihilation of positronium in the p-state. *Sov. Phys. JETP*, 36:1312, 1959.

[77] A. I. Alekseev. Two-photon annihilation of positronium in the p-state. *Sov. Phys. JETP*, 34:826, 1958.

[78] V. Weisskopf and E. Wigner. Berechnung der natürlichen Linienbreite auf Grund der Diracschen Lichttheorie. *Z. Physik*, 63:54–73, 1930.

[79] S. M. Curry. Combined Zeeman and Motional Stark Effects in the First Excited State of Positroninm. *Phys. Rev. A*, 7:447–450, 1973.

[80] F. Castelli, I. Boscolo, S. Cialdi, M. G. Giammarchi, and D. Comparat. Efficient positronium laser excitation for antihydrogen production in a magnetic field. *Phys. Rev. A*, 78:052512, 2008.

[81] R. Caravita. Towards measuring gravity on neutral antimatter. PhD Thesis, 2017.

[82] F. Villa. Laser system for positronium excitation to Rydberg levels for experiment. PhD Thesis, 2011.

[83] H. Grotch and R. Kashuba. Magnetic Interactions of One-Electron Atoms and of Positronium. *Phys. Rev. A*, 8:575, 1973.

[84] P. J. Schultz and K. G. Lynn. Interaction of positron beams with surfaces, thin films and interfaces. *Rev. Mod. Phys.*, 60(3):701–779, 1988.

[85] J. W. Humberston. Positronium - its Formation and Interaction with Simple Systems. *Advances in Atomic and Molecular Physics*, 22:1–36, 1986.

[86] S. Valkealahti and R. M. Nieminen. Monte-Carlo calculations of keV electron and positron slowing down in solids. *Appl. Phys. A*, 32:95–106, 1983.

[87] J. Dryzek and P. Horodek. GEANT4 simulation of slow positron beam implantation profiles. *Nucl. Instr. Meth. B*, 266:4000–4009, 2008.

[88] R. M. Nieminen and J. Oliva. Theory of positronium formation and positron emission at metal surfaces. *Phys. Rev. B*, 22:2226–2247, 1980.

[89] E. Soininen, J. Mäkinen, D. Beyer, and P. Hautojärvi. High-temperature positron diffusion in Si, GaAs and Ge. *Phys. Rev. B*, 46:13104–13118, 1992.

[90] D. B. Cassidy, S. H. M. Deng, H. K. M. Tanaka, and A. P. Mills Jr. Single shot positron annihilation lifetime spectroscopy. *Appl. Phys. Lett.*, 88:194105, 2006.

[91] L. Penasa, L. Di Noto, M. Bettonte, S. Mariazzi, G. Nebbia, and R. S. Brusa. Positron bunching system for producing positronium clouds into vacuum. *J. Phys.: Conf. Ser.*, 505:012031, 2014.

[92] S. Mariazzi, P. Bettotti, and R. S. Brusa. Positronium cooling and emission in vacuum from nanochannels at cryogenic temperature. *Phys. Rev. Lett.*, 104:243401, 2010.

[93] D. B. Cassidy, T. H. Hisakado, H. W. K. Tom, and A. P. Mills Jr. Positronium formation via excitonlike states on Si and Ge surfaces. *Phys. Rev. B*, 84:195312, 2011.

[94] S. Agostinelli et al. Geant4 - a simulation toolkit. *Nucl. Instr. Meth. A*, 506:205–303, 2003.

[95] S. Marder, V. W. Hughes, C. S. Wu, and W. Bennett. Effect of an Electric Field on Positronium Formation in Gases: Experimental. *Phys. Rev.*, 103:1258, 1956.

[96] A. P. Mills Jr. Positronium Formation at Surfaces. *Phys. Rev. Lett.*, 41:1828, 1978.

[97] H. H. Jorch, K. G. Lynn, and T. McMullen. Positron diffusion in germanium. *Phys. Rev. B*, 30:93–105, 1984.

[98] A. Dupasquier and A. Zecca. Atomic and Solid-State Physics Experiments with Slow-Positron Beams. *Riv. Nuovo Cim.*, 8:1–73, 1985.

[99] E. Soininen, A. Schwab, and K. G. Lynn. Positron-induced Auger-electron study of the Ge(100) surface: Positron thermal desorption and surface condition. *Phys. Rev. B*, 43:10051–10061, 1991.

[100] H. Huomo, E. Soininen, and A. Vehanen. Analysis of Positron Diffusion Data. *Appl. Phys, A*, 49:647–658, 1989.

[101] B. Rienäcker, T. Gigl, G. Nebbia, F. Pino, and C. Hugenschmidt. Absolute fraction of emitted Ps determined by GEANT4-supported analysis of gamma spectra. *Phys. Rev. A*, 102:062212, Dec 2020.

[102] C. Hugenschmidt, B. Löwe, J. Mayer, P. Piochacz, P. Pikart, R. Repper, M. Stadlbauer, and K. Schreckenbach. Unprecedented intensity of a low-energy positron beam. *Nucl. Instr. Meth. A*, 593:616–618, 2008.

[103] V. R. Vanin, R. M. de Castro, and E. Browne. *Table de Radionucléides Eu152.* BNM-LNHB/CEA, 2001–2004.

[104] N. Buarissa, B. Abbar, J. P. Dufour, N. Amrane, and H. Aourag. Work function and energy levels of positrons in elemental semiconductors. *Mat. Chem. Phys*, 44:267–272, 1996.

[105] J. Zhang, S. Fan, J. Liu, C. Liu, B. Ye, X. Gao, and D. Yao. Evaluation of point-core approximation effect on the positron energy levels in diamond structure solids. *Computational Materials Science*, 141:75–81, 2018.

[106] A. Camper et al. (AEgIS collaboration). Imaging a positronium cloud in a 1 Tesla. *EPJ Web Conf.*, 198:00004, 2019.

[107] J. Main, M. Schwacke, and G. Wunner. Hydrogen atom in combined electric and magnetic fields with arbitrary mutual orientations. *Phys. Rev. A*, 57:1149–1157, 1998.

[108] A. Landè. Termstruktur und Zeemanneffekt der Multipletts. *Z. Physik*, 15:189–205, 1923.

[109] M. K. Oberthaler, S. Bernet, E. M. Rasel, J. Schmiedmayer, and A. Zeilinger. Inertial sensing with classical atomic beams. *Phys. Rev. A*, 54(4):3165–3176, 1996.

[110] F. Guatieri. Production and excitation of cold Ps for anti-H formation by charge exchange: towards a gravitational measurement on antimatter. PhD Thesis, 2018.

[111] A. Demetrio. Feasibility of a gravity measurement on antimatter using a Talbot-Lau interferometer. PhD Thesis, 2018.

[112] M. Boström and Bo E. Sernelius. van der Waals energy of an atom in the proximity of thin metal films. *Phys. Rev. A*, 61:052703, 2000.

[113] G. Vidali and M. W. Cole. The interaction between an atom and a surface at large separation. *Surf. Sci.*, 110:10–18, 1981.

[114] J. Mitroy, M. S. Safronova, and C. W. Clark. Theory and applications of atomic and ionic polarizabilities. *J. Phys. B: At. Mol. Phys.*, 43:202001, 2010.

[115] T. P. Hezel, J. J. Leventhal, et al. Classical view of the Stark effect in hydrogen atoms. *American J. Phys.*, 60:324, 1992.

[116] C. Fabre, M. Gross, J. M. Raimond, and S. Haroche. Measuring atomic dimensions by transmission of Rydberg atoms through micrometre size slits. *J. Phys. B: At. Mol. Phys.*, 16:671–677, 1983.

[117] M. W. Kohlhoff. Interaction of Rydberg atoms with surfaces. *Eur. Phys. J. Spec. Top.*, 225:3061–3085, 2016.

[118] C. Amsler et al. (AEgIS collaboration). Pulsed Production of Antihydrogen. *Commun. Phys.*, 4:19, 2021.

[119] D. Krasnický, R. Caravita, C. Canali, and G. Testera. Cross-section for Rydberg Antihydrogen Production via Charge Exchange Between Rydberg Positronium and Antiprotons in Magnetic Field. *Phys. Rev. A*, 94(94):022714, 2016.

[120] A. S. Kadyrov, I. Bray, M. Charlton, and I. I. Fabrikant. Quantum suppression of antihydrogen formation in positronium-antiproton scattering. *Nat. Commun.*, 8(1544), 2017.

[121] D. Krasnický, G. Testera, and N. Zurlo. Comparison of classical and quantum models of anti-hydrogen formation through charge-exchange. *J. Phys. B: At. Mol. Opt. Phys.*, 52:115202, 2019.

[122] R. Caravita et al. (AEgIS collaboration). Hybrid imaging and timing Ps laser excitation diagnostics for pulsed antihydrogen production. *Acta Phys. Pol. A*, 2019. submitted.

[123] R. Caravita, S. Mariazzi et al. (AEgIS collaboration). Positronium Rydberg excitation diagnostic in a 1T cryogenic environment. *AIP Conf. Proc.*, 2182:030002, 2019.

[124] M. Antonello et al. (AEgIS collaboration). Rydberg-positronium velocity and self-ionization studies in a 1t magnetic field and cryogenic environment. *Phys. Rev. A*, 102:013101, Jul 2020.

[125] D. B. Cassidy, P. Crivelli, T. H. Hisakado, L. Liszkay, V. E. Meligne, P. Perez, H. W. K. Tom, and A. P. Mills Jr. Positronium cooling in porous silica measured via Doppler spectroscopy. *Phys. Rev. A*, 81:039904, 2010.

[126] R. H. Howell, I. J. Rosenberg, M. J. Fluss, R. E. Goldberg, and R. B. Laughlin. Positronium time-of-flight spectroscopy of dissimilar metals. *Phys. Rev. B*, 35:5303–5306, 1987.

[127] D. B. Cassidy, T. H. Hisakado, V. E. Meligne, H. W. K. Tom, and A. P. Mills Jr. Delayed emission of cold positronium from mesoporous materials. *Phys. Rev. A*, 82:052511, 2010.

[128] A. Deller, B. S. Cooper, T. E. Wall, and D. B. Cassidy. Positronium emission from mesoporous silica studied by laser-enhanced time-of-flight spectroscopy. *New J. Phys.*, 17:043059, 2015.

[129] F. Guatieri, S. Mariazzi, and R. S. Brusa. Monte Carlo simulation of the positronium cooling inside a nanochanneled structure. *Eur. Phys. J. D*, 72:198, 2018.

[130] S. D. Hogan. Rydberg-Stark deceleration of atoms and molecules. *EPJ Techn. Instrum.*, 3:2, 2016.

[131] T. F. Gallagher. *Rydberg Atoms*. Cambridge University Press, 2005.

[132] F. Castelli. The positronium atom as a benchmark for rydberg excitation experiments in atomic physics. *Eur. Phys. J. Spec. Top.*, 203, 2012.

[133] E. Lazzarini. A comprehensive model for positronium formation and related phenomena of its inhibition and enhancement. *Radiat. Phys. Chem.*, 28:49–54, 1986.

[134] Y. Nagashima, Y. Morinaka, T. Kurihara, Y. Nagai, T. Hyodo, T. Shidara, and K. Nakahara. Origins of positronium emitted from SiO_2. *Phys. Rev. B*, 58:12676, 1998.

[135] A. M. Alonso, L. Gurung, B. A. D. Sukra, S. D. Hogan, and D. B. Cassidy. State-selective electric-field ionization of Rydberg positronium. *Phys. Rev. A*, 98:053417, 2018.

[136] Koji Michishio, Susumu Kuma, Yugo Nagata, Luca Chiari, Taro Iizuka, Riki Mikami, Toshiyuki Azuma, and Yasuyuki Nagashima. Threshold Photodetachment Spectroscopy of the Positronium Negative Ion. *Phys. Rev. Lett.*, 125:063001, 2020.

[137] S. Van Petegem, C. Dauwe, T. Van Hoecke, J. De Baerdemaeker, and D. Segers. Diffusion length of positrons and positronium investigated using a positron beam with longitudinal geometry. *Phys. Rev. B*, 70:115410, 2004.

[138] S. Mariazzi, P. Bettotti, S. Larcheri, L. Toniutti, and R. S. Brusa. High positronium yield and emission into the vacuum from oxidized tunable nanochannels in silicon. *Phys. Rev. B*, 81:235418, 2010.

[139] F. Guatieri, S. Mariazzi, and R. S. Brusa. Simulating Positron to Positronium Conversion in Nanostructured Materials. *Acta Phys. Pol. A*, 137:113–117, 2020.

[140] S. L. Andersen, R. R. Johansen, J. B. Overgaard, et al. Positronium Formation from Porous Silica in Backscattering and Transmission Geometries. *Eur. Phys. J. D*, 68:124, 2014.

[141] S. L. Andersen, D. B. Cassidy, J. Chevallier, B. S. Cooper, A. Deller, T. E. Wall, and U. I. Uggerhøj. Positronium emission and cooling in reflection and transmission from thin meso-structured silica films. *J. Phys. B: At. Mol. Opt. Phys.*, 48(20):204003, 2015.

[142] S. Aghion et al. (AEgIS collaboration). Characterization of a transmission positron/positronium converter for antihydrogen production. *Nucl. Instr. Meth. B*, 407:55–66, 2017.

[143] R. L. Smith and Collins S. D. Porous silicon formation mechanisms. *J. Appl. Phys*, 71, 1992.

[144] O. Bisi, S. Ossicini, and L. Pavesi. Porous silicon: a quantum sponge structure for silicon based optoelectronics. *Surf. Science Rep.*, 38:1–126, 2000.

[145] V. Lehmann. *Electrochemistry of Silicon: Instrumentation, Science, Materials and Applications*. Wiley, 2002.

[146] R. L. Smith and S. D. Collins. Generalized model for the diffusion-limited aggregation and Eden models of cluster growth. *Phys. Rev. A*, 39:5409–5413, 1989.

[147] M. I. J. Beale, N. G. Chew, M. J. Uren, A. G. Cullis, and J. D. Benjamin. Microstructure and formation mechanism of porous silicon. *Appl. Phys. Lett*, 46:86, 1985.

[148] R. E. Oosterbroek et al. Etching Methodologies in 111-Oriented Silicon Wafers. *Journal of Microelectromechanical Systems*, 9:390–398, 2000.

[149] C.A. Palacio, J. De Baerdemaeker, D. Van Thourhout, and C. Dauwe. Emission of positronium in a nanometric pmma film. *Applied Surface Science*, 255(1):197 – 200, 2008. Proceedings of the Eleventh International Workshop on Slow Positron Beam Techniques for Solids and Surfaces.

[150] R. S. Brusa, L. Di Noto, S. Mariazzi, and G. Nebbia. Positronium cooling at cryogenic temperature for advanced experiments. *J. Phys.: Conf. Ser.*, 505:012038, 2014.

[151] O. Meyer, O. M. Jones, J. C. Giacalone, J. Y. Pascal, D. Raulin, H. Xu, M. H. Aumeunier, R. Baude, A. Escarguel, C. Gil, J. H. Harris, J.-C. Hatchressian, C. C. Klepper, S. Larroque, Ph. Lotte, Ph. Moreau, B. Pégourié, and S. Vartanian. Development of visible spectroscopy diagnostics for W sources assessment in WEST. *Review of Scientific Instruments*, 87(11):11E309, 2016.

Appendix A

Acronyms

AD Antiproton Decelerator

AEGIS Antimatter Experiment: Gravity, Interferometry, Spectroscopy

ALPHA Antihydrogen Laser PHysics Apparatus

ASACUSA Atomic Spectroscopy And Collisions Using Slow Antiprotons

ATRAP Antihydrogen TRAP

AWAKE Advanced WAKefield Experiment

BASE Baryon Antibaryon Symmetry Experiment

BW BandWidth

CAD Computer-Aided Design

CERN Organisation Européenne pour la Recherche Nucléaire

CDBS Coincidence Doppler-Broadening Spectroscopy

CMOS Complementary Metal–Oxide Semiconductor

CPT Charge, Parity, Time

DAQ Data AcQuisition

ELENA Extra Low ENergy Antiprotons

EP Equivalence Principle

FWHM Full-Width-Half-Maximum

GBAR Gravitational Behaviour of Antihydrogen at Rest

GEANT4 GEometry ANd Tracking software toolkit

GLAD GLancing Angle Deposition

HF Hydrofluoric acid

HPGe High Purity Germanium

HWHM Half-Width-Half-Maximum

IR InfraRed

ISOLDE Isotope Separator On Line DEvice

LEP Large Electron-Positron Collider

LHe Liquid Helium

LN2 Liquid Nitrogen

MACOR MAchinable ceramic by CORning Inc.

MC Monte Carlo

MCA MultiChannel Analyzer

MCP MicroChannel Plate

NASA National Aeronautics and Space Administration

NEPOMUC NEutron induced POsitron source MUniCh

Nd:YAG Neodymium doped Yttrium Aluminium Garnet

NMR Nuclear Magnetic Resonance

OPA Optical Parametric Amplifier

OPG Optical Parametric Generator

PALS Positron Annihilation Lifetime Spectroscopy

PET Positron Emission Tomography

PM Penning-Malmberg

PMMA PolyMethyl-MethAcrylate

PMT Photo Multiplier Tube

Ps Positronium

o-Ps Ortho-positronium

p-Ps Para-positronium

Ps* Rydberg-positronium

QED Quantum Electrodynamics

RW Rotating Wall

SEM Scanning Electron Microscope

SFG Sum Frequency Generator

SSPALS Single-Shot Positron Annihilation Lifetime Spectroscopy

TOF Time-Of-Flight

UHV Ultra High Vacuum

UV Ultraviolett

WEP Weak Equivalence Principle

Special thanks

Finally I wish to express my heartfelt gratitude to many wonderful people. Without them, their support, friendship and conviction this work would never have seen the light of the world:

First of all, I would like to thank Christoph Hugenschmidt for supervising me through my Bachelor studies at NEPOMUC in Munich, for employing me several years and then guiding me towards this day, where I finish my PhD. Thank you, Christoph, for the inspiring scientific discussions which always showed me how many more details can still be discovered — even if a topic seemed quite exhausted at the first glance; for all the beamtime you allocated for me whenever the research reactor was on; for the freedom you granted me during my PhD, especially because I spent my time mostly at CERN. There are two other people formerly working at NEPOMUC to whom I am also very grateful: Christian Piochacz, who guided me through my first steps as a positron novice. He showed me my first positron-electron annihilation event on an oscilloscope. That had quite an impact, as one might guess now. Thomas Gigl, to whom I sometimes referred as my secret joker. Whenever I suddenly needed a 3D-printed clip for some plastic boxes or — a bit more sophisticated — an aluminum holder for my targets, he just made it. Within five minutes. Impressive. Of course I also thank all the others at NEPOMUC for the good and interesting times we spent: Sebastian Vohburger, Marcel Dickmann, Markus Reiner, Phillip Pikart, Samantha Zimnik, Michael Leitner, Markus Singer, Thomas Schmitt, Johannes Mitteneder, Matthias Dodenhöft, Vassily Burwitz and all the others who I mainly met on the Christmas parties.

Now it is time to thank the many people who are my colleagues and friends at CERN. Thank you Michael Doser, for giving a talk about antihydrogen production in Munich, just down the street where I was living — no later than a few days after I wrote to you asking about the possibility of a Master's thesis within AEgIS. I know it was a coincidence, but that makes it even more incredible. Of course I decided to join and when the time for my PhD came, you just had an open doctoral student's fellowship under your sleeve. Here I knew: When AEgIS created the first antihydrogen atoms, I would be part of it. There

are far too many good memories associated with people and situations along the way to write them all down here. Still, at the very least, I am greatly indebted to you, Sebastiano Mariazzi, for you taught me how to save the world (alias how to do positronium physics). Your mentorship, always calm, sophisticated and accommodating, was only surpassed by your friendship. Thanks for more than 900 joyful memories. Then, I bow to you, Stefan Haider, aiding me through these years with lectures about cabling and vacuum-related methods, but especially for tirelessly supplying chocolate and coffee. Notably, the only two (Stefan) rules were: The last piece of chocolate belongs to the person who bought it (not defining what 'piece' actually means) and students of any kind never pay for coffee. I also thank you, Ruggero Caravita, Antoine Camper, Lillian Smestad, Olga Khalidova, Craig Evans and Philip Hackstock, for not only being my inspiring colleagues, but also dear friends with whom I spent a lot of time — for example in the wine-fields, plucking grapes, taking part in pub quizzes or just going out for a beer in between two consecutive hour-long antihydrogen production cycles. Many thanks also to the other positron-ducklings, as we were occasionally referred to: Ola Kenji Forslund, Ine Jernelev, Lisa Marx, Laura Resch, Milena Vujanovic. Together, we survived power-cuts which left us in utter darkness near the experiment, and operated liquid helium transfers until all of us were really cool with it (that was a so-called Benji joke, not to be confused with the Benji oven, whose purpose had been to bake out dirty displacers and save the day).

Here, I wish also to express my heartfelt gratitude to Roberto Brusa, Giancarlo Nebbia and Gemma Testera, who enabled many things on the road in a really helpful way making sure there was progress. A progress that would have not been possible if not for the efforts of many other (former) colleagues inside the collaboration such as Germano Bonomi, Chloe Malbrunot, Nicola Zurlo, Lilian Nowak, Fabrizio Castelli, Alexander Ekman, Luca Penasa, Francesco Guatieri, Daniel Comparat, Daniel Krasnický, Angela Gligorova, Ingmari Tietje, Pauline Yzombard (Tea outside?), Mattia Fani, Lisa Glöggler and the whole BOREALIS team: Sebastian Gerber, Christian Zimmer, Julian Fesel, Alexander Hinterberger, Emanuel Oswald. Thank you all.

More than a simple *thank you* could ever tell, I raise my head, look into the eyes of my dear mother, my dear father and my dear sister and with a tear of joy I say: I love you, thank you for all your support, your belief in me! You leveled ever so gently my path towards this goal and built a strong, unwavering bound between us on which I can always rely. Thank you so much, also for answering my first questions about physics at the age of five, when it puzzled me and my curiosity what lightening actually is and why it occurs in this impressive manner. And of course I thank you, too, dear aunt Claudi, because you were my first shining example of how it would look like to complete a doctoral degree.

The greatest impact on my life had you, Tanja, for you became my dear love when we first met in the student's dormitory in Munich. I thought I was well prepared, but nothing could have readied me for you, because you are quite unique. In those years of my PhD you chased the same goal for yourself, with quite some more obstacles in the way, following me to the local area of CERN and providing me a home, a family to always come back to. Let me tell you, Tanja, I love you. Thanks for bringing color into my life.

At this point, I need to say only one last thing. My PhD may have been quite some work and it felt like a big project, but in fact, one more 'project' has been growing for the past five years and it is greater than any other: It is you, Dunaja, my beloved daughter.

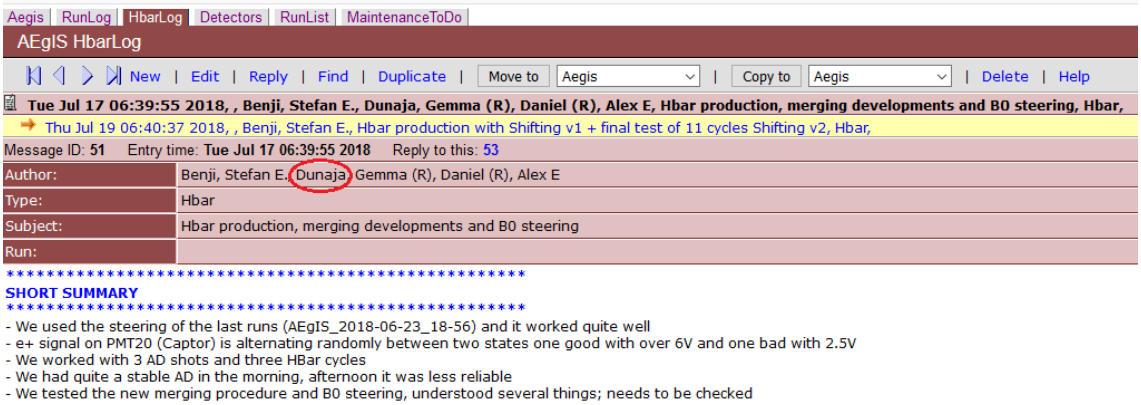

Figure 5.1: Proof that Dunaja helped creating antihydrogen.